Multiscale modelling of axon durotaxis



Christoforos Kassianides

Jesus College

University of Oxford

A thesis submitted for the degree of

Doctor of Philosophy

Trinity 2026

Abstract

During development, axons navigate to their targets in part by responding to spatial variation in substrate stiffness, a phenomenon termed *durotaxis*. Yet, existing theories of axon guidance lack a framework that connects environmental stiffness, focal-adhesion-mediated traction generation, and the deformation and reorientation of the axon shaft. This thesis develops such a framework, built on the hypothesis that guidance cues act by modulating growth cone traction, which in turn reorients the axon through its mechanical response.

Our analysis proceeds from the microscale upwards. The motor–clutch system on a deformable substrate is formulated as a differential Chapman–Kolmogorov equation for the full linker-extension distribution. The single-linker steady state is solved exactly, giving a statistical characterisation of dynamical regimes previously identified only from simulated trajectories; a mean-field treatment of the many-linker case yields an explicit expression for the optimal substrate stiffness and the conditions under which it exists. Coupling this traction law to a remodelling beam model of the axon shaft gives the Axon-Beam-Clutch model, which produces both positive and negative durotaxis and predicts a guidance mode not previously described: convergence onto trajectories parallel to lines of optimal stiffness, a behaviour that depends on the finite spatial extent of the axon and therefore on long-range mechanical sensing by the shaft.

The bending stiffness of the axon, a parameter required by the model, is inferred from pulling experiments using an extensible beam description in place of the conventional elastic string. The same data are shown to support either of the two estimates reported in the literature, $\mathcal{B} \sim 10^{-21}\,\mathrm{Nm}^2$ and $\mathcal{B} \sim 10^{-19}\,\mathrm{Nm}^2$, depending on whether the axon is treated as isotropic.

The Axon-Beam-Clutch framework is then applied to neurite interaction with sharp stiffness interfaces, guidance of Xenopus retinal ganglion cell axons along the optic tract, and segmented outgrowth of motor axons in the peripheral nervous system, in each case identifying what traction-based guidance can account for in isolation.

Acknowledgements

My five years at Oxford have been the most rewarding and fulfilling of my life so far. I would like to thank the following people, who made these years special, and without whose help this thesis would not have been finished:

Above all else, my supervisor, Alain Goriely, for his mentorship and guidance.

Hadrien Oliveri, for our years of collaboration.

Nicola Kirkham, for her administrative and moral support.

My friends who made Oxford such a magical place: Christoffer Gretarsson Alexandersen, Kyu Min Huh, Francis Bertschinger, Marina Kathidjioti, Andrew Ó hEachteirn, Raphael Bradenbrink, Jake Beck, Luka Kovacevic, Lucas Mangas, Edgar Sucar, Frank Tarimo, Andronikos Kassianides, Lucas Irwin.

My friends who were always there when I needed a break from Oxford: Eleana Kasoulide, Alexandros Constantinou, Ioannis Irinarchos, Matthew Beatty, Aristides Artemiou.

My parents, Symeon and Beatriz; my brothers, Dimitris and Andronikos; and my grandmother, Gloria — for their love and encouragement.

I would also like to thank the Engineering and Physical Sciences Research Council for funding my research through a studentship under project reference 2580825.

Thank you all.

Contents

1 Introduction **1**

1.1 Neurons and axon guidance 1

1.2 The growth cone 2

1.3 Developmental roles of axon durotaxis 3

1.4 Proposed mechanisms of axon durotaxis 4

1.5 The role of traction forces in axon guidance 4

1.6 Mathematical and computational modelling of focal adhesion dynamics and traction generation 6

1.7 Mathematical and computational models of axon guidance 9

1.8 Summary of contributions and thesis structure 13

2 An analytical study of focal adhesion traction - stiffness curves. **15**

2.1 Overview 15

2.2 The system: Focal adhesions 17

2.3 The basic equations: Chapman-Kolmogorov equation for the focal adhesion system 19

2.4 Discussion of the different cases to be studied 22

2.5 Case 1: $N_T = 1$ 23

2.5.1 Steady state distribution 24

2.5.2 Classification of steady state solutions 24

2.5.3 Traction and optimal stiffness 28

2.6 Case 2: Mean-field - Rigid substrate 29

2.6.1 Steady state distribution 30

2.6.2 Classification of solutions 31

2.6.3 Multiple solutions and break down of the mean-field approximation 34

2.6.4 Comparison with exact $\chi > 0$ 35

2.7 Case 3: Mean-field - Deformable substrate 36

2.7.1 Steady State Analysis - Constant, homogeneous extension rate . 37

2.7.2 Properties of T 38

2.7.3 Traction-stiffness curves . . . 39
2.7.4 Derivation of an expression for the optimal stiffness . . . 40
2.7.5 Behaviour of F_{crit} . . . 42
2.7.6 Behaviour of χ^* . . . 42
2.7.7 Deriving an expression for $T''(\chi^*)$ . . . 43
2.7.8 Behaviour of $T''(\chi^*)$ . . . 44
2.7.9 Speed-imposition interpretation of myosin action . . . 45
2.8 Literature comparison . . . 46
2.8.1 Qualitative regimes of system trajectories . . . 47
2.8.2 Rigid substrate: Mean field . . . 48
2.8.3 Optimal Stiffness . . . 49
2.9 Conclusion . . . 56

3 The Axon - Beam - Clutch (ABC) model and simple motions 58
3.1 Overview . . . 58
3.2 Growth Cone force . . . 59
3.3 The Axon Beam model . . . 61
3.3.1 Morphoelastic rod model . . . 62
3.3.2 Tip growth approximation . . . 65
3.3.3 Derivation of the beam model . . . 66
3.3.4 Numerics and implementation details . . . 71
3.4 Constant growth cone force - Timescale of axon turning . . . 73
3.5 Motion in a stiffness field of constant gradient . . . 79
3.5.1 General motion away from lines of optimal stiffness . . . 80
3.5.2 Motion near lines of optimal stiffness . . . 81
3.5.3 A reduced axon model - The importance of long range sensing by the axon . . . 83
3.6 Conclusion . . . 85

4 On the Estimation of Axonal Mechanical Properties Using Beam Models 87
4.1 Introduction . . . 87
4.1.1 Estimating $\mathcal{B}$ from axon-pulling experiments . . . 88
4.1.2 A mechanistic explanation for the discrepancy in estimates of $\mathcal{B}$ . . . 88
4.1.3 Experimental data . . . 89
4.1.4 Prior work on Three Point Bending Tests . . . 90
4.2 Overview . . . 90
4.3 Description of the pulling experiment . . . 91

4.4 Inference procedure . . . 91
4.5 Discussion of the different models . . . 92
4.6 Extensible beam model for the axon . . . 94
4.6.1 Body forces . . . 95
4.6.2 Boundary conditions . . . 95
4.6.3 General Boundary Value Problem . . . 96
4.6.4 Symmetric ansatz for the extensible beam equation . . . 97
4.6.5 Midpoint displacement as a function of force . . . 97
4.6.6 Non-dimensionalization of the beam system . . . 98
4.6.7 Series expansion of the beam state variables in f . . . 99
4.6.8 Series expansion coefficients for $F(H)$: Pinned . . . 100
4.6.9 Series expansion coefficients for $F(H)$: Clamped . . . 100
4.7 Elastic String Model . . . 100
4.8 Inferences: Elastic String . . . 101
4.9 Inferences: Isotropic Beam . . . 102
4.9.1 Pinned case . . . 102
4.9.2 Clamped case . . . 103
4.10 Anisotropic Beam - Zero Initial Strain (ZS) . . . 103
4.10.1 Pinned case . . . 103
4.10.2 Clamped case . . . 104
4.11 Summary of determined models . . . 104
4.12 Anisotropic Beam with Non-Zero Initial Strain . . . 105
4.13 Conclusion . . . 108

5 ABC Applications 109
5.1 Overview . . . 109
5.2 Reflection and refraction at a straight stiffness interface . . . 110
5.2.1 Reflection and refraction curves, critical angle . . . 112
5.2.2 Time Irreversibility . . . 116
5.3 Sharp Boundary Experiment . . . 122
5.4 Optic Tract . . . 128
5.5 Segmented outgrowth of motor axons in the PNS . . . 134
5.5.1 2D Somite stiffness field . . . 134
5.5.2 Segmentation efficiency . . . 137
5.5.3 Initial conditions . . . 140
5.5.4 Results . . . 140
5.6 Conclusion . . . 145

6 Conclusion **149**
6.1 Summary of results . . . 149
6.2 Limitations . . . 152
6.3 Future work . . . 153

A Focal Adhesions **156**
A.1 Numerical simulation of the focal adhesion dynamics . . . 156
A.2 Properties of N, constant extension case . . . 157
A.3 Properties of $\tau(d_1, k)$ . . . 158
A.4 Properties of T . . . 160
A.5 Behaviour of F_{crit} . . . 161
A.6 Behaviour of χ^* as a function of $k_{\text{on}}, k_{\text{off}}$ . . . 165
A.7 Properties of $\frac{\partial^2 T}{\partial {v_e}^2}(v^*)$ . . . 166
A.8 Formulation with constant binding rate . . . 167

B Bending stiffness **169**
B.1 Elastic String Model: Extracting load-deflection curves from Bernal et al. [9] . . . 169
B.2 Extracting A and L_x . . . 170
B.3 Resolution of the identified inconsistency . . . 173
B.4 Extensible beam perturbation series for $f \ll 1$ . . . 176
B.5 Anisotropic model: Neurite 3 . . . 176

Bibliography **176**

Chapter 1

Introduction

1.1 Neurons and axon guidance

All forms of interaction with the external world, as well as with our own internal state, are fundamentally mediated by the nervous system. Sensation, movement, cognition, and behaviour all depend on the formation and function of neural circuits. The emergence of these circuits during development therefore underlies the organism's ability to perceive, respond to, and act upon its environment. For this reason, understanding the immensely complex process through which the nervous system forms has been a fundamental problem of basic science.

Neurons are the fundamental building blocks of the nervous system. They consist of a cell body (soma), dendrites, and an axon (see Fig. 1.1(c)). Axons are long cellular projections responsible for transmitting signals across the nervous system.

During neurodevelopment, neurons extend their axons to reach target cells-typically other neurons-and establish functional connections. In doing so, axons navigate through the extracellular environment under the influence of a variety of environmental cues, including gradients in chemical and mechanical properties. This process is known as *axon guidance*.

Historically, the primary focus has been on *chemotaxis*, the guidance of axons by gradients in the concentration of diffusing chemicals [48]. The underlying molecular mechanisms of chemotaxis are relatively well understood and have been extensively modelled [52]. In contrast, *durotaxis*-the directed motion of cells along gradients in extracellular matrix stiffness [67, 21]-has only more recently been identified in axons and remains comparatively poorly understood, particularly at a mechanistic level. While experimental evidence indicates that axons respond to stiffness gradients, a quantitative theoretical framework linking substrate mechanics to force generation and axon steering is still lacking. This thesis is concerned with laying the theoretical foundations for understanding axonal durotaxis.

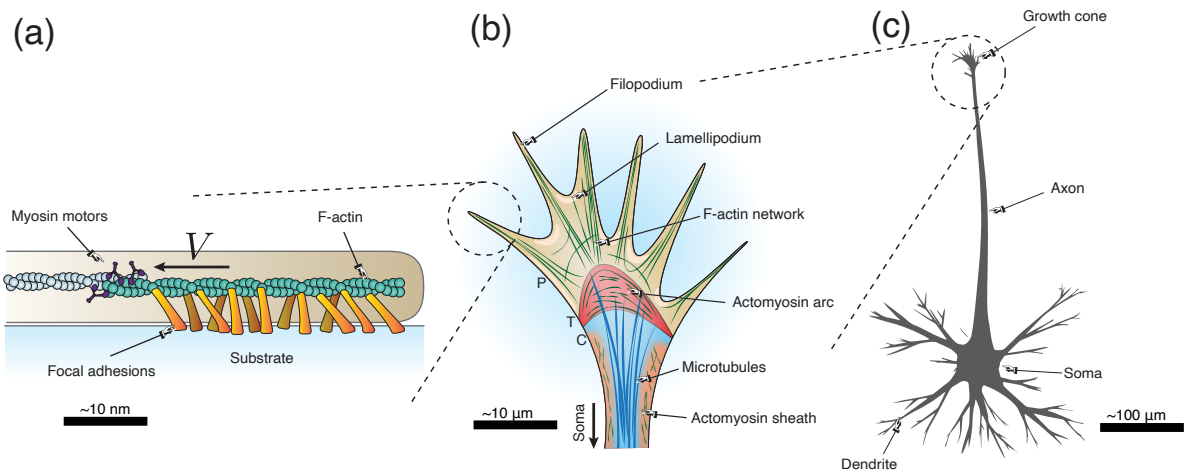


Figure 1.1: The structure of a developing neuron. (a) Molecular scale: Schematic of the focal adhesion system. An actin filament is pulled towards the rear of the growth cone by myosin motors. Actin is coupled mechanically to the substrate via transmembrane adhesive proteins which may detach and attach, producing an overall frictional force. These adhesive proteins constitute a focal adhesion. (b) Growth cone scale: schematic representation of the cytoskeleton in a migrating neurite. The shaft (lower part) is essentially composed of cross-linked microtubules surrounded by an actomyosin sheath. The growth cone is a lamellipodium-like structure that confers motility to the neurite and probes the environment. (c) Cellular scale. Schematic of a typical growing neuron showing the soma, the dendrites, and the axon with its growth cone.

1.2 The growth cone

At the tip of a growing axon lies a highly motile structure known as the growth cone, which explores the surrounding environment and directs the trajectory of the growing axon by processing environmental cues. Thus, the growth cone is central to axon guidance.

The growth cone can be conceptually divided into three spatial regions: the central (C), transition (T), and peripheral (P) zones (see Fig. 1.1(b)). In the central zone, microtubules from the axon shaft extend into the growth cone, and myosin II motors (motor proteins that are capable of exerting contractile forces) are predominantly localized. The transition zone consists of the lamellipodium, a dense, branched network of actin filaments. The peripheral zone contains filopodia-finger-like protrusions composed of bundled actin filaments-into which microtubules may occasionally extend.

A key functional aspect of the growth cone is its ability to generate forces against its environment. Within the peripheral and transition zones, transient adhesion structures known as *point contacts* (also and henceforth known as *focal adhesions*) form. These complexes consist of molecular linkers, such as integrins, that couple the actin cytoskeleton to the extracellular matrix. Through these adhesions, the growth cone transmits forces to its environment and generates traction stresses. Mechanistically, traction arises from

actomyosin contractility and actin polymerization. Myosin II motors generate contractile forces that drive a retrograde flow of actin filaments from the peripheral zone toward the central region. When actin filaments engage with the substrate via point contacts, this retrograde motion loads the adhesion complexes, generating tension within them. See Fig. 1.1(a) for a schematic of this process. This tension is transmitted to the substrate, resulting in its deformation and the emergence of traction stresses. The ability of the growth cone to generate traction forces plays a crucial role in axon guidance. We touch upon this issue later in this introduction.

1.3 Developmental roles of axon durotaxis

Although axon guidance during neurodevelopment has traditionally been understood primarily through the lens of chemotaxis, increasing evidence suggests that durotaxis may also play an important role.

A key example is provided by the developing visual system of *Xenopus laevis* (the African clawed frog), a well-established model for studying neural development. Koser et al. demonstrated that retinal ganglion cell axons in the embryonic *Xenopus* brain respond to spatial variations in tissue stiffness, both *in vitro* and *in vivo* [38]. Using atomic force microscopy, they identified stiffness gradients in the embryonic brain along the optic tract–the pathway formed by retinal axons projecting through the brain–and found that axons preferentially extended toward softer tissue. Moreover, perturbing brain stiffness or interfering with mechanotransduction led to abnormal axonal growth and pathfinding errors. These results provide strong evidence that durotaxis contributes to the proper wiring of the developing visual system.

A second example arises during development of the peripheral nervous system, where motor axons extend from the neural tube in a segmented pattern. Notably, this initial segmentation occurs even in the absence of chemotactic cues. By studying the development of chick embryos, Schaeffer et al. showed that, during this early phase, the substrate traversed by motor axons exhibits a periodic pattern in stiffness, with axons preferentially extending through the softer regions [65]. These findings suggest that durotaxis may contribute to the segmentation of the developing peripheral nervous system.

Taken together, these studies indicate that durotaxis can play an important role in specific contexts of neurodevelopment.

1.4 Proposed mechanisms of axon durotaxis

Among the mechanisms proposed to account for axon durotaxis, two have been particularly prominent in the experimental and theoretical literature.

In Koser et al., pharmacological inhibition of mechanosensitive ion channels and knockdown of Piezo1 disrupted normal pathfinding, suggesting that local tissue stiffness is sensed through mechanotransduction pathways involving mechanically gated ion channels [38]. Piezo1 is a mechanically gated ion channel that converts mechanical stimuli, such as membrane tension, into intracellular ionic signals. Mechanotransduction is the process by which mechanical stimuli are converted into biochemical signals. Such pathways may, in turn, regulate protrusion, adhesion turnover, and cytoskeletal remodeling, thus biasing the direction of growth-cone advance. In this view, the external guidance cue remains mechanical, but its effects on growth-cone behaviour are mediated through intracellular biochemical signalling.

A different perspective is provided by the motor-clutch hypothesis. In motor-clutch models, actomyosin-driven retrograde flow is coupled to the substrate through transient adhesion bonds that repeatedly engage and disengage. Because the loading and lifetime of these bonds depend on substrate stiffness, the resulting traction force is likewise stiffness-dependent [37, 13]. Within this framework, a growth cone exposed to a stiffness gradient may develop a left-right asymmetry in traction, thereby biasing its direction of turning. This mechanical perspective forms the basis of the modelling approach developed in this thesis. We proceed by synthesizing experimental evidence to argue that traction forces play a central role in durotaxis and axon guidance more generally.

1.5 The role of traction forces in axon guidance

A growing body of evidence suggests that the ability of the growth cone to generate traction on its substrate is required for steering, and hence for directed axon guidance. Support for this claim can be found in the synthesis of two key experimental findings: First, application of blebbistatin (a molecule which inhibits the action of non-muscle myosin II) to growing axons abolishes traction force generation at the growth cone [37]. Second, and critically, the same pharmacological intervention eliminates the axon's ability to turn and renders it insensitive to guidance cues [75]. The co-abolition of traction and steering by a single intervention suggests a causal, rather than merely correlational, relationship between the two. This interpretation is further reinforced by direct observation: an asymmetric redistribution of growth cone traction forces is followed by a reorientation of the axon shaft toward the net traction force vector [33], establishing a link between force asymmetry and turning behaviour. Together, these findings support

the view that axon shaft reorientation is governed by the net traction force exerted by the growth cone on its environment. Since axon guidance proceeds through a sequence of such reorientations, growth cone traction emerges as a central mechanical driver of the guidance process.

If traction is indeed a central driver of axon steering, then the question arises as to whether there exists any evidence that links established forms of axon guidance phenomena with growth cone traction. For example, the most prominent example of an axon guidance process is chemotaxis. If the hypothesis holds, then one would expect that chemical guidance cues modulate growth cone traction generation in some way. Experimental evidence supports this idea. Growth cones have been shown to exert substantially larger forces on optically trapped beads coated with netrin-1, an attractive guidance cue, than on uncoated beads or beads coated with a repellent cue [46]. Moreover, when such beads are positioned off-axis relative to the axon shaft, there proceeds a reorientation of the axon toward the bead. These observations suggest that chemical guidance cues can locally modulate traction forces, thereby influencing axon steering.

Although comparable high-resolution experiments have not yet been performed for stiffness gradients, it has been shown that growth cones exert different traction stresses on substrates of different stiffness [37]. It is therefore natural to hypothesise that, when exposed to spatial variations in substrate stiffness, a growth cone may develop an asymmetry in traction across its periphery. This would result in a biased net traction force and, consequently, axon steering up or down the stiffness gradient. This hypothesis provides a mechanistic basis for axon durotaxis and motivates the modelling framework developed in this thesis.

All this evidence suggests a general formulation of axon guidance: (1) the local environment determines the traction generated by the growth cone, and (2) the resulting net traction vector reorients the axon shaft. This perspective provides a unifying mechanical framework. Chemical cues, stiffness gradients, and other environmental signals may act through distinct biological pathways, yet their effect can be interpreted in a common way if they bias local force generation at the growth cone. In this sense, diverse guidance mechanisms can be understood within a single mechanical principle: *the modulation of traction forces*. This view is consistent with the broader argument that guidance cues ultimately influence axon behaviour through mechanical forces [22].

This perspective forms the conceptual basis of this thesis, in which axon guidance is treated as a mechanically mediated process governed by the generation and spatial distribution of traction forces.

If traction is to play a central role in the theory of axon guidance, a mechanical theory of the axon must be developed that provides a physically consistent relation between

growth cone traction and axon steering. In this context, the literature is lacking in two respects: (1) There is an absence of models which link growth cone traction generation to the mechanics of the axon. (2) There is a scarcity of models of axon durotaxis. Thus, the aim of this thesis is to develop a theoretical framework that relates environmental properties to traction generation and, in turn, to axon steering, with particular emphasis on the role of substrate stiffness.

1.6 Mathematical and computational modelling of focal adhesion dynamics and traction generation

The generation of traction forces through focal adhesions is most commonly described within the molecular clutch framework, in which stochastic binding and unbinding of adhesion molecules couple actin retrograde flow to the extracellular substrate (see Fig. 1.1(a) for a schematic of a focal adhesion). Existing modelling approaches may be broadly divided into two categories: *computational stochastic models*, which explicitly simulate individual adhesion bonds, and *analytical models*, which seek to describe the collective behaviour of many bonds through coarse-grained or mean-field formulations.

Early work by Chan and Odde [13] introduced a stochastic motor-clutch model for filopodial protrusion, in which individual adhesion molecules (also called clutches) bind and unbind according to force-dependent kinetics. Using Monte Carlo simulations, they showed that substrate stiffness governs a transition between regimes of frictional slippage (characterised by rapid actin retrograde flow and weak force transmission) and load-and-fail dynamics (in which clutches transiently bear load before collective failure), and predicts the existence of an optimal stiffness at which traction force is maximized. These results established the key qualitative features of stiffness-dependent traction generation within the motor-clutch framework. However, as a simulation-based approach, the model does not provide a framework for deriving explicit relationships between system parameters and emergent quantities such as traction or optimal stiffness, and therefore does not yield an analytical characterisation of stiffness-dependent behaviour.

Subsequent work by Bangasser et al. [3, 4] used stochastic motor-clutch simulations to investigate both the origin and the parameter dependence of an optimal substrate stiffness for traction generation. Their earlier work indicated that the biphasic traction-stiffness relation arises from a competition between clutch binding dynamics and the timescale of force buildup, thereby explaining why maximal force transmission occurs at an intermediate stiffness. Subsequent work showed that this optimal stiffness is not fixed, but can shift over orders of magnitude as motor activity and clutch number are varied, linking cell-specific molecular parameters to distinct mechanosensitive responses. These

studies established optimal stiffness as a robust but highly tunable feature of the motor-clutch framework. However, the dependence of the optimal stiffness on model parameters is established through stochastic simulations and parameter sweeps, so that its origin and scaling behaviour are characterised empirically rather than derived analytically.

Within this computational framework, subsequent studies have extended the original motor-clutch model of Chan and Odde by incorporating increasing molecular detail and mechanochemical feedback. In particular, Elosegui-Artola et al. [17, 18] introduced integrin-specific binding kinetics, talin unfolding, and vinculin-mediated reinforcement, thereby embedding key components of focal adhesion biology into the stochastic clutch dynamics. Within this framework, they showed how molecular composition and force loading rates regulate rigidity sensing [19]. While highly influential, the increased molecular detail introduces additional complexity that makes it difficult to isolate general principles governing traction generation, and the framework is not designed to yield analytical descriptions of stiffness-dependent behaviour.

In parallel with these computational studies, a number of works have sought analytical descriptions of adhesion dynamics. A useful precursor to analytical studies of motor-clutch dynamics is the work of Erdmann and Schwarz [20], who analysed stochastic adhesion clusters under shared load. Their model provides a rigorous treatment of force-dependent bond rupture and rebinding, and shows how these processes regulate cluster stability and lifetime. However, the applied force is prescribed externally, rather than generated dynamically through the interaction of actomyosin flow, adhesion, and substrate mechanics. As such, the model does not address traction generation directly, but it establishes analytical ideas for the stochastic treatment of bond ensembles under load that later studies of focal adhesion dynamics would build upon.

Bangasser and Odde [2] introduced a mean-field description of the motor-clutch model in the presence of a compliant substrate. In their formulation, the stochastic dynamics are approximated through equations for the probability of clutch engagement and the mean clutch extension. From this master-equation-based model, the expression for the optimal stiffness is introduced through a timescale argument rather than derived directly from the governing equations, so that the connection between the model dynamics and the resulting optimum is not established in a self-consistent analytical framework. Furthermore, the resulting expression does not fully capture the qualitative behaviour observed in computational models.

Sens [66] developed an analytically tractable model of stochastic sliding friction, in which force is transmitted through transient linker bonds. Within this minimal framework, he showed that a finite substrate rigidity can maximise traction, thereby providing an analytical description of stiffness-dependent traction in a reduced stochastic linker

model. However, in this model actin speed is a prescribed quantity. Therefore, the model does not incorporate the motor-clutch coupling between actomyosin force generation, clutch dynamics, and substrate deformation, and therefore does not provide an analytical description of stiffness-dependent traction within a motor-clutch framework.

Srinivasan and Walcott [70] developed a continuum, density-based model for bond formation and rupture in a velocity-driven setting. Their framework focuses on force-velocity relations and frictional response, rather than on an explicitly motor-driven clutch mechanism, and therefore does not directly capture the feedback between actomyosin force generation and adhesion dynamics that characterises motor-clutch models. While the authors study the effects of compliance in an external loading apparatus, the model does not treat substrate deformability and therefore does not provide a framework for analysing stiffness-dependent traction or optimal substrate stiffness within a motor-clutch setting. Nevertheless, their continuum formulation can be viewed as an early precursor to later density-based approaches, and the force-velocity relations they analyse reappear in subsequent mean-field treatments of motor-clutch dynamics.

A more direct analytical treatment of the motor-clutch system was developed by Sabass and Schwarz [64], who studied a stochastic formulation closely aligned with the framework of Chan and Odde, but restricted to the rigid-substrate case. In their model, adhesion bonds bind and unbind stochastically while coupling retrograde actin flow to a fixed substrate, with an additional viscous dissipation term representing internal relaxation within the actin network. Importantly, they formulated the exact stochastic bond dynamics through a Chapman-Kolmogorov equation and used it to derive a mean-field approximation of the system, which they then compared directly with stochastic simulations. Their analysis showed that weak internal dissipation promotes cooperative rupture cascades and irregular stick-slip dynamics, whereas strong dissipation suppresses correlations and improves agreement with mean-field theory. However, because substrate compliance is absent, the model cannot capture the coupling between adhesion dynamics and substrate deformation that underlies stiffness-dependent traction generation, and therefore does not provide a framework for analysing optimal stiffness in deformable environments. This rigid-substrate Chapman-Kolmogorov framework was later extended by Bressloff [12], who incorporated spatial diffusion of adhesion bonds into the stochastic motor-clutch description.

Recent work by Alonso-Matilla et al. [1] developed a continuum description of the motor-clutch system in the case of a compliant substrate, introducing a probability density over clutch extensions and deriving conservation equations for its evolution. Among existing models for compliant substrates, this represents a significant advance beyond low-dimensional mean-field descriptions, allowing for a richer account of the system and

the incorporation of additional biological features such as catch bonds and bond reinforcement. However, the formulation is not derived from a Chapman-Kolmogorov description of the underlying stochastic dynamics. Furthermore, traction-stiffness curves and optimal stiffness are analysed primarily numerically, with the proposed expression for the optimal stiffness obtained by fitting to numerically computed solutions of the model.

Taken together, the existing literature establishes the molecular clutch as a central paradigm for understanding traction generation, but also reveals a clear methodological divide. Computational stochastic models capture the full bond dynamics but offer limited analytical insight, whereas existing analytical approaches either treat simplified or rigid-substrate systems or, in the compliant-substrate case, rely on heuristic continuum descriptions rather than formulations derived directly from a Chapman-Kolmogorov equation for the underlying stochastic process. As a result, even key aspects of the problem, such as the existence and parameter dependence of an optimal substrate stiffness, have not been analysed in a fully systematic way.

The work in this thesis addresses this gap by formulating motor-clutch dynamics on deformable substrates at the level of a Chapman-Kolmogorov equation for the full extension distribution. In this way, it helps bridge the gap between computational and analytical approaches, while providing a systematic mathematical framework for the study of traction generation on compliant substrates.

1.7 Mathematical and computational models of axon guidance

Mathematical and computational models of axon guidance seek to explain or predict how environmental conditions determine axon growth and trajectories. Although there is a vast literature regarding the one dimensional modeling of axons, we focus here on models which relate environmental conditions to the 2D or 3D trajectories of axons. These models differ in the level of description, ranging from simple random walk models aiming to capture the statistics of growth cone motion to models that model the mechanics of the axon shaft.

Random walk models

For the steering problem, many models focus on the trajectory of the growth cone, describing its motion as a biased random walk. In this framework, the position $\mathbf{x}(t)$ of the growth cone evolves according to

$$\dot{\mathbf{x}} = \mathbf{v}(\mathbf{x}, t) + \boldsymbol{\eta}(t),$$

where $\mathbf{v}$ represents a deterministic drift induced by guidance cues and $\boldsymbol{\eta}(t)$ is a stochastic noise term.

A prototypical example is the model of Hentschel and Van Ooyen [29], in which the drift velocity is taken to be proportional to gradients of ligand concentrations,

$$\mathbf{v} \propto \sum_i \lambda_i \nabla \rho_i(\mathbf{x}, t),$$

with coefficients λ_i encoding sensitivity to different cues and ρ_i the concentration of different ligands. This framework allows for the simultaneous incorporation of multiple attractive and repulsive signals and has been used to study bundling and guidance during neural network formation [30].

Persistent random walk models

In random walk models, a particle's trajectory does not have any directional persistence. Thus, in such a model, particles perform an unbiased random walk in the absence of guidance cues: their expected displacement is zero and successive displacements are independent. Equivalently, the direction of motion is immediately decorrelated from one step to the next, so individual trajectories are highly tortuous rather than approximately straight. This behaviour is unrepresentative of how axons actually grow. As might be expected from their geometry, axons tend to grow straight in the absence of guidance cues [36].

In an attempt to better represent axon trajectories, many studies have modelled the motion of the growth cone as a persistent random walk. In this framework, the evolution of the position of the growth cone $\boldsymbol{x}(t)$ is controlled by a polar angle $\theta(t)$, which determines its direction of motion. The system for the evolution of the growth cone position $\boldsymbol{x}$ can now be written as

$$\dot{\mathbf{x}} = V(\mathbf{x}, \theta, t)\ (\cos(\theta), \sin(\theta)),$$

and

$$\dot{\theta} = q(\mathbf{x}, \theta, t) + \xi(t),$$

where V is the growth rate of the axon, $q(\mathbf{x}, \theta, t)$ is a function encoding the effect of guidance cues and the environment on axon turning and $\xi(t)$ is a stochastic noise term (usually Gaussian noise). Under this formulation, simulated axon trajectories tend to be straighter.

A vast number of studies have used this approach to model axon guidance. We highlight a few notable applications: this formulation has been used to describe axon turning statistics [57], model chemotaxis [41], study axon guidance by chemotaxis in the

spinal cords of *Xenopus* tadpoles and also the establishment of pioneer neural circuits in the same organism [11, 62] and study the role of the internal stress of the folding brain on axon guidance [69].

Bayesian agent approaches

Other approaches to modelling axon guidance treat the growth cone as an information-processing system that uses environmental cues to bias its direction of growth. A particularly influential formulation casts this problem in Bayesian, or "ideal observer", terms: the growth cone is assumed to infer the direction of an external chemical gradient from noisy receptor-binding measurements. In this perspective, guidance is formulated as a problem of statistical inference under uncertainty, in which spatially distributed receptors sample a molecular environment stochastically and their binding states are combined to estimate the most likely gradient direction. This approach has been used to quantify the fundamental limits imposed by receptor-binding noise on axonal gradient sensing and to derive Bayes-optimal strategies for extracting directional information from chemical guidance cues [47, 49].

Mechanical approaches: Modelling of the axon shaft

Although the models mentioned so far are suitable for describing the statistics of axon turning, they provide a limited framework for understanding mechanistically how axon guidance occurs. Furthermore, they do not provide a framework within which the role of growth cone traction and axon mechanics can be incorporated in a principled manner.

A notable step towards a mechanistic, mechanical theory of axon guidance was made by García-Grajales et al. [26]. The authors develop a continuum-mechanical model of the axonal shaft and use this framework to study growth, collapse, stalling and mechanically induced turning. Importantly, in this model, the turning of the axon shaft is induced by the off-axis component of the growth cone traction, which appears in the model as an input. However, the authors do not relate this growth cone traction to properties of the environment, such as its stiffness. As such, this framework is incomplete as a theory of axon guidance in the sense that it does not provide a mapping between environment variables and axon trajectories. Furthermore, no investigation of specific modes of axon guidance, such as durotaxis, is carried out. Thus, this work provides an important mechanical precursor to the traction-based theory developed here, but does not by itself close the loop from environmental properties to traction generation and axon trajectories.

Modelling of axon durotaxis

The majority of existing models of axon guidance focus on chemotaxis and relatively few studies have addressed axon durotaxis. The first clear direct theory paper on axon durotaxis is the work of Oliveri et al. [53], which studies how *axon bundles* may be guided by stiffness gradients. In the paper, an *axon bundle* is modelled as a growing morphoelastic rod whose tip dynamics depends on substrate stiffness. A striking outcome of this framework is the emergence of an analogy with geometric optics: axon bundle trajectories at stiffness interfaces obey Snell-type refraction and reflection laws.

Although this study is an important step towards attaining understanding of axon durotaxis, in this model durotaxis of the bundle emerges from a mechanism that fundamentally relies on the interaction of multiple axons within the bundle. As such, the theory developed is inapplicable to understanding the durotactic phenomena exhibited by lone axons. Furthermore, as implemented in the paper, the theory developed was unable to account for in-vivo instances of axon durotaxis, such as the durotaxis exhibited by axons along the optic tract in Xenopus laevis (see Section 1.3).

Summary and limitations

Taken together, existing mathematical models of axon guidance provide important but partial descriptions of the guidance problem. Random-walk and persistent-random-walk models offer useful low-dimensional descriptions of axon trajectories and turning statistics, but usually encode the effect of environmental cues through effective drift or turning rules rather than through the underlying physical mechanisms. Bayesian agent models provide a principled, agent-based treatment of noisy cue sensing, but have primarily been developed for chemical guidance and do not directly incorporate growth-cone traction. Mechanical models of the axon shaft, by contrast, provide a natural framework for describing deformation, elongation and turning of the axon, but, as of yet, have not incorporated mechanisms to convert information from the environment into guidance through turning of the axon shaft. Furthermore, none of the above frameworks have been used to study the durotaxis of lone axons.

This leaves a significant gap in the theoretical description of mechanically mediated axon guidance. In particular, there is currently no unified framework that connects stochastic adhesion dynamics and traction generation at the growth cone, the mechanical properties of the substrate, and the deformation and reorientation of the axon shaft. This limitation is especially important in the context of axon durotaxis, where the relevant environmental cue is mechanical stiffness itself and where guidance must arise through the coupling between substrate mechanics, force generation and axonal motion.

The main challenge is therefore to combine these ingredients into a model that connects molecular processes inside the growth cone to axon trajectories observed at cellular and tissue scales. The modelling framework developed in this thesis aims to address this gap by linking focal-adhesion-mediated traction generation to continuum descriptions of axon mechanics, thereby providing a direct route from environmental mechanical properties to axonal guidance.

1.8 Summary of contributions and thesis structure

This thesis develops a multiscale mechanical framework for axon guidance based on the hypothesis that environmental cues influence axonal trajectories through their modulation of growth-cone traction forces. Within this framework, we derive analytical and continuum models that link substrate mechanics to traction generation and, in turn, to axon steering and growth.

The main contributions of the thesis may be summarised, along chapter lines, as follows:

- In Chapter 2, we develop an analytical treatment of substrate-dependent focal adhesion dynamics on deformable substrates. In the single-linker case, it provides an exact statistical characterisation of the steady states and a precise definition of the three qualitative regimes previously described only from simulations. In the mean-field setting, it derives an exact expression for the optimal substrate stiffness under the homogeneous extension-rate approximation and identifies the conditions under which this optimum exists. Furthermore, the second derivative of the traction-stiffness curve at the optimal stiffness is investigated for the first time.

- In Chapter 3, we derive the Axon-Beam-Clutch (ABC) model, which combines the molecular clutch model of growth-cone traction generation with a remodelling beam model of the axon. This provides a mechanics-based framework for axon growth and guidance which links local environmental mechanical conditions to axonal trajectories. Using this model, we identify and analyse a novel mode of axon guidance: convergence to travelling parallel to lines of optimal stiffness. This result highlights the importance of the finite spatial extent of the axon and suggests that long-range mechanical sensing by the shaft may play a significant role in guidance.

- In Chapter 4, we address the inference of axonal mechanical parameters, with particular emphasis on bending stiffness. We examine the modelling assumptions required to interpret deformation experiments in a manner consistent with beam-based descriptions of the axon.

- In Chapter 5, we apply the theory in the previous chapters to several biologically relevant scenarios, including neurite interactions with sharp boundaries, guidance of *Xenopus* retinal ganglion cell axons to the optic tectum, and the segmented outgrowth of motor axons in the PNS. These applications illustrate how the proposed framework can account for experimentally observed guidance behaviours across a range of biological contexts.

Together, these results establish a quantitative, mechanics-based framework for axon guidance and provide new insights into the role of substrate mechanics in shaping neuronal development.

Chapter 2

An analytical study of focal adhesion traction - stiffness curves.

2.1 Overview

In Chapter 1, we argued that growth cone traction plays a crucial role in axon guidance. Furthermore, we explained how growth cone and cellular traction generation is best understood through models of the motor-clutch system. We also identified a gap in the literature when it comes to analytical studies of the motor-clutch system interacting with a deformable substrate. This chapter is concerned with addressing that gap, by studying the interaction between focal adhesions and deformable substrates using analytic methods.

We begin in Section 2.3 by describing the differential *Chapman–Kolmogorov* (CK) equation for a focal adhesion interacting with myosin motors, an actin filament and a deformable substrate. The solution of this equation completely characterizes the statistics of this system. We proceed in Section 2.5 with an exact analysis of the CK equation in the case of a deformable substrate and a focal adhesion composed of a single stochastic linker ($N_T = 1$). Such an analysis is novel to the literature. We find that the expected traction of the system exhibits an *optimal stiffness*. Furthermore, we show that the system's steady state statistical distribution falls into one of three categories (also known as regimes). These three categories correspond to ones previously identified in the literature through observations of individual trajectories of the system. Our work provides an exact quantitative definition of each regime in terms of the system's statistics, and, at least for $N_T = 1$, establishes necessary and sufficient conditions for belonging to each regime.

Little can be said for systems with $N_T > 1$ without the use of approximations. A standard approach for such systems is to analyse the system under a mean-field *ansatz*, which is expected to be accurate in the limit $N_T \gg 1$. Previous studies assumed that in the mean-field limit, bound stochastic linkers extend at a rate which is approximately

independent of their current extension. We call this approximation the *homogeneous extension rate approximation*. In Section 2.6, we set aside this approximation and we derive the exact extension rate in the mean-field and in the limit of a rigid substrate. We find that the exact mean-field equation is structurally identical to the non-approximate system for $N_T = 1$. Thus, we extend our analysis of the three qualitative regimes to the case of a rigid substrate when $N_T \gg 1$.

In the case of a deformable substrate, we are unable to derive the exact extension rate in the mean-field. For this reason, in Section 2.7, we use the homogeneous extension rate approximation to derive an approximate mean-field equation for deformable substrates. The rest of this chapter is concerned with the study of the steady state traction of this system.

We proceed with the description of traction stiffness curves and in Section 2.7.4 we derive an exact expression for the *optimal stiffness* of the system. This is the first exact expression for the optimal stiffness to be derived for this system. In Section 2.8.3 we compare it with other derivations and results from computational models. We study the behaviour of the optimal stiffness under various parameters of the system and provide necessary and sufficient conditions for its existence.

A feature of the traction stiffness curve that will appear later in the thesis, which is of particular importance for the determination of the trajectories of axons on certain substrates, is the second derivative of the traction stiffness curve at the optimal stiffness. In Section 2.7.8, we proceed with a derivation of the exact expression for this quantity. Then, we study its behaviour under various parameters of the system.

Finally, in Section 2.7.9 we address how a different, but commonly held, interpretation of the system parameters leads to different physical predictions for system quantities, such as the behaviour of the optimal stiffness, even though the underlying mathematical structure is the same.

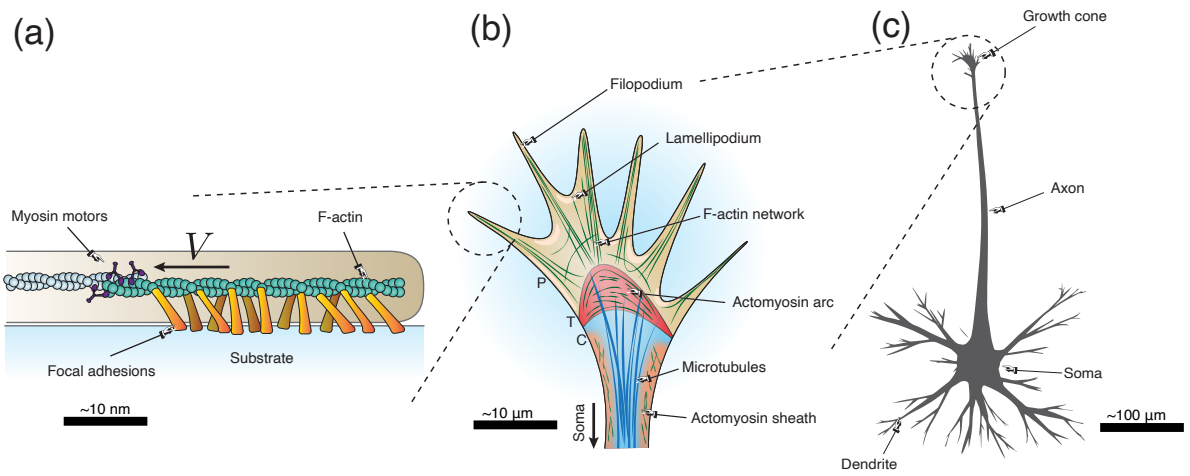


Figure 2.1: The multiscale structure of the axon. (a) Molecular scale. An actin filament is pulled towards the rear of the growth cone by myosin motors. Actin is coupled mechanically to the substrate via transmembrane adhesive proteins which may detach and attach, producing an overall frictional force. This frictional force is key for axon locomotion. (b) Growth cone scale: schematic representation of the cytoskeleton in a migrating neurite. The shaft (lower part) is essentially composed of cross-linked microtubules surrounded by an actomyosin sheath. The growth cone is a lamellipodium-like structure that confers motility to the neurite and probes the environment. (c) Cellular scale. Schematic of a typical growing neuron showing the soma, the dendrites, and the axon with its growth cone.

2.2 The system: Focal adhesions

We consider a focal adhesion interacting with an actin filament and a deformable substrate. The actin filament is also acted upon by myosin motors (see Fig. 2.2). As described in Chapter 1, traction is generated on the substrate by the interaction of the above elements. Contractile forces generated by myosin motors act on the actin filaments, causing a displacement of the filaments from the peripheral zone towards the central zone. By this displacement, the filaments generate a tension within the adhesive proteins that link the filaments to the substrate. This tension is transmitted to and deforms the substrate.

To model this traction generation process, we adapt several past approaches [12, 13, 64, 66, 70]. The filament is modelled as a straight, infinite rigid rod moving relative to the substrate with speed V, as shown in Fig. 2.2.

The focal adhesion is modelled as a collection of $N_T \in \mathbb{N}$ adhesion proteins, henceforth generically termed *clutches*, *stochastic-linkers*, *cross-linkers*, or just *linkers*. We assume that each linker may be in one of two states: attached or detached. We will also use the terms bound and unbound, respectively. We introduce the occupancy variable $q \in \{0, 1\}$, corresponding to the attached and detached states respectively.

When attached, we assume that each linker acts as a linearly elastic spring connecting

the actin filament to the substrate. Each spring has an individual tension f, elongation x, and spring constant κ related through Hooke's law by

$$f = \kappa x. \tag{2.1}$$

The change in the cross-linker tension in a time interval of length $\Delta t \ll 1$ is related to the actin filament speed V. Indeed, for a perfectly rigid substrate, the change in tension of a single cross-linker in such a time interval is $\Delta f \approx \kappa V \Delta t$ (neglecting the geometric nonlinearity due to the distance between the actin filament and the substrate). The situation is more complex in the case of a deformable substrate where the cross-linkers may interact indirectly and non-locally with one another through short- and long-range deformations of the substrate [51]. This deformation may be expressed in terms of the Green solution for an infinite half-plane subject to surface traction [32, 66, 51].

Here, for simplicity, we assume that the substrate is soft so that cross-linkers interact mechanically as the substrate deforms almost uniformly. The substrate is then modelled as a single spring with spring constant κ_s and with extension x_s, with which all cross-linkers are connected in parallel.

To model the kinetics of cross-linker detachment, we assume that the probability that a cross-linker detaches in a small time-interval Δt is related to its tension f according to

$$p_{\text{off}} = \Delta t \, r\left(f\right). \tag{2.2}$$

It is standard [13, 3, 4, 2] to assume that the kinetic off-rate follows a Bell-type law [8] which corresponds to a detachment probability of the form

$$p_{\text{off}} = k_{\text{off}} \Delta t \, \mathrm{e}^{f/F_b}, \tag{2.3}$$

where F_b is the characteristic force scale of detachment and k_{off} is the kinetic off-rate at rest. We note that other forms of $r(f)$ have also been considered [18, 1].

We assume that cross-linkers attach in the unstretched state at a constant rate k_{on}, so the probability of attachment during Δt is

$$p_{\text{on}} = k_{\text{on}} \Delta t. \tag{2.4}$$

Given the above assumptions regarding stochastic linkers and their transition dynamics, the current state of all N_T linkers can be completely characterized by two vectors: the vector of current linker extensions $\boldsymbol{x} = (x_1, x_2, \ldots, x_{N_T})$, and the vector of linker occupancy variables, $\boldsymbol{q} = (q_1, q_2, \ldots, q_{N_T})$.

2.3 The basic equations: Chapman-Kolmogorov equation for the focal adhesion system

In the limit of $\Delta t \to 0^+$, the above rules generate a continuous stochastic process. In this limit, the probability density of the system being in a given state $(\boldsymbol{x}, \boldsymbol{q})$ at time t is described by a differential Chapman–Kolmogorov equation. Let $\rho(\boldsymbol{X}, \boldsymbol{Q}, t)$ denote the probability density that at time t we have $\boldsymbol{x} = \boldsymbol{X}$ and $\boldsymbol{q} = \boldsymbol{Q}$. Then, in the continuous-time limit $\Delta t \to 0^+$, ρ satisfies [12, 64]

$$\frac{\partial \rho(\boldsymbol{x}, \boldsymbol{q}, t)}{\partial t} = -\sum_{i=1}^{N_T} q_i \frac{\partial J(\boldsymbol{x}, \boldsymbol{q}, t)}{\partial x_i} - \sum_{i=1}^{N_T} q_i \, r(x_i) \, \rho(\boldsymbol{x}, \boldsymbol{q}, t) - \sum_{i=1}^{N_T} (1 - q_i) \, k_{\text{on}} \, \rho(\boldsymbol{x}, \boldsymbol{q}, t)$$
$$+ \sum_{i=1}^{N_T} \delta(x_i) \left\{ \int_0^{+\infty} (1 - q_i) r(X_i) \rho(\boldsymbol{x}, \boldsymbol{q}, t)|_{(x_i, q_i) = (X_i, 1)} \; + \; q_i \, k_{\text{on}} \rho(\boldsymbol{x}, \boldsymbol{q}, t)|_{(x_i, q_i) = (X_i, 0)} \, \mathrm{d}X_i \right\}, \tag{2.5}$$

where

$$J(\boldsymbol{x}, \boldsymbol{q}, t) = v_e(\boldsymbol{x}, \boldsymbol{q}) \, \rho(\boldsymbol{x}, \boldsymbol{q}, t). \tag{2.6}$$

Here, $v_e(\boldsymbol{x}, \boldsymbol{q})$ is the extension rate of attached linkers, which depends on the current state and other material parameters. We will specify its form in different scenarios in the next section. As mentioned previously, function $r(x)$ describes the extension-dependent off-rate of bound linkers. We will later assume that

$$r(x) = k_{\text{off}} \exp(\kappa x / F_b). \tag{2.7}$$

The right-hand side of (2.5) consists of transport, loss, and gain terms. The first term describes the deterministic evolution of linker extensions. When linker i is bound, so that $q_i = 1$, its extension evolves continuously at rate $v_e(\boldsymbol{x}, \boldsymbol{q})$, inducing a probability flux in extension space. This gives rise to an advection term in the variables x_i.

The second and third terms represent loss of probability due to stochastic transitions. The second term corresponds to unbinding events: when $q_i = 1$, linker i detaches at rate $r(x_i)$, removing probability from the current state. The third term corresponds to binding: when $q_i = 0$, linker i binds at rate k_{on}, and the system leaves the current state for one in which that linker is attached.

The final line contains the corresponding gain terms. These are localised at $x_i = 0$ through the factor $\delta(x_i)$, reflecting the assumption that newly bound linkers form in the unstretched state. The term proportional to $(1 - q_i)$ accounts for gain into states with linker i unbound due to unbinding events from states in which the same linker was previously bound with extension X_i; the integral reflects that unbinding may occur from

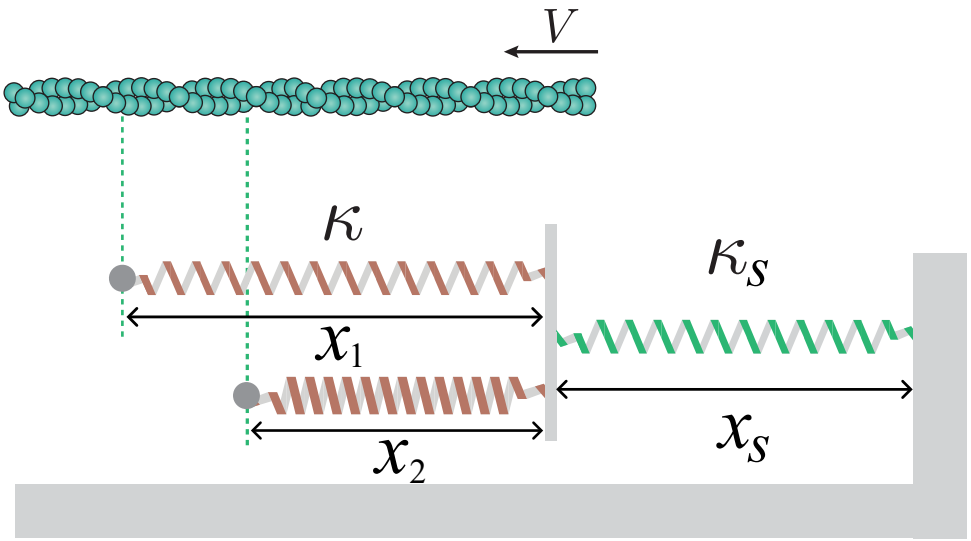


Figure 2.2: Schematic of an actin filament flowing with speed $V > 0$, attached to the substrate spring through linker springs. The substrate spring has extension x_s and spring constant κ_s. The ith linker spring has extensions x_i and spring constant κ.

any extension $X_i \geq 0$. The term proportional to q_i accounts for gain into states with linker i bound due to binding from the corresponding state with $q_i = 0$.

Together, these gain and loss terms encode the stochastic switching between bound and unbound states, while the transport term describes the deterministic evolution between such transitions.

To close the system, we must relate the extension rate of attached linkers, v_e, to the current state of the system, $\boldsymbol{x}$ and $\boldsymbol{q}$.

State dependent, linker extension rate - $v_e(\boldsymbol{x}, \boldsymbol{q})$

For a deformable substrate, the instantaneous extension rate can be linked to the instantaneous actin speed through the below considerations. In the below analysis, x_i denotes the extension of an arbitrary linker and x_s denotes the extension of the substrate. Linkers have spring constant κ and the substrate has spring constant κ_s. See Fig. 2.2 for a schematic.

Consider the extension of an arbitrarily chosen bound linker, x_i. The extension rate of this linker is equal to the difference between the actin speed and the rate of extension of the substrate. That is

$$\dot{x}_i = V - \dot{x}_s. \tag{2.8}$$

From the above expression, it follows that all bound linkers have the same extension rate. We assume that the substrate spring, is always in balance with the total internal tension

of the focal adhesion. Consequently,

$$x_s = \frac{\kappa}{\kappa_s} \sum_{i=1}^{N_T} q_i \, x_i. \tag{2.9}$$

Differentiating with respect to t and noting that, between any linker attachment or detachment events, q_i is constant, we obtain that,

$$\dot{x}_s = \frac{\kappa}{\kappa_s} \sum_{i=1}^{N_T} q_i \, \dot{x}_i = \frac{\kappa}{\kappa_s} \, \dot{x}_i \sum_{i=1}^{N_T} q_i = \frac{\kappa}{\kappa_s} \, N(t) \, \dot{x}_i, \tag{2.10}$$

between attachment or detachment events, where $N(t)$ denotes the total number of bound linkers at time t. Substituting (2.10) into (2.8) and rearranging, we obtain

$$\dot{x}_i = \frac{V}{1 + \chi^{-1} N(t)}, \tag{2.11}$$

where we have introduced the dimensionless substrate stiffness $\chi = \kappa_s / \kappa$.

The above expression links the bound linker extension rate with the current actin filament speed and substrate stiffness. However, the motion of actin itself results from the activity of myosin motors at the rear of the growth cone, thus, the speed V is not prescribed, but is instead an unknown that is obtained from the force balance between actin and the myosin motors.

The forces acting on a single actin filament are generated by myosin contraction [44] modelled as a constant force F [64, 12]. In addition, actin is subject to viscous friction generated from its interaction with the cytoplasm (with constant ξ), as well as the traction force generated by the focal adhesion (equal to the total internal tension). Thus, neglecting inertial effects, the force balance reads

$$F = T + \xi \, V, \;\; T = \kappa \sum_{i=1}^{N_T} q_i \, x_i. \tag{2.12}$$

Rearranging, one obtains

$$V = \frac{1}{\xi} \left(F - T \right). \tag{2.13}$$

Thus, the extension rate of bound cross-linkers is

$$v_e(\boldsymbol{x}, \boldsymbol{q}) = \dot{x}_i = \frac{1}{\xi} \frac{F - T}{1 + \chi^{-1} \, N}. \tag{2.14}$$

In the case of a rigid substrate, $\chi = +\infty$, and

$$v_e(\boldsymbol{x}, \boldsymbol{q}) = \frac{1}{\xi} \left(F - \kappa \sum_{i=1}^{N_T} q_i \, x_i \right) = V, \tag{2.15}$$

as expected.

2.4 Discussion of the different cases to be studied

Equation (2.5), introduced in Section 2.3, provides a complete probabilistic description of the dynamics of a focal adhesion interacting with a deformable substrate and with myosin motors. However, because the state space grows rapidly with the number of linkers, a direct analytical treatment is only feasible in special settings. For this reason, we organise the chapter around a hierarchy of cases, each corresponding to a different level of approximation. We begin with an exact analysis of the single-linker system, followed by mean-field treatments for larger adhesions, first on a rigid substrate and then on a deformable one.

We begin with the simplest non-trivial case, namely a focal adhesion consisting of a single stochastic linker, $N_T = 1$. In this setting, the Chapman–Kolmogorov equation can be analysed exactly, even when the substrate is deformable. Although this is the smallest possible adhesion, it already captures the essential stochastic mechanisms of attachment, detachment, force buildup, and substrate-dependent loading. The main results of this section are: (i) derivation of the exact steady state distribution of the system; (ii) categorization of all possible steady state distributions of the system into one of three categories; (iii) demonstration of the existence of an optimal stiffness for the single-linker system.

We then turn to the case of many linkers, $N_T \gg 1$, on a rigid substrate. A standard way to proceed is to introduce a *mean-field* ansatz, under which the linkers are assumed to be statistically independent in the limit $N_T \gg 1$, allowing the probability density ρ to be expressed as a product of independent one-linker probability densities. The main contributions of this section are: (i) derivation of the exact equation for the mean-field distribution; (ii) extension of the categorisation scheme of steady state distributions to the rigid mean-field regime.

Finally, we consider the physically most relevant case for the purposes of this thesis: many linkers that interact with a deformable substrate. In this regime, an exact mean-field closure is no longer available. For this reason, we introduce the homogeneous extension-rate approximation, following previous approaches, and use it to obtain a closed mean-field model on a deformable substrate. The main contributions of this section are: (i) derivation of an analytical expression for the optimal stiffness and determination that the optimal stiffness only exists when the myosin force F is larger than a critical force F_{crit}; (ii) examination of the behaviour of F_{crit} under the variation of the parameters of the system; (iii) examination of the behaviour of the optimal stiffness under variation of the parameters of the system; (iv) derivation of an exact expression for the second

derivative of the traction as a function of substrate stiffness, when the substrate stiffness is equal to the optimal stiffness.

2.5 Case 1: $N_T = 1$

In this section, we analyse the statistics of a focal adhesion that contains a single cross-linker ($N_T = 1$), interacting with a deformable substrate. For $N_T = 1$, (2.5) becomes

$$\frac{\partial \rho(x,q,t)}{\partial t} = -\,q\frac{\partial}{\partial x}\left[v_e(x,q)\rho(x,q,t)\right] - q\,r(x)\,\rho(x,q,t) - (1-q)\,k_{\text{on}}\,\rho(x,q,t) \tag{2.16}$$

$$+\,\delta(x)\left\{\int_0^{+\infty}(1-q)\,r(X)\rho(x,q,t)|_{(x,q)=(X,1)} \;+\; q\,k_{\text{on}}\rho(x,q,t)|_{(x,q)=(X,0)}\,\mathrm{d}X\right\}, \tag{2.17}$$

where $x \in \mathbb{R}_+$, $q \in \{0,1\}$. To simplify this equation, we represent the probability density function $\rho(x,q,t)$ as

$$\rho(x,q,t) = q\,\rho(x,t) + (1-q)\,P_0(t)\,\delta(x). \tag{2.18}$$

The function $\rho(x,t)$ represents, at time t, the density of being bound with extension x and $P_0(t)\,\delta(x)$ represents, at time t, the probability mass of the unbound state, concentrated at $x = 0$. Then,

$$\frac{\partial \rho(x,t)}{\partial t} = -\frac{\partial}{\partial x}\left[v_e(x,1)\rho(x,t)\right] - r(x)\,\rho(x,t) + k_{\text{on}}P_0(t)\,\delta(x), \tag{2.19}$$

$$\frac{\mathrm{d}P_0}{\mathrm{d}t} = -k_{\text{on}}\,P_0(t) + \int_0^{+\infty} r(X)\,\rho(X,t)\,\mathrm{d}X. \tag{2.20}$$

With the above definition, the following normalization condition is satisfied:

$$\int_0^{+\infty}\rho(X,t)\,\mathrm{d}X + P_0(t) = 1. \tag{2.21}$$

The extension rate when the linker is attached, is

$$v_e(x,1) = \frac{F - \kappa\,x}{\xi\,(1+\chi^{-1})}. \tag{2.22}$$

Therefore, equation (2.19) reduces to

$$\frac{\partial \rho}{\partial t} + \frac{F-\kappa\,x}{\xi\,(1+\chi^{-1})}\frac{\partial \rho}{\partial x} = \left[\frac{\kappa}{\xi\,(1+\chi^{-1})} - r(x)\right]\rho(x,t) + k_{\text{on}}P_0(t)\,\delta(x). \tag{2.23}$$

2.5.1 Steady state distribution

Steady state solutions, $\rho(x)$, P_0, satisfy

$$\frac{F-\kappa\, x}{\xi\,(1+\chi^{-1})}\frac{\partial \rho}{\partial x} = \left[\frac{\kappa}{\xi\,(1+\chi^{-1})} - r(x)\right]\rho(x) + k_{\text{on}} P_0\,\delta(x), \tag{2.24}$$

$$k_{\text{on}}\,P_0 = \int_0^{+\infty} r(X)\,\rho(X)\,\mathrm{d}X. \tag{2.25}$$

which can be combined to give a single equation for $\rho(x)$:

$$\frac{F-\kappa\, x}{\xi\,(1+\chi^{-1})}\frac{\partial \rho}{\partial x} = \left[\frac{\kappa}{\xi\,(1+\chi^{-1})} - r(x)\right]\rho(x) + \delta(x)\int_0^{+\infty} r(X)\,\rho(X)\,\mathrm{d}X\,. \tag{2.26}$$

To solve the above equation, we start by assuming that $\rho(x) = p(x)\,H(x)$ for $x \in \mathbb{R}$. Furthermore, we seek solutions where the maximal linker extension is F/κ, since the system stalls and the filament stops moving when the linker reaches this extension (as can be seen from the extension rate (2.22)). Thus, we assume that $p \equiv 0$ for $x > F/\kappa$. With these assumptions, (2.26) reduces to

$$\frac{F-\kappa\, x}{\xi\,(1+\chi^{-1})}\frac{\partial p}{\partial x} = \left[\frac{\kappa}{\xi\,(1+\chi^{-1})} - r(x)\right]p(x), \tag{2.27}$$

$$p(0) = \frac{\xi\,(1+\chi^{-1})}{F}\int_0^{F/\kappa} r(X)\,p(X)\,\mathrm{d}X\,, \tag{2.28}$$

to be solved for $x \in (0, F/\kappa)$.

In the case of the Bell-type dissociation rate (2.7), we solve (2.27) - (2.28) to obtain

$$p(x) = \frac{\frac{F}{F-\kappa x}\,\mathrm{e}^{-g(x)}}{\int_0^{F/\kappa}\left[1+\frac{k_{\text{off}}}{k_{\text{on}}}\mathrm{e}^{\kappa s/F_b}\right]\frac{F}{F-\kappa s}\,\mathrm{e}^{-g(s)}\,\mathrm{d}s}, \tag{2.29}$$

where

$$g(x) := -\frac{k_{\text{off}}\,\mathrm{e}^{F/F_b}\,\xi(1+\chi)\mathrm{Ei}\left(-\frac{(F-\kappa x)}{F_b}\right)}{\kappa\,\chi}. \tag{2.30}$$

2.5.2 Classification of steady state solutions

The location and type of critical points of the steady state distribution $p(x)$ can be determined. Furthermore, for the Bell-type law (2.7), steady state solutions belong to one of three categories, depending on the system parameters.

General detachment rate

Setting $p'(x) = 0$ in (2.27) and assuming that $p \not\equiv 0$, we obtain the algebraic equation

$$r(X) - \frac{\kappa}{\xi\,(1+\chi^{-1})} = 0. \tag{2.31}$$

Roots of the above equation, X, are critical points of the distribution as long as $X \in [0, F/\kappa]$. Assuming that $p(x)$ is twice continuously differentiable in $(0, F/\kappa)$, differentiating (2.27) and setting $x = X$ we obtain

$$\frac{\partial^2 p}{\partial x^2}(X) = -\frac{\xi\,(1+\chi)\,r'(X)}{\chi\,(F-\kappa\,X)}p(X). \tag{2.32}$$

It follows from the above expression that for $X \in (0, F/\kappa)$, X is a local maximum if $r'(X) > 0$ and a local minimum if $r'(X) < 0$. Furthermore, if such a root is unique in the interval $(0, F/\kappa)$, it follows that it is a global maximum of the distribution over $[0, F/\kappa]$ if $r'(X) > 0$, and a global minimum if $r'(X) < 0$. If there is no root for (2.31) in $[0, F/\kappa]$, then $p(x)$ is strictly decreasing or strictly increasing, depending on the sign of $\kappa/\left(\xi\,(1+\chi^{-1})\right) - r(x)$ in $[0, F/\kappa]$ (decreasing if the sign is negative and increasing if the sign is positive).

Bell's detachment rate

We now focus on the particular case $r(x) = k_{\text{off}}\exp(\kappa\,x/F_b)$. For this dissociation rate, equation (2.31) has a single root, given by the expression

$$X = \frac{F_b}{\kappa}\log\left(\frac{\kappa\,\chi}{k_{\text{off}}\,\xi\,(1+\chi)}\right). \tag{2.33}$$

Since $r'(x) > 0$ for all $x \in \mathbb{R}$, it follows that X is a global maximum over $[0, F/\kappa]$ and therefore is the mode of $p(x)$, as long as $0 < X < F/\kappa$.

Thus the probability density function $p(x)$ belongs to one of three categories. These categories are: (i) The *motor dominated* (*MD*) category, where $p(x)$ is a strictly decreasing distribution with mode at $x = 0$; (ii) The *motor-clutch balanced* (*MCB*) category, where $p(x)$ is an initially increasing, then decreasing distribution with mode at $x = X$, $X \in (0, F/\kappa)$ (iii) The *clutch dominated* (*CD*) category, where $p(x)$ is a strictly increasing distribution with mode at $x = F/\kappa$. See Fig. 2.3 (bottom) for representative examples of each type of solution.

In the case of MD, when bound, the linker is most likely to have zero extension. As such, newly formed bonds rupture rapidly due to the action of myosin motors. The action of the motors dominates that of the clutch.

In the case of MCB, the stochastic linker spends most of its time at a non-zero extension smaller than F/κ. Consequently, the filament spends most of its time traveling at a non-zero speed, which, however, is slower than if the filament were free-flowing. Since, when bound, the linker manages to spend most of its time in a loaded state which still allows the filament to move, there is a balance between myosin contractility and the resistance offered by the clutch.

In the case of CD, each bound linker spends most of its time at the maximal extension of F/κ. At this extension the stochastic linker completely counterbalances the myosin contractile force and the system 'stalls'. Consequently, the actin filament spends a significant portion of time at, or close to, rest. Thus, the resistance of the clutch dominates the contractile action of myosin.

Conditions for membership in each category - Bell type law

The exact expression for the location of the critical point X (2.33) enables us to derive the exact conditions under which $p(x)$ falls in each of the three regimes (i)-(iii). We proceed by stating these conditions.

Category MD occurs if and only if

$$\frac{\kappa}{k_{\text{off}}\xi} \leq 1 \text{ OR } \left(\frac{\kappa}{k_{\text{off}}\xi} > 1 \text{ AND } 0 < \chi < \frac{k_{\text{off}}\xi}{\kappa - k_{\text{off}}\,\xi} \right). \tag{2.34}$$

For the category MCB, we distinguish two cases: Firstly, we note that it is a necessary condition for $X > 0$ that $\kappa > k_{\text{off}}\,\xi$. Given this assumption, the two possible cases are: $k_{\text{off}}\,\xi\,\mathrm{e}^{F/F_b}/\kappa > 1$, in which case $X \in (0, F/\kappa)$ if and only if

$$\chi > \frac{k_{\text{off}}\xi}{\kappa - k_{\text{off}}\,\xi}. \tag{2.35}$$

The second case corresponds to $k_{\text{off}}\,\xi\,\mathrm{e}^{F/F_b}/\kappa \leq 1$, in which case $X \in (0, F/\kappa)$ if and only if

$$\frac{k_{\text{off}}\xi}{\kappa - k_{\text{off}}\xi} < \chi < \frac{k_{\text{off}}\xi \mathrm{e}^{F/F_b}}{\kappa - k_{\text{off}}\xi\,\mathrm{e}^{F/F_b}}. \tag{2.36}$$

Finally, category CD occurs if and only if

$$F < F_b \log\left(\frac{\kappa\,\chi}{k_{\text{off}}\,\xi\,(1+\chi)} \right), \tag{2.37}$$

equivalently, if and only if $k_{\text{off}}\,\xi\,\mathrm{e}^{F/F_b}/\kappa < 1$ and

$$\chi > \frac{k_{\text{off}}\,\xi\,\mathrm{e}^{F/F_b}}{\kappa - k_{\text{off}}\,\xi\,\mathrm{e}^{F/F_b}}. \tag{2.38}$$

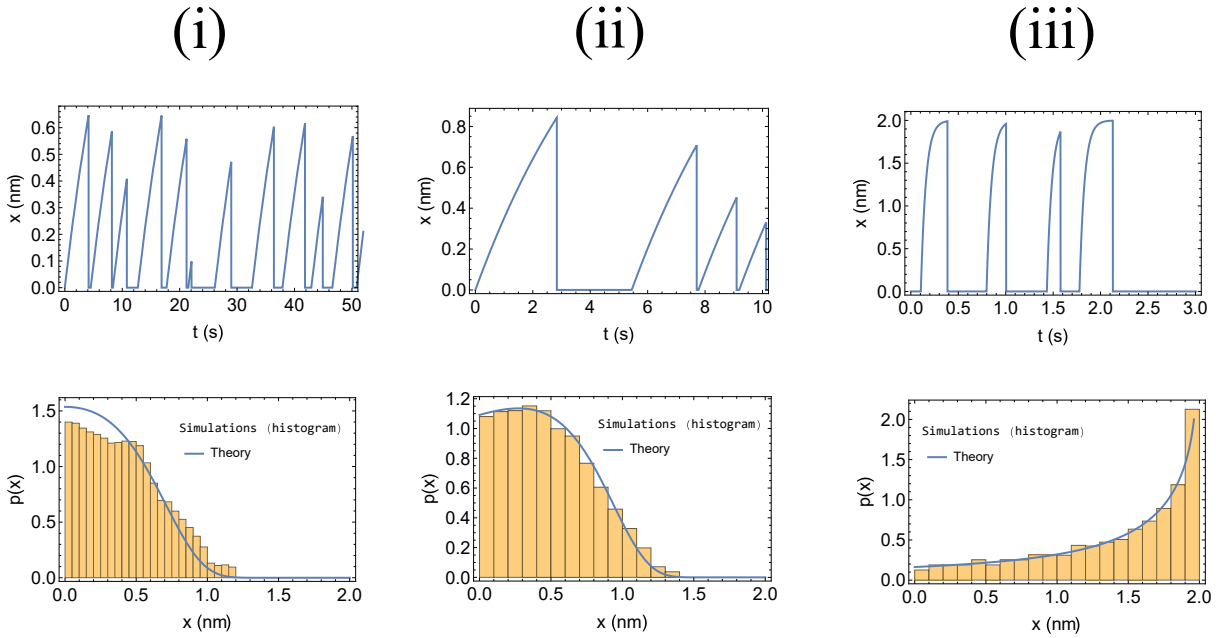


Figure 2.3: Representative trajectories (top) and distributions (bottom) exhibited by the single bond focal adhesion in each of the three dynamical regimes: (i) Motor dominated regime, $\chi = 0.005$ (ii) Motor - Clutch balanced regime, $\chi = 0.01$ (iii) Clutch dominated regime, $\chi = 20$. Common parameters: $F = 0.1 \times 10^{-10}$N, $F_b = 2 \times 10^{-12}$N, $\xi = 0.25 \times 10^{-3}$Ns/m, $\kappa = 5 \times 10^{-3}$N/m, $k_{\text{on}} = 1.0\,\text{s}^{-1}$, $k_{\text{off}} = 0.1\,\text{s}^{-1}$. Trajectories of the system were simulated using the methodology outlined in Section A.1.

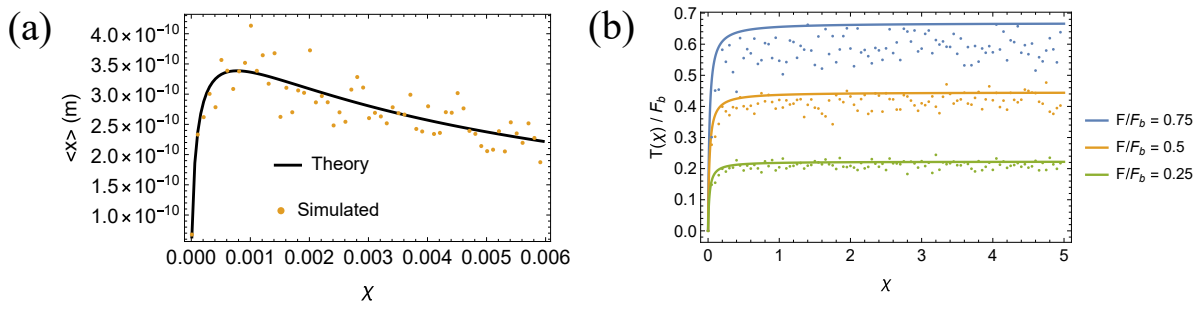


Figure 2.4: (a) Plot of theoretical expression for $\mathbb{E}(x) = T/\kappa$ as a function of χ (solid) and the time-averaged traction force obtained from a stochastic simulation ($F = 1\,\mathrm{nN}$, with $F/F_b = 500$). (b) Plot of the traction approximation (2.40) (solid) compared with the time averaged traction obtained from stochastic simulations (scatter) for different values of F/F_b. Parameters: $F_b = 2 \times 10^{-12}\mathrm{N}$, $\xi = 0.25 \times 10^{-3}\mathrm{Ns/m}$, $\kappa = 5 \times 10^{-3}\mathrm{N/m}$, $k_{\mathrm{on}} = 1.0\,\mathrm{s}^{-1}$, $k_{\mathrm{off}} = 0.1\,\mathrm{s}^{-1}$

2.5.3 Traction and optimal stiffness

We proceed by investigating the traction force generated by the single-linker focal adhesion. The expected traction exerted by the focal adhesion onto the substrate can be computed by

$$T = \kappa\,\mathbb{E}(x) = \kappa \int_0^{F/\kappa} x\,p(x)\,\mathrm{d}x \tag{2.39}$$
$$= \frac{\kappa \int_0^{F/\kappa} \frac{F\,s}{F-\kappa\,s} \mathrm{e}^{-g(s)}\,\mathrm{d}s}{\int_0^{F/\kappa} \left[1 + \frac{k_{\mathrm{off}}}{k_{\mathrm{on}}} \mathrm{e}^{\kappa s/F_b}\right] \frac{F}{F-\kappa s}\,\mathrm{e}^{-g(s)}\,\mathrm{d}s}$$

This expression gives the *ensemble average* of the system. That is, the average traction obtained by considering many independent realizations of the system. In general, this need not coincide with the *time average* of the traction for a single realization of the system. When the time average and ensemble average coincide, the system is said to be *ergodic*. For $N_T = 1$, from simulations the system appears to be ergodic, as there is good agreement between the time average and ensemble average of the traction (see Fig. 2.4 for comparison). The results shown in Fig. 2.4, as well as in later figures involving simulations, are obtained from numerical simulations of the stochastic system; the simulation method is described in Section A.1.

Existence of Optimal Stiffness

It is known from computational studies [13, 3] that when $N_T \gg 1$ the system may exhibit a global maximum in the traction-stiffness curve for some non-zero $\chi^* > 0$. This value of non-dimensional stiffness, χ^*, is termed the *optimal stiffness*. The dimensional optimal

stiffness is denoted by $\kappa^* = \kappa\,\chi^*$. The optimal stiffness may, or may not exist, depending on the particular parameter values of the system.

Numerical evaluation of (2.39) demonstrates that an optimal stiffness may also exist in the single-linker case. The ensemble-averaged traction, computed from (2.39), exhibits a global maximum at an intermediate value of the stiffness χ (see Fig. 2.4(a)). Moreover, although the time-averaged traction obtained from a single simulation is noisy, it closely tracks the ensemble average. This suggests that the same optimal stiffness also arises in time averages of the system.

Optimal stiffness in the weak contractility limit

A principle we will establish later in this chapter is that, in large adhesions, the optimal stiffness does not exist if myosin contractility is sufficiently weak. Here, we investigate whether the same principle applies to the single-linker system.

To do so, we expand T in the limit $F/F_b \ll 1$. To first order in F/F_b, we obtain

$$\frac{T}{F_b} \sim \frac{(F/F_b)}{\left(1+\frac{k_{\text{off}}}{k_{\text{on}}}\right)\left(1+\frac{k_{\text{off}}\,\xi\,(1+\chi)}{\kappa\chi}\right)}, \quad F/F_b \ll 1. \tag{2.40}$$

For small F/F_b, there is good agreement between the above approximation and simulation results (see Fig. 2.4(b)). The above approximation is a strictly increasing function of χ, with $T(0) = 0$ and

$$T(+\infty) = \frac{F}{\left(1+\frac{k_{\text{off}}}{k_{\text{on}}}\right)\left(1+\frac{k_{\text{off}}\,\xi}{\kappa}\right)}. \tag{2.41}$$

Since T is strictly increasing, an optimal stiffness does not exist for the above traction-stiffness curve. This suggests that the optimal stiffness may be pushed to infinity in the limit $F/F_b \ll 1$. Whether the optimal stiffness is eliminated from the traction stiffness curve for a finite but sufficiently small F/F_b or whether the optimal stiffness always exists but appears in higher order terms, is to be established.

2.6 Case 2: Mean-field - Rigid substrate

Our primary interest lies in studying the system for $\chi > 0$, $N_T \gg 1$. However, we briefly expand our analysis from above to the case $\chi = +\infty$, $N_T \gg 1$. In this section we derive the exact equation for the mean-field ansatz and show that our classification of steady states carries over into this regime.

In the rigid substrate case, we have

$$v_e(\boldsymbol{x}, \boldsymbol{q}) = \frac{1}{\xi}\left(F - \kappa \sum_{i=1}^{N_T} q_i\, x_i\right). \tag{2.42}$$

In the mean-field ansatz, one assumes that linkers become uncorrelated in the limit $N_T \to +\infty$. This entails assuming a distribution of the form

$$\rho(\boldsymbol{x}, \boldsymbol{q}, t) = \prod_{j=1}^{N_T} (q_j p(x_j, t) + (1 - q_j) P_0(t) \delta(x_j)). \tag{2.43}$$

Then, if one sums the CK equation (2.5) with respect to q_i and integrates with respect to x_i for all $i \neq k$, where $k \in \{1, \dots, N_T\}$ is chosen arbitrarily, and relabels $x_k = x$, one obtains

$$\frac{\partial p}{\partial t} + \frac{1}{\xi} \left(F - \kappa\, x - \kappa(N_T - 1)\mathbb{E}[x]\right) \frac{\partial p}{\partial x} = \left(\frac{\kappa}{\xi} - r(x)\right) p(x,t) + k_{\text{on}} P_0(t)\, \delta(x), \tag{2.44}$$

$$\frac{\mathrm{d}P_0}{\mathrm{d}t} = -k_{\text{on}} P_0(t) + \int_0^{+\infty} r(X) p(X,t)\, \mathrm{d}X. \tag{2.45}$$

The steady state distribution satisfies

$$\frac{1}{\xi} \left(F - \kappa\, x - \kappa(N_T - 1)\mathbb{E}[x]\right) \frac{\partial p}{\partial x} = \left(\frac{\kappa}{\xi} - r(x)\right) p(x) + \int_0^{+\infty} r(X) p(X)\, \mathrm{d}X\, \delta(x), \tag{2.46}$$

$$P_0 = \frac{1}{k_{\text{on}}} \int_0^{+\infty} r(X) p(X)\, \mathrm{d}X, \tag{2.47}$$

with the normalization condition

$$\int_0^{+\infty} p(X)\, \mathrm{d}X + P_0 = 1. \tag{2.48}$$

2.6.1 Steady state distribution

Solving (2.46) for the steady state, one obtains a family of equations for $p(x)$, parametrised by $\mu := \mathbb{E}(x)$:

$$p(x;\mu) = \frac{\mathrm{e}^{-G(x)}}{(F - \kappa\mu(N_T - 1) - \kappa\, x) \int_0^{\frac{F}{\kappa} - \mu(N_T - 1)} \left[1 + \frac{k_{\text{off}}}{k_{\text{on}}} \mathrm{e}^{\kappa s / F_b}\right] \frac{\mathrm{e}^{-G(s)}}{F - \kappa\mu(N_T - 1) - \kappa\, s}\, \mathrm{d}s}, \tag{2.49}$$

where

$$G(x) := -\frac{k_{\text{off}}\, \xi}{\kappa} \exp\left[\frac{F - \kappa\, \mu(N_T - 1)}{F_b}\right] \mathrm{Ei}\left(-\frac{(F - \kappa\, \mu(N_T - 1) - \kappa x)}{F_b}\right). \tag{2.50}$$

Just as in the $N_T = 1$ case, we restrict the domain of definition of $p(x)$ up to the extension at which the system stalls. This maximal extension is obtained by solving

$$F - \kappa\, x_{\max} - \kappa(N_T - 1)\mu = 0,$$

for $x_{\max}$. Doing so, we obtain the domain of definition of $p(x)$: $x \in [0, (F/\kappa) - (N_T - 1)\mu)$. Since μ is defined as the first moment of this distribution, it must satisfy the consistency condition

$$\mu = \int_0^{(F/\kappa)-(N_T-1)\mu} X\, p(X;\mu)\, \mathrm{d}X. \tag{2.51}$$

This is a non-linear equation for μ. For each μ that solves the above consistency condition, there exists a corresponding probability density function which is a solution to (2.46).

An upper bound for μ can be directly obtained from (2.51). It follows from this equality that μ must satisfy the following inequality

$$\mu \leq \left[\frac{F}{\kappa} - (N_T - 1)\mu\right] \int_0^{(F/\kappa)-(N_T-1)\mu} p(X;\mu)\, \mathrm{d}X \leq (F/\kappa) - (N_T - 1)\mu. \tag{2.52}$$

Rearranging, one obtains

$$0 \leq \mu \leq \frac{F}{\kappa\, N_T}. \tag{2.53}$$

2.6.2 Classification of solutions

Similar to the case $N_T = 1$, solutions of (2.46) belong to one of the three categories MD, MCB, CD (see Section 2.5). Just like in the case $N_T = 1$, the regime to which each solution belongs depends on the location of possible critical points of the distribution, which in this case are obtained through the solution of

$$r(X) = \frac{\kappa}{\xi}. \tag{2.54}$$

For the Bell-type dissociation rate, X is uniquely given by

$$X = \frac{F_b}{\kappa} \log\left(\frac{\kappa}{k_{\text{off}}\, \xi}\right).$$

Whether X is below, in or above the interval $(0, (F/\kappa) - (N_T - 1)\mu)$ determines whether a solution belongs to MD, MCB or CD, respectively.

Conditions for membership

Unlike in the case of $N_T = 1$, we cannot derive conditions which are necessary *and* sufficient for the membership of solutions to each regime. Achieving such a derivation is intractable, as it would necessitate knowing exactly the possible values of μ for a given set of parameters. To do so would require solving (2.51) exactly, which we cannot do, due to its non-linearity.

Although finding the boundaries between the different regimes in parameter space is intractable, by utilizing (2.53), we can derive some sufficient conditions for membership in each category.

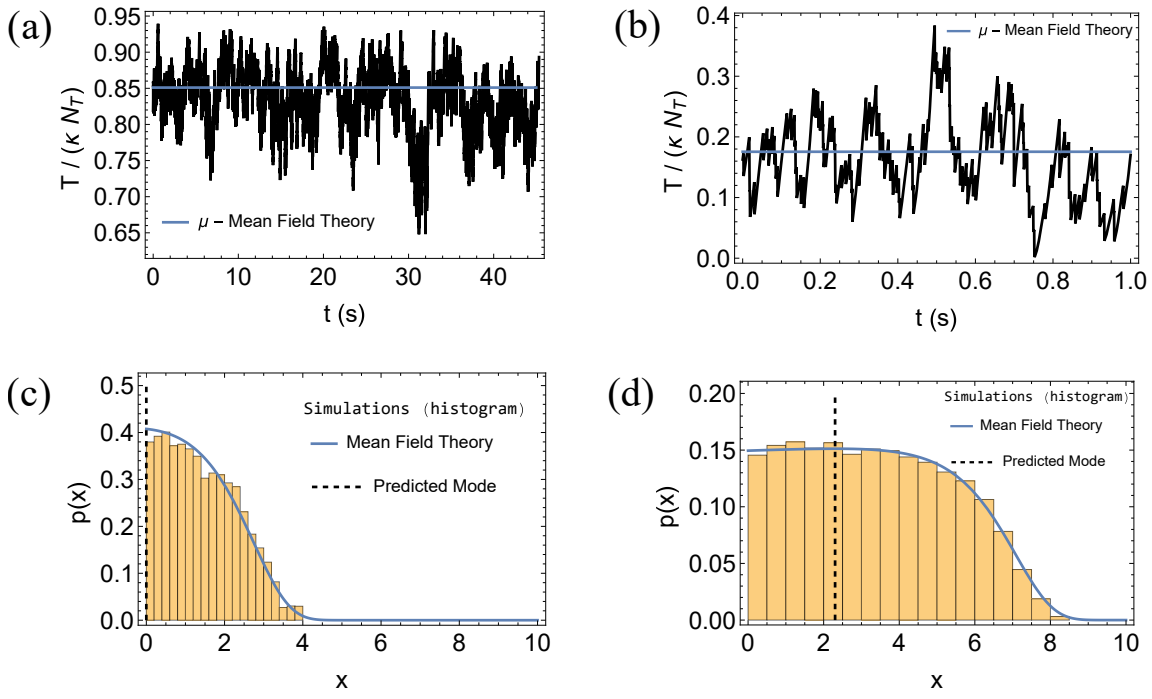


Figure 2.5: (a) Plot of $T/(\kappa N_T)$ for a motor-filament-focal adhesion system in the motor dominated regime (i). Parameters: $F = 150\text{N}, F_b = 1\text{N}, \xi = 15\text{N s/m}, \kappa = 1\text{N/m}, k_{\text{on}} = 1\text{s}^{-1}, k_{\text{off}} = 0.1\text{s}^{-1}, N_T = 150$. (b) Plot of $T/(\kappa N_T)$ for a motor-filament-focal adhesion system in the motor-clutch balanced regime (ii). Parameters: $F = 150\text{N}, F_b = 1\text{N}, \xi = 1\text{N s/m}, \kappa = 1\text{N/m}, k_{\text{on}} = 1\text{s}^{-1}, k_{\text{off}} = 0.1\text{s}^{-1}, N_T = 150$. (c) Comparison between a histogram plot obtained from the same simulation data used to generate (a) and mean-field theory prediction for the extension distribution of a randomly selected linker, conditioned on it being bound. (d) Comparison between a histogram plot obtained from the same simulation data used to generate (b) and mean-field theory prediction for the extension distribution of a randomly selected linker, conditioned on it being bound.

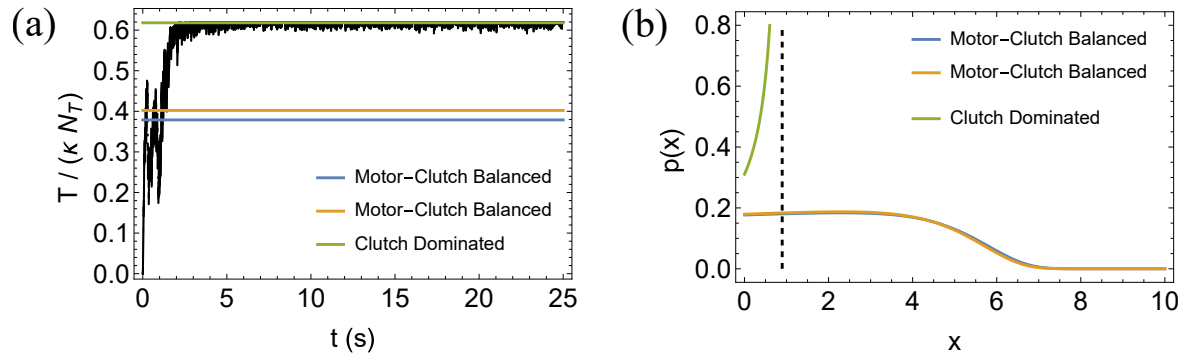


Figure 2.6: Illustration of the exhibition of stick-slip when there exist multiple steady states in the mean-field equation. (a) The system enters an initial phase which belongs to the motor-clutch balanced regime and then transitions to a clutch dominated regime. Horizontal lines indicate the expected extension predicted by the mean-field steady states. (b) Plot of the steady state solutions to the mean field equations, normalized by the probability of being bound, for the parameter values used for the simulation shown in (a). Asymptote indicates the maximal extension corresponding to the solution belonging to the clutch dominated regime. Parameters: $F = 93\,\mathrm{N}, F_b = 1\,\mathrm{N}, \xi = 1\,\mathrm{N\,s/m}$, $\kappa = 1\mathrm{N/m}$, $k_{\mathrm{on}} = 1\mathrm{s}^{-1}, k_{\mathrm{off}} = 0.1\mathrm{s}^{-1}, N_T = 150$.

Most obviously, if $\kappa/(k_{\mathrm{off}}\,\xi) \leq 1$ then $X \leq 0$ and so the system will be in the MD category. This is also a necessary condition. Thus, the system can only be in MD category if and only if $\kappa/(k_{\mathrm{off}}\,\xi) \leq 1$.

Now, assume that $1 < \kappa/(k_{\mathrm{off}}\,\xi) < \exp(F/(F_b N_T))$. It then follows that

$$0 < X < \frac{F}{\kappa\, N_T}.$$

Since μ satisfies (2.53), it follows that

$$\frac{F}{\kappa\, N_T} \leq \frac{F}{\kappa} - (N_T - 1)\mu,$$

and therefore it follows that

$$0 < X < \frac{F}{\kappa} - (N_T - 1)\mu.$$

Thus, if $1 < \kappa/(k_{\mathrm{off}}\,\xi) < \exp(F/(F_b N_T))$, the system is in the MCB category.

A sufficient condition for the system being in the CD category is $\exp(F/F_b) \leq \kappa/(k_{\mathrm{off}}\,\xi)$. If this inequality holds, it follows that

$$\frac{F}{\kappa} - (N_T - 1)\mu \leq \frac{F}{\kappa} < X,$$

which guarantees that X is outside the interval of definition.

2.6.3 Multiple solutions and break down of the mean-field approximation

Since the consistency condition (2.51) is non-linear for $N_T > 1$, it is possible that multiple solutions exist. Furthermore, more than one of these solutions may be attractive to nearby trajectories of the system.

When multiple attractive steady states exist, the system may occasionally transition between them. In this case, the observed distribution of a single realization of the system will be multi-modal and the long-term behaviour of a particular trajectory may depend on its initial condition. In this case, the mean-field approximation breaks down.

Although the mean-field approximation breaks down when multiple steady state solutions exist and the observed extension distribution does not coincide with those of the theoretical steady states, we observe numerically that the first moments of these solutions give accurate locations around which single trajectories of the traction localise and transition between.

Furthermore, each of these steady states falls into one of the categories MD, MCB, or CD. Simulations suggest that, between transitions, individual trajectories of the system exhibit qualitative behaviour characteristic of the category of the steady state around which the traction is temporarily localised. For example, a single trajectory may switch from a clutch-dominated regime (*sticking*) to a motor-clutch-balanced regime (*slipping*) (see Fig. 2.6 for an example). In such cases, the system exhibits the well-known *stick-slip* motion reported in motor-filament-focal-adhesion systems.

The mean-field can also break down when only a single solution exists. Specifically, from simulations we observe that when the system is in the clutch dominated regime the predicted distribution for the extension lengths of individual proteins does not agree with the observed distributions. Paradoxically, we observe that the ensemble average of traction predicted by the mean field theory, $\kappa\,\mu$, still accurately represents the time average of traction, as long as the CD steady state is the only one that exists. Why the mean-field theory breaks down for the CD category is uncertain. It may be because in this regime, the filament is mostly at rest. This may allow for stronger cooperative effects between linkers when the filament is perturbed and starts moving again. As such, the bound linkers of the system may become highly correlated. Consequently, the assumption of statistical independence would be strongly violated.

We observe that the mean field equation is quite good at capturing the statistics of individual proteins when the system is in either the motor dominated regime or the motor - clutch balanced regime (See Fig. 2.5).

Classification of co-existing steady states

From our previous analysis, we conclude that regime (i) cannot co-exist with any of the other regimes. This is because the location of the mode, X, is common for all co-existing solutions, and the determinant of whether a solution belongs to a given regime is whether X falls in the domain of definition of each solution, which depends on its first moment, μ. If X is negative, it straightforwardly follows that all possible solutions must fall into regime (i).

Because we derived sufficient conditions for membership in regimes (ii) and (iii), it follows that co-existence of these solutions (and thus the existence of the stick slip phenomenon) can only occur when these sufficient conditions are violated. Specifically, for the co-existence of regimes (ii) and (iii), we must have

$$\mathrm{e}^{\frac{F}{F_b N_T}} \leq \frac{\kappa}{k_{\mathrm{off}}\,\xi} < \mathrm{e}^{\frac{F}{F_b}}.$$

In terms of the myosin force, this can be written as

$$\log\left(\frac{\kappa}{k_{\mathrm{off}}\,\xi}\right) < \frac{F}{F_b} \leq N_T \log\left(\frac{\kappa}{k_{\mathrm{off}}\,\xi}\right). \tag{2.55}$$

2.6.4 Comparison with exact $\chi > 0$

The mean-field equation for $N_T > 1$ shares some features with the case $N_T = 1$. Equation (2.44) is identical to the single-linker equation in the case $\chi = +\infty$ (2.23), apart from the additional term $-\kappa(N_T - 1)\mathbb{E}[x]$ appearing in the extension rate. This term represents the average tension generated by all other linkers in the system.

2.7 Case 3: Mean-field - Deformable substrate

In the case of a finite substrate stiffness, the mean-field equation obtained by performing the summation and integration of the CK equation outlined in Section 2.6 is not analytically tractable in the limit $N_T \gg 1$. This is because of the expression for the marginal flux J_k that appears in the resulting equation, where

$$J_k = \sum_{\boldsymbol{q}} \delta_{q_k,1} \int_{(\mathbb{R}_+)^{N_T}} v_e(\boldsymbol{x},\boldsymbol{q})\rho(\boldsymbol{x},\boldsymbol{q},t)\,\delta(x_k - x)\,\mathrm{d}x_1\,\mathrm{d}x_2\ldots\mathrm{d}x_{N_T}, \tag{2.56}$$

which cannot be cleanly expressed in terms of a finite number of moments of the distribution p. This is different to the rigid substrate case, where the above sum could be expressed as an affine function of the first moment of the distribution p, $\mathbb{E}[x]$, for every $N_T > 1$.

To obtain an analytically tractable equation when $\chi > 0$, we follow the method of [64, 12] and use a homogeneous extension rate approximation:

$$\sum_{\boldsymbol{q}} \delta_{q_k,1} \int_{(\mathbb{R}_+)^{N_T}} v_e(\boldsymbol{x},\boldsymbol{q})\rho(\boldsymbol{x},\boldsymbol{q},t)\,\delta(x_k - x)\,\mathrm{d}x_1\,\mathrm{d}x_2\ldots\mathrm{d}x_{N_T} \approx \langle v\rangle p(x,t), \tag{2.57}$$

where

$$\langle v\rangle = \frac{F - \kappa N_T \int_0^{+\infty} x\,p(x,t)\,\mathrm{d}x}{\xi\left(1 + \chi^{-1} N_T \int_0^{+\infty} p(x,t)\,\mathrm{d}x\right)}. \tag{2.58}$$

This amounts to replacing the quantities $\sum_{i=1}^{N_T} q_i\,x_i$, $\sum_{i=1}^{N_T} q_i$ (which denote the total extension of linkers and the total number of bound linkers, respectively) in $v_e(\boldsymbol{x},\boldsymbol{q})$ with their mean-field equivalents $N_T \int_0^{+\infty} x\,p(x,t)\,\mathrm{d}x$, $N_T \int_0^{+\infty} p(x,t)\,\mathrm{d}x$. Thus, with this approximation the mean-field system for $p(x,t), P_0(t)$ simplifies to

$$\frac{\partial p(x,t)}{\partial t} + \langle v\rangle \frac{\partial p(x,t)}{\partial x} = -k_{\mathrm{off}} \mathrm{e}^{\frac{\kappa\,x}{F_b}} p(x,t) + \delta(x) k_{\mathrm{on}} P_0(t), \tag{2.59}$$

$$\frac{\mathrm{d}P_0}{\mathrm{d}t} = -k_{\mathrm{on}} P_0(t) + \int_0^{+\infty} r(X) p(X,t)\,\mathrm{d}X. \tag{2.60}$$

Defining $n(x,t) := N_T\,p(x,t)$, $N := \int_0^{+\infty} n(x,t)\,\mathrm{d}x$, multiplying the mean field equations by N_T and noting the normalization condition

$$N_T \int_0^{+\infty} p(x,t)\,\mathrm{d}x + N_T P_0 = N_T, \tag{2.61}$$

we obtain the equations

$$\frac{\partial n(x,t)}{\partial t} + \langle v\rangle \frac{\partial n(x,t)}{\partial x} = -k_{\mathrm{off}} \mathrm{e}^{\frac{\kappa\,x}{F_b}} n(x,t) + \delta(x) k_{\mathrm{on}} N_T P_0(t), \tag{2.62}$$

$$\frac{\mathrm{d}}{\mathrm{d}t}\left[N_T P_0\right] = -k_{\mathrm{on}} N_T P_0(t) + \int_0^{+\infty} k_{\mathrm{off}} \mathrm{e}^{\frac{\kappa X}{F_b}}\, n(X,t)\,\mathrm{d}X, \tag{2.63}$$

which can be written as a single, closed equation for $n(x,t)$:

$$\frac{\partial n(x,t)}{\partial t} + \frac{F - \kappa \int_0^{+\infty} x\, n(x,t)\,\mathrm{d}x}{\xi\left(1+\chi^{-1}N\right)} \frac{\partial n(x,t)}{\partial x} = -k_{\mathrm{off}} \mathrm{e}^{\frac{\kappa x}{F_b}}\, n(x,t) + k_{\mathrm{on}}\left(N_T - N\right)\,\delta(x). \tag{2.64}$$

The function $n(x,t)$ can be interpreted as describing the expected density of linkers with extension x at time t. That is, for small Δx, the expected number of linkers with extension in the interval $[x,\, x+\Delta x)$ is equal to $n(x,t)\,\Delta x$. Steady state solutions of (2.64) satisfy

$$\langle v \rangle \frac{\partial n}{\partial x}(x) = -k_{\mathrm{off}} \mathrm{e}^{\frac{\kappa x}{F_b}}\, n(x) + k_{\mathrm{on}}\left(N_T - N\right)\,\delta(x), \tag{2.65}$$

where the homogeneous extension rate $\langle v \rangle$ must solve

$$\langle v \rangle = \frac{F - \kappa \int_0^{+\infty} x\, n(x,t)\,\mathrm{d}x}{\xi\left(1+\chi^{-1}N\right)}. \tag{2.66}$$

Note that under the homogeneous extension rate approximation we do not need to restrict the domain of definition to any maximal extension and thus the domain of definition of $n(x)$ is $\mathbb{R}_+$. We will devote the rest of the chapter to studying the steady states of this equation.

2.7.1 Steady State Analysis - Constant, homogeneous extension rate

Solutions of (2.65) can be obtained by first solving

$$v_e \frac{\partial n}{\partial x}(x) = -k_{\mathrm{off}} \mathrm{e}^{\frac{\kappa x}{F_b}}\, n(x) + k_{\mathrm{on}}\left(N_T - N\right)\,\delta(x), \tag{2.67}$$

for arbitrary $v_e \in (0, +\infty)$ to obtain a family of solutions $n(x; v_e)$ and then solving the algebraic equation

$$v_e = \frac{F - \kappa \int_0^{+\infty} x\, n(x;v_e)\,\mathrm{d}x}{\xi\left(1+\chi^{-1}\int_0^{+\infty} n(x;v_e)\,\mathrm{d}x\right)}. \tag{2.68}$$

Thus, the first step in obtaining solutions to (2.65) is to obtain $n(x; v_e)$. Solving (2.67) we obtain

$$n(x;v_e) = \frac{k_{\mathrm{on}}\left(N_T - N\right)}{v_e} \exp\left(-\int_0^x \frac{k_{\mathrm{off}} \mathrm{e}^{\frac{\kappa s}{F_b}}}{v_e}\mathrm{d}s\right). \tag{2.69}$$

The quantity N is defined in terms of $n(x; v_e)$ and thus must satisfy a consistency condition:

$$N = \int_0^{+\infty} n(x;v_e)\mathrm{d}x.$$

It follows from the above equation that

$$N = \int_0^{+\infty} \frac{k_{\text{on}}\left(N_T - N\right)}{v_e} \exp\left(-\int_0^x \frac{k_{\text{off}} \mathrm{e}^{\frac{\kappa s}{F_b}}}{v_e} \mathrm{d}s\right) \mathrm{d}x.$$

This is a linear equation for N. Solving it, we obtain

$$N = N_T \frac{\mathcal{Z}\left(\nu, k_{\text{on}}/k_{\text{off}}\right)}{1 + \mathcal{Z}\left(\nu, k_{\text{on}}/k_{\text{off}}\right)}, \tag{2.70}$$

where we define

$$\mathcal{Z}\left(\nu, \mathcal{K}\right) := -\mathcal{K} \frac{1}{\nu} \exp\left(\frac{1}{\nu}\right) \mathrm{Ei}\left(-\frac{1}{\nu}\right), \tag{2.71}$$

$\mathrm{Ei}(x)$ is the exponential integral and

$$\nu = \frac{\kappa}{k_{\text{off}} F_b} v_e, \quad \mathcal{K} = k_{\text{on}}/k_{\text{off}}, \tag{2.72}$$

are the non-dimensional extension-rate and the equilibrium constant, respectively. Traction is given by

$$T = \kappa \int_0^{+\infty} x\, n(x; v_e) \mathrm{d}x,$$

which simplifies to

$$T = F_b\, N_{\mathrm{T}} \mathcal{K}\, \frac{\mathcal{H}\left(\frac{1}{\nu}\right)}{1 + x\left(\nu, k_{\text{on}}/k_{\text{off}}\right)}, \tag{2.73}$$

where

$$\mathcal{H}\left(u\right) := u\mathrm{e}^u \int_0^{\infty} y \exp\left(-u\mathrm{e}^y\right)\, \mathrm{d}y, \quad u > 0. \tag{2.74}$$

The function $\mathcal{H}(u)$ is positive, with $\mathcal{H}(0) = 0$. It is initially increasing and then decreasing, tending asymptotically to 0 as $u \to +\infty$. It has a global maximum at $u = u^* \approx 0.387$.

As can be seen from the above expressions, the total number of bound proteins N and the non-dimensional traction T/F_b, are completely determined by the non-dimensional parameters N_T, ν and $\mathcal{K}$.

2.7.2 Properties of T

Some properties of T under the constant extension rate will be important when we study the optimal stiffness of traction-stiffness curves. In this section we describe some of these properties. We leave the properties of N for the Appendix (Section A.2).

To analyze the behavior of T, we first define the following non-dimensional function:

$$\tau\left(d_1, \mathcal{K}\right) := \frac{\mathcal{K}}{1 + \mathcal{K}\,\mathcal{G}\left(d_1\right)} \mathcal{H}\left(d_1\right), \tag{2.75}$$

where

$$\mathcal{G}(x) = -\,x\,\mathrm{e}^{x}\,\mathrm{Ei}\,(-x)\,, \tag{2.76}$$

is a positive and strictly increasing function, with $\mathcal{G}\,(0^+) = 0$ and $\mathcal{G}(+\infty) = 1$.

Using this definition, T can be expressed as

$$T = F_b\,N_T\,\tau\left(\frac{1}{\nu}, \mathcal{K}\right). \tag{2.77}$$

Thus, the function $\tau(d_1, \mathcal{K})$ determines the response of T to $\nu, \mathcal{K}$. The properties of τ are outlined in detail in the appendix (Section A.3). Of these properties, the most significant is that, as a function of d_1, τ possesses a global maximum for all $\mathcal{K} > 0$ at $d_1 = d_1^*(\mathcal{K})$. Furthermore, the function $d_1^*(\mathcal{K})$ is positive and strictly decreasing with $d_1^*(\mathcal{K}) \to 0$ as $\mathcal{K} \to +\infty$ and $d_1^*(0^+) = u^*$.

An important consequence of the existence of a global maximum of τ, in d_1, is that T, as a function of v_e, possesses a global maximum at

$$v_e = v^* = \frac{k_{\mathrm{off}}\,F_b}{\kappa\,d_1^*(\mathcal{K})}, \tag{2.78}$$

for all $\mathcal{K} > 0$. This fact will be important when we derive the optimal stiffness of the system in Section 2.7.4.

2.7.3 Traction-stiffness curves

We proceed with a study of how traction, T, depends on the non-dimensional substrate stiffness χ. In this section we define *traction-stiffness* curves.

For each χ, possible values of the steady state extension rate v_e solve

$$V(v_e, \chi) = \frac{1}{\xi}\left(F - T(v_e)\right), \tag{2.79}$$

where (see (2.68))

$$V(v_e, \chi) = v_e\,\left(1 + \chi^{-1}N(v_e)\right). \tag{2.80}$$

Such solutions generate an admissible steady state solution $n(x; v_e)$. Suppose there exists some solution (χ_0, v_e^0) to the equation

$$F - T(v_e) - \xi\,V(v_e, \chi) = 0. \tag{2.81}$$

Then, as long as

$$-T'(v_e^0) - \xi\frac{\partial V}{\partial v_e}(\chi_0, v_e^0) \neq 0, \tag{2.82}$$

the Implicit Function Theorem guarantees the existence of a unique function $v_e(\chi)$, such that $v_e(\chi_0) = v_e^0$. Furthermore, this function solves the force balance equation in a neighbourhood of χ_0, i.e.

$$F - T(v_e(\chi)) - \xi\, V(v_e(\chi), \chi) = 0, \tag{2.83}$$

for all χ in the provided neighbourhood of χ_0. The composite function $T(\chi) = T(v_e(\chi))$ relates steady state traction to substrate stiffness. Such a function is referred to as a traction-stiffness curve. Note that since for each χ there may exist multiple solutions to the force balance equation, there may exist multiple such traction stiffness curves, for a given χ_0.

For a given root (χ_0, v_e^0), $v_e(\chi)$ can be obtained by integrating the first order differential equation

$$\frac{\mathrm{d}v_e}{\mathrm{d}\chi}(\chi) = \frac{-\xi \frac{\partial V}{\partial \chi}(v_e(\chi), \chi)}{\frac{\partial T}{\partial v_e}(v_e(\chi)) + \xi \frac{\partial V}{\partial v_e}(v_e(\chi), \chi)}, \quad v_e(\chi_0) = v_e^0. \tag{2.84}$$

For sufficiently large N_T and F, there exists only one solution to the force balance equation for each χ. We proceed with this assumption. In this regime, the traction stiffness curve exhibits one of two behaviours which is determined by how F relates to a critical force F_{crit} (see Fig. 2.7): (i) If $F \leq F_{\text{crit}}$, then $T(\chi)$ is a bounded, strictly increasing function, tending to a limiting value of T_∞. (ii) If $F > F_{\text{crit}}$, $T(\chi)$ exhibits a global maximum at $\chi = \chi^*$. For $\chi < \chi^*$, $T(\chi)$ is strictly increasing. For $\chi > \chi^*$, $T(\chi)$ is strictly decreasing, tending to a limiting value of $T_\infty > 0$. In the next sections, we study χ^* and F_{crit}.

2.7.4 Derivation of an expression for the optimal stiffness

The function $T(\chi)$ may exhibit a global maximum at a stiffness value of χ^*, for a range of parameters. We call χ^* the *optimal stiffness*. At that value of χ, the ability of the growth cone to develop traction forces on the substrate is maximal. Here, we derive the expression for χ^* as a function of the system parameters.

An exact expression for the optimal stiffness can be obtained through the observation that $T(\chi)$ must also be *locally* maximal at $\chi = \chi^*$. Thus, it must be the case that $T'(\chi^*) = 0$. By applying the chain rule to $T(\chi) = T(v_e(\chi))$, we obtain

$$\frac{\partial T}{\partial v_e}(v_e(\chi^*))v_e'(\chi^*) = 0. \tag{2.85}$$

Thus, a critical point of $T(\chi)$ can be obtained by setting

$$\frac{\partial T}{\partial v_e}(v_e(\chi^*)) = 0. \tag{2.86}$$

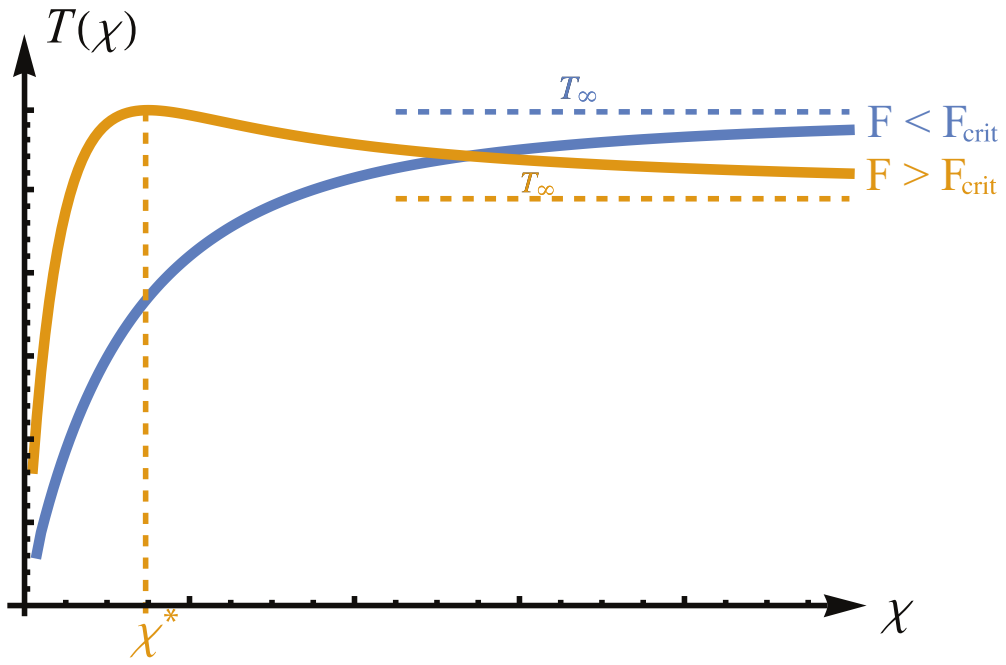


Figure 2.7: Profile of the traction-stiffness curve $T(\chi)$. For small myosin contraction, $F < F_{\text{crit}}$, the traction increases monotonically as a function of the stiffness. For large myosin contractility, $F > F_{\text{crit}}$, traction has a maximum value at the optimal stiffness χ^*.

As argued previously, the function $T(v_e)$ has a single unique local maximum at $v_e = v^*$. Thus, the above condition is met if and only if

$$v_e(\chi^*) = v^*. \tag{2.87}$$

Using the force balance equation, we can explicitly derive an expression for χ^* that satisfies $v_e(\chi^*) = v^*$. From the force balance equation it follows that

$$F - T(v_e(\chi^*)) - \xi\, V(v_e(\chi^*), \chi^*) = 0, \tag{2.88}$$

from which it follows that

$$F - T(v^*) - \xi\, V(v^*, \chi^*) = 0. \tag{2.89}$$

The above equality is equivalent to

$$F - T(v^*) - \xi\, v^* \left(1 + \frac{N(v^*)}{\chi^*}\right) = 0. \tag{2.90}$$

Solving for χ^*, which is possible because the value of v^* is independent of χ^*, we obtain

$$\chi^* = \frac{\xi\, v^*\, N(v^*)}{F - T(v^*) - \xi\, v^*}. \tag{2.91}$$

The above expression gives an exact location for a critical point of $T(\chi)$. Numerically, we observe that only one such critical point exists which is equal to the optimal stiffness, when it exists. Therefore, we identify the above expression with the optimal stiffness.

We can utilize this expression to derive a necessary condition for the existence of the optimal stiffness in the traction stiffness curve. This condition follows from the requirement that the optimal stiffness be positive. Since $v^*, N(v^*) > 0$, it follows that $\chi^* > 0$ if and only if

$$F - T(v^*) - \xi\, v^* > 0. \tag{2.92}$$

As mentioned previously in this chapter, this condition has a simple interpretation. Let $F_{\text{crit}} := T(v^*) + \xi\, v^*$. This quantity has units of force and is independent of F. With this definition, condition (2.92) is equivalent to

$$F > F_{\text{crit}}, \tag{2.93}$$

i.e. the optimal stiffness can only exist when myosin contractility is stronger than a critical force. Noting that $T(v^*)$ is the maximal resistance that the focal adhesion can provide against myosin contractility, it follows that the optimal stiffness only exists if myosin contractility is greater than the maximal resistance that the focal adhesion can provide.

2.7.5 Behaviour of F_{crit}

The value F_{crit} takes for different parameter values delineates the conditions under which an optimal stiffness exists. Here, we describe the behaviour of F_{crit} under variation of the kinetic parameters k_{on}, k_{off}. Technical details are outlined in Section A.5. A key finding is that the dependence of F_{crit} on k_{on} and k_{off} is qualitatively different.

We find that increasing k_{on} leads to a monotonic increase in the critical force, with $F_{\text{crit}} \to +\infty$ as $k_{\text{on}} \to +\infty$. This reflects the strengthening of the adhesion through increased binding.

As a function of k_{off}, we find that F_{crit} diverges in both limits $k_{\text{off}} \to 0^+$ and $k_{\text{off}} \to +\infty$. Furthermore, F_{crit} has a single global minimum, whose location is a decreasing function of the non-dimensional parameter $\tilde{\xi}_- := k_{\text{on}}\xi / (\kappa N_T)$.

2.7.6 Behaviour of χ^*

As we will see in later chapters, the location of the optimal stiffness on the traction-stiffness curve plays a crucial role in axon guidance. For this reason, in this section we describe how χ^* behaves according to the different parameters of the system.

It is clear from (2.91) that the optimal stiffness, for $F > F_{\text{crit}}$ is a strictly decreasing function of F with $\chi^* = \mathrm{O}(1/F)$ as $F \to +\infty$. So increasing myosin contractility decreases the optimal stiffness, whilst decreasing myosin contractility increases the optimal stiffness. Furthermore, $\chi^* \to +\infty$ as $F \to F_{\text{crit}}^+$. For $F < F_{\text{crit}}$ there does not exist an optimal stiffness.

The effect of the viscous friction parameter ξ is also straightforward to determine from (2.91). When $\xi = 0$, we have $\chi^* = 0$. As ξ increases, so does the optimal stiffness. Furthermore, $\chi^* \to +\infty$ as $\xi \to (F - T(v^*))/{v^*}^-$. For $\xi > (F - T(v^*))/v^*$ there does not exist an optimal stiffness.

We now describe the effect of the kinetic parameters $k_{\text{on}}, k_{\text{off}}$. Technical details can be found in Section A.6. When only varying k_{on}, χ^* is an increasing function of $k_{\text{on}} > 0$, tending to $+\infty$ as $F_{\text{crit}} \to F$, which occurs at a finite value of $k_{\text{on}} > 0$, which we denote by ${k_{\text{on}}}^R$ (see Fig. 2.8(a)). The optimal stiffness does not exist for values of k_{on} greater than ${k_{\text{on}}}^R$.

For a given set of system parameters, there exist two values of k_{off} such that $F_{\text{crit}} = F$. We denote these by ${k_{\text{off}}}^L, {k_{\text{off}}}^R$, where ${k_{\text{off}}}^L < {k_{\text{off}}}^R$. As a function of k_{off}, the expression for χ^* is only positive on the finite interval $k_{\text{off}} \in \left({k_{\text{off}}}^L, {k_{\text{off}}}^R\right)$. Thus, the optimal stiffness only exists on this interval of detachment rates. Furthermore, we have that $\chi^* \to +\infty$ in both limits $k_{\text{off}} \to {k_{\text{off}}}^{L^+}$, $k_{\text{off}} \to {k_{\text{off}}}^{R^-}$. Between the two end-points ${k_{\text{off}}}^L, {k_{\text{off}}}^R$, χ^* initially decreases and then increases, exhibiting a global minimum for some ${k_{\text{off}}}^* \in ({k_{\text{off}}}^L, {k_{\text{off}}}^R)$ (see Fig. 2.8(b)).

2.7.7 Deriving an expression for $T''(\chi^*)$

As we shall see in later chapters, a feature of the traction stiffness curve which is important for axon guidance is its second derivative at the optimal stiffness, denoted by $T''(\chi^*)$. Here, we derive the exact expression for this quantity.

Firstly, we start with the familiar equality $T(\chi) = T(v_e(\chi))$. By differentiating each side of this equality twice with respect to χ we obtain

$$T''(\chi) = \frac{\partial^2 T}{\partial {v_e}^2}(v_e(\chi)) \ \left(v_e'(\chi)\right)^2 + \frac{\partial T}{\partial v_e}(v_e(\chi))\, v_e''(\chi). \tag{2.94}$$

From the fact that $v_e(\chi^*) = v^*$, it follows that

$$T''(\chi^*) = \frac{\partial^2 T}{\partial {v_e}^2}(v^*) \times \left(v_e'(\chi^*)\right)^2. \tag{2.95}$$

The term $v_e'(\chi^*)$ can be determined by observing that

$$v_e'(\chi) = -\xi \, \frac{\frac{\partial V}{\partial \chi}\left(v_e(\chi), \chi\right)}{\frac{\partial T}{\partial v_e}(v_e(\chi)) + \xi \frac{\partial V}{\partial v_e}(v_e(\chi), \chi)}. \tag{2.96}$$

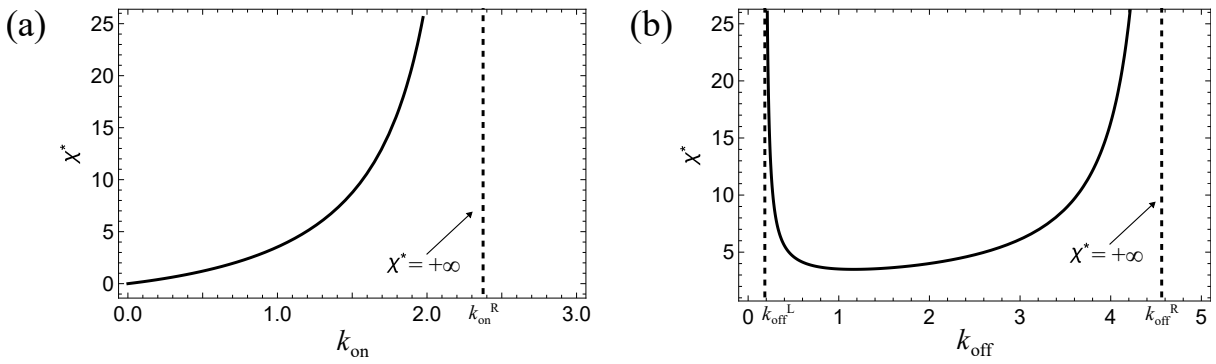


Figure 2.8: (a) Optimal stiffness, χ^*, as a function of k_{on}. As k_{on} tends to k_{on}^R, χ^* tends to $+\infty$. Parameters: $k_{\text{off}} = 1\,\text{s}^{-1}, \kappa = 1\,\text{N/m}$, $F_b = 1\,\text{N}$, $\xi = 1\,\text{N s/m}$, $F = 15\,\text{N}$, $N_T = 20$. (b) Optimal stiffness, χ^*, as a function of k_{off}. As k_{off} tends to k_{off}^L and k_{off}^R, χ^* tends to $+\infty$. Parameters: $k_{\text{on}} = 1\,\text{s}^{-1}, \kappa = 1\,\text{N/m}$, $F_b = 1\,\text{N}$, $\xi = 1\,\text{N s/m}$, $F = 15\,\text{N}$, $N_T = 20$.

The function $V(v_e, \chi)$ was defined in (2.80). Using again the fact that $v_e(\chi^*) = v^*$, it follows that

$$v_e'(\chi^*) = -\xi \frac{\frac{\partial V}{\partial \chi}(v^*, \chi^*)}{\frac{\partial T}{\partial v_e}(v^*) + \xi \frac{\partial V}{\partial v_e}(v^*, \chi^*)} = -\xi \frac{\frac{\partial V}{\partial \chi}(v^*, \chi^*)}{\xi \frac{\partial V}{\partial v_e}(v^*, \chi^*)} = -\frac{\frac{\partial V}{\partial \chi}(v^*, \chi^*)}{\frac{\partial V}{\partial v_e}(v^*, \chi^*)}. \tag{2.97}$$

We compute $(\partial V/\partial \chi)(v^*, \chi^*)$ and $(\partial V/\partial v_e)(v^*, \chi^*)$ using (2.80) and input these into the right-most side of the above equality, to obtain

$$v_e'(\chi^*) = \frac{v^* N(v^*)}{\chi^* \left(\chi^* + N(v^*) + v^* \frac{\partial N}{\partial v_e}(v^*)\right)}. \tag{2.98}$$

Consequently,

$$T''(\chi^*) = \frac{\partial^2 T}{\partial {v_e}^2}(v^*) \frac{{v^*}^2 N(v^*)^2}{{\chi^*}^2 \left(\chi^* + N(v^*) + v^* \frac{\partial N}{\partial v_e}(v^*)\right)^2}. \tag{2.99}$$

The derivation of the precise expression for $(\partial^2 T/\partial v_e^2)(v^*)$ and its dependence on the parameters of the system is outlined in Section A.7 . Thus, written in full, the expression for $T''(\chi^*)$ is

$$T''(\chi^*) = F_b N_T \times \frac{\partial^2}{\partial \nu^2} \left[\tau\left(1/\nu, s\right)\right]_{\nu = \nu^*} \frac{{\nu^*}^2 N(\nu^*)^2}{{\chi^*}^2 \left(\chi^* + N(\nu^*) + \nu^* \frac{\partial N}{\partial \nu}(\nu^*)\right)^2}, \tag{2.100}$$

where $\nu^* = 1/d_1^*(s)$, $s = k_{\text{on}}/k_{\text{off}}$. We note that $T''(\chi^*) < 0$ whenever the optimal stiffness exists ($\chi^* > 0$).

2.7.8 Behaviour of $T''(\chi^*)$

Having derived the expression for $T''(\chi^*)$, here we describe how various parameters of the system determine its value.

A rather useful general principle can be derived regarding the behaviour of $T''(\chi^*)$. The principle is that, all else equal, the smaller χ^*, the larger the magnitude of $T''(\chi^*)$. In other words, all else equal, traction stiffness curves with an optimal stiffness closer to the origin will have a more sharply curved optimum. This property of $T''(\chi^*)$ stems from the fact that, treating χ^* as an independent variable, the expression (2.100) is $\mathcal{O}\left(1/\left(\chi^*\right)^2\right)$ as $\chi^* \to 0^+$.

Myosin contractility, quantified by F, affects $T''(\chi^*)$ only through χ^*. Thus, as F increases, χ^* decreases, and consequently the magnitude of $T''(\chi^*)$ increases.

The kinetic parameters $k_{\text{on}}, k_{\text{off}}$ have the following effects on $T''(\chi^*)$: (i) As a function of k_{on}, $|T''(\chi^*)|$ is strictly decreasing, with $|T''(\chi^*)| \to +\infty$ as $k_{\text{on}} \to 0^+$ and $T''(\chi^*) \to 0$ as k_{on} tends to ${k_{\text{on}}}^R$ (at which point $F_{\text{crit}} = F$ and $\chi^* = +\infty$, see Section 2.7.6). (ii) As a function of k_{off}, $|T''(\chi^*)|$ increases from 0 at $k_{\text{off}} = {k_{\text{off}}}^L$, reaching a global maximum at an intermediate value of k_{off}, and then decreases to 0 as k_{off} approaches ${k_{\text{off}}}^R$ (at which point $F_{\text{crit}} = F$ and $\chi^* = +\infty$, see Section 2.7.6).

2.7.9 Speed-imposition interpretation of myosin action

Most studies of focal adhesion dynamics assume a force balance law of the form (2.12). However, a force balance law of this form may arise from different physical situations leading to different interpretations of the parameters. Consequently, although the underlying manifold that the parameters explore is the same, the different physical interpretations of the parameters will lead to different predictions for the behaviour of the system.

So far, we have followed the example of [64, 12] in assuming that myosin exerts a constant contractile force and that the term linear in V in the force balance equation arises from a viscous drag which the cell cytosol exerts on the filament. However, many studies assume a different mechanism for the determination of the filamentary flow speed. This mechanism assumes that myosin motors *impose* a speed on the filament which is a linear function of the force resisting the action of the motors [13, 1, 18, 17]. For this reason, we call this interpretation the *speed-imposition* interpretation of motor action.

Specifically, it is assumed that

$$V = V_u \left[1 - \frac{T}{F_{\text{stall}}}\right], \tag{2.101}$$

where T, as before, is the tension in the focal adhesion, F_{stall} is the force, exerted on the filament against the motors, at which the myosin motors *stall* and V_u is the speed that motors impose on the filament when there are no forces resisting their action. When the motors stall, the flow speed is equal to 0.

Rearranging the above expression, we obtain

$$\frac{F_{\text{stall}}}{V_u} V + T = F_{\text{stall}}. \tag{2.102}$$

This expression has the same form as the force balance law (2.12), with

$$\xi = \frac{F_{\text{stall}}}{V_u}, \tag{2.103}$$

$$F = F_{\text{stall}}. \tag{2.104}$$

Notably, F_{stall} is equivalent to the myosin contraction parameter F. However, an important consequence of this interpretation is that the parameters ξ and F are not independent. Thus, if this interpretation holds, pharmacological treatments that target F_{stall} will also affect ξ. In this case, we should expect the system to behave differently when varying F_{stall} than when varying F and ξ independently.

To illustrate the difference between the two interpretations, we observe χ^* under the speed-imposition interpretation. Under this interpretation, we have

$$\chi^* = \frac{F\, v^*\, N(v^*)}{(V_u - v^*)\, F - V_u T(v^*)}. \tag{2.105}$$

Although the precondition for the existence of χ^* still remains that F is greater than a critical force, the particular form of F_{crit} is different. Under this interpretation, the critical myosin force takes the form

$$F_{\text{crit}} = \frac{V_u}{V_u - v^*} T(v^*). \tag{2.106}$$

Furthermore, it is also necessary that

$$V_u > v^*. \tag{2.107}$$

The limiting behaviour of χ^* for $F \gg 1$ is also different. Taking the limit $F \to +\infty$, we obtain

$$\chi^* \to \frac{v^*\, N(v^*)}{(V_u - v^*)}. \tag{2.108}$$

This is positive for $V_u > v^*$, which contrasts with the prediction that $\chi^* \to 0^+$ under the constant contraction interpretation. The above results show that, although the different interpretations have the same mathematical structure, each interpretation makes different physical predictions.

2.8 Literature comparison

In this section, we compare the results of this chapter with previous work on the motor-clutch system, particularly in the case of a deformable substrate. The aim is to identify where the present analysis agrees with existing results, where it differs, and what additional insight is gained from the Chapman-Kolmogorov formulation used here.

2.8.1 Qualitative regimes of system trajectories

In Section 2.5, we showed that all steady states for the bound linker distribution of the single-linker system ($N_T = 1$) can be classified into one of three categories. Each category (also called a regime) identified above corresponds to one previously identified in the literature. As in this chapter, in the literature these have been referred to as: (i) the motor dominated regime (ii) the motor-clutch balanced regime (iii) the clutch dominated regime [1].

Previously, the identification of these regimes was made on the basis of observations of the dynamic evolution of trajectories of the system. For example, the system would be identified as being in the clutch dominated regime if it was observed that there was frequent stalling of the system. As such, previous classifications were heuristic and did not give precise, quantitative conditions for membership in each category. Importantly, no link was previously made between the statistics of the system and each regime. Naturally, such a link is necessary for a precise definition of each regime, due to the stochasticity of the system. In this chapter, we were able to make this connection, with the descriptions of the regimes arising directly from the CK equation of the system.

Our direct analysis of the CK equation of the system also allowed us to illuminate further issues with previous understanding of the three regimes. Specifically, it was previously thought that *load-and-fail* dynamics could only occur in the motor dominated and the motor-clutch balanced regimes, but not in the clutch dominated regimes [1]. The system $N_T = 1$ provides a direct counter-example to this hypothesis. For this system, load-and-fail dynamics are exhibited in all three regimes. As expected, in the clutch dominated regime, when the stochastic linker binds it initiates its loading phase and the speed of the filament decreases and the system eventually stalls. However, when the filament disengages, there exist no other linkers to offer any resistance to the motion of the filament. As such, the clutch 'fails' and the filament flows freely until the re-engagement of the filament.

Although this counter-example might be seen as a curious exception, it illustrates how many concepts appearing in the motor-clutch-deformable substrate literature are heuristic and have not been well-defined, owing to the fact that these concepts have arisen mainly from computational studies, where the primary method of understanding the system is observing simulation results over parameter ranges. The approach taken here is to find analytical constructs arising directly from the CK equation that can capture the intuitive picture that has developed about the system through observations of simulations. Thus, the work in this chapter illustrates the need and utility of studying the motor-clutch system on a deformable substrate with analytical techniques, when possible.

2.8.2 Rigid substrate: Mean field

Of the different cases of the motor-clutch-substrate system studied, the rigid substrate case is the one that has previously been studied analytically through the CK equation [64, 12]. Furthermore, in Section 2.7, we used the approximation techniques employed by previous studies to investigate the mean-field limit of the deformable substrate case.

Specifically, the approximation employed is to assume that all bound clutches extend at a homogeneous rate in the mean-field limit. Even in this limit, this assumption is not true. However, the approximation is employed when the marginal probability flux $J_k(x,t)$ (see (2.56)) cannot be computed as a function of a finite number of moments of the single linker distribution $p(x,t)$.

Unlike previous works, here we managed to compute the marginal probability flux in terms of the first moment of the single linker distribution, resulting in the mean-field equation

$$\frac{\partial p}{\partial t} + \frac{1}{\xi}\left(F - \kappa\, x - \kappa(N_T - 1)\mathbb{E}[x]\right)\frac{\partial p}{\partial x} = \left(\frac{\kappa}{\xi} - r(x)\right)p(x,t) + k_{\text{on}}P_0(t)\,\delta(x), \tag{2.109}$$

To compare the above equation with previous works, we state the mean field equation for the single-linker distribution $p(x,t)$ obtained under the homogeneous extension rate approximation:

$$\frac{\partial p}{\partial t} + \langle v\rangle \frac{\partial p}{\partial x} = -r(x)\,p(x,t) + k_{\text{on}}P_0(t)\,\delta(x), \tag{2.110}$$

where the homogeneous extension rate $\langle v\rangle$ is assumed to satisfy the force balance relation

$$F = \xi\,\langle v\rangle + \kappa N_T \mathbb{E}[x]. \tag{2.111}$$

There are two important differences between the exact mean-field equation (2.109) and the equation resulting from the homogeneous extension rate approximation (2.110): Firstly, under the exact mean-field description, the extension rate of each linker depends on its current extension. Secondly, under the exact mean-field equation the steady state statistics also exhibit the three regimes studied in the case of $N_T = 1, \chi > 0$, whilst in the homogeneous mean field approximation, the steady state distribution of protein extensions is strictly decreasing.

Although the mean-field under the homogeneous extension rate was found to compare well with simulation results over a broad range of parameter values, a consequence of this approach is that information is lost about the finer structure of steady states. Specifically, any information regarding the three categories of steady states is lost. The approach outlined in this chapter captures these finer details and also compares well with simulation results.

2.8.3 Optimal Stiffness

A large portion of this chapter was dedicated to studying the optimal stiffness, under what conditions it exists and how it is affected by the various system parameters. There are numerous studies on the optimal stiffness. These are mostly computational in nature, though there are also some attempts to investigate this quantity through analytical methods. Here we compare our results regarding the optimal stiffness with those of the literature. We note that all studies we compare to use the exact same assumptions for the motor-clutch-deformable substrate system. What differs between those approaches and our work here are the mathematical tools utilised to study the system, with the added caveat that most studies hold the speed-imposition interpretation of motor action instead of the force-contraction interpretation.

On the transition from load-and-fail dynamics to frictional-slippage dynamics

A commonly made statement in the literature is that the existence of the optimal stiffness occurs at a transition in the dynamics of the system from load-and-fail to frictional slippage. Specifically, it is believed that the system is in a state of frictional slippage below and above the optimal stiffness, but in a state of load-and-fail in a neighborhood of the optimal stiffness [3, 13]. We find this not to be the case. To show this, we revert to the $N_T = 1$ system. The $N_T = 1$ system is always in a state of load-and-fail but still exhibits an optimal stiffness in its traction stiffness curve. This result further highlights the need for analytical studies of the motor-clutch-deformable substrate system.

Behaviour of Optimal stiffness according to simulation results

Bangasser et al. [3], conducted an extensive simulation study of the dimensional optimal stiffness, $\kappa_s^* = \kappa\chi$, of the motor-clutch system we studied in this chapter. In this study, the authors investigated its response to changes in the parameters of the system. The response of κ_s^* to the variation of single parameters is summarised in Table 2.1. Below, we will use these simulation results as a benchmark to evaluate the analytical expression derived in this chapter and those found elsewhere in the literature.

Analytical expressions for the Optimal Stiffness

In Section 2.7.4, we derived the exact expression for the optimal stiffness of the mean-field approximation of the motor-clutch-deformable substrate system. Various attempts have been made in the past to derive such an expression for this same system [1, 2]. These other attempts have followed a common approach that differs from our own. First, we describe this approach. Then we describe the analytical expressions for the optimal stiffness that

Response of κ^* to increasing stated parameter, all else equal [3]	
Parameter	Simulations
k_{on}	Increasing
k_{off}	Decreasing
F_b	Increasing
N_T	Increasing
κ	No effect
F_{stall}	Decreasing
V_u	Decreasing

Table 2.1: Response of κ^* to increasing stated parameter, all else equal, according to [3].

have been derived using it. We then proceed with comparing these expressions with the one derived in this chapter. Finally, all expressions are compared with the simulation data of Bangasser, et al [3].

The common approach followed by studies such as Bangasser and Odde [2] and Alonso-Matilla et al. [1] utilises a heuristic regarding the conditions under which an optimal stiffness should exist. This heuristic states that for force transmission to be maximal at an intermediate stiffness, the system must be in a state of load-and-fail dynamics and furthermore that the full clutch ensemble must be recruited between failures of the focal adhesion.

This requirement for maximal force transmission can be expressed as a comparison between two timescales: The average time between the onset of loading and collective clutch failure, which is called the cycle time and denoted by t_{cycle}, and the expected time required for all clutches to bind from a state where all clutches are unbound, denoted by t_{bind}. It is argued that maximal force transmission occurs when $t_{\text{bind}} = t_{\text{cycle}}$.

This argument proceeds as follows: If $t_{\text{bind}} > t_{\text{cycle}}$, the cycle ends before all clutches are recruited, so the full resisting capacity of the clutch ensemble is not utilized. If $t_{\text{bind}} < t_{\text{cycle}}$, then the cycle is sufficiently long such that bound clutches begin to spontaneously unbind before collective failure is reached, again reducing force transmission. This motivates the conclusion that maximal force transmission occurs when $t_{\text{bind}} = t_{\text{cycle}}$.

The value of t_{bind} is independent of the substrate stiffness, whereas t_{cycle} depends on κ_s. Thus, the condition $t_{\text{bind}} = t_{\text{cycle}}$ can be viewed as an equation for κ_s. According to the heuristic, the solution of this equation defines the optimal stiffness, κ_s^*.

One might ask why there exist different expressions for κ_s^* arising from the same heuristic principle. Although the heuristic principle is well-defined, the specific expression for κ_s^* that arises from its application depends on how the system is formalised analytically. A different analytical formulation of the system results in different expressions for t_{bind} and t_{cycle}, resulting in a different expression for κ_s^*.

We proceed with the description of the different expressions for κ_s^*.

Bangasser and Odde [2]

The paper studies the motor-clutch system utilising a master-equation approach. In this formulation, each clutch is described by the probability of being bound and its current extension. The assumptions regarding the kinetics and behaviour of individual clutches is identical to those made in this chapter.

To make the system analytically tractable, the authors assume that at any one time the distribution of bound extensions follows a gamma distribution. This assumption essentially serves as a dimensional reduction of the system, such that the dynamics of the system may be approximated using the parameters of the gamma distribution.

Under these assumptions, the authors estimate that

$$t_{\text{bind}} \sim \frac{\ln(N_T)}{k_{\text{on}}}, \tag{2.112}$$

in the limit $N_T \gg 1$, and

$$t_{\text{cycle}} = \frac{F}{V_u\,\kappa_s} \ln\left(\frac{1}{\varepsilon}\right), \tag{2.113}$$

where κ_s denotes the substrate spring constant and V_u was defined in Section 2.7.9. The constant ε is defined by assuming that the loading cycle ends when the substrate displacement reaches the fraction $(1-\varepsilon)$ of its asymptotic maximum value. Equivalently, if $x_s^{\max} = F/\kappa_s$, then the cycle is taken to end when $x_s(t_{\text{cycle}}) = (1-\varepsilon)x_s^{\max}$, with $0 < \varepsilon < 1$. Here, x_s denotes the extension of the substrate spring. No analytic method is proposed for determining ε. However, the authors suggest a choice of $\varepsilon = 0.01$ on the basis of simulation data.

Solving $t_{\text{bind}} = t_{\text{cycle}}$, one obtains

$$\kappa_s^* = \frac{F\,k_{\text{on}}}{V_u \ln(N_T)} \ln\left(\frac{1}{\varepsilon}\right). \tag{2.114}$$

Noticeably, the above expression for the dimensional optimal stiffness has a very different structure to the expression derived in this chapter (2.91). We will expand on this later.

Alonso-Matilla et al. [1]

In this study, the authors proposed a continuum, or equivalently, density approach for studying the system in question. The resultant equation is similar to (2.64), but not identical. Differences between this and our model arise from the fact that the derivation in Alonso-Matilla, et al. is not grounded in a mean-field approximation of the Chapman-Kolmogorov equation of the system.

The authors use dimensional analysis to argue that

$$t_{\text{bind}} \propto \frac{1}{k_{\text{on}} + k_{\text{off}}}, \tag{2.115}$$

and

$$t_{\text{cycle}} \propto \frac{k_{\text{on}}}{k_{\text{on}} + k_{\text{off}}} \frac{N_T F_b}{\kappa_s V_u} \left(1 + C_3 \frac{\kappa_s V_u}{k_{\text{off}} F}\right), \tag{2.116}$$

where C_3 is an unknown constant. Solving $t_{\text{cycle}} = t_{\text{bind}}$ for κ_s, one obtains

$$\kappa_s^* = C_2 \frac{N_T F_b k_{\text{on}}}{V_u} \frac{F}{F - C_3 N_T F_b \frac{k_{\text{on}}}{k_{\text{off}}}}, \tag{2.117}$$

where C_2 is another unknown constant. The authors estimate that $C_2 = 0.4$, $C_3 = 0.05$ by fitting the above expression to simulation data, with which it compares well.

Unlike [2], this expression has a similar structure to our derived expression and some of the same properties (assuming the speed imposition interpretation of our model). We can show that (2.91) reduces to the above form in certain parameter regimes. Assuming $k_{\text{on}}/k_{\text{off}} \ll 1$ and taking the limit $\kappa \to +\infty$ of $\kappa_s^* = \kappa \chi^*$, we obtain

$$\lim_{\kappa \to +\infty} \kappa_s^* = \frac{k_{\text{on}} N_T \xi F_b \, \mathrm{e}^{u^*} \Gamma(0, u^*)}{F - F_b N_T \frac{k_{\text{on}}}{k_{\text{off}}} \mathcal{H}(u^*)}. \tag{2.118}$$

Under the speed imposition interpretation, we have $\xi = F/V_u$. Thus,

$$\lim_{\kappa \to +\infty} \kappa_s^* = \mathrm{e}^{u^*} \Gamma(0, u^*) \frac{N_T F_b k_{\text{on}}}{V_u} \frac{F}{F - \mathcal{H}(u^*) F_b N_T \frac{k_{\text{on}}}{k_{\text{off}}}}, \tag{2.119}$$

which is of the same form as (2.117). However, $\mathrm{e}^{u^*} \Gamma(0, u^*) \approx 1.068$, $\mathcal{H}(u^*) \approx 0.298$, and thus are not equal to the estimates for C_2, C_3. Thus, the expression derived here for the optimal stiffness agrees qualitatively, but not quantitatively, with the heuristic expression of [1], for all parameters, in the limit $k_{\text{on}}/k_{\text{off}} \ll 1$ and $\kappa \to +\infty$.

Comparison of expressions

Here, we compare the qualitative behaviour of the three expressions (2.105, 2.114, 2.117), to that of the optimal stiffness obtained from simulations [3].

As can be seen in Table 2.2, (2.114) has the least agreement with the simulation data. In fact, agreement is restricted to the parameters $k_{\text{on}}, \kappa, V_u$. Expression (2.117) has the most agreement with the simulation data (see Table 2.3), exhibiting qualitative agreement across all parameters. Expression (2.105), derived in this chapter, agrees with all parameters except κ and k_{off} (see Table 2.4). We proceed by exploring these discrepancies.

Table 2.2: Response of κ_s^* to increasing a single stated parameter, all else equal.

Response of κ_s^* to increasing single stated parameter, all else equal			
Parameter	Simulations [3]	(2.114)	Agreement between simulations and (2.114)
k_{on}	Increasing	Increasing	✓
k_{off}	Decreasing	No effect	×
F_b	Increasing	No effect	×
N_T	Increasing	Decreasing	×
κ	No effect	No effect	✓
F	Decreasing	Increasing	×
V_u	Decreasing	Decreasing	✓

Table 2.3: Response of κ_s^* to increasing a single stated parameter, all else equal.

Response of κ_s^* to increasing single stated parameter, all else equal			
Parameter	Simulations [3]	(2.117)	Agreement between simulations and (2.117)
k_{on}	Increasing	Increasing	✓
k_{off}	Decreasing	Decreasing	✓
F_b	Increasing	Increasing	✓
N_T	Increasing	Increasing	✓
κ	No effect	No effect	✓
F	Decreasing	Decreasing	✓
V_u	Decreasing	Decreasing	✓

Table 2.4: Response of the optimal stiffness to increasing a single stated parameter.

Response of κ_s^* to increasing single stated parameter, all else equal			
Parameter	Simulations [3]	(2.105)	Agreement between simulations and (2.105)
k_{on}	Increasing	Increasing	✓
k_{off}	Decreasing	Decreasing, then Increasing	-
F_b	Increasing	Increasing	✓
N_T	Increasing	Increasing	✓
κ	No effect	Decreasing	×
F	Decreasing	Decreasing	✓
V_u	Decreasing	Decreasing	✓

Parameter	Symbol	Value
Motor parameters		
Motor stall force	F_{stall}	100 pN
Motor unloaded velocity	V_u	120 nm/s
Clutch parameters		
Number of clutches	N_T	50
Clutch bond rupture force	F_b	2 pN
Clutch on-rate	k_{on}	0.3 s^{-1}
Clutch unloaded off-rate	k_{off}	0.1 s^{-1}
Clutch spring constant	κ	0.8 pN/nm

Table 2.5: Motor-clutch model base parameter set from [3].

Discrepancies between simulation data and (2.105)

There are a couple of discrepancies between the simulation data results of [3] and our model. Specifically: (1) We predict that κ_s^* should decrease with κ, while the simulation data from [3] suggests that there is no effect from varying κ. (2) We predict that κ_s^* should decrease and then increase as a function of k_{off}, while the authors find that κ_s^* only decreases with k_{off}.

We investigate each discrepancy independently. As we shall see, the two discrepancies are resolved in the limit $k_{\text{off}}\xi/(N_T\kappa) \ll 1$.

Effect of clutch spring constant, κ

In our formulation, the optimal stiffness is sensitive to κ, whilst [3] report that for the range of values they tested, the simulation data did not indicate any sensitivity to κ. It might be possible to reconcile these two facts. In our model, the optimal stiffness decreases and rapidly converges as a function of the spring constant. In fact,

$$\lim_{\kappa\to+\infty} \kappa_s^* = \frac{k_{\text{off}}\,\xi\,\mathcal{J}\left(s\right)}{\frac{F}{F_b\,N_T} - \tau\left(d_1^*\left(s\right), s\right)}. \tag{2.120}$$

As such, the optimal stiffness rapidly loses sensitivity to the clutch spring constant in our model. The value of κ_s^* can be re-expressed as

$$\kappa_s^* = \frac{k_{\text{off}}\,\xi\,\mathcal{J}\left(s\right)}{\frac{F}{F_b\,N_T} - \tau\left(d_1^*\left(s\right), s\right) - \frac{k_{\text{off}}\,\xi}{N_T\,\kappa}\,\frac{1}{d_1^*(s)}}. \tag{2.121}$$

From the above expression, it is evident that κ_s^* approaches limit (2.120) asymptotically for $k_{\text{off}}\xi/(N_T\,\kappa) \ll 1$. For the base parameter values used in [3], shown in Table 2.5, we have $k_{\text{off}}\xi/(N_T\,\kappa) \approx 0.0021$ that is in the regime of κ_s^* insensitivity to κ. Furthermore, the ratio $k_{\text{off}}\xi/(N_T\kappa)$ remains small throughout the range of κ values considered by the authors. Thus, it is plausible that simulation data was only collected from a parameter

regime where the system is insensitive to κ. This would explain the discrepancy between (2.105) and [3].

Effect of unbinding rate, k_{off}

Our model predicts a non-monotone relationship between the optimal stiffness and k_{off}. Initially, κ_s^* is a decreasing function of k_{off} and then increasing. However, the function to which κ_s^* converges for $k_{\text{off}}\xi/(N_T\,\kappa) \ll 1$ (i.e. (2.120)) is a decreasing function of k_{off}.

To see that (2.120) is decreasing for large k_{off}, we observe that

$$\begin{aligned}\frac{\partial}{\partial k}\left[\tau\left(d_1^*(k),k\right)\right] &= \frac{\partial \tau}{\partial k}\left(d_1^*(k),k\right)\\ &= \frac{1}{\left[1+k\,\mathcal{G}(d_1(k))\right]^2} > 0,\end{aligned}$$

where $k = k_{\text{on}}/k_{\text{off}}$. It follows that

$$\frac{1}{F-\tau\left(d_1^*(1/x),1/x\right)},$$

is a decreasing function of $x = k_{\text{off}}/k_{\text{on}}$, when $F > \tau\left(d_1^*(1/x),1/x\right)$ (i.e. when the optimal stiffness exists). Furthermore, if we can show that $x\,\mathcal{J}(1/x)$ is decreasing for $x \gg 1$, we will have shown that (2.120) is a decreasing function of k_{off}, at least for $k_{\text{off}} \gg k_{\text{on}}$, where κ_s^* would normally be increasing, for finite $k_{\text{off}}\xi/(N_T\,\kappa)$ (as long as the optimal stiffness exists).

To show that $x\,\mathcal{J}(1/x)$ is decreasing for $x \gg 1$, it suffices to show that $\mathcal{J}(s)/s$ is increasing for $s \ll 1$. To show this, it is sufficient to check that $\mathrm{d}\left[\mathcal{J}(s)/s\right]/\mathrm{d}s$ is positive at $s = 0$. We compute that

$$\begin{aligned}&\frac{\mathrm{d}}{\mathrm{d}s}\left[\mathcal{J}(s)/s\right](0)\\ &= -\frac{1}{d_1^*(0)^2}\left(d_1^*(0)\,\mathrm{e}^{2/d_1^*(0)}\,\mathrm{Ei}\left(-\frac{1}{d_1^*(0)}\right)^2 - d_1^{*\prime}(0)\,\mathrm{e}^{1/d_1^*(0)}\,\mathrm{Ei}\left(-\frac{1}{d_1^*(0)}\right) - d_1^*(0)\,d_1^{*\prime}(0)\right)\\ &\approx 1.19\times 10^7 > 0.\end{aligned}$$

Therefore, $\mathcal{J}(s)/s$ is increasing for $0 < s \ll 1$. Thus, (2.120) is a decreasing function of k_{off}, for $k_{\text{off}} \gg k_{\text{on}}$. Numerically, we observe that it is also decreasing for intermediate values of k_{off}. This suggests that, for all values of k_{off} where the optimal stiffness exists, our exact expression for κ_s^* is a decreasing function of k_{off} in the limiting case $k_{\text{off}}\xi/(N_T\,\kappa) \to 0^+$.

2.9 Conclusion

In this chapter, our objective was to develop an analytical framework for the study of focal adhesion traction generation on deformable substrates.

Our starting point was the differential Chapman–Kolmogorov description of the motor–filament–focal-adhesion system, where the focal adhesion was constituted by N_T stochastic linkers. For the case $N_T = 1$, we obtained an exact steady-state description of the linker extension distribution and showed that it falls into one of three qualitative regimes. These three regimes correspond to ones that have been previously identified in the literature: motor dominated, motor–clutch balanced, or clutch dominated. In contrast to earlier descriptions based primarily on inspection of individual trajectories, the present analysis gives precise quantitative definitions of these regimes in terms of the steady-state statistics of the system, together with necessary and sufficient conditions for membership in each regime. We also showed that, even in the single-linker system, an optimal substrate stiffness can arise. This is an important result, since it demonstrates that the existence of an optimal stiffness does not rely on a transition between load-and-fail and frictional-slippage dynamics, but is already present in the fully stochastic single-linker problem.

For larger adhesions, we considered the mean-field limit of the system. In the rigid-substrate case, we derived the exact mean-field equation for the system and found that it is structurally identical to the $N_T = 1$ problem, allowing elements of the three-regime analysis to be extended to the case $N_T \gg 1$. In the deformable-substrate case, an exact mean-field closure was not available, so we adopted the homogeneous extension-rate approximation, commonly used in the literature, and used it to study the steady-state traction–stiffness curve of the system. Within this framework, we derived an exact expression for the optimal stiffness χ^*, identified the critical myosin force threshold required for its existence, and examined how both χ^* and the curvature $T''(\chi^*)$ depend on the system parameters.

We also compared the derived expression for the optimal stiffness, with previous formulas derived on the basis of heuristics. This comparison showed that earlier formulas can reproduce some to all of the qualitative behaviours known in the literature regarding the response of the optimal stiffness to system parameters. These behaviours have been previously established through the study of generated simulation data [3]. However, the derivation demonstrated in this chapter provides a systematic and exact derivation of the optimal stiffness. Moreover, apparent discrepancies with simulation results were shown to disappear in an appropriate asymptotic limit. Finally, we showed that different physical

interpretations of the force-balance law which relates v_e to T, although mathematically similar, can lead to distinct predictions for the behaviour of the optimal stiffness.

Overall, this chapter establishes the analytical foundation for how growth cones interact with a deformable substrate, which is fundamental for understanding how axon trajectories are determined in a substrate of heterogeneous stiffness. Furthermore, it clarifies the statistical origin of the three regimes of focal-adhesion traction dynamics, and places the phenomenon of optimal substrate stiffness on a firmer theoretical footing.

Chapter 3

The Axon - Beam - Clutch (ABC) model and simple motions

3.1 Overview

In this chapter, we derive a mechanical model for an axon growing on a two-dimensional substrate. Unlike other models of axon growth, this model considers the geometry and mechanical structure of the axon, and most importantly the fact that axons resist bending. The model we derive treats the axon as a mechanical beam, a two-dimensional curve on a plane.

In this model, the path of the axon is determined by the *growth cone* (GC) force, which is obtained as the integral of local traction across the periphery of the growth cone. We derive this force in Section 3.2. Local tractions at the GC periphery take the form derived in the previous chapter and depend on local substrate conditions. To be able to integrate the local tractions across the GC periphery we assume a simplified geometry for the growth cone. This allows us to derive an expression for the total growth cone force and furthermore derive useful approximations to it.

We proceed in Section 3.3, by proposing a possible morphoelastic framework for describing the axon. However, such a framework presents difficulties in numerical simulations. For this reason, we reduce this system to a remodelling beam model of the axon. This beam model will form the basis of the study of axon guidance in the rest of the thesis. The beam model relates mechanical parameters such as the bending stiffness of the axon with the GC traction force to produce axonal trajectories in specified substrates. Furthermore, it can be easily integrated numerically. Its derivation can be found in Section 3.3.3. Our algorithm for numerical integration of this system can be found in Section 3.3.4 .

The foundation of our theory of axon guidance is that environmental information can be encoded in the GC force and that axon guidance is determined by the integration of

the beam model under the application of this tip force. Having defined how the force and axon interact, we proceed by studying how a constant environmental signal - encoded as a constant GC force, determines the trajectories of growing axons. A quantity of particular experimental significance is the *timescale of turning* for the axon. That is, given some environmental signal, such as some guidance cue, how quickly will an axon turn? This quantity describes the strength of a guidance cue. In Section 3.4, we study an axon subjected to a constant force and study the timescale of turning.

Apart from providing a general framework for axon guidance, this thesis is also particularly focused on understanding axon durotaxis. Thus, we proceed in Section 3.5 with the study of the motion of axons in a substrate of linearly varying substrate stiffness. Our key, novel, result here is that axons are attracted and converge to traveling parallel to lines of optimal stiffness. Surprisingly, previous models of axon durotaxis did not predict this mode of guidance. By studying a toy model of the beam framework for the axon, we uncover that the key feature which allows for this mode of guidance is the finite spatial extent of the axon. As we shall see in later chapters, the finite length of the deformable axon plays an important role in instances of axon guidance in biological scenarios.

3.2 Growth Cone force

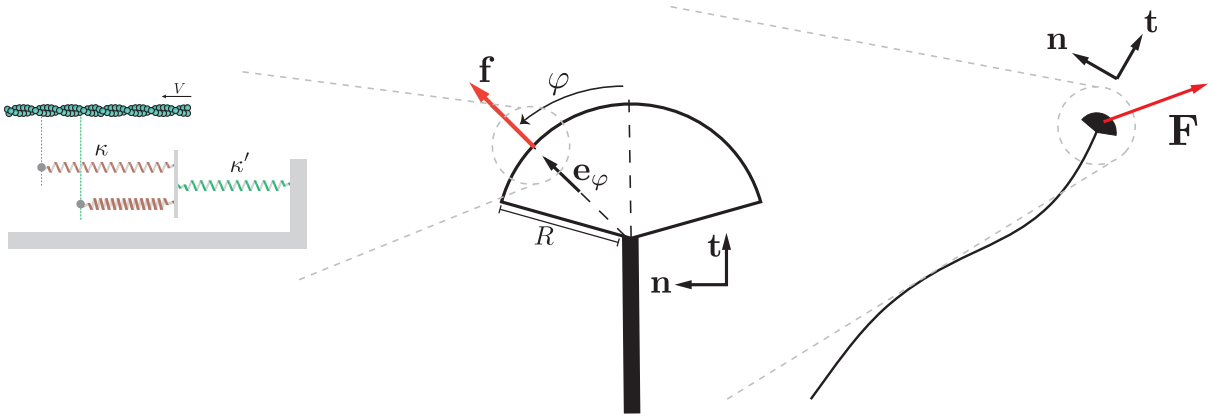


Figure 3.1: General structure of the model. From left to right: microscopic scale–an actin filament is modelled as a rigid rod moving with velocity V w.r.t. the substrate. The filament is connected to the substrate through an evolving collection of springs modelling adhesive cross-linkers and the deformable substrate; mesoscopic scale–the growth cone is viewed as a continuous distribution of centripetally-aligned actin filaments with individual traction forces summing up to generate global net force on the axonal shaft; macroscopic scale–the axon is modelled as a morphoelastic filament subject to frictional forces between the shaft and the substrate and growth-cone-induced locomotory force.

Macroscopically, the total force generated by the growth cone results from the centripetal flow of all actin filaments organised radially in the lamellipodium towards the growth cone base. We assume that the specific shape of the growth cone has little effect on the net force generated by the cone. Hence we model it as a circular sector with central angle $2\varphi_0$ and radius R; see Fig. 3.1. Here, we denote by $\boldsymbol{r}$ the position of the base of the growth cone in the laboratory frame equipped with the canonical basis $\{\boldsymbol{e}_x, \boldsymbol{e}_y\}$. We denote by $\boldsymbol{t}$ the unit vector along the axis of symmetry of the growth cone that is also the tangent to the axon attached to the growth cone, and $\boldsymbol{t}^\perp$ the normal unit vector to $\boldsymbol{t}$. We define $\boldsymbol{e}_\varphi = \cos\varphi\,\boldsymbol{t} + \sin\varphi\,\boldsymbol{t}^\perp$, with $\varphi \in [-\varphi_0, \varphi_0]$, the unit vector pointing outward in the direction φ.

The force density applied at the edge of the disk along the direction φ depends on the local environmental conditions at the lamellipodium edge at this location, i.e. at the point $\boldsymbol{r} + R\boldsymbol{e}_{\boldsymbol{\varphi}}$. Neglecting the mutual mechanical interactions between the filaments, the resultant force applied at the distal end of the axon shaft is given by

$$\boldsymbol{F}(\boldsymbol{r}, \boldsymbol{t}) = \int_{-\varphi_0}^{\varphi_0} \rho T\left(\boldsymbol{J}|_{\boldsymbol{r}+R\boldsymbol{e}_{\boldsymbol{\varphi}}}\right) \boldsymbol{e}_{\boldsymbol{\varphi}}\, R\,\mathrm{d}\varphi. \tag{3.1}$$

with ρ the density of adhesion sites per unit arclength along the growth cone edge (which we assume to be constant), $\boldsymbol{J} = (\chi, K, \kappa, ...)$ is the vector encoding the local parameters of the environment at the leading edge; and where $T(\boldsymbol{J})$ is the individual filament force derived in the previous chapter, evaluated at the edge of the growth cone where adhesion sites are located. Since this thesis is particularly focused on studying axon durotaxis we assume that only the stiffness field χ varies with space and thus denote $T(\boldsymbol{J}) = T(\chi)$. Note that, since all the filaments point towards the base of the growth cone, there is no induced torque about that point, thus changes in direction may only be induced through an asymmetric distribution of forces across the growth cone. The expression (3.1) is difficult to work with as it implies evaluating T for every φ. To make progress, we assume that local environmental conditions vary slowly in the vicinity of the growth cone–equivalently that the growth cone is small–so we expand (3.1) to $O(R^2)$ to obtain

$$\boldsymbol{F}(\boldsymbol{r}, \boldsymbol{t}) = 2R\rho\sin\varphi_0 T(\chi)\,\boldsymbol{t} + R^2\rho\varphi_0 T'(\chi)\,\mathbf{P}(\varphi_0)\,\nabla\chi + O(R^3), \tag{3.2}$$

where χ and $\nabla\chi$ are evaluated at $\boldsymbol{r}$; and where the tensor $\mathbf{P}$ reflects the geometry of the growth cone only and is given by

$$\mathbf{P}(\varphi_0) := \int_{-\varphi_0}^{\varphi_0} \boldsymbol{e}_{\boldsymbol{\varphi}} \otimes \boldsymbol{e}_{\boldsymbol{\varphi}} \frac{\mathrm{d}\varphi}{\varphi_0} = \mathbf{1} + \frac{\sin 2\varphi_0}{2\varphi_0}\left(\boldsymbol{t}\otimes\boldsymbol{t} - \boldsymbol{t}^\perp\otimes\boldsymbol{t}^\perp\right), \tag{3.3}$$

Here, $\mathbf{1}$ is the identity tensor, and '$\otimes$' denotes the tensor product (i.e. given vectors $\boldsymbol{u}$ and $\boldsymbol{v}$, the Cartesian components of $\boldsymbol{u} \otimes \boldsymbol{v}$ are $(\boldsymbol{u} \otimes \boldsymbol{v})_{ij} = u_i v_j$). From this expansion, the role of substrate stiffness and its gradient can be interpreted physically.

The first term on the r.h.s. of (3.2) is a stiffness-dependent force component in the current direction of the axon, regulating the longitudinal growth velocity. The second term captures the durotactic effect induced by a gradient in substrate stiffness $\nabla\chi$, which will cause the axon to steer away or towards stiffness gradients. In the special cases $\varphi_0 = \pi/2$ (half-disk) or $\varphi_0 = \pi$ (full disk), the durotactic component is aligned with $\nabla\chi$ as $\mathbf{P}(\pi) = \mathbf{P}(\pi/2) = \mathbf{1}$. More generally, the durotactic force component is not aligned with $\nabla\chi$ as $\nabla\chi \times \mathbf{P}\nabla\chi \neq \mathbf{0}$. However, since $\mathbf{P}$ is symmetric positive, we have that $\nabla\chi \cdot (\mathbf{P}\nabla\chi) \geq 0$, thus, if $T'(\chi) > 0$, the durotactic force makes an acute angle with the stiffness gradient. Consequently, the orientation of the durotactic force, that is, whether the axon progresses towards soft or stiff substrate, is only governed by the sign of $T'(\chi)$. We have *positive durotaxis* if $T'(\chi) > 0$ and *negative durotaxis* if $T'(\chi) < 0$. Note that, as expected, the normal component of the durotactic force vanishes when the axon is aligned with the gradient.

From (3.2), we can directly obtain the factors determining the strength of the durotactic force. We define the dimensionless *durotactic sensitivity* as

$$\vartheta(\chi) = \frac{\varphi_0}{\sin\varphi_0}\frac{T'(\chi)}{T(\chi)}, \tag{3.4}$$

measuring the relative effect of the deflective force to the longitudinal traction. From the previous chapter, it follows that ϑ vanishes at the optimal stiffness χ^*, the stationary point of T. For $\chi < \chi^*$, we have $\vartheta > 0$ and, conversely, $\vartheta < 0$ for $\chi > \chi^*$.

From the analysis of the growth cone force, we conclude that: *Axons growing on substrates with stiffness smaller than the optimal stiffness χ^* can only exhibit positive durotaxis; conversely, axons on substrates stiffer than the optimal stiffness can only exhibit negative durotaxis.* In particular, if condition (2.92) is violated, axons can only undergo positive durotaxis.

3.3 The Axon Beam model

In the previous section, we have derived the overall net force applied to the tip of the growing axon due to the interaction of the growth cone with the substrate. We can now use this force and model the axon as a morphoelastic rod, i.e. a growing elastic rod [see Chap. 5 and 6 of 27] subject to the end loading due to the growth cone and to the frictional force exerted by the substrate, thus generalising the approach of [56] to curved trajectories.

3.3.1 Morphoelastic rod model

Initially, a morphoelastic rod is defined by a smooth curve $\boldsymbol{R}_0(S_0) = (X_0(S_0), Y_0(S_0)) \in \mathbb{R}^2$ with arclength $S_0 \in [0, L_0]$. We choose $S_0 = 0$ to be at the base (the soma) and $S_0 = L_0$ at the axon tip (growth cone). As the axon grows and deforms elastically under loads, the rod adopts a new *current* configuration parameterised by the material coordinate S_0 and time t by $\boldsymbol{r}(S_0, t) = (x(S_0, t), y(S_0, t))$. We define $s(S_0, t)$ the arclength in the current configuration, i.e. the contour length between the base and the material point that was at position S_0 and time $t = 0$. The Frenet-Serret frame of the current curve is composed of the unit tangent vector $\boldsymbol{\tau} = \partial \boldsymbol{r}/\partial s$ (pointing towards the growth cone) and the unit normal vector $\boldsymbol{\tau}^\perp$, perpendicular to $\boldsymbol{\tau}$. Both can be encoded by a single angle θ between the x-axis and the tangent vector so that

$$\boldsymbol{\tau} = (\cos\theta, \sin\theta), \quad \boldsymbol{\tau}^\perp = (-\sin\theta, \cos\theta). \tag{3.5}$$

At the tip, the orientation of the axon agrees with that of the growth cone so that $\boldsymbol{\tau}(L_0) = \boldsymbol{t}$ and $\boldsymbol{\tau}^\perp(L_0) = \boldsymbol{t}^\perp$. Then the Frenet-Serret equations can be written as

$$\frac{\partial x}{\partial S_0} = \lambda \cos\theta, \quad \frac{\partial y}{\partial S_0} = \lambda \sin\theta, \quad \frac{\partial \theta}{\partial S_0} = \lambda k, \quad \lambda = \frac{\partial s}{\partial S_0}, \tag{3.6}$$

where λ is the stretch and k the signed curvature. The pair of scalar fields (λ, k) then fully describes the geometry of the rod (stretching and bending).

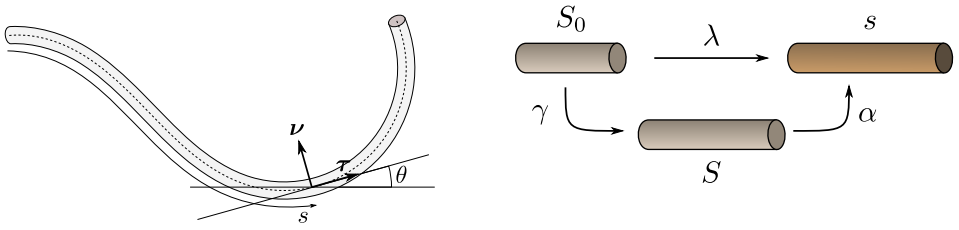


Figure 3.2: A morphoelastic rod model. Left: At a point s in the current configuration, we defined the tangent vector $\boldsymbol{\tau}$ and normal vector $\boldsymbol{\tau}^\perp$ through the angle θ. Right: In the growth model we assume that an infinitesimal element of the rod located initially at S_0 is subject to both a growth deformation γ and an elastic deformation α, such that the total stretch is $\lambda = \alpha\gamma$.

Neglecting inertial effects and body torques, the balance of linear and angular momenta is expressed in terms of the internal resultant force $\boldsymbol{n} = (n_x, n_y)$ and moment m applied by a cross-section S_0^+ onto a cross-section S_0^- as [see chapter 5 of 27, for details]

$$n_x' + \lambda b_x = 0, \tag{3.7a}$$

$$n_y' + \lambda b_y = 0, \tag{3.7b}$$

$$m' + \lambda(n_y \cos\theta - n_x \sin\theta) = 0, \tag{3.7c}$$

where the apostrophe denotes differentiation w.r.t. S_0; and $\boldsymbol{b} = (b_x, b_y)$ is a density of body force per unit current length, that is used to model the adhesion between the growing shaft and the substrate as a linear frictional force with coefficient ζ [56, 53, 52]

$$\boldsymbol{b} = -\zeta \dot{\boldsymbol{r}}. \tag{3.8}$$

Here the overdot denotes the material derivative, linked to the Eulerian derivative through the formula $\dot{\boldsymbol{r}} - \dot{s}\boldsymbol{\tau} = \partial \boldsymbol{r}(s,t)/\partial t$.

To close the system, we must formulate constitutive relationships that relate stresses to deformations. We assume that the rod is extensible but unshearable. In a growing rod, only part of the deformation results in stresses, reflecting the remodelling and growth of the material and the resulting change in reference configuration. To model this effect, we introduce an intermediate reference configuration $\boldsymbol{R}(S_0, t)$ with arclength $S(S_0, t)$, representing the equilibrium configuration of the rod achieved upon removal of the loads. We decompose the total deformation multiplicatively, in terms of the elastic, and growth stretches, respectively $\alpha := \partial s/\partial S$ and $\gamma := \partial S/\partial S_0$:

$$\lambda = \alpha\gamma. \tag{3.9}$$

Constitutively, we assume that stresses and moments are generated only by the elastic part of the deformation, i.e. by the extensional and bending strains measured between the intermediate and current configurations, so that growth alone is stress-free. Therefore, we posit a quadratic elastic energy density (energy per unit intermediate length) for a morphoelastic rod with intrinsic curvature $\hat{k}$, of the form

$$W\left(\alpha, \tilde{k}\right) = \frac{1}{2}\mathcal{K}\left(\alpha - 1\right)^2 + \frac{1}{2}\mathcal{B}(\tilde{k} - \hat{k})^2, \tag{3.10}$$

where $\tilde{k} = \alpha k$ is the angular strain between the virtual and current configurations, $\mathcal{K}$ and $\mathcal{B}$ are the extensional and bending stiffnesses, respectively. The corresponding constitutive relations are

$$n = \frac{\partial W}{\partial \alpha} = \mathcal{K}\left(\alpha - 1\right), \tag{3.11a}$$

$$m = \frac{\partial W}{\partial \tilde{k}} = \mathcal{B}(\tilde{k} - \hat{k}), \tag{3.11b}$$

with $n := \boldsymbol{n} \cdot \boldsymbol{\tau} = n_x \cos\theta + n_y \sin\theta$, the longitudinal tension.

There are two remaining important components to model, the growth of the axonal shaft specified by γ, and the remodelling of the curvature $\hat{k}$. Physically, growth is due to mechanical stresses along the shaft that cause the axon to creep irreversibly above some

critical tension [23, 71, 28], while new cytoplasmic material is incorporated simultaneously into the shaft [55, 54]. During this process, cross-sectional area remains mostly constant, indicating that the cell maintains a homoeostatic density [16, 42]; thus we assume that $\mathcal{K}$ and B are constant in time and uniform along the rod. To model diffuse growth at each point, we use the exponential growth law [52]

$$\frac{1}{\gamma}\frac{\partial \gamma}{\partial t} = \frac{(n-n_0)_+}{\eta}, \tag{3.12}$$

where $(n-n_0)_+ = n - n_0$ for $n \geq n_0$ (0 otherwise); $n_0 \geq 0$ is the *critical tension* below which no growth occurs ; and η plays the role of a morphoelastic viscosity (in unit force times time). Henceforth, for simplicity, we neglect the threshold effect and we set $n_0 = 0$.

We also assume a relaxation process for the bending moment due to internal remodelling by using the curvature evolution law

$$\dot{\hat{k}} = \frac{k - \hat{k}}{\tau_k}, \tag{3.13}$$

with a characteristic timescale τ_k of the same order as η/n_0.

The connection to the mesoscopic model is obtained through the boundary conditions. At the base $S_0 = 0$, the rod is clamped

$$\boldsymbol{r}(0) = \boldsymbol{r}_0, \quad \theta(0) = \theta_0, \tag{3.14}$$

where $\boldsymbol{r}_0$ and θ_0 are the base position and angle. At its tip, the rod is subject to the traction exerted by the growth cone:

$$m(L_0) = 0, \quad \boldsymbol{n}(L_0) = \boldsymbol{F}(\boldsymbol{r}(L_0), \theta(L_0)), \tag{3.15}$$

where $\boldsymbol{F}$ depends on the growth cone position and orientation through the mesoscopic law (3.2).

There are three important parameters in the problem, the dimensionless parameter $\mathcal{Z} := \mathcal{B}\zeta/\mathcal{K}\eta$, which measures the relative effect of adhesion w.r.t. viscosity, and the two characteristic lengths

$$\Lambda = \sqrt{\eta/\zeta}, \quad \mathcal{L} = \sqrt{\mathcal{B}/F}. \tag{3.16}$$

The *growth length* Λ measures the distance over which axonal tension and energy dissipate into the substrate due to friction [56, 53], and $\mathcal{L}$ is the *bending length* that measures the typical curvature radius of a beam due to the typical transverse traction F from the growth cone.

At any time, given $\gamma(S_0, t)$ and $\hat{k}(S_0, t)$, the boundary-value problem formed by (3.6, 3.7, 3.8, 3.9, 3.11, 3.12) with the boundary conditions (3.14, 3.15), can be solved numerically to obtain the axon's trajectory. However, the frictional interaction between the axon and its substrate dissipates traction forces over a region close to the growth cone which becomes short, relatively to the entire axon, as time progresses. Thus, only a short and essentially constant distal section of the axon is dynamic, rapidly causing important computational difficulties due to our Lagrangian specification of the problem. Rather than solving for the system directly, we can take advantage of this effect and focus our attention on the growth process localised in a distal region, and freeze the most proximal part of the axon to account for permanent adhesion between the axon and the substrate (and discard that frozen region from the problem). This process is described in the next section.

3.3.2 Tip growth approximation

The existence of a characteristic lengthscale Λ can be used to further simplify the problem. For axons, we have $\Lambda \ll \mathcal{L}$ as the force applied by the growth cone only creates small deflections (hence a large radius of curvature $\mathcal{L}$). This scaling has two important consequences.

First, the effect of the force applied at the tip of the axon by the growth cone on the rest of the axon vanishes quickly away from the tip. It implies that only a short zone at the tip of length L that is of order Λ is subject to a force. In terms of modelling, we exploit this result computationally by constraining the dynamic region of the axon to a moving active portion of fixed arclength L while segments of the axon found at a greater arclength are fixed and do not need to be updated. In morphoelasticity, this process is referred as *tip growth* [27] and is found in plant shoots or roots, which undergo elongation over an effectively finite apical (or sub-apical) region [68].

Second, since the active zone is small w.r.t. the typical radius of curvature, only small deflections away from the natural state take place in response to the growth cone. The distal end of the beam–the axon's tip–is subject to the locomotory force $\boldsymbol{F}$ produced by the growth cone. The basal end makes the junction between the dynamic region and the frozen region, and is assumed to be clamped from the point of view of the elastic quasi-equilibrium. Therefore, we can approximate the shape of the active zone by

$$\boldsymbol{r}(\sigma, t) = \hat{\boldsymbol{r}}\,(t) + \mathsf{x}(\sigma, t)\,\hat{\boldsymbol{\tau}}(t) + \mathsf{y}(\sigma, t)\,\hat{\boldsymbol{\nu}}(t), \quad \sigma \in [0, L], \tag{3.17}$$

where $\hat{\boldsymbol{r}} = (\hat{x}, \hat{y})$ is the position of the clamp; $\hat{\boldsymbol{\tau}} = \cos\hat{\theta}\,\boldsymbol{e}_x + \sin\hat{\theta}\,\boldsymbol{e}_y$ and $\hat{\boldsymbol{\nu}} = -\sin\hat{\theta}\,\boldsymbol{e}_x + \cos\hat{\theta}\,\boldsymbol{e}_y$ are the tangent and normal vectors to the curve at the base, with $\hat{\theta}$ the angle of the clamp to the horizontal $\boldsymbol{e}_x$ (henceforth, we denote quantities evaluated at the base of

the beam with a circumflex); x and y, typeset in the sans-serif font, denote the coordinates of the rod in the frame of the clamp. For small deflection we have $\mathsf{x}(\sigma, t) \approx \sigma$, and the rod equations of the previous section simplify to the beam equations [27, p. 147].

There is however an important subtlety appearing in the problem. Since the active zone is moving in time, we have to properly advect the position of the beam element as the axon grows. We keep track of the position and direction of the clamp through the position vector $\hat{\boldsymbol{r}}(t)$ and model the evolution of $\boldsymbol{r}(\sigma, t)$ as the limit in small time step Δt of the following process (Fig. 3.3): At t the beam is clamped at $\hat{\boldsymbol{r}}(t)$ with direction $\hat{\boldsymbol{\tau}}(t)$ and is subject to a distal load $\boldsymbol{F}(t)$ and viscous friction along its length. First, $\mathsf{y}(\sigma, t)$ evolves according to the linear beam equations for a time interval of length $\Delta t \ll 1$. Then, a linear segment of length $c(t)\,\Delta t$ is added to the end of the beam in the direction of the tip. We call $c(t)$ the growth rate of the axon. Finally, the length constraint is enforced by setting the new profile of the beam, $\boldsymbol{r}(\sigma, t + \Delta t)$ to be the segment of length L from the tip of the grown, deflected beam profile. In the next section we derive the continuous-time evolution equations for this process in the limit $\Delta t \to 0$.

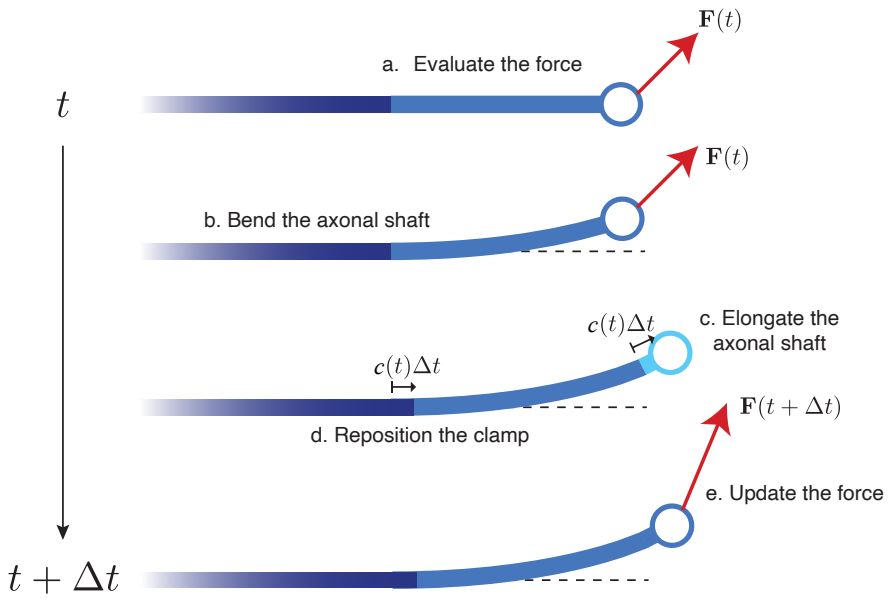


Figure 3.3: Schematic of the incremental axonal growth process. We assume that only a segment of length L and clamp angle $\hat{\theta}$ is subject to bending and remodelling. When a force is applied, this clamped beam element bends. Once deformed it grows by an amount $c(t)\Delta t$ and the new clamp is moved and rotated to the new angle $\hat{\theta}(t)$.

3.3.3 Derivation of the beam model

Here we derive the evolution laws for the dynamic section modelled by an inextensible growing beam (Section 3.3.2). The dynamic distal section of the axon is represented by

a spatial curve $\boldsymbol{r}(\sigma, t)$ given as

$$\boldsymbol{r}(\sigma, t) = \hat{\boldsymbol{r}}\,(t) + \mathsf{x}(\sigma, t)\,\hat{\boldsymbol{\tau}}(t) + \mathsf{y}(\sigma, t)\,\hat{\boldsymbol{\nu}}(t) \tag{3.18}$$

Here, $\sigma \in [0, L]$ measures the arclength from the base of the dynamic section; and where $\hat{\boldsymbol{r}}$, $\hat{\boldsymbol{\tau}}$ and $\hat{\boldsymbol{\nu}}$ indicate respectively the position, and the tangent and normal vectors to the curve at $\sigma = 0$. The coordinates x and y indicate the position of the curve in the local frame $\{\hat{\boldsymbol{\tau}}, \hat{\boldsymbol{\nu}}\}$. These definitions imply the boundary conditions

$$\mathsf{x}\,(0, t) = \mathsf{y}\,(0, t) = 0, \quad \frac{\partial \mathsf{x}}{\partial \sigma}\,(0, t) = 1, \quad \frac{\partial \mathsf{y}}{\partial \sigma}\,(0, t) = 0. \tag{3.19}$$

Further, x, y can be obtained by integrating the system

$$\frac{\partial \mathsf{x}}{\partial \sigma} = \cos\theta, \quad \frac{\partial \mathsf{y}}{\partial \sigma} = \sin\theta, \tag{3.20}$$

where $\theta\,(\sigma, t)$ indicates the polar angle of the tangent $\partial \boldsymbol{r}/\partial \sigma$ at arclength σ and time t, in the local frame $\{\hat{\boldsymbol{\tau}}, \hat{\boldsymbol{\nu}}\}$. That is,

$$\frac{\partial \boldsymbol{r}}{\partial \sigma} = \cos\theta\,\hat{\boldsymbol{\tau}} + \sin\theta\,\hat{\boldsymbol{\nu}}. \tag{3.21}$$

During a small time increment ΔT we update the shape of the axon by first evolving the curve according to the over-damped beam equations (3.23), assuming that the axon is clamped at $\hat{\boldsymbol{r}}\,(t)$ with angle $\hat{\theta}\,(t)$, and subject to the force $\boldsymbol{F}\,(t)$ applied at $\sigma = L$ with zero torque. We introduce the auxiliary function

$$\tilde{\boldsymbol{r}}\,(\sigma, T, t) = \hat{\boldsymbol{r}}\,(t) + \tilde{\mathsf{x}}\,(\sigma, T, t)\;\hat{\boldsymbol{\tau}} + \tilde{\mathsf{y}}\,(\sigma, T, t)\,\hat{\boldsymbol{\nu}}. \tag{3.22}$$

Here, $\tilde{\boldsymbol{r}}\,(\sigma, T, t)$ describes the evolution of the axon profile, in time T, with initial condition $\boldsymbol{r}\,(\sigma, t)$ and clamp angle $\hat{\theta}\,(t)$, subjected to constant force $\boldsymbol{F}\,(t)$. The functions $\tilde{\mathsf{x}}\,(\sigma, T, t)$ and $\tilde{\mathsf{y}}\,(\sigma, T, t)$ satisfy the over-damped beam equations in the frame $\{\hat{\boldsymbol{\tau}}, \hat{\boldsymbol{\nu}}\}$, with spatial variable σ and time variable T.

$$\mathcal{B}\frac{\partial^2 \tilde{\theta}}{\partial \sigma^2} + \tilde{\mathsf{n}}_y \cos\tilde{\theta} - \tilde{\mathsf{n}}_x \sin\tilde{\theta} = 0, \tag{3.23a}$$

$$\frac{\partial \tilde{\mathsf{n}}_x}{\partial \sigma} = \zeta\frac{\partial \tilde{\mathsf{x}}}{\partial T}, \quad \frac{\partial \tilde{\mathsf{n}}_y}{\partial \sigma} = \zeta\frac{\partial \tilde{\mathsf{y}}}{\partial T}, \tag{3.23b}$$

$$\frac{\partial \tilde{\mathsf{x}}}{\partial \sigma} = \cos\tilde{\theta}, \quad \frac{\partial \tilde{\mathsf{y}}}{\partial \sigma} = \sin\tilde{\theta}, \tag{3.23c}$$

where $\tilde{\mathsf{n}}_x$ and $\tilde{\mathsf{n}}_y$ are the components of the internal resultant force $\tilde{\mathbf{n}} = \tilde{\mathsf{n}}_x\hat{\boldsymbol{\tau}} + \tilde{\mathsf{n}}_y\hat{\boldsymbol{\nu}}$ at time T. We enforce the boundary and initial conditions

$$\tilde{\mathsf{n}}_x\left(L,T,t\right)=\boldsymbol{F}\left(t\right)\cdot\hat{\boldsymbol{\tau}}(t),\quad \tilde{\mathsf{n}}_y\left(L,T,t\right)=\boldsymbol{F}\left(t\right)\cdot\hat{\boldsymbol{\nu}}(t), \tag{3.24a}$$

$$\tilde{\theta}\left(0,T,t\right)=0,\quad \frac{\partial\tilde{\theta}}{\partial\sigma}\left(L,T,t\right)=0, \tag{3.24b}$$

$$\tilde{\mathsf{x}}\left(0,T,t\right)=0,\quad \tilde{\mathsf{y}}\left(0,T,t\right)=0, \tag{3.24c}$$

$$\tilde{\mathsf{x}}\left(\sigma,0,t\right)=\mathsf{x}\left(\sigma,t\right),\quad \tilde{\mathsf{y}}\left(\sigma,0,t\right)=\mathsf{y}\left(\sigma,t\right). \tag{3.24d}$$

From here, we can update the axon's shape according to (3.23) integrated over a small time increment ΔT. That is, we define an intermediate curve

$$\tilde{\boldsymbol{r}}_{\text{inter}}\left(\sigma\right)=\tilde{\boldsymbol{r}}\left(\sigma,\Delta T,t\right). \tag{3.25}$$

The updated axon after growth is then obtained by advancing the clamp position along this intermediate profile by a small length $\Delta\sigma=c\left(t\right)\Delta T$,

$$\boldsymbol{r}\left(\sigma,t+\Delta T\right)=\tilde{\boldsymbol{r}}_{\text{inter}}\left(\sigma+\Delta\sigma\right), \tag{3.26}$$

for $\sigma\in[0,L-\Delta\sigma]$, and we extrapolate the profile linearly for $\sigma\in(L-\Delta\sigma,L]$. Expanding the r.h.s. to second order in ΔT, rearranging the terms and taking the limit $\Delta T\to 0$, we obtain

$$\begin{aligned}\frac{\partial\boldsymbol{r}}{\partial t}\left(\sigma,t\right)=&\left(c(t)\frac{\partial\tilde{\mathsf{x}}}{\partial\sigma}\left(\sigma,0,t\right)+\frac{\partial\tilde{\mathsf{x}}}{\partial T}\left(\sigma,0,t\right)\right)\hat{\boldsymbol{\tau}}\\&+\left(c(t)\frac{\partial\tilde{\mathsf{y}}}{\partial\sigma}\left(\sigma,0,t\right)+\frac{\partial\tilde{\mathsf{y}}}{\partial T}\left(\sigma,0,t\right)\right)\hat{\boldsymbol{\nu}}.\end{aligned} \tag{3.27}$$

Differentiating (3.18) we derive

$$\frac{\partial\boldsymbol{r}}{\partial t}\left(\sigma,t\right)=\frac{\mathrm{d}\hat{\boldsymbol{r}}}{\mathrm{d}t}+\left(\frac{\partial\mathsf{x}}{\partial t}-\mathsf{y}\frac{\mathrm{d}\hat{\theta}}{\mathrm{d}t}\right)\hat{\boldsymbol{\tau}}+\left(\frac{\partial\mathsf{y}}{\partial t}+\mathsf{x}\frac{\partial\hat{\theta}}{\partial t}\right)\hat{\boldsymbol{\nu}}, \tag{3.28}$$

where $\hat{\theta}$ is the angle between $\hat{\boldsymbol{\tau}}$ and the horizontal direction. Equating the r.h.s. of (3.27, 3.28) we obtain

$$\frac{\partial\mathsf{x}}{\partial t}-\mathsf{y}\frac{\mathrm{d}\hat{\theta}}{\mathrm{d}t}+\frac{\partial\hat{\boldsymbol{r}}}{\partial t}\cdot\hat{\boldsymbol{\tau}}=c(t)\frac{\partial\tilde{\mathsf{x}}}{\partial\sigma}\left(\sigma,0,t\right)+\frac{\partial\tilde{\mathsf{x}}}{\partial T}\left(\sigma,0,t\right), \tag{3.29a}$$

$$\frac{\partial\mathsf{y}}{\partial t}+\mathsf{x}\frac{\mathrm{d}\hat{\theta}}{\mathrm{d}t}+\frac{\partial\hat{\boldsymbol{r}}}{\partial t}\cdot\hat{\boldsymbol{\nu}}=c(t)\frac{\partial\tilde{\mathsf{y}}}{\partial\sigma}\left(\sigma,0,t\right)+\frac{\partial\tilde{\mathsf{y}}}{\partial T}\left(\sigma,0,t\right). \tag{3.29b}$$

To obtain the evolution equation for $\hat{\boldsymbol{r}}$ we set $\sigma=0$ in the above equations. We note that, due to (3.19), we have $\partial\mathsf{x}/\partial t\left(0,t\right)=\partial\mathsf{y}/\partial t\left(0,t\right)=0$ and so

$$\frac{\partial\hat{\boldsymbol{r}}}{\partial t}=c(t)\hat{\boldsymbol{\tau}}. \tag{3.30}$$

We derive the evolution equation for $\hat{\theta}$ by imposing (to first order in ΔT) that

$$\frac{\partial \boldsymbol{r}}{\partial \sigma}(0, t+\Delta T)=\frac{\partial \boldsymbol{r}}{\partial \sigma}(c(t) \Delta T, t) . \tag{3.31}$$

Expanding the l.h.s. in t and the r.h.s. in σ to second order in ΔT, rearranging and taking the limit $\Delta T \rightarrow 0$ gives

$$\frac{\mathrm{d}}{\mathrm{d} t}\left(\frac{\partial \boldsymbol{r}}{\partial \sigma}(0, t)\right)=c(t) \frac{\partial^2 \boldsymbol{r}}{\partial \sigma^2}(0, t) , \tag{3.32}$$

which simplifies to

$$\frac{\partial^2 \mathsf{x}}{\partial \sigma^2}(0, t)=0, \tag{3.33a}$$

$$\frac{\mathrm{d} \hat{\theta}}{\mathrm{d} t}=c(t) \frac{\partial^2 \mathsf{y}}{\partial \sigma^2}(0, t) . \tag{3.33b}$$

Therefore the governing equations become

$$\frac{\partial \mathsf{x}}{\partial t}-\mathsf{y} c(t) \frac{\partial^2 \mathsf{y}}{\partial \sigma^2}(0, t)+c(t)=c(t) \frac{\partial \tilde{\mathsf{x}}}{\partial \sigma}(\sigma, 0, t)+\frac{\partial \tilde{\mathsf{x}}}{\partial T}(\sigma, 0, t) , \tag{3.34a}$$

$$\frac{\partial \mathsf{y}}{\partial t}+\mathsf{x} c(t) \frac{\partial^2 \mathsf{y}}{\partial \sigma^2}(0, t)=c(t) \frac{\partial \tilde{\mathsf{y}}}{\partial \sigma}(\sigma, 0, t)+\frac{\partial \tilde{\mathsf{y}}}{\partial T}(\sigma, 0, t) . \tag{3.34b}$$

Next, we assume that the normal component of the force $\boldsymbol{F}$ w.r.t. the clamp axis is small. That is,

$$\boldsymbol{F} \cdot \hat{\boldsymbol{\nu}}=\epsilon N_y, \tag{3.35}$$

for $\epsilon \ll 1$ and where $\boldsymbol{F} \cdot \hat{\boldsymbol{\tau}}$ and N_y are $\mathcal{O}(1)$. Consequently, the axon is subject to small deflections from the axis spanned by $\hat{\boldsymbol{\tau}}$. i.e.

$$\mathsf{x}=\sigma+O\left(\epsilon^2\right), \quad \mathsf{y}=\epsilon Y(\sigma, t)+O\left(\epsilon^2\right), \quad \theta=\epsilon \Theta(\sigma, t)+O\left(\epsilon^2\right), \tag{3.36}$$

for $\epsilon \ll 1$. Plugging (3.36) into (3.34) we obtain

$$\frac{\partial \tilde{\mathsf{x}}}{\partial T}(\sigma, 0, t)=O\left(\epsilon^2\right), \tag{3.37a}$$

$$\frac{\partial \tilde{\mathsf{y}}}{\partial T}(\sigma, 0, t)-\epsilon\left(\dot{Y}+\sigma c(t) \frac{\partial^2 Y}{\partial \sigma^2}(0, t)-c(t) \frac{\partial Y}{\partial \sigma}\right)=O\left(\epsilon^2\right) . \tag{3.37b}$$

For the next step, it is important to note that since we have $\partial \mathsf{y} / \partial \sigma=\sin \theta$ and $\tilde{y}(\sigma, 0, t)=y(\sigma, t)$, it follows that $\partial \tilde{\mathsf{y}} / \partial \sigma(\sigma, 0, t)=\partial \mathsf{y} / \partial \sigma$ and therefore

$$\tilde{\theta}(\sigma, 0, t)=\theta(\sigma, t) . \tag{3.38}$$

We can now obtain an expression for $\partial \tilde{\mathsf{y}} / \partial T(\sigma, 0, t)$ to first order in ϵ. Positing

$$\tilde{\theta}(\sigma, 0, t)=\theta(\sigma, t)=\epsilon \Theta(\sigma, t)+O\left(\epsilon^2\right) . \tag{3.39}$$

with Θ a function of order unit, using (3.23a, 3.23c), and differentiating w.r.t. σ, we obtain

$$\epsilon\mathcal{B}\frac{\partial^3\Theta}{\partial\sigma^3}+\frac{\partial\tilde{\mathsf{n}}_y}{\partial\sigma}-\tilde{\mathsf{n}}_x\frac{\partial^2\tilde{\mathsf{y}}}{\partial\sigma^2}(\sigma,0;t)=O\left(\epsilon^2\right), \tag{3.40}$$

which is equivalent to the beam equation

$$\epsilon\mathcal{B}\frac{\partial^4 Y}{\partial\sigma^4}+\zeta\frac{\partial\tilde{\mathsf{y}}}{\partial T}-\epsilon\tilde{\mathsf{n}}_x\frac{\partial^2 Y}{\partial\sigma^2}=O\left(\epsilon^2\right). \tag{3.41}$$

Thus,

$$\frac{\partial\tilde{\mathsf{y}}}{\partial T}(\sigma,0;t)=\frac{\epsilon}{\zeta}\left(\tilde{\mathsf{n}}_x\frac{\partial^2 Y}{\partial\sigma^2}-\mathcal{B}\frac{\partial^4 Y}{\partial\sigma^4}\right)+O(\epsilon^2). \tag{3.42}$$

To leading order we thus have

$$\frac{\partial Y}{\partial t}-c(t)\frac{\partial Y}{\partial\sigma}=\frac{1}{\zeta}\left(\boldsymbol{F}(t)\cdot\hat{\boldsymbol{\tau}}\frac{\partial^2 Y}{\partial\sigma^2}-\mathcal{B}\frac{\partial^4 Y}{\partial\sigma^4}\right)-\sigma c(t)\frac{\partial^2 Y}{\partial\sigma^2}(0,t). \tag{3.43}$$

We obtain the first three boundary conditions for Y by evaluating (3.24b, 3.24c) at $T=0$, to first order in ϵ, giving

$$Y(0,t)=0,\quad \frac{\partial Y}{\partial\sigma}(0,t)=0,\quad \frac{\partial^2 Y}{\partial\sigma^2}(L,t)=0. \tag{3.44}$$

The fourth boundary condition for Y is obtained similarly, by evaluating (3.23a) at $\sigma=L$ and $T=0$, to $O(\epsilon)$,

$$\mathcal{B}\frac{\partial^3 Y}{\partial\sigma^3}(L,t)-\boldsymbol{F}\cdot\hat{\boldsymbol{\tau}}\frac{\partial Y}{\partial\sigma}(L,t)=-N_y. \tag{3.45}$$

Eq. (3.43) along with boundary conditions (3.44, 3.45) constitute the linearised system for Y under small deflections. Multiplying each of these equations by ϵ, we obtain the linearised equation for y, to first order in ϵ. The full system is then

$$\frac{\partial\mathsf{y}}{\partial t}-c(t)\frac{\partial\mathsf{y}}{\partial\sigma}=\frac{1}{\zeta}\left(\frac{\partial^2\mathsf{y}}{\partial\sigma^2}\boldsymbol{F}\cdot\hat{\boldsymbol{\tau}}-\mathcal{B}\frac{\partial^4\mathsf{y}}{\partial\sigma^4}\right)-\sigma\,\widehat{\mathcal{R}}(t), \tag{3.46a}$$

$$\frac{\partial\hat{\theta}}{\partial t}=\widehat{\mathcal{R}}(t), \tag{3.46b}$$

$$\frac{\partial\hat{\boldsymbol{r}}}{\partial t}=c(t)\,\hat{\boldsymbol{\tau}}, \tag{3.46c}$$

$$\widehat{\mathcal{R}}(t):=c(t)\frac{\partial^2\mathsf{y}}{\partial\sigma^2}(0,t). \tag{3.46d}$$

The deflection $\mathsf{y}(\sigma,t)$ satisfies the boundary conditions

$$\mathsf{y}(0,t)=0,\quad \frac{\partial\mathsf{y}}{\partial\sigma}(0,t)=0, \tag{3.47a}$$

$$\frac{\partial^2\mathsf{y}}{\partial\sigma^2}(L,t)=0,\quad \mathcal{B}\frac{\partial^3\mathsf{y}}{\partial\sigma^3}(L,t)-\boldsymbol{F}\cdot\hat{\boldsymbol{\tau}}\frac{\partial\mathsf{y}}{\partial\sigma}(L,t)=-\boldsymbol{F}\cdot\hat{\boldsymbol{\nu}}. \tag{3.47b}$$

Conditions (3.47a) define a clamp at $\sigma = 0$, while (3.47b) enforces the load $\boldsymbol{F}$ applied with no torque on the beam at $\sigma = L$.

The growth speed c depends on the force exerted by the growth cone on the tip of the axon. Solving the system in the steady regime for rectilinear expansion [see 56, 52, 53], provides, for small deflection and to leading order, a growth velocity of the form

$$c = \frac{\boldsymbol{F} \cdot \boldsymbol{t}}{\sqrt{\eta\zeta}}. \tag{3.48}$$

We have developed a minimal model with two main components. From the microscopic model we have a mapping from substrate rigidity to the traction exerted by the growth cone, and from the mesoscopic model we obtain the shape of the axon as a function of time by locally integrating a clamped beam equation and advecting the clamp accordingly. We are now in a position to use this model to understand the effects of varying substrate rigidity on the motion and shape of axons. We next describe our numerical method for the integration of the above system.

3.3.4 Numerics and implementation details

To solve the system for $(\hat{\boldsymbol{r}}, \hat{\theta}, \mathsf{y})$ we spatially discretise (3.46a) using a spectral method. This approach approximates the derivatives of a given function by the derivatives of a Chebyshev polynomial interpolation of that function on a discrete grid [74, 61]. To that end, we first transform the spatial domain to the interval $[-1, 1]$. We start by rewriting (3.46a) in terms of the dimensionless variable

$$X = 2\sigma/L - 1 \in [-1, 1]\,. \tag{3.49}$$

This allows us to discretise the spatial domain according to the Chebyshev grid [74]

$$X_j = \cos\left(j\pi/N\right), \quad j = 0, \ldots, N. \tag{3.50}$$

Thus, we can convert the PDE (3.46a) into a system of ordinary differential equations. First, we define

$$\mathsf{y}_j\left(t\right) = \mathsf{y}\left(X_j, t\right), \tag{3.51}$$

and the vector

$$\mathbf{y} = \left(\mathsf{y}_0, \ldots, \mathsf{y}_N\right). \tag{3.52}$$

The spatial derivatives of $\mathsf{y}(X, t)$ evaluated on the Chebyshev grid may be approximated by multiplying $\mathbf{y}$ with the Chebyshev differentiation matrix D_N [74]. e.g.

$$\frac{\partial^k \mathsf{y}}{\partial X^k}\left(X_j, t\right) \approx \left[D_N^k \mathbf{y}\right]_j. \tag{3.53}$$

By replacing instances of the spatial derivatives of $\mathsf{y}(X,t)$ with the above approximation in the rescaled equation, we obtain an ordinary differential equation for $\mathbf{y}(t)$ of the form

$$\frac{\mathrm{d}\mathbf{y}}{\mathrm{d}t} = g\left(t, \hat{\theta}, \hat{\boldsymbol{r}}, \mathbf{y}\right). \tag{3.54}$$

Once instances of spatial derivatives have been replaced according to (3.53), the boundary conditions constitute conditions that $\mathbf{y}$ must satisfy. Solving these equations for $\mathsf{y}_0, \mathsf{y}_1, \mathsf{y}_{N-1}, \mathsf{y}_N$ in terms of $\mathsf{y}_2, \ldots, \mathsf{y}_{N-2}$ ensures that $\mathbf{y}$ satisfies these conditions.

Using the boundary conditions we can constrain y_0, y_1, y_{N-1} and y_N. The first three boundary conditions,

$$\mathsf{y}(0,t) = 0, \quad \frac{\partial \mathsf{y}}{\partial \sigma}(0,t) = 0, \quad \frac{\partial^2 \mathsf{y}}{\partial \sigma^2}(L,t) = 0. \tag{3.55}$$

are linear, which allows to express directly $\mathsf{y}_1, \mathsf{y}_{N-1}, \mathsf{y}_N$ in terms of y_0, $\mathsf{y}_2, ..., \mathsf{y}_{N-2}$. The boundary condition

$$\mathcal{B}\frac{\partial^3 \mathsf{y}}{\partial \sigma^3}(L,t) - \boldsymbol{F}\cdot\hat{\boldsymbol{\tau}}\frac{\partial \mathsf{y}}{\partial \sigma}(L,t) = -\boldsymbol{F}\cdot\hat{\boldsymbol{\nu}}, \tag{3.56}$$

can be discretised as

$$\mathcal{B}\,(2/L)^3\left[D_N^3\mathbf{y}\right]_0 - (2/L)\,\boldsymbol{F}\cdot\hat{\boldsymbol{\tau}}\left[D_N\mathbf{y}\right]_0 = -\boldsymbol{F}\cdot\hat{\boldsymbol{\nu}}; \tag{3.57}$$

noting that $\partial^k \mathsf{y}/\partial X^k = (L/2)^k\,\partial^k \mathsf{y}/\partial \sigma^k$ (3.49). Here, $\boldsymbol{F}$ depends on the position of the tip, thus (3.57) is a nonlinear equation for y_0 for which no closed-form solution can be found in general. In principle, one can solve this nonlinear equation numerically for y_0 using a root-finding procedure at each time step. Alternatively, we may simplify the problem by evaluating the tangent at the tip at the neighbouring point $X = X_2$ (instead of X_1), i.e.,

$$\boldsymbol{t} = \frac{\partial \boldsymbol{r}/\partial\sigma(L,t)}{\|\partial \boldsymbol{r}/\partial\sigma(L,t)\|} \approx \left(1 + \left(\frac{2}{L}\frac{\mathsf{y}_2 - \mathsf{y}_3}{X_2 - X_3}\right)^2\right)^{-1/2}\left(\hat{\boldsymbol{\tau}} + \frac{2}{L}\frac{\mathsf{y}_2 - \mathsf{y}_3}{X_2 - X_3}\hat{\boldsymbol{\nu}}\right), \tag{3.58}$$

so as to eliminate the explicit dependence upon y_0. The error produced by the approximation (3.58) for the tangent is $\mathcal{O}\left(1/N^2\right)$ as $N \to \infty$. This converts the above equation to a linear one, which allows us to obtain a closed-form expression for y_0 in terms of $\mathsf{y}_2, \ldots, \mathsf{y}_{N-2}$.

Thus, (3.46a) can be approximated by an equation of the form

$$\frac{\mathrm{d}\mathbf{Y}}{\mathrm{d}t} = G\left(t, \hat{\theta}, \hat{\boldsymbol{r}}, \mathbf{Y}\right), \tag{3.59}$$

where $\mathbf{Y} := (\mathsf{y}_2, \ldots, \mathsf{y}_{N-2})$ denotes the vector of discrete variables after truncation of the boundary values y_0, y_1, y_N and y_{N-1} (which are now fixed); and $G(t, \hat{\theta}, \hat{\boldsymbol{r}}, \mathbf{Y}) := g(t, \hat{\theta}, \hat{\boldsymbol{r}}, \mathbf{y}(\mathbf{Y}))$. Finally, (3.46b) can be re-written as

$$\frac{\mathrm{d}\hat{\theta}}{\mathrm{d}t} = (2/L)^2\, c(t)\left[D_N^2\mathbf{y}\right]_N, \tag{3.60}$$

and (3.46c) remains unchanged. The equations

$$\frac{\mathrm{d}\mathbf{Y}}{\mathrm{d}t} = G\left(t, \hat{\theta}, \hat{\boldsymbol{r}}, \mathbf{Y}\right), \tag{3.61a}$$

$$\frac{\mathrm{d}\hat{\theta}}{\mathrm{d}t} = (2/L)^2\, c(t)\left[D_N^2 \mathsf{y}\right]_N, \tag{3.61b}$$

$$\frac{\mathrm{d}\hat{\boldsymbol{r}}}{\mathrm{d}t} = c(t)\,\hat{\boldsymbol{\tau}}, \tag{3.61c}$$

form a simple IVP which can be integrated numerically (here we used the built-in function *NDSolve* implemented in *Mathematica 13.3*). In all our simulations we initialize the system with $\mathbf{Y} = \mathbf{0}$.

3.4 Constant growth cone force - Timescale of axon turning

In order to understand the role of the growth cone force on axon pathfinding it is illustrative to study the basic example where the growth cone force is constant. A constant growth cone force may, for example, model a guidance cue which directs the axon towards a constant direction and whose strength does not change with space or time. In this case, we assume

$$\boldsymbol{F} = f\left(\cos\theta, \sin\theta\right), \tag{3.62}$$

which is a force of magnitude f and polar angle θ.

Under this force, there exists a solution to (3.46 - 3.47) where

$$\mathsf{y}(\sigma, t) = 0, \hat{\theta}(t) = \theta, \hat{\boldsymbol{r}}(t) = \boldsymbol{r}_0 + \frac{f\,t}{\sqrt{\eta\zeta}}\hat{\boldsymbol{\tau}}, \tag{3.63}$$

i.e. the axon grows along a straight line along the force vector $\boldsymbol{F}$. Thus, a natural question is whether nearby trajectories of the system converge to solutions parallel to this one. Furthermore, in the case where nearby trajectories do converge to this solution, a quantity of experimental interest is the rate of this convergence, since it is a measure of how sensitive the axon is to specific guidance cues.

Intuition suggests that this solution should be locally attractive: we expect that upon application of a force to the axon tip which is off-axis of the axon shaft, the axon will bend and start turning in the direction of the force. This bending and turning will continue until the axon shaft at the tip is aligned with the applied force, at which point the axon will start growing along a straight line. As the clamp is displaced along the axon profile, it will eventually reach the newly formed straight portion of the axon, at which point the system will have reached the steady state solution.

In fact, numerical integration of the full system (3.46 - 3.47) under the constant force (3.62), shows that initial conditions of the system which are close to the steady state converge to it (See Fig. 3.4). This suggests that the role of the growth cone force is to determine the final direction of growth of the system and direct the axon accordingly.

Analytically, whether nearby trajectories converge to (3.63) is determined by the eigenvalues of the linearised evolution operator about this solution. If all eigenvalues of the linearised operator have a positive real part it follows that solutions will converge to this solution, at least locally (positive because of the notation we use below). Furthermore, the rate of this convergence is given by the smallest positive real part of all eigenvalues. To determine these eigenvalues, we linearise (3.46 - 3.47) about (3.63). To aid our analysis, we assume without loss of generality a constant force of the form

$$\boldsymbol{F} = f\,(1,0)\,. \tag{3.64}$$

The fact that $\boldsymbol{F}$ is constant and unrelated to the clamp position $\hat{\boldsymbol{r}}$ means that equations (3.46a - 3.46b) decouple from (3.46c). Thus, we focus on equations (3.46a - 3.46b). In this case, the solution of the IBVP is given by the pair $\hat{\theta}(t), y(x,t)$, where

$$y(x,t) = \int_0^x \int_0^X \kappa\,(\xi,t)\,\mathrm{d}\xi \mathrm{d}X, \tag{3.65}$$

and $\hat{\theta}, \kappa$ solve the IBVP

$$\frac{\partial \kappa}{\partial t} - c(t)\frac{\partial \kappa}{\partial x} = \frac{1}{\zeta}\left(\boldsymbol{F}\cdot\hat{\boldsymbol{\tau}}\frac{\partial^2 \kappa}{\partial x^2} - \mathcal{B}\frac{\partial^4 \kappa}{\partial x^4}\right), \tag{3.66}$$

$$\frac{\partial \hat{\theta}}{\partial t} = c(t)\kappa(0,t), \tag{3.67}$$

$$\kappa(L,T) = 0, \quad \mathcal{B}\frac{\partial \kappa}{\partial x}\,(L,t) - (\boldsymbol{F}\cdot\hat{\boldsymbol{\tau}})\int_0^L \kappa \mathrm{d}x = -\boldsymbol{F}\cdot\hat{\boldsymbol{\nu}}, \tag{3.68}$$

$$\mathcal{B}\frac{\partial^2 \kappa}{\partial x^2}(0,t) - (\boldsymbol{F}\cdot\hat{\boldsymbol{\tau}})\,\kappa(0,t) = 0, \quad \mathcal{B}\frac{\partial^3 \kappa}{\partial x^3}(0,t) - (\boldsymbol{F}\cdot\hat{\boldsymbol{\tau}})\,\frac{\partial \kappa}{\partial x}(0,t) = 0. \tag{3.69}$$

Linearising about $\kappa = 0, \hat{\theta} = 0$ the above system reduces to

$$\frac{\partial \hat{\theta}}{\partial t} = \frac{f}{\sqrt{\eta\zeta}}\kappa(0,t), \tag{3.70}$$

$$\frac{\partial \kappa}{\partial t} - \frac{f}{\sqrt{\eta\zeta}}\frac{\partial \kappa}{\partial x} = \frac{1}{\zeta}\left(f\frac{\partial^2 \kappa}{\partial x^2} - \mathcal{B}\frac{\partial^4 \kappa}{\partial x^4}\right), \tag{3.71}$$

$$\kappa(L,T) = 0, \quad \mathcal{B}\frac{\partial \kappa}{\partial x}\,(L,t) - f\int_0^L \kappa \mathrm{d}x = f\,\hat{\theta}, \tag{3.72}$$

$$\mathcal{B}\frac{\partial^2 \kappa}{\partial x^2}(0,t) - f\kappa(0,t) = 0, \quad \mathcal{B}\frac{\partial^3 \kappa}{\partial x^3}(0,t) - f\frac{\partial \kappa}{\partial x}(0,t) = 0. \tag{3.73}$$

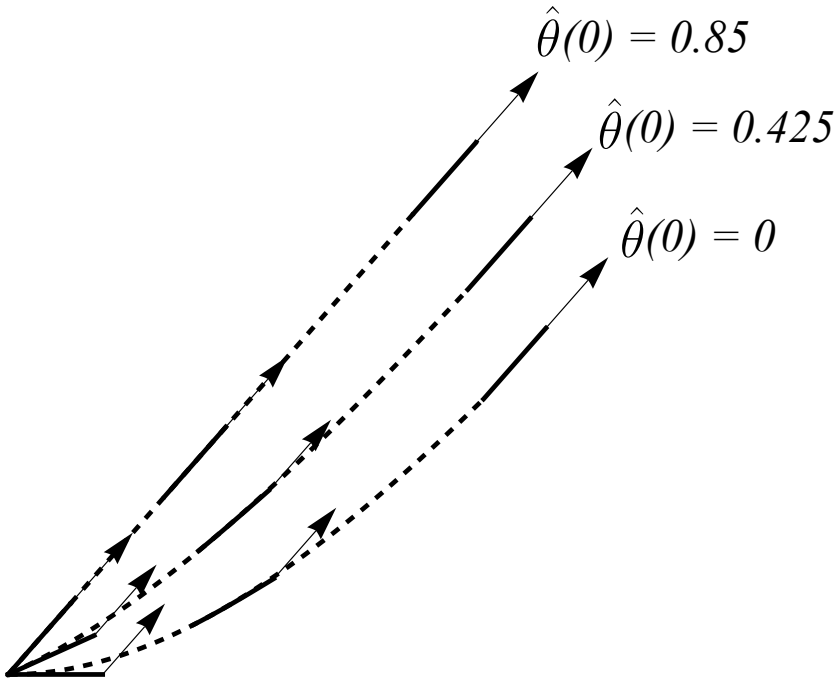


Figure 3.4: Simulation of a few axons (black solid lines) illustrating convergence to trajectories parallel to the constant force vector 3.62 (arrow). Trajectory of the clamps indicated by the black dashed lines. Parameters: $L = 32$ µm, $\mathcal{B} = 10^{-19}$ Nm^2, $R = L/2$, $\varphi_0 = \pi/2$, $\eta = 10^{-5}$Ns, $\zeta = 10^4$ Pa s, $\boldsymbol{F} = f\ (\cos(0.85), \sin(0.85))$, $f = 0.05\, F_{\text{char}}$, $F_{\text{char}} = 10^{-9}$N.

Testing solutions of the form $\kappa(x,t) = u(x)\mathrm{e}^{-st}, \hat{\theta}(t) = \vartheta \mathrm{e}^{-st}$ we obtain the following eigenvalue problem for s

$$\frac{\mathcal{B}}{\zeta}u^{(4)}(x) - \frac{f}{\zeta}u^{(2)}(x) - \frac{f}{\sqrt{\eta\zeta}}u'(x) = s\,u(x), \tag{3.74a}$$

$$u(L) = 0, \quad \mathcal{B}u'(L) - f\int_0^L u(x)\mathrm{d}x = f\,\vartheta, \tag{3.74b}$$

$$\mathcal{B}u''(0) - fu(0) = 0, \quad \mathcal{B}u'''(0) - fu'(0) = 0, \tag{3.74c}$$

$$\frac{f}{\sqrt{\eta\zeta}}u(0) + s\vartheta = 0. \tag{3.74d}$$

The constant ϑ can be eliminated using (3.74d), giving an eigenvalue problem which depends only on u:

$$\frac{\mathcal{B}}{\zeta}u^{(4)}(x) - \frac{f}{\zeta}u^{(2)}(x) - \frac{f}{\sqrt{\eta\zeta}}u'(x) = s\,u(x), \tag{3.75}$$

$$u(L) = 0, \quad \mathcal{B}u'(L) - f\int_0^L u(x)\mathrm{d}x + \frac{1}{s}\frac{f^2}{\sqrt{\eta\zeta}}u(0) = 0, \tag{3.76}$$

$$\mathcal{B}u''(0) - fu(0) = 0, \quad \mathcal{B}u'''(0) - fu'(0) = 0. \tag{3.77}$$

To make evident the effect of the length of the axon, L, on the eigenvalues we non-dimensionalize the above system using $u(x) = L^{-1}\,U(x/L)$ to obtain

$$\mathcal{A}\,U = \lambda\,U, \tag{3.78}$$

where

$$\mathcal{A}\,U = U^{(4)}(X) - \epsilon_1 U^{(2)}(X) - \epsilon_1\epsilon_2 U'(X), \tag{3.79a}$$

$$U(1) = 0, \quad U''(0) - \epsilon_1 U(0) = 0, \tag{3.79b}$$

$$U'(1) - \epsilon_1\int_0^1 U(X)\mathrm{d}X + \frac{\epsilon_1^2\epsilon_2}{\lambda}U(0) = 0, \tag{3.79c}$$

$$U'''(0) - \epsilon_1 U'(0) = 0. \tag{3.79d}$$

where

$$s = \frac{\mathcal{B}}{L^4\zeta}\lambda, \;\; \epsilon_1 = \frac{fL^2}{\mathcal{B}}, \;\; \epsilon_2 = L\sqrt{\frac{\zeta}{\eta}}. \tag{3.80}$$

We note that by assumption $\epsilon_2 = \mathcal{O}(1)$ (Section 3.3.2). Thus, we assume $\epsilon_2 = 1$. The non-local boundary condition 3.79c can be transformed into a local one upon the observation that

$$\begin{aligned}\int_0^1 \lambda\,U(X)\,\mathrm{d}X &= \int_0^1 U^{(4)}(X) - \epsilon_1 U^{(2)}(X) - \epsilon_1 U'(X)\,\mathrm{d}X \\ &= \left[U^{(3)}(X) - \epsilon_1 U'(X) - \epsilon_1 U(X)\right]_0^1 \\ &= U^{(3)}(1) - \epsilon_1 U'(1) + \epsilon_1 U(0),\end{aligned}$$

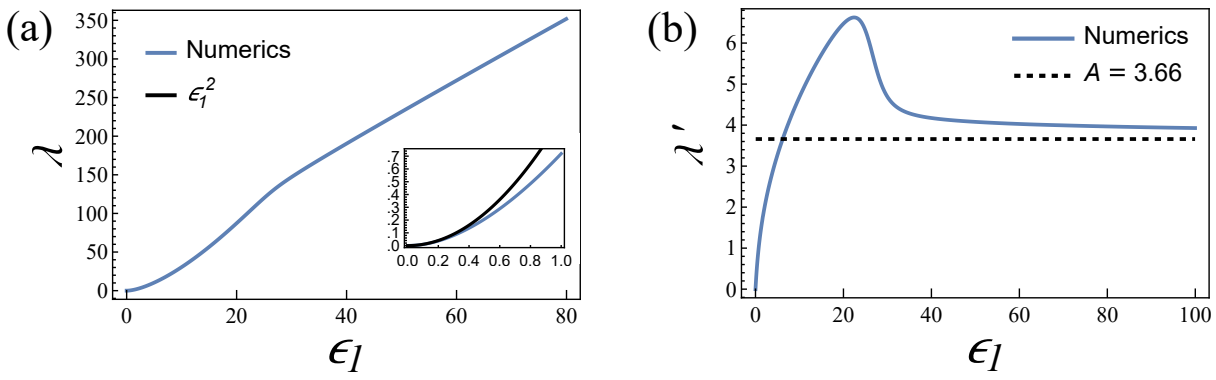


Figure 3.5: Investigations on turning rate. (A) Dimensionless turning rate λ as a function of ϵ_1 (B) Plot of $\lambda'(\epsilon_1)$ indicates that the turning rate becomes linear with slope $A = 3.66$ as $\epsilon_1 \gg 1$.

where the last equality is arrived at by the use of BC (3.79d). Therefore, BC (3.79c) is equivalent to

$$\epsilon_1 U^{(3)}(1) - \left(\lambda + \epsilon_1^2\right) U'(1) = 0. \tag{3.81}$$

This eigenvalue problem has a couple of notable features. First of all, the operator $\mathcal{A}$ is non-self-adjoint on the subset of $L^2[0,1]$ of sufficiently smooth functions which satisfy boundary conditions (3.79b - 3.79d), which is not uncommon for advection operators. This suggests that the eigenvectors may not be orthogonal with respect to the appropriate inner product. This makes it non-trivial to express an initial condition in terms of a basis of eigenvectors. However, in this formulation, the long-time asymptotic behavior of solutions is still determined by the eigenvalue with smallest positive real part, denoted by λ^*. Finally, the eigenvalue also appears in the BCs, something which is frequently observed in combined systems, such as a clamped-free beam with a concentrated mass attached by a spring to the free end.

Note that λ^* is completely determined by $\epsilon_1 = fL^2/\mathcal{B} = f\eta/(\mathcal{B}\zeta)$, so we denote it as $\lambda^* = \lambda^*(\epsilon_1)$. In dimensional units, the corresponding eigenvalue is given by

$$s^* = \frac{\mathcal{B}\zeta}{\eta^2}\lambda^*(\epsilon_1), \tag{3.82}$$

where the prefactor $\eta^2/(\mathcal{B}\zeta)$ has dimensions of time.

The constant $\lambda \in \mathbb{C}$ is an eigenvalue of $\mathcal{A}$ if the BVP (3.78 - 3.79d) has non-trivial solutions. The general solution for this linear equation is given by a sum of four linearly independent solutions. The general solution can be used to find the eigenvalues λ using a determinant method. Suppose the general solution is given by

$$U(X) = A_1 U_1(X) + A_2 U_2(X) + A_3 U_3(X) + A_4 U_4(X), \tag{3.83}$$

where U_i are linearly independent solutions of the BVP. Boundary conditions (3.79b - 3.79d) can be expressed in matrix form as

$$M(\lambda, \epsilon_1) \begin{bmatrix} A_1 \\ A_2 \\ A_3 \\ A_4 \end{bmatrix} = \begin{bmatrix} 0 \\ 0 \\ 0 \\ 0 \end{bmatrix}. \tag{3.84}$$

Therefore, λ is an eigenvalue if the above system has non-trivial solutions, which is equivalent to the matrix $M(\lambda, \epsilon_1)$ being singular. That is

$$\det\left(M(\lambda, \epsilon_1)\right) = 0. \tag{3.85}$$

For simpler problems, roots of the above equation can be determined exactly. In this case, numerical root-finding methods need to be employed. Another numerical method to derive numerical approximations to the eigenvalues of this operator is by looking at the eigenvalues of the discretised operator derived in Section 3.3.4, linearised about the steady state $\hat{\theta} = 0, y = 0$. We employed both methods and found that they agreed to a high degree of accuracy.

The dependence of λ^* on ϵ_1 can be seen in Fig. 3.5. We observe that $\lambda^*(\epsilon_1)$ is real and is a strictly increasing function of ϵ_1 (Fig. 3.5(A)). This is expected as ϵ_1 describes the dimensionless growth cone force. The greater the growth cone force, the faster the convergence to the force-aligned trajectory. The numerics suggest that around $\epsilon_1 = 0$, $\lambda^*(\epsilon_1)$ has zero slope, whilst it becomes linear for $\epsilon_1 \gg 1$.

It is straightforward to derive an analytic approximation for $\lambda^*(\epsilon_1)$ when $\epsilon_1 \ll 1$. In this limit, we expand

$$U = U_0 + \epsilon_1 U_1 + \epsilon_1^2 U_2 + \epsilon_1^3 U_3 + \ldots \tag{3.86}$$

$$\lambda = \lambda_0 + \epsilon_1 \lambda_1 + \epsilon_1^2 \lambda_2 + \epsilon_1^3 \lambda_3 + \ldots \tag{3.87}$$

For $\epsilon_1 = 0$ there exist non-trivial solutions with $\lambda_0 = 0$. Our numerics indicate that this is the branch that we are interested in. At each order the BC obtained from BC (3.81) gives a condition which determines the value of the coefficient of the series λ^* at that order. Solving for the coefficient at each order we obtain the following series expansion

$$\lambda^*(\epsilon_1) = \epsilon_1^2 - \frac{11}{24}\epsilon_1^3 + \frac{43}{140}\epsilon_1^4 - \frac{31027}{134400}\epsilon_1^5 + \frac{13745483}{74131200}\epsilon_1^6 + \mathcal{O}(\epsilon_1^7), \tag{3.88}$$

There is good agreement between the numerics and (3.88) for small ϵ_1. See Fig. 3.5(A) for comparison between $\lambda^*(\epsilon_1)$ and the series expansion (truncated to second order). For $\epsilon_1 \gg 1$, our numerics suggest

$$\lambda^*(\epsilon_1) \sim A\,\epsilon_1, \tag{3.89}$$

where $A \approx 3.66$ (see Fig. 3.5(B) for a plot of $\lambda^{*\prime}(\epsilon_1)$).

The quadratic behaviour of $\lambda^*(\epsilon_1)$ for $\epsilon_1 \ll 1$ and its linear behaviour for $\epsilon_1 \gg 1$ suggests that there is an inherent non-linear sensitivity of the axon to guidance cues, determined by $\lambda^{*\prime}(\epsilon_1)$, as the strength of the cue, measured by ϵ_1, varies. For small values of ϵ_1, the sensitivity of the axon increases, reaching maximal sensitivity at an intermediate value $\epsilon_1 = \epsilon_{\max}$. Beyond $\epsilon_{\max}$ the sensitivity of the axon to guidance cue is decreasing. Furthermore, since our analysis relies solely on consideration of the magnitude of the growth cone force, it follows that this non-linear sensitivity is independent of the particular mechanism through which a guidance cue determines the growth cone force.

The above analysis shows that nearby solutions do converge to the trajectory (3.63). Furthermore, the rate of this convergence is characterised by the eigenvalue λ^*, for which we derived approximations (3.88) and (3.89) in the limits $\epsilon_1 \ll 1$ and $\epsilon_1 \gg 1$, respectively.

3.5 Motion in a stiffness field of constant gradient

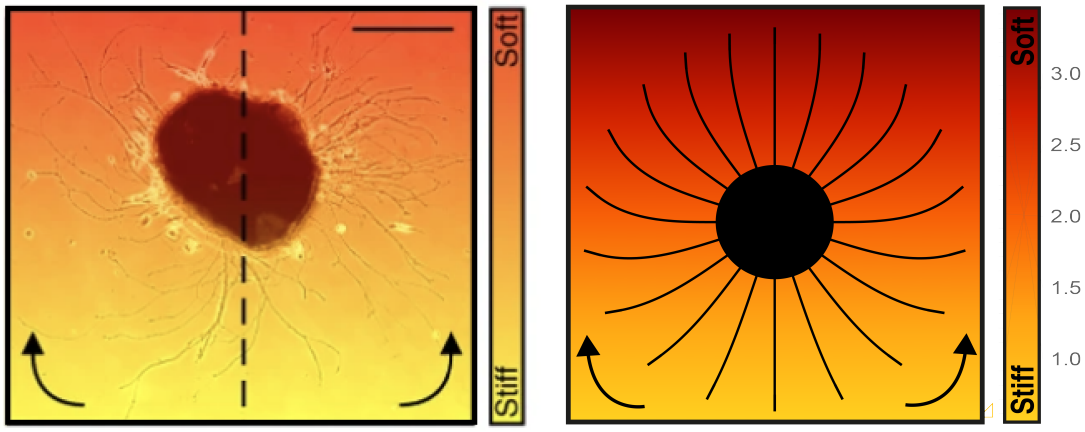


Figure 3.6: (Left) Axons growing from a Xenopus retina, cultured on a substrate with a linear stiffness gradient. As can be seen, the axons tend to grow more towards the soft side of the substrate [38]. Scale bar: 200µm. (Right) Simulation of the beam model, with axons initialised on the boundary of a disk, in the stiffness field (3.90), showing qualitatively similar growth pattern. $m_\chi = -0.1$, $\chi^* = 0.56$, $L = 32$ µm, $\mathcal{B} = 10^{-19}$ Nm^2, $R = L/2$, $\varphi_0 = \pi/2$, $2\rho R\, T(\chi^*) = 10^{-9}$ N.

Having addressed the behaviour of the axon in the simple scenario of a constant growth cone force, we turn our attention to the simplest scenario of axon durotaxis: a stiffness field of constant gradient. This type of stiffness field is frequently employed in in-vitro experiments to investigate the effect of stiffness on axonal pathfinding [38] and allows us to understand the basic effect of the stiffness gradient. As we shall see, the

non-monotonicity of $T(\chi)$ has important consequences for the possible trajectories in a linear stiffness field.

Without loss of generality we investigate a stiffness field of the form

$$\chi(x, y) = m_\chi y + \chi^*, \tag{3.90}$$

where χ^* is the optimal stiffness of the growth cone and $m_\chi \boldsymbol{e}_y$ is the stiffness gradient. In this case we have that

$$\nabla\chi = m_\chi \boldsymbol{e}_y. \tag{3.91}$$

The line $y = 0$ defines a set upon which the value of the field is equal to the optimal stiffness. As we shall see, axons exhibit a particularly interesting behaviour when close to this 'line of optimal stiffness'.

3.5.1 General motion away from lines of optimal stiffness

Here we investigate the behaviour of axons, in the linear stiffness field, in regions away from the line of optimal stiffness. We approximate the growth cone force by (3.2).

Firstly, as a simple illustration of growth on a graded substrate, we initiate multiple axons on the boundary of a disk in a linear stiffness field, mimicking the experimental setup in [38]. The growth pattern obtained matches qualitatively that seen experimentally; see Fig. 3.6, where axons are gradually deflected towards softer regions.

For axons in regions $y > 0$, $y < 0$, there exist axon trajectories of the form

$$\mathsf{y}(\sigma, \mathsf{t}) = 0, \hat{\theta} = \pm\pi/2, \tag{3.92}$$

which in both regions correspond to one axon traveling parallel to the stiffness gradient towards the line of optimal stiffness and another traveling away from the line of optimal stiffness.

Although in either region there exist trajectories travelling both towards and away from the line of optimal stiffness, numerical simulation suggests that only the trajectories traveling towards the line of optimal stiffness are stable. To see this, we look at $F_n = \boldsymbol{F} \cdot \boldsymbol{n}$ in each case, where $\boldsymbol{n}$ corresponds to the normal vector at the axon tip. F_n is the component of the growth cone force normal to the axon tip. If under a small perturbation of the axon profile this component is positive or negative, the sign of the force will tell us whether this normal component acts as a restoring force which tends to reorient the axon towards the initial direction of motion or if it further repels this axon, making the initial deviation larger.

In the following, we assume that $m_\chi > 0$ without loss of generality. Denoting the polar angle of the growth cone tip by ψ and expanding F_n to first order about $\psi = \pi/2$ we obtain

$$F_n = -m_\chi T'(\chi_{\text{tip}}) R^2 \rho \left(\varphi_0 - \frac{\sin(2\varphi_0)}{2}\right)\left(\psi - \frac{\pi}{2}\right). \tag{3.93}$$

In the case $y > 0$ we have $\chi_{\text{tip}} > \chi^*$ which implies $T'(\chi_{\text{tip}}) < 0$. Therefore,

$$-m_\chi T'(\chi_{\text{tip}}) R^2 \rho \left(\varphi_0 - \frac{\sin(2\varphi_0)}{2}\right) > 0,$$

and so any deviation from the line $\psi = \pi/2$ will generate a normal component of the growth cone force which further directs the axon away from this line. Therefore, it follows that this trajectory is unstable. Conversely, in the case $y < 0$ we have

$$-m_\chi T'(\chi_{\text{tip}}) R^2 \rho \left(\varphi_0 - \frac{\sin(2\varphi_0)}{2}\right) < 0,$$

in which case deviations from the line $\psi = \pi/2$ generate a normal force component directing the axon back to line $\psi = \pi/2$. This calculation suggests for $y < 0$, the trajectory along $\psi = \pi/2$ is stable. Expanding F_n about $\psi = -\pi/2$ and conducting the same analysis we obtain similar results.

In summary, these calculations show that solutions (3.92) are stable when the axon is traveling towards the line of optimal stiffness and unstable when traveling away from the line of optimal stiffness. Thus, the general tendency of axons in the regions away from the line of optimal stiffness in a linear stiffness field is to align themselves with the stiffness gradient in a direction leading towards a region where the stiffness is equal to the optimal stiffness.

3.5.2 Motion near lines of optimal stiffness

More generally, the local traction exerted by the growth cone exhibits a maximum on the line $\mathcal{D}$ of optimal stiffness $y = 0$. We will show that $\mathcal{D}$ is a locally attracting set for our system in the sense that nearby trajectories are attracted asymptotically to $\mathcal{D}$. This property is a consequence of the non-monotonic dependence of the traction force T upon the stiffness χ.

We consider an axon travelling in a neighbourhood of $\mathcal{D}$ of typical size R. Hence, the growth cone is initially located at the position $\boldsymbol{r} = rR\boldsymbol{e}_y$, with r of order one, and travelling nearly parallel to the axis with $\boldsymbol{t} = \boldsymbol{e}_x + \psi \boldsymbol{e}_y + \ldots$ with the growth cone angle $\psi \ll 1$. We obtain the behaviour of this axon by expanding the traction (3.1) about χ^*,

while treating R and ψ as small parameters:

$$\rho^{-1}\boldsymbol{F}(\boldsymbol{r},\boldsymbol{t}) = 2R\sin\varphi_0 T(\chi^*)\boldsymbol{t} + r^2R^3\sin\varphi_0 T''(\chi^*)\, m_\chi^2\boldsymbol{t} + rR^3\varphi_0 T''(\chi^*)m_\chi \mathbf{P}(\varphi_0)\nabla\chi + \frac{R^3\varphi_0}{2}T''(\chi^*)\mathbb{P}(\varphi_0) : \nabla\chi\otimes\nabla\chi + O(R^4), \tag{3.94}$$

where $\mathbb{P}(\varphi_0) := \int_{-\varphi_0}^{\varphi_0} \boldsymbol{e}_{\boldsymbol{\varphi}}\otimes\boldsymbol{e}_{\boldsymbol{\varphi}}\otimes\boldsymbol{e}_{\boldsymbol{\varphi}}\,(\mathrm{d}\varphi/\varphi_0)$, and $\mathbf{P}(\varphi_0)$ is defined in (3.3). Eq. (3.94) extends (3.2) to higher order. This is necessary for our analysis, since the leading-order deflection of $O(R^2)$ vanishes at $\chi=\chi^*$. Of particular interest is the transverse component $F_n := \boldsymbol{F}\cdot\boldsymbol{n}$, given by

$$F_n = \frac{1}{6}R^3\rho T''(\chi^*)m_\chi^2\left(3r\left(\varphi_0-\sin\varphi_0\cos\varphi_0\right)+4\psi\sin^3\varphi_0\right)+\text{h.o.t.} \tag{3.95}$$

Since $F_n=0$ when $\psi=r=0$, there exist trajectories along $\mathcal{D}$ (however, with a small drift appearing at higher orders and controlled by the third derivative $T'''(\chi^*)$). For $r\gg\psi$, the first term in the parentheses dominates, and, since $T''(\chi^*)<0$, the deflection component has opposite sign of r and grows with r in magnitude. Thus we interpret this term as an elastic-like restoring force which pulls the axon back to the optimal stiffness line $\mathcal{D}$. Conversely, very close to $\mathcal{D}$, i.e. for $r\ll\psi$, the deflection is dominated by the second term and takes now the opposite sign of ψ, which, again, will tend to reorient the axon towards the horizontal. We conclude that, close to the line of optimal stiffness, durotaxis has a restoring, stabilising effect which tends to maintain the axon near this line.

Note, however, that the longitudinal component $F_t := \boldsymbol{F}\cdot\boldsymbol{t} \gg F_n$ dominates in the balance of forces, thus there may exist, in principle, conditions for which durotaxis will not suffice to keep the axon in the vicinity of $\mathcal{D}$. From this analysis of the growth cone force, it cannot be directly concluded whether the stable trajectory is attracting (exponential stability), or whether axons will oscillate around it and repeatedly overshoot it.

To further explore the dynamics of the axon near $\mathcal{D}$, we perform numerical simulations shown in Fig. 3.7. Firstly, Fig. 3.7(a) illustrates that, in the vicinity of $\mathcal{D}$ and for small initial inclination, axons are attracted and converge towards this stable manifold. Second, Fig. 3.7(b) shows that there may exist an escape angle above which durotaxis is insufficient to keep the axon closer to $\mathcal{D}$ despite the negative durotaxis in that region. Clearly, if the axon crosses perpendicularly the line of optimal stiffness, it will not curve back. Whether nearby directions also escape in an infinite domain is neither easy to establish nor directly relevant to the problem. Indeed, in a much larger domain, it is possible that such trajectories curve back to the line of optimal stiffness. However, in a realistic scenario, such axons would have migrated away from the region of optimal stiffness and be subject to other stimuli.

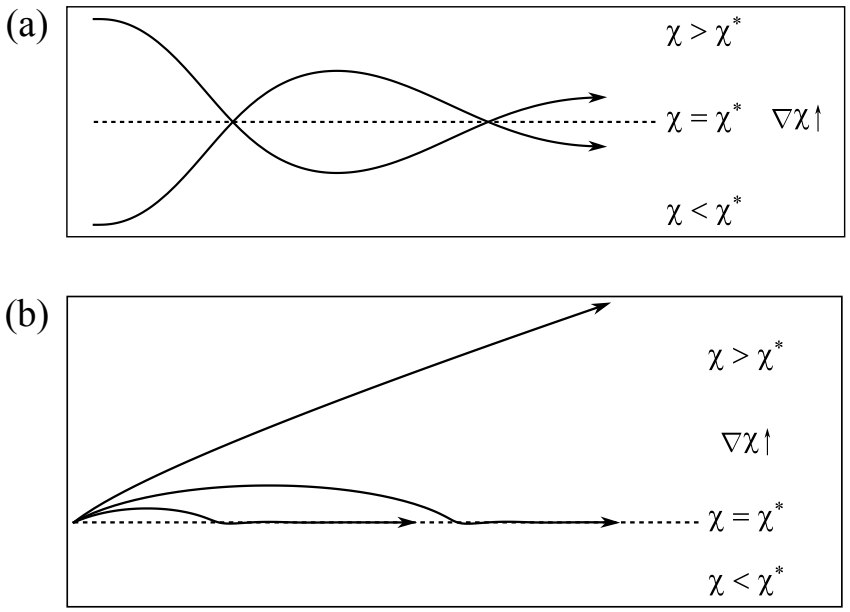


Figure 3.7: (a) Axons trajectories converge to the line of optimal stiffness, $\mathcal{D}$, if sufficiently close to it with sufficiently small inclination. (b) Axons with sufficiently large inclination escape the vicinity of $\mathcal{D}$.

The above results indicate that axons in the vicinity of lines of optimal stiffness are attracted to them. Furthermore, axons converge to trajectories parallel to lines of optimal stiffness. A natural corollary is that axons also converge to travelling parallel to curves of optimal stiffness. This capacity of the durotactic axon suggests a new mode of axon durotaxis: Guidance by curves of optimal stiffness.

3.5.3 A reduced axon model - The importance of long range sensing by the axon

The idea of an 'optimal stiffness' for the growth cone goes back to [13]. However, surprisingly, previous work had not identified convergence of axons to travelling parallel to lines of optimal stiffness as a new phenomenon. Rather, we identify two precursor ideas: (i) That motile cells would travel both down and up stiffness gradients to reach regions of optimal stiffness (experimentally verified in [34]) (ii) That axon guidance along a linear manifold can be achieved by appropriate specification of the stiffness field in the form of a duroduct, which is a one-dimensional manifold along which the stiffness of the environment is locally minimum in the direction perpendicular to the manifold [53]. We note that a corollary of the model definition in (ii) is that traction is also maximal along the duroduct centerline which makes the link between their model and ours in the case of line of optimal stiffness clear, though this is not provided as the explanation for guidance along duroducts.

Whilst these ideas separately suggest that axons are attracted to regions of optimal stiffness and that there may be mechanisms to precisely guide axons along 1D manifolds, the concept of a line of optimal stiffness suggests that these two phenomena co-occur and that such attraction and guidance may occur in as simple as a constant-gradient stiffness field. Given that this new mode of guidance may be important in understanding the role of axon durotaxis during the development of the nervous system, it is important to understand what is inherently novel in our model that allows for it. In this section we attempt to answer this question.

To make analytical progress, we further simplify the model. We define the *Long-Range Reduced* ABC model (henceforth abbreviated as *LRR*), valid for $\epsilon_1 \ll 1$, by the following set of equations

$$\dot{\hat{\boldsymbol{r}}}(t) = \frac{\boldsymbol{F}(\boldsymbol{r}_{\text{tip}}, \varphi) \cdot \boldsymbol{t}(\varphi)}{\sqrt{\eta\zeta}} \boldsymbol{t}(\varphi), \tag{3.96}$$

$$\dot{\varphi} = \frac{1}{\mathcal{B}\zeta} \left(\boldsymbol{F}(\boldsymbol{r}_{\text{tip}}, \varphi) \cdot \boldsymbol{t}(\varphi)\right) \left(\boldsymbol{F}(\boldsymbol{r}_{\text{tip}}, \varphi) \cdot \boldsymbol{n}(\varphi)\right). \tag{3.97}$$

The variables $\hat{\boldsymbol{r}}$, φ represent the position and polar angle of the clamp, respectively. The variable $\boldsymbol{r}_{\text{tip}}$, represents the position of the axon tip. The equation for $\hat{\boldsymbol{r}}$ is identical to that of the PDE system. To close the system, we must approximate $\boldsymbol{r}_{\text{tip}}$. This can be done straightforwardly in the limit $\epsilon_1 \ll 1$. In this limit we expect that the axon will be approximately straight so we assume

$$\boldsymbol{r}_{\text{tip}} \approx \hat{\boldsymbol{r}} + L\boldsymbol{t}(\varphi). \tag{3.98}$$

The particular choice for $\dot{\varphi}$ is made for the following reasons: (i) $\dot{\varphi}$ should have a multiplicative prefactor proportional to $c(t)$, just like in the full system (ii) At steady state, the alignment of the axon should be parallel to the growth cone force vector $\boldsymbol{F}$ (iii) In the case of a constant $\boldsymbol{F}$, the rate of convergence of φ, under the linearised system about the state which describes the axon traveling parallel to the force vector, should be equal to $s^*(\epsilon_1)$ - this guarantees that the reduced system has the same long time behaviour as the full system. Presumably in the limit $\epsilon_1 \gg 1$ an appropriate ODE simplification of the full system would differ from (3.97).

We proceed with an analysis of the trajectory of an axon defined according to (3.97) in the vicinity of a line of optimal stiffness. In this case, the dynamics of y, φ are independent from that of x, where

$$\hat{\boldsymbol{r}} = (x(t), y(t)). \tag{3.99}$$

This allows us to study the two-dimensional $y - \varphi$ system. Assuming that the growth-cone force $\boldsymbol{F}(\boldsymbol{r}, \boldsymbol{t})$ can be approximated by (3.2), truncated at second order in R, the full

system of equations is

$$\dot{y} = J\left(y,\varphi\right)\,\frac{m_\chi^2 T''\left(\chi^*\right)}{\sqrt{\eta\zeta}}\,\sin\varphi,$$
$$\dot{\varphi} = -J\left(y,\varphi\right)\,\frac{R\,m_\chi^4|T''\left(\chi^*\right)|^2}{\mathcal{B}\zeta}\left(\frac{\sin\left(2\varphi_0\right)}{2}-\varphi_0\right)\left(L\sin\varphi+y\right)\,\cos\varphi,$$

where

$$J = \sin\varphi_0(L\sin\varphi+y)^2 + R\sin\varphi\left(\varphi_0+\frac{\sin\left(2\varphi_0\right)}{2}\right)\left(L\sin\varphi+y\right)$$
$$+\,\frac{2T\left(\chi^*\right)}{m_\chi^2 T''\left(\chi^*\right)}\sin\left(\varphi_0\right).$$

The axon trajectory travelling parallel to the line of optimal stiffness is represented by the fixed point $(y,\varphi)=(0,0)$. Linearising about this fixed point we obtain

$$\dot{y} = \frac{2\sin\varphi_0 T\left(\chi^*\right)}{\sqrt{\eta\zeta}}\,\varphi, \tag{3.100a}$$
$$\dot{\varphi} = \beta\, y + L\beta\varphi, \tag{3.100b}$$

where

$$\beta = \frac{2R\sin\varphi_0 m_\chi^2 T''\left(\chi^*\right)T\left(\chi^*\right)}{\mathcal{B}\zeta}\left(\varphi_0-\frac{\sin\left(2\varphi_0\right)}{2}\right) < 0. \tag{3.101}$$

A further differentiation of (3.100b) gives

$$\ddot{\varphi} = -L|\beta|\dot{\varphi} - |\beta|\frac{2\sin\varphi_0 T\left(\chi^*\right)}{\sqrt{\eta\zeta}}\varphi. \tag{3.102}$$

All solutions to the above equation converge to $\varphi=0$ and consequently to $y=0$ - i.e. axons asymptotically travel parallel to lines of optimal stiffness. As can be seen, the finite spatial extent of the axon introduces a damping term that leads to convergence of the system to the fixed point $(y,\varphi)=(0,0)$. If we ignore the length of the axon, setting $L=0$, the damping term disappears, and the fixed point $(y,\varphi)=(0,0)$ is a center, so axons do not converge to travelling parallel to the line of optimal stiffness.

Therefore, we conclude, the ability of axons to converge to lines of optimal stiffness is contingent on the non-zero, finite, spatial extent of the axon. It follows that this long range sensing capacity may therefore be an important element of axon guidance.

3.6 Conclusion

In this chapter, we developed a framework for axon guidance which combines the mechanical properties of the axon and the growth cone force (determined by the environment).

In Section 3.2 we derived an expression for the growth cone force as a function of substrate stiffness. Then, we derived an approximation to this force which clarifies the role of the substrate stiffness gradient. Using this approximation, we found that the stiffness gradient induces a durotactic force component which, under differing conditions, causes the axon to steer toward or away from the stiffness gradient. In the special cases where the growth cone is a half-disk or full-disk, the durotactic force component is aligned with the stiffness gradient. Whilst in-vitro experiments of axons have only observed negative durotaxis (migration towards softer substrates), our analysis suggests that axons should be able to exhibit both types of durotaxis, positive and negative, depending on whether the local substrate stiffness is, respectively, less or greater than the optimal stiffness.

Having derived a remodelling beam model for the axon in Section 3.3 and describing an algorithm for numerical integration of this model in Section 3.3.4, we proceeded in Section 3.4 with the study of axon trajectories under a constant growth cone force, which could model a guidance cue of constant strength and direction. This analysis yielded a few important results: (i) that axons converge to traveling parallel to the GC force, revealing that the role of the growth cone is to prescribe the direction of growth; (ii) the particular shape of the turning rate as a function of the dimensionless GC force; (iii) that the sensitivity of the axon to guidance cues is non-monotonic as a function of the dimensionless GC force.

Finally, since this thesis is particularly focused on the durotaxis of axons, in Section 3.5 we studied the behavior of axons in the simplest possible stiffness field, that of constant stiffness gradient. We observed two general behaviors: First, as expected, axons away from lines of optimal stiffness generally align with the stiffness gradient in a direction leading towards the optimal stiffness, leading to positive or negative durotaxis depending on the initial stiffness. Second, surprisingly, we observe that axons close to lines of optimal stiffness converge to traveling parallel to them. This phenomenon suggests a new mode of axon guidance: guidance by lines of optimal stiffness. Furthermore, we find that this phenomenon is linked to the finite length of the deformable segment of the axon, suggesting that the long range sensing capability of the axon may play an important role in axon guidance.

The work in this chapter lays the foundations for a theory of axon guidance based on traction generation. Furthermore, we were able to study the basic features of this framework and uncover the general principles underlying axon durotaxis (according to this theory). In Chapter 5, we apply this theory to particular known instances of axon durotaxis which appear both in-vivo and in-vitro. First, we proceed with a study of the bending stiffness of axons.

Chapter 4

On the Estimation of Axonal Mechanical Properties Using Beam Models

4.1 Introduction

In Chapter 3, we derived a remodeling beam model for the axon. As with any model, its ability to make predictions depends on the values of its free parameters. Therefore, determining the values of these parameters is fundamental for any investigation of axon pathfinding. Our model integrates multiple mechanisms and scales relevant to axon pathfinding, each associated with distinct material parameters. The aim of this chapter is to estimate the elastic modulus, E, and bending stiffness, $\mathcal{B}$, associated with the rod-like mechanical response of the axon.

So far in the literature, there has been a particular focus on the investigation of E. Importantly, there exist numerous studies which infer E directly from data [9, 10, 31]. By contrast, only one study has inferred $\mathcal{B}$ directly from data [24]. This study used *Thermal Fluctuation Spectroscopy* (TFS), fitting the *Power Spectral Density* (PSD) of the displacement of a point on the neurite from its rest position, and obtained $\mathcal{B} \sim 10^{-19}\text{Nm}^2$.

Although the TFS estimate is the only direct inference of $\mathcal{B}$ from data, many other estimates appear in the literature. These are best described as prior estimates, since they obtain $\mathcal{B}$ from known geometric or mechanical properties of the axon rather than by fitting a mechanical model directly to data. For example, bending stiffness is often estimated from the isotropic-beam relation $\mathcal{B} = EI_{\text{axon}}$. Such methods are useful because they avoid the need for direct measurement, but they have led to large discrepancies in the quoted values of $\mathcal{B}$. Some studies report $\mathcal{B} \sim 10^{-22}\,\text{Nm}^2$ or smaller [40, 43], whereas others use values of order $\mathcal{B} \sim 10^{-19}\,\text{Nm}^2$ or larger [43, 25, 35], in closer agreement with the TFS measurement. Thus, despite the existence of a direct TFS estimate, the value of

$\mathcal{B}$ remains unsettled. In this chapter, we ask whether this disagreement reflects the data themselves, or instead the mechanical models used to interpret them.

In particular, we investigate whether neurite-pulling data, often taken to imply $\mathcal{B} \sim 10^{-22}\,\mathrm{Nm}^2$, are also compatible with $\mathcal{B} \sim 10^{-19}\,\mathrm{Nm}^2$ when interpreted using an extensible beam model.

4.1.1 Estimating $\mathcal{B}$ from axon-pulling experiments

A reliable value of $\mathcal{B}$ will require agreement between independent methods of inference. In this chapter we investigate how a frequently conducted experiment on axons can be used to measure $\mathcal{B}$.

The experiment in question is the so-called axon-pulling experiment, which is similar to the three-point bending test for beams. Neurites are grown and anchored between two points. The experimenter, using a micro-needle, pulls the axon or neurite perpendicularly at its midpoint to obtain a load-deflection curve for the midpoint (see Fig. 4.1). This curve describes the steady-state perpendicular deflection of the midpoint of the neurite from its rest position under the application of a constant force F. The parameters of a mechanical model for the axon can then be inferred by fitting the load-deflection curves.

One reason to investigate the three-point bending test for axons despite the existence of the TFS measurement is to provide an independent inference for $\mathcal{B}$. Another is that numerous datasets already exist for axons, which can be analysed using the analytical tools developed in this chapter. Another advantage of the three-point bending test over TFS is that it allows for simultaneous estimation of E and $\mathcal{B}$, whereas TFS only provides $\mathcal{B}$, as it assumes that the axon is inextensible. A further disadvantage of TFS arises from its dynamic nature. A consequence of measuring the axon or neurite under dynamic oscillations is that most mechanical parameters (including $\mathcal{B}$) cannot be extracted from the measurements without prior knowledge of the effective coefficient of viscosity between the neurite and the environment. Since the three-point bending test assumes static conditions, no such knowledge is required and $E, \mathcal{B}$ can be measured directly.

4.1.2 A mechanistic explanation for the discrepancy in estimates of $\mathcal{B}$

The discrepancy in the values reported for the axonal bending stiffness, $\mathcal{B}$, arises from two different estimation procedures. One approach estimates $\mathcal{B}$ from axonal microstructure, taking into account the composition and arrangement of microtubules and the surrounding membrane. This calculation, described in Appendix B of [43], gives $\mathcal{B} \sim 10^{-19}\,\mathrm{N\,m}^2$. A second approach assumes that the axon behaves as an isotropic beam, so that $\mathcal{B} = EI$.

Using typical experimental estimates $E \sim 10\,\mathrm{kPa}$, this gives $\mathcal{B} \sim 10^{-22}\,\mathrm{N\,m^2}$. Thus, the two estimates differ by approximately three orders of magnitude.

A plausible explanation is that the isotropic assumption is inappropriate for the axon. The microstructural estimate assumes that bending resistance is primarily determined by microtubules. By contrast, the isotropic estimate implicitly assumes that the structures responsible for axial extension are also responsible for bending. These assumptions are difficult to reconcile if different components within the axon dominate the two modes of deformation.

There is evidence that the experimentally inferred axial modulus of the axon is not primarily determined by microtubule stretch. A microstructural estimate based on the axonal cross-section gives $E \sim 12\,\mathrm{MPa}$, which is three orders of magnitude larger than typical experimental values (See [25] Equation (9) and Figure 5). Conversely, models in which axonal stretch is mediated by tau crosslinks between approximately rigid microtubules predict elastic moduli in the range 10-100 kPa [54]. Similarly, computational studies suggest that microtubule stretch becomes significant only at tensile stresses of order 1 MPa [58], far above the stresses expected in three-point bending experiments if $E \sim 10\,\mathrm{kPa}$.

This suggests a simple mechanistic resolution of the discrepancy: axial stretch may be resisted primarily by tau crosslinks, whereas bending may be resisted primarily by microtubules, provided that the microtubules bend coherently with the axon shaft. Under this interpretation, the axon is strongly anisotropic, and E and $\mathcal{B}$ should be treated as independent mechanical parameters rather than being related through the isotropic-beam identity $\mathcal{B} = EI$.

This mechanistic interpretation has direct consequences for the analysis of axon-pulling experiments. Existing load-deflection data are often interpreted using elastic-string models, which neglect bending stiffness by setting $\mathcal{B} = 0$ [9]. However, if axial extension and bending are governed by different components, then the appropriate model is an extensible beam in which E and $\mathcal{B}$ are treated as independent parameters.

4.1.3 Experimental data

In the experiment of [9], the authors performed pulling experiments on PC12 neurites. The ends of the neurite are anchored in place by focal adhesions. A force of constant magnitude F is applied perpendicularly to the neurite midpoint (see Fig. 4.1). The authors fit the resulting load-deflection curve using an elastic string model. Their analysis concluded that $E \sim 12 \pm 2\mathrm{kPa}$.

However, there is an error in the derivation of their string model. We describe this error in Section B.3. The error implies that the correct estimate based on their data should be $E \sim 6 \pm 1\text{kPa}$.

4.1.4 Prior work on Three Point Bending Tests

Three-point bending is a problem of beam mechanics that has been widely studied. There is no shortage of studies investigating variations of this problem or of a beam under a concentrated midpoint force. Notable variations include studying the snapping of a buckled beam under a midpoint force [14, 15], variation of the contact points [50], the bending response of different materials [59] under three-point bending, etc. Furthermore, numerous studies have looked at the large deflections of a beam under a midpoint force, which are directly relevant to our question.

In [5], the author investigates large deflections of an inextensible, uniformly isotropic beam under different boundary supports. The general solution is expressed in terms of elliptic functions, with constants determined numerically from algebraic equations encoding the boundary conditions. Since this does not yield a closed-form load-deflection curve, the author derives Taylor approximations for the midpoint force as a function of midpoint deflection and also considers the inverse problem of estimating mechanical parameters from experimental data. However, the analysis is restricted to inextensible beams and is therefore not directly applicable to the extensible beam model considered here.

Several papers have treated the equivalent problem for an extensible, shearable beam - a Reissner beam, for which the general solution can be derived [76, 7]. Relevantly, the load-deflection curves of such a beam under various boundary conditions is given in [6] numerically.

4.2 Overview

The remainder of this chapter is organised as follows. We first describe the axon-pulling experiment and the inference procedure used to estimate mechanical parameters from load-deflection data (Sections 4.3, 4.4). We then introduce the hierarchy of models considered: the elastic string model, the isotropic extensible beam model, and the anisotropic extensible beam model (Section 4.5). Next, we formulate the governing equations for an extensible beam under a midpoint force and derive the corresponding small-deflection load-deflection expansion under pinned and clamped boundary conditions (Section 4.6). Finally, we apply these formulae to the experimental data, beginning with the elastic

string and isotropic beam models before considering the anisotropic model with zero and non-zero initial strain (Sections 4.7, 4.9, 4.10, 4.12).

4.3 Description of the pulling experiment

In the pulling experiment, an axon or neurite fixed between two points is pulled perpendicularly at its midsection by a fixed force F, as shown in Fig. 4.1(A). The maximum deflection of the axon is observed in the midsection and is denoted by H. The length of the axon before displacement (span) is denoted by L_x.

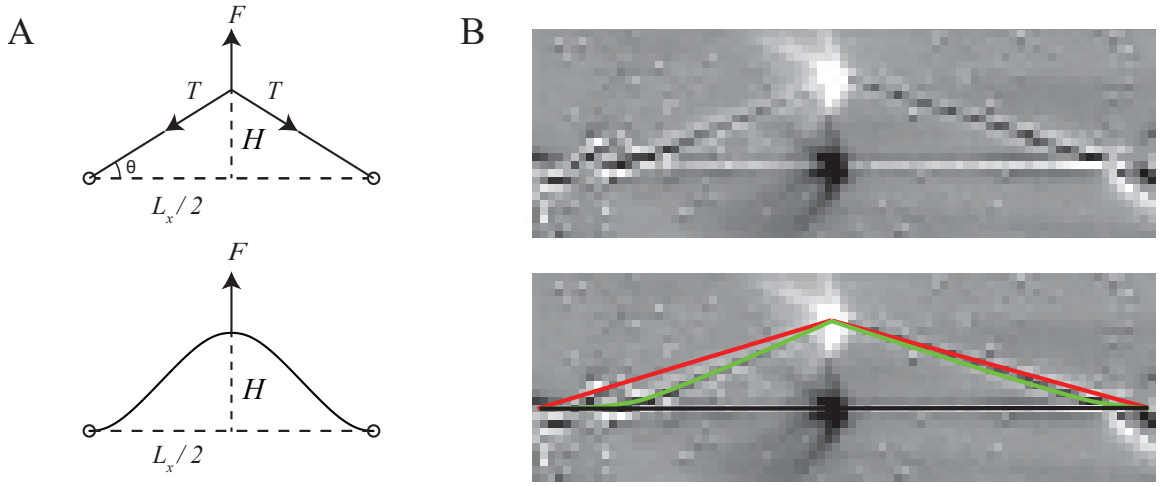


Figure 4.1: (A) Top: Axon deformation as described by the elastic string model for the pulling experiment. Bottom: Axon deformation as described by the elastic beam model (with non-zero bending stiffness) for the pulling experiment with clamped boundary conditions. (B) Top: Image of an axon undergoing mechanical stretching. The axon deforms from its initial configuration (white line) to a new deformed configuration (dark line). Bottom: Same image as *Top* with the centerline manually traced in post-processing (green). The observed centerline close to the boundaries deviates from a straight line indicating that the assumption of pinned boundary conditions may not be adequate for this experiment. Image taken from [9].

4.4 Inference procedure

In our analysis, we focus on three mechanical parameters. In addition to E and $\mathcal{B}$ we use the rest length L_0, which denotes the reference length of the beam ($L_0 \leq L_x$). A related parameter is the initial strain of the axon,

$$\varepsilon_0 = \frac{L_x - L_0}{L_0}, \tag{4.1}$$

which describes the axon axial strain before midpoint deflection.

To infer the mechanical parameters E, $\mathcal{B}, L_0$, we use a procedure similar to Bernal et al. [9]. For each model, we determine the derivatives $F'(0)$ and $F'''(0)$ of the theoretical load-deflection curve $F(H)$, where $F(H)$ denotes the force required to achieve a midpoint displacement H.

Once load-deflection data are obtained from the pulling experiment, a cubic polynomial is fitted to the data [9]. Since the quadratic term vanishes for each of the models investigated, we use a polynomial of the form

$$F(H) = a_1 H + a_3 H^3.$$

To obtain estimates for $E, \mathcal{B}$ and L_0, one then solves the algebraic system

$$\frac{\mathrm{d}F}{\mathrm{d}H}(0) = a_1, \qquad \frac{1}{6}\frac{\mathrm{d}^3F}{\mathrm{d}H^3}(0) = a_3, \tag{4.2}$$

for the three parameters. When the three parameters are treated as independent, this system is underdetermined. Additional modelling assumptions can remove one degree of freedom. We discuss this identifiability issue further in Section 4.5.

From the figures of Bernal et al. [9] we can obtain the load-deflection curves of three axons. These are:

$$F_1(H) = 5.05 \cdot 10^{-5}\frac{\mathrm{N}}{\mathrm{m}}H + 337559\frac{\mathrm{N}}{\mathrm{m}^3}H^3, \tag{4.3}$$

$$F_2(H) = 43214\frac{\mathrm{N}}{\mathrm{m}^3}H^3, \tag{4.4}$$

$$F_3(H) = 5.57 \cdot 10^{-6}\frac{\mathrm{N}}{\mathrm{m}}H + 34517\frac{\mathrm{N}}{\mathrm{m}^3}H^3. \tag{4.5}$$

See Section B.1 for a description of the procedure used to extract these estimates. We ignore the load-deflection curve (4.4), as we argue in Section B.1 that the estimate $a_1 = 0$ is unphysical.

4.5 Discussion of the different models

Here we discuss different models used to investigate the load-deflection data from the neurite pulling experiments.

Elastic String model

The elastic-string model is the standard model used to interpret neurite load-deflection data, and is therefore the natural baseline against which the beam models should be compared. In this model, the neurite is idealized as a perfectly flexible extensible filament: bending rigidity is neglected, so the transverse resistance to midpoint deflection arises entirely from axial tension.

Extensible Beam: Isotropic model

In the *Introduction* (Section 4.1), we argued that the axon is not an isotropic rod and, therefore, its bending and extensional stiffnesses are independent. However, it is informative to investigate the inference on $(E, \mathcal{B})$ which follows from the assumption of isotropy and to compare it with the inference derived from the elastic string model and the anisotropic beam model. A question of particular interest is whether the isotropic rod model infers a value for E that is similar to the value inferred by the elastic string model, as the latter is usually used as a substitute for the former.

As we shall see, a particular difficulty arises with the anisotropic model. In the case of the anisotropic model there are three unknowns, $(E, \mathcal{B}, L_0)$, but there are only two equations in the algebraic system (4.2) to determine their values. Therefore, the algebraic system for the parameters $(E, \mathcal{B}, L_0)$ is under-determined. Consequently, the set of parameters $(E, \mathcal{B}, L_0)$ that solve this algebraic system may be infinite. This fact creates an issue of non-identifiability for the three parameters. It is therefore a nontrivial matter to extract useful information about the true value of $(E, \mathcal{B}, L_0)$ from this set.

The assumption that the rod is isotropic eliminates one of the three free parameters, the bending stiffness, by relating it to the elastic modulus by $\mathcal{B} = EI$. The constant I is the second moment of area of the cross-section of the rod. For a circular cross-section, the second moment of area can be expressed in terms of the cross-sectional area; $I = A^2/(4\pi)$. It follows that the algebraic system for the isotropic rod for (E, L_0) is determined, and consequently the set of solutions to the system is finite. Therefore, the isotropic assumption is a convenient starting point for our analysis.

Extensible Beam: Anisotropic with Zero Initial Strain (ZS)

In the case of the anisotropic beam, a natural starting point to remove a parameter is the case of zero initial strain, $\varepsilon_0 = 0$. This assumption is reasonable when initial strains are expected to be small, and it also provides a useful limiting case against which the elastic-string model can be compared. The elastic string corresponds to the case $\mathcal{B} = 0$ with $\varepsilon_0 \geq 0$, so any resistance to transverse deflection is attributed entirely to axial stretching and pre-strain. In contrast, the zero-strain anisotropic beam assumes $\mathcal{B} \neq 0$ and $\varepsilon_0 = 0$, so the fitted response is attributed more strongly to bending stiffness. Thus, while the elastic-string model underestimates $\mathcal{B}$ by construction, the zero-strain anisotropic beam provides a complementary estimate in which $\mathcal{B}$ is expected to be overestimated and ε_0 underestimated by assumption.

For this reason, the zero-initial-strain case is not only a convenient starting point, but also provides an upper-bound estimate for the bending stiffness $\mathcal{B}$ of a given neurite, once the fitted coefficients a_1 and a_3 are specified.

Extensible Beam: Anisotropic model

The full anisotropic extensible beam is the most general beam model considered in this chapter. The previous beam models can be interpreted as special or restricted cases of the anisotropic formulation.

Despite missing an equation to fit $(E, \mathcal{B}, L_0)$, the anisotropic model can still be used to characterize the range of mechanical parameters compatible with the data. Rather than seeking a single inferred value of E, $\mathcal{B}$ and L_0, we fix one parameter and determine the corresponding values of the remaining two. In practice, it is most convenient to parametrize the solution set by the initial strain ε_0. For each prescribed value of ε_0, the system in (4.2) can be solved for the corresponding values of E and $\mathcal{B}$.

This parametrization allows us to examine how the inferred extensional and bending stiffnesses depend on the assumed initial strain. In this way, the anisotropic model produces a family of admissible parameter triples $(E, \mathcal{B}, \varepsilon_0)$ consistent with the observed load-deflection coefficients.

4.6 Extensible beam model for the axon

Here we develop the extensible beam model for the axon, which we use to infer E, $\mathcal{B}$ and ε_0 from load-deflection data. We assume that the axon is an elastic, extensible planar beam with elastic modulus E, bending stiffness $\mathcal{B}$, cross-sectional area A, rest length L_0 (where $L_0 \leq L_x$) and initial strain ε_0. The governing equations for the steady state of such a beam are

$$\frac{\partial x}{\partial S_0} = \alpha \cos\theta, \qquad \frac{\partial y}{\partial S_0} = \alpha \sin\theta, \tag{4.6}$$

$$\frac{\partial \theta}{\partial S_0} = \alpha\kappa, \qquad \alpha = \frac{\partial s}{\partial S_0}, \tag{4.7}$$

$$\frac{\partial n_x}{\partial S_0} + \alpha b_x = 0, \qquad \frac{\partial n_y}{\partial S_0} + \alpha b_y = 0, \tag{4.8}$$

$$\frac{\partial m}{\partial S_0} + \alpha\left(n_y \cos\theta - n_x \sin\theta\right) = 0. \tag{4.9}$$

Here S_0 denotes the arclength in the reference configuration, while s denotes the arclength in the current configuration. The variables $x(S_0)$ and $y(S_0)$ describe the centreline of the beam, $\theta(S_0)$ is the angle made by the tangent with the horizontal axis, κ is the curvature of the beam in the current configuration, and α is the stretch. The quantities n_x and n_y are the Cartesian components of the resultant force, m is the resultant bending moment, and (b_x, b_y) is the density of body force per unit current length.

We assume that the moment is proportional to angular strain and that the axial force is linearly related to the axial strain $\alpha - 1$, giving

$$m = \mathcal{B}\frac{\partial\theta}{\partial S_0}, \tag{4.10}$$

$$n = n_x \cos\theta + n_y \sin\theta = EA\,(\alpha - 1)\,, \tag{4.11}$$

where n is the tangential component of the internal force, i.e. the axial force in the beam. Thus, $\alpha = 1$ corresponds to an unstretched beam, while $\alpha > 1$ and $\alpha < 1$ correspond to extension and compression, respectively.

Using (4.10), we can rewrite the moment-balance equation as

$$\mathcal{B}\frac{\partial^2\theta}{\partial {S_0}^2} + \alpha\,(n_y \cos\theta - n_x \sin\theta) = 0. \tag{4.12}$$

4.6.1 Body forces

We model the external force exerted on the axon by the needle in the pulling experiment as a vertical force of constant magnitude applied at the material midpoint $S_0 = L_0/2$,

$$b_x = 0,\ \ \alpha b_y = F\delta\,(S_0 - L_0/2)\,. \tag{4.13}$$

Under this body force, (4.8) can be integrated to give that $n_x = N_X$, a constant to be determined and

$$n_y = N_Y - F\mathrm{H}\,(S_0 - L_0/2)\,, \tag{4.14}$$

where N_Y is an unknown constant and $\mathrm{H}\,(\,\cdot\,)$ is the Heaviside function.

4.6.2 Boundary conditions

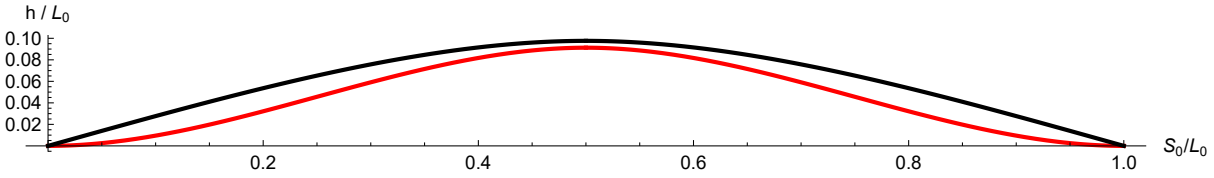


Figure 4.2: Example solutions of the extensible beam equation for pinned boundary conditions (black) and clamped boundary conditions (red). $B = 2.5 \cdot 10^{-19}\mathrm{Nm}^2$, $E = 1500\mathrm{Pa}$, $A = \pi\,(0.75)^2\,(\mu\mathrm{m})^2$, $L_0 = 100\mu\mathrm{m}$, $L_x = 1.025 \cdot L_0$. A different F was used in each case.

We assume that the ends of the axon are held fixed along the horizontal line $y = 0$ a distance L_x apart. Thus,

$$y(0) = 0 = y(L_0). \tag{4.15}$$

and

$$x(L_0) - x(0) = L_x. \tag{4.16}$$

In most experiments, it is assumed that the axon is pinned. This means that the ends of the axon are free to rotate. As a result, in equilibrium there is zero bending moment at the ends and hence $\theta' = 0$ at the boundaries. Solutions of the system of equations under these boundary conditions (see Fig. 4.2) only develop curvature close to the point of force application. It is evident from images of such experiments that the axon in these experiments is not in fact straight for most of its length and that curvature does also develop close to the boundaries (see Fig. 4.1(B)). This is reminiscent of the effect of clamped boundary conditions (see Fig. 4.2, red). Thus we assume that there is a mechanism at the boundaries that resists the turning of the axon shaft. A simple way to model this mechanism is to assume torsional springs are attached to the ends creating a restoring moment which tends to return the shaft to the horizontal position at the ends. The strength of this restorative moment is described by the torsional spring constant κ_τ, which leads to

$$\mathcal{B}\,\theta'(0) = \kappa_\tau \theta(0), \qquad \mathcal{B}\,\theta'(L_0) = -\kappa_\tau \theta(L_0). \tag{4.17}$$

Note that the case $\kappa_\tau = 0$ corresponds to the pinned case and $\kappa_\tau = +\infty$ corresponds to the clamped case.

4.6.3 General Boundary Value Problem

The angle, θ, that the tangent of the axon makes with the positive x-axis in the pulling experiment satisfies the BVP

$$\mathcal{B}\frac{\partial^2 \theta}{\partial {S_0}^2} + \alpha\left(n_y \cos\theta - n_x \sin\theta\right) = 0, \tag{4.18}$$

$$\mathcal{B}\,\theta'(0) = \kappa_\tau \theta(0), \tag{4.19}$$

$$\mathcal{B}\,\theta'(L_0) = -\kappa_\tau \theta(L_0), \tag{4.20}$$

$$x(L_0) - x(0) = \int_0^{L_0} \alpha\, \cos\theta \, \mathrm{d}S_0 = L_x, \tag{4.21}$$

$$y(L_0) - y(0) = \int_0^{L_0} \alpha\, \sin\theta \, \mathrm{d}S_0 = 0, \tag{4.22}$$

$$n_x = N_X, \tag{4.23}$$

$$n_y = N_Y - F\mathrm{H}(S_0 - L_0/2), \tag{4.24}$$

where the constants N_X, N_Y are to be determined. Having solved the above BVP, the profile of the axon can be obtained by integrating (4.6).

4.6.4 Symmetric ansatz for the extensible beam equation

We can exploit a symmetry of (4.12) to further simplify the problem. For $N_Y = F/2$ we have the following fact: Given a function $\theta_1(S_0)$ which solves (4.12) on the interval $(0, L_0/2)$ and also satisfies (4.17) then the function

$$\theta = \begin{cases} \theta_1(S_0) & \text{if } S_0 \in (0, L_0/2) \\ -\theta_1(L_0 - S_0) & \text{if } S_0 \in (L_0/2, L_0) \end{cases} \tag{4.25}$$

solves the BVP (4.18). From (4.25) it follows that

$$\theta_1(L_0/2) = 0. \tag{4.26}$$

Thus, we focus on the following BVP for θ_1:

$$\begin{aligned} &\mathcal{B}\frac{\partial^2 \theta_1}{\partial {S_0}^2} + \left[1 + \frac{N_X \cos\theta_1 + \frac{F}{2}\sin\theta_1}{EA}\right]\left(\frac{F}{2}\cos\theta_1 - N_X \sin\theta_1\right) = 0, \\ &\mathcal{B}\,\theta_1'(0) = \kappa_\tau \theta_1(0), \\ &\theta_1(L_0/2) = 0, \\ &\int_0^{L_0/2} \left[1 + \frac{N_X \cos\theta_1 + \frac{F}{2}\sin\theta_1}{EA}\right] \cos\theta_1 \,\mathrm{d}S_0 = \frac{L_x}{2}. \end{aligned} \tag{4.27}$$

The constant N_X is determined by solving the above integral condition.

4.6.5 Midpoint displacement as a function of force

To calibrate the beam model to the pulling experiment we look at the force-displacement curve $F(H)$. The particular form of the BVP (4.27) means that we must start our analysis by looking at the inverse of $F(H)$, which is $H(F)$. The function $H(F)$ can be directly defined from the state variables of the beam by

$$H(F) = y(L_0/2; F), \tag{4.28}$$

where F is considered a parameter of the model. The midpoint displacement $y(L_0/2)$ can be directly computed using the function θ_1 with the expression

$$y(L_0/2) = \int_0^{L_0/2} \alpha \sin\left(\theta_1(S_0)\right) \mathrm{d}S_0, \tag{4.29}$$

and more explicitly by

$$y(L_0/2) = \int_0^{L_0/2} \left(1 + \frac{N_X \cos\left(\theta_1(S_0)\right) + (F/2)\sin\left(\theta_1(S_0)\right)}{EA}\right) \sin\left(\theta_1(S_0)\right) \mathrm{d}S_0. \tag{4.30}$$

Treating the above expression as a function of F, we have

$$H(F) = \int_0^{L_0/2} \left(1 + \frac{N_X(F)\cos(\theta_1(S_0;F)) + (F/2)\sin(\theta_1(S_0;F))}{EA}\right) \sin(\theta_1(S_0;F))\mathrm{d}S_0, \tag{4.31}$$

where $N_X(F)$ is now treated as a function of F. This is a continuous function of F. Further, the greater the force applied the greater the displacement, meaning that $H(F)$ is a strictly increasing function of F. By the Inverse Function Theorem, there exists a function $F(H)$ such that $F(H(F)) = F$.

The function $F(H)$ is not directly computable from the BVP. However, since the solution at $F = 0$ is known and satisfies $H(0) = 0$, we can develop a perturbation series for small values of F. This will enable us to obtain the derivatives of $H(F)$ at $F = 0$ and subsequently the derivatives of $F(H)$ at $H = 0$ (since $H = 0$ when $F = 0$).

4.6.6 Non-dimensionalization of the beam system

To develop a perturbation series for θ_1 for small F we first non-dimensionalize our system. We choose the characteristic length scale to be $\lambda := \sqrt{\mathcal{B}/(EA)}$ and the characteristic force scale to be EA. With these choices our BVP transforms to

$$\frac{\partial^2\Theta_1}{\partial\sigma^2} + \left(1 + n_x\cos\Theta_1 + \frac{f}{2}\sin\Theta_1\right)\left(\frac{f}{2}\cos\Theta_1 - n_x\sin\Theta_1\right) = 0. \tag{4.32}$$

with conditions

$$\int_0^{L_0/(2\lambda)} \left(1 + n_x\cos\Theta_1 + \frac{f}{2}\sin\Theta_1\right)\cos\Theta_1\,\mathrm{d}\sigma = \frac{L_x}{2\lambda}, \tag{4.33}$$

$$\frac{\partial\Theta_1}{\partial\sigma}(0) - \tilde{\kappa}\,\Theta_1(0) = 0, \tag{4.34}$$

$$\Theta_1(L_0/(2\lambda)) = 0, \tag{4.35}$$

where

$$\begin{aligned}
&\Theta_1(\sigma) = \theta_1(S_0),\\
&n_x(f) = N_X(F)/EA,\\
&\sigma = S_0/\lambda,\\
&f = F/EA,\\
&\tilde{\kappa} = \kappa_\tau/\sqrt{\mathcal{B}EA}.
\end{aligned}$$

4.6.7 Series expansion of the beam state variables in f

To obtain the series expansion for $H(F)$, we develop the perturbation series for Θ_1 and n_x in f. Expanding in f around $f = 0$ we obtain

$$\Theta_1(\sigma) = \tilde{\theta}_0(\sigma) + \sum_{i=1}^{\infty} f^i \tilde{\theta}_i(\sigma), \tag{4.36a}$$

$$n_x(f) = n_0 + \sum_{i=1}^{\infty} f^i n_i. \tag{4.36b}$$

The terms $\tilde{\theta}_0(\sigma)$ and n_0 correspond to the solution of the BVP for $f = 0$, which is given by

$$\tilde{\theta}_0(\sigma) = 0, n_0 = (L_x - L_0)/L_0. \tag{4.37}$$

Inputting series (4.36) into the BVP and collecting terms at each order (See Section B.4), we solve for $(\tilde{\theta}_i, n_i)$.

Series (4.36) can be used to compute the series for $h(f) = H(F)/\lambda$:

$$h(f) = \int_0^{L_0/(2\lambda)} \left(1 + n_x \cos\Theta_1 + \frac{f}{2}\sin\Theta_1\right) \sin\Theta_1 \, \mathrm{d}\sigma. \tag{4.38}$$

The series expansion of the integrand up to third order in f is

$$\begin{aligned} I(\sigma, f) = f\,&\frac{L_x}{L_0}\tilde{\theta}_1(\sigma) + \\ &\frac{1}{2}f^2\left(2\,\tilde{\theta}_3(\sigma) + 2\,\frac{L_x - L_0}{L_0}\tilde{\theta}_3(\sigma) + 2\,\tilde{\theta}_1(\sigma)\,n_x'(0)\right) + \\ &\frac{1}{6}f^3\left(3\,\tilde{\theta}_1(\sigma)^2 - \tilde{\theta}_1(\sigma)^3 - 4\,\frac{L_x - L_0}{L_0}\tilde{\theta}_1(\sigma)^3\right. \\ &\left. + 6\tilde{\theta}_3(\sigma) + 6\,\frac{L_x - L_0}{L_0}\tilde{\theta}_3(\sigma) + 6\tilde{\theta}_3(\sigma)\,n_x'(0) + 3\tilde{\theta}_1(\sigma)\,n_x''(0)\right) + \ldots, \end{aligned}$$

The derivatives of the inverse of $h(f)$, $f(h)$, can be obtained by repeated differentiation of

$$f'(\eta) = \frac{1}{h'(f(\eta))}. \tag{4.39}$$

For the rest of the chapter we revert to using dimensional variables F, H as this makes a direct comparison to the elastic string model easier.

4.6.8 Series expansion coefficients for $F(H)$: Pinned

Here we state the expansion coefficients for $F(H)$ under the assumption that the beam is pinned. We give the coefficients for $L_0 = L_x$:

$$\frac{\mathrm{d}F}{\mathrm{d}H}(0) = \frac{48\mathcal{B}}{L_x^3}, \tag{4.40}$$

$$\frac{1}{6}\frac{\mathrm{d}^3F}{\mathrm{d}H^3}(0) = -\frac{288\,(560\mathcal{B}^2 + 160\mathcal{B}EA\,L_x^2 - 7(EA)^2L_x^4)}{175EAL_x^7}. \tag{4.41}$$

4.6.9 Series expansion coefficients for $F(H)$: Clamped

Here we state the expansion coefficients for $F(H)$ under the assumption that the beam is clamped. Like in the pinned case, we give the case $L_0 = L_x$:

$$\frac{\mathrm{d}F}{\mathrm{d}H}(0) = \frac{192\mathcal{B}}{L_x^3}, \tag{4.42}$$

$$\frac{1}{6}\frac{\mathrm{d}^3F}{\mathrm{d}H^3}(0) = -\frac{288\,(8960\mathcal{B}^2 + 640\mathcal{B}EA\,L_x^2 - 7(EA)^2L_x^4)}{175EAL_x^7}. \tag{4.43}$$

4.7 Elastic String Model

We assume that the string is fixed at two endpoints separated by a horizontal distance L_x, and that the applied force produces a symmetric midpoint displacement H. Since the elastic string has no bending stiffness, the deformed configuration consists of two straight segments meeting at the midpoint.

For a midpoint displacement of H, the total length of the deformed string is

$$\sqrt{4H^2 + L_x^2}.$$

Thus, the internal tension in the elastic string is

$$T = \kappa\left(\sqrt{4H^2 + L_x^2} - L_0\right), \tag{4.44}$$

where L_0 is the rest length of the string and κ is its axial spring constant. This constant is related to the elastic modulus E and cross-sectional area A of the string by

$$\kappa = \frac{EA}{L_0}.$$

For a steady configuration of the elastic string, the vertical load force applied at the midpoint, F, is balanced by the vertical components of the internal tension in the two straight segments (see Fig. 4.1(A), Top). Thus,

$$F = 2T\sin\theta, \tag{4.45}$$

where θ is the angle between either deformed segment of the string and the horizontal axis. Since each segment has vertical projection H,

$$\sin\theta = \frac{H}{\sqrt{H^2 + \frac{L_x^2}{4}}}. \tag{4.46}$$

It follows that

$$F = 2\kappa \left(L_x - \frac{L_0}{\sqrt{\left(\frac{2H}{L_x}\right)^2 + 1}} \right) \left(\frac{2H}{L_x}\right). \tag{4.47}$$

For small displacements, $H \ll L_x/2$, we expand the right-hand side to obtain

$$\begin{aligned} F &= 2T_0 \left(\frac{2H}{L_x}\right) + EA \left(\frac{2H}{L_x}\right)^3 + \mathcal{O}\left(\left(\frac{2H}{L_x}\right)^4\right) \\ &= \frac{4T_0}{L_x} H + \frac{8EA}{L_x^3} H^3 + \mathcal{O}\left(\left(\frac{2H}{L_x}\right)^4\right), \end{aligned} \tag{4.48}$$

where

$$T_0 = \kappa(L_x - L_0)$$

is the initial tension of the string before any midpoint displacement. Thus, in the elastic-string model, the linear coefficient a_1 is determined by the initial tension, while the cubic coefficient a_3 is determined by the axial stiffness EA and is independent of the initial tension.

Given the fitted coefficients a_1 and a_3, the coefficient-matching system 4.2 becomes

$$\begin{aligned} a_1 &= \frac{4EA\,(L_x - L_0)}{L_x L_0}, \\ a_3 &= \frac{8EA}{L_x^3}. \end{aligned}$$

This system can be solved exactly to give

$$E_{\text{string}} = \frac{L_x^3}{8A} a_3, \tag{4.49a}$$

$$L_0 = \frac{L_x^3}{L_x^2 + 2(a_1/a_3)}, \tag{4.49b}$$

$$\varepsilon_{\text{string}} = \varepsilon_0 = \frac{2a_1}{L_x^2 a_3}. \tag{4.49c}$$

4.8 Inferences: Elastic String

We obtain the inferred values for E and ε_0 according to the elastic string model by inputting the coefficients obtained from the fits (4.3) and (4.5) into (4.49):

$$(E_1, \varepsilon_0^1) = (5312.35\,\text{Pa},\ 4.40\%)\,, (E_3,\ \varepsilon_0^3) = (3937.85\,\text{Pa},\ 2.07\%), \tag{4.50}$$

$$(T_0)_1 = 1.04\text{nN},\ (T_0)_3 = 0.174\text{nN}. \tag{4.51}$$

4.9 Inferences: Isotropic Beam

4.9.1 Pinned case

For the pinned isotropic beam, solving the system (4.2) we obtain E and ε_0 for each neurite. No exact solution can be derived for E, ε_0, so we solved the system numerically. Due to the possible data corruption outlined previously, we refrain from conducting the analysis on Axon 2. For axons $1, 3$ we estimate:

$$(E_1, \varepsilon_0^1) = (4605.42\,\text{Pa},\ 4.62\%)\,, (E_3,\ \varepsilon_0^3) = (3687.48\,\text{Pa},\ 2.09\%), \tag{4.52}$$

$$\mathcal{B}_1 = 7.29 \cdot 10^{-21}\text{Nm}^2,\ \mathcal{B}_3 = 1.34 \cdot 10^{-21}\text{Nm}^2, \tag{4.53}$$

$$(T_0)_1 = 0.95\text{nN},\ (T_0)_3 = 0.17\text{nN}. \tag{4.54}$$

The first thing to note is that the value inferred for ε_0 by this model is approximately equal to the value inferred by the elastic string model. However, the elastic modulus is smaller in each case, and consequently so is the initial tension, though these differences are quite small. Given that the elastic moduli differ by a small amount from those inferred by the elastic string model, it follows that the inferred value for $\mathcal{B}$ will similarly differ by only a small amount to the approximation $\mathcal{B} = E_{\text{string}} I$. For these two axons we obtain $\mathcal{B} \sim 10^{-21}\text{Nm}^2$.

The above results indicate that, for these neurites, the elastic string model can accurately infer the mechanical parameters of a pinned isotropic beam, with the caveat that it will overestimate the initial tension T_0 and the elastic modulus E. There is a clear physical explanation for the overestimate of T_0 by the string model. In an isotropic beam, both T_0 and $\mathcal{B}$ contribute to the initial resistance to deformation, whose magnitude is described by the constant a_1. Since for the elastic string $\mathcal{B} = 0$, all of the initial resistance must be accounted for by T_0. Thus any resistance arising from $\mathcal{B}$ is necessarily misclassified as additional initial tension by the string model. It is not so clear why E is also overestimated.

4.9.2 Clamped case

Using the clamped boundary conditions, we estimate:

$$(E_1, \varepsilon_0^1) = (4330.84\,\text{Pa},\ 4.54\%)\,,\ (E_3,\ \varepsilon_0^3) = (3529.85\,\text{Pa},\ 2.08\%), \tag{4.55}$$

$$\mathcal{B}_1 = 6.86 \times 10^{-21}\text{Nm}^2,\ \mathcal{B}_3 = 1.29 \times 10^{-21}\text{Nm}^2, \tag{4.56}$$

$$(T_0)_1 = 0.88\text{nN},\ (T_0)_3 = 0.16\text{nN}. \tag{4.57}$$

The inferences are largely similar to those obtained using the pinned boundary conditions, with the difference that under the pinned boundary conditions one estimates a higher elastic modulus and initial strain.

4.10 Anisotropic Beam - Zero Initial Strain (ZS)

Here we look at the inferences for $(E, \mathcal{B})$ according to the anisotropic model under the assumption that there is zero initial strain ($L_0 = L_x$). Owing to the simplicity of the coefficients under this assumption, we can directly compute E and $\mathcal{B}$ as functions of the coefficients a_1 and a_3. We call these functions the *inference functions* for E and $\mathcal{B}$

4.10.1 Pinned case

With the coefficients of the load-deflection curve for pinned boundary conditions when $L_0 = L_x$, system (4.2) can be solved exactly:

$$\mathcal{B} = \frac{L_x^3 a_1}{48}, \tag{4.58}$$

$$E \in \{E_-, E_+\}\,, \tag{4.59}$$

$$E_- = \frac{960 L_x a_1 + 175\, L_x^3 a_3 - \sqrt{564480 L_x^2 a_1^2 + 25\,(192\, L_x a_1 + 35\, L_x^3 a_3)^2}}{4032 A}, \tag{4.60}$$

$$E_+ = \frac{960 L_x a_1 + 175\, L_x^3 a_3 + \sqrt{564480 L_x^2 a_1^2 + 25\,(192\, L_x a_1 + 35\, L_x^3 a_3)^2}}{4032 A}. \tag{4.61}$$

The surprising thing here is that although $\mathcal{B}$ is uniquely determined, there exist two possible values of E that fit the data. The set of possible values for E for each neurite are:

$$\hat{E}_1 \in \{-7.32, 4141.28\}\text{Pa}, \hat{E}_3 \in \{-1.27, 2890.82\}\text{Pa}, \tag{4.62}$$

$$\mathcal{B}^1_{\text{pinned}} = 5.91 \times 10^{-19}\text{Nm}^2, \mathcal{B}^3_{\text{pinned}} = 2.27 \times 10^{-19}\text{Nm}^2, \tag{4.63}$$

In each case, only one of the two possible values of E is positive and therefore physical.

While the admissible estimates for E are still quite close to the estimates of the isotropic model, the inferred bending stiffnesses are several orders of magnitude larger. Surprisingly, this model estimates that $\mathcal{B}$ is on the order of 10^{-19}Nm^2, which is of the same order as the estimate provided by the microstructure method mentioned in the *Introduction*. The fact that this model can both estimate E close to the estimates of the previous models and also estimate $\mathcal{B}$ close to our a-priori expectations, provides support for the hypothesis that extensional resistance is primarily due to adhesive proteins linking the microtubules of the neurite and bending resistance is primarily due to the microtubules of the neurite.

4.10.2 Clamped case

With the coefficients of the load-deflection curve for clamped boundary conditions when $L_0 = L_x$, system (4.2) can be solved exactly:

$$\mathcal{B} = \frac{L_x^3 a_1}{192}, \tag{4.64}$$

$$E \in \{E_-, E_+\}, \tag{4.65}$$

$$E_- = \frac{960 L_x a_1 + 175\, L_x^3 a_3 - \sqrt{564480 L_x^2 a_1^2 + 25\left(192\, L_x a_1 + 35\, L_x^3 a_3\right)^2}}{4032 A}, \tag{4.66}$$

$$E_+ = \frac{960 L_x a_1 + 175\, L_x^3 a_3 + \sqrt{564480 L_x^2 a_1^2 + 25\left(192\, L_x a_1 + 35\, L_x^3 a_3\right)^2}}{4032 A}. \tag{4.67}$$

There are two things to note here. The inferred value of the bending stiffness under the clamped boundary conditions is four times smaller than under the pinned boundary conditions. Surprisingly, the elastic modulus inference is identical under both clamped and pinned boundary conditions. Thus, the inferred values of the parameters under the clamped boundary conditions are:

$$\hat{E}_1 \in \{-7.32, 4141.28\}\text{Pa}, \hat{E}_3 \in \{-1.27, 2890.82\}\text{Pa}, \tag{4.68}$$

$$\mathcal{B}^1_{\text{clamped}} = 1.48 \times 10^{-19}\text{Nm}^2, \mathcal{B}^3_{\text{clamped}} = 0.57 \times 10^{-19}\text{Nm}^2, \tag{4.69}$$

Thus, under the clamped boundary conditions, for these neurites, we have $\mathcal{B} \sim 10^{-19}\text{Nm}^2$, and E close to the values inferred by the elastic string model.

4.11 Summary of determined models

Before moving on to our analysis of the non-zero initial strain anisotropic model, we summarize here the results of the models so far: The elastic string model inferred the largest elastic modulus of all models. The isotropic models inferred a similar, but smaller

elastic modulus than the elastic string model. The zero initial strain anisotropic models inferred the smallest elastic modulus (see Table 4.1). Similarly, the elastic string model inferred the largest initial strain and tension. The isotropic models inferred similar but smaller initial strain and tension. By assumption, the zero initial strain anisotropic models inferred the smallest (zero) initial strain and tension (see Tables 4.3, 4.4). In contrast, the zero initial strain anisotropic models inferred the largest bending stiffness. The isotropic models inferred a bending stiffness around two orders of magnitude smaller. The elastic string model inferred (by assumption) $\mathcal{B} = 0$ (see Table 4.2).

E/**Pa according to each model**	Neurite 1	Neurite 3
Elastic String Model	5312.35	3937.85
Isotropic - Pinned	4605.42	3687.48
Isotropic - Clamped	4330.84	3529.85
Anisotropic (ZS) - Pinned	4141.28	2890.82
Anisotropic (ZS) - Clamped	4141.28	2890.82

Table 4.1: Estimated value of E according to each model for Neurite 1 and Neurite 3.

$\mathcal{B}/\mathrm{Nm}^2$ **according to each model**	Neurite 1	Neurite 3
Elastic String Model	0	0
Isotropic - Pinned	$7.29 \cdot 10^{-21}$	$1.34 \cdot 10^{-21}$
Isotropic - Clamped	$6.86 \cdot 10^{-21}$	$1.29 \cdot 10^{-21}$
Anisotropic (ZS) - Pinned	$5.91 \cdot 10^{-19}$	$2.27 \cdot 10^{-19}$
Anisotropic (ZS) - Clamped	$1.48 \cdot 10^{-19}$	$0.57 \cdot 10^{-19}$

Table 4.2: Estimated value of $\mathcal{B}$ according to each model for Neurite 1 and Neurite 3.

$\varepsilon_0/\%$ **according to each model**	Neurite 1	Neurite 3
Elastic String Model	4.40	2.07
Isotropic - Pinned	4.62	2.09
Isotropic - Clamped	4.54	2.08
Anisotropic (ZS) - Pinned	0	0
Anisotropic (ZS) - Clamped	0	0

Table 4.3: Estimated value of ε_0 according to each model for Neurite 1 and Neurite 3.

4.12 Anisotropic Beam with Non-Zero Initial Strain

In the anisotropic model, imposing $\varepsilon_0 = 0$ allowed us to solve system (4.2) for E and $\mathcal{B}$. Under this assumption, the inferred value of $\mathcal{B}$ also provides an upper bound on the bending stiffness of each axon within the anisotropic beam model. However, axons are

T_0/nN **according to each model**	Neurite 1	Neurite 3
Elastic String Model	1.04	0.174
Isotropic - Pinned	0.95	0.17
Isotropic - Clamped	0.88	0.16
Anisotropic (ZS) - Pinned	0.0	0.0
Anisotropic (ZS) - Clamped	0.0	0.0

Table 4.4: Estimated value of T_0 according to each model for Neurite 1 and Neurite 3.

expected to be under tension, and hence to have $\varepsilon_0 > 0$. It is therefore important to allow for non-zero initial strain in the inference procedure.

When $\varepsilon_0 \neq 0$, system (4.2) can no longer be solved exactly. We therefore fix $\varepsilon_0 > 0$ and solve (4.2) numerically for E and $\mathcal{B}$.

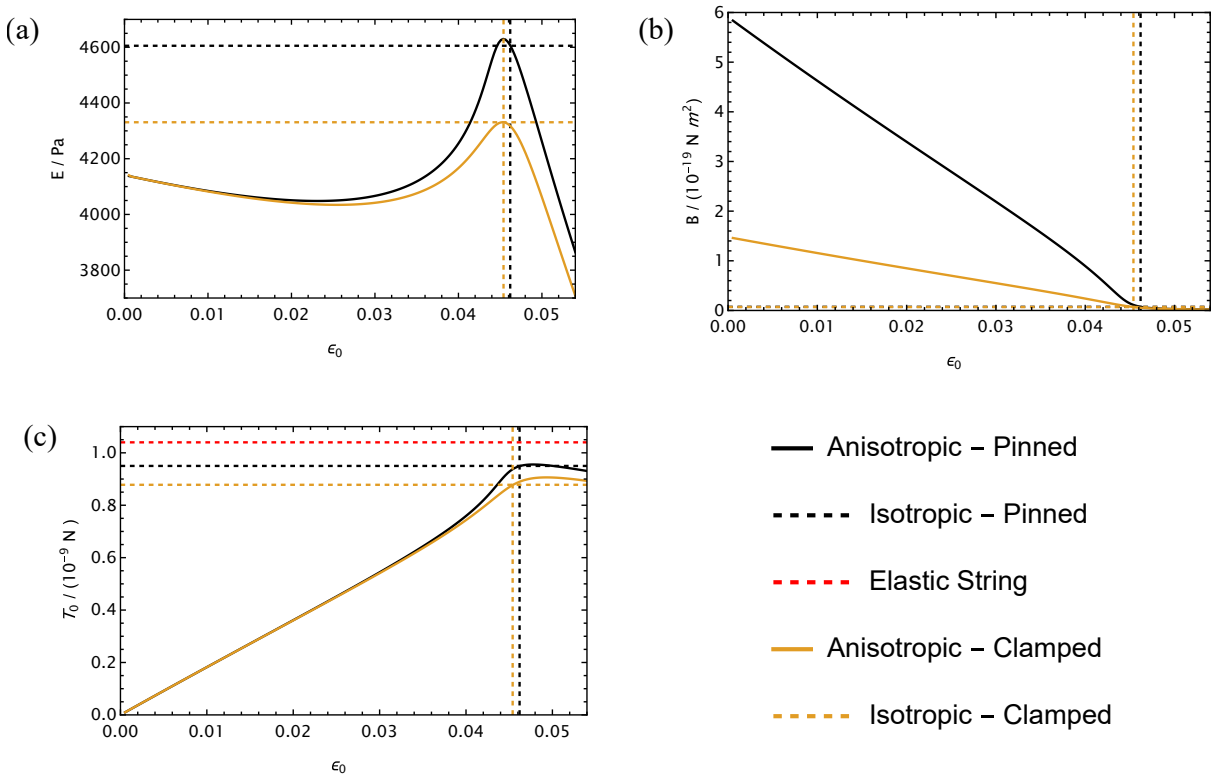


Figure 4.3: Estimated values of E, $\mathcal{B}$, and T_0 for Neurite 1, shown in panels (a), (b), and (c), respectively, as functions of the imposed initial strain ε_0 under the anisotropic beam model. Results are shown for pinned boundary conditions (black solid line) and clamped boundary conditions (orange solid line). The dashed black and orange lines indicate the corresponding estimates obtained from the isotropic beam model, while the dashed red line in panel (c) indicates the value of T_0 inferred from the elastic string model.

Varying ε_0 traces solution curves of (4.2) which emanate from the zero-strain solutions $(E_-, \mathcal{B}_0)$ and $(E_+, \mathcal{B}_0)$, where $\mathcal{B}_0$ denotes the inferred bending stiffness when $\varepsilon_0 = 0$. Thus, for sufficiently small $\varepsilon_0 > 0$, there are at least two distinct solution branches. We do not

consider the branch emanating from $(E_-, \mathcal{B}_0)$ further, since the corresponding elastic modulus remains negative over the range of ε_0 tested.

Fig. 4.3 shows the inferred values of E, $\mathcal{B}$, and T_0 for Neurite 1 as ε_0 is varied; the corresponding estimates for Neurite 3 are given in Section B.5, though the qualitative behaviour of the estimates as functions of ε_0 is similar. For both pinned and clamped boundary conditions, the inferred elastic modulus is a non-monotone function of ε_0. The clamped model consistently gives an estimate of E that is less than or equal to the corresponding estimate under pinned boundary conditions. For small values of ε_0, the pinned and clamped estimates are in close agreement.

In contrast, the inferred bending stiffness decreases monotonically with increasing ε_0 for both sets of boundary conditions. In the range tested, $\mathcal{B}$ approaches zero as ε_0 increases. As expected, the clamped boundary condition gives a smaller estimate of $\mathcal{B}$ than the pinned boundary condition throughout the solution curve.

The inferred initial tension T_0 remains below the value inferred from the elastic string model. The pinned model gives a slightly larger estimate of T_0 than the clamped model, although the two estimates remain close across the range of ε_0 considered.

Over the tested range of ε_0, the inferred values of E remain close to the estimates obtained from the isotropic beam model. Indeed, the isotropic estimates are recovered at particular points along the anisotropic solution curves. By contrast, the inferred values of $\mathcal{B}$ differ substantially from the isotropic estimates over most of the interval. This indicates that the inference of E is relatively insensitive to the imposed value of ε_0, whereas the inference of $\mathcal{B}$ is strongly dependent on it. Thus, while the isotropic model may provide a reasonable estimate of the elastic modulus, it does not necessarily provide a reliable estimate of the bending stiffness.

Interestingly, the values inferred from the elastic string model are not recovered along the anisotropic beam solution curves. This may reflect the fact that the elastic string model corresponds to the singular limit $\mathcal{B} \to 0$ of the extensible beam model, rather than to a regular point on the anisotropic solution branch.

Most importantly, these results show that an analysis based on an anisotropic beam model can recover bending stiffnesses of order $\mathcal{B} \sim 10^{-19}\,\mathrm{Nm}^2$ from the pulling experiment, while still giving reasonable values for both E and T_0. Thus, once E and $\mathcal{B}$ are allowed to vary independently, the neurite-pulling data are compatible with the larger bending stiffness estimates obtained from TFS and microstructure-based arguments, suggesting that the much smaller isotropic estimates are a result of the modelling assumption $\mathcal{B} = EI$ rather than from the data themselves.

4.13 Conclusion

In this chapter, we inferred the mechanical parameters of axons from neurite pulling experiments by extending the elastic-string model to an extensible beam model with bending stiffness. After describing the experiment and inference procedure in Sections 4.3, 4.4, we developed the beam formulation in Section 4.6. This provided a framework for testing how different mechanical assumptions affect the inferred values of E, $\mathcal{B}$ and ε_0. To our knowledge, this is the first work to fit a beam model directly to neurite load–deflection data.

In Section 4.9, we considered the isotropic assumption, $\mathcal{B} = EI$. Under this assumption, the extensible beam model gives estimates close to those obtained from the elastic-string model in Section 4.7, with $E_{\text{isotropic}} < E_{\text{string}}$. The choice between pinned and clamped boundary conditions has only a small effect on the inferred parameters. Thus, if the axon is treated as an isotropic rod, the elastic-string estimate provides a reasonable estimate of E, and $\mathcal{B} = E_{\text{string}}I$ gives a consistent estimate of the bending stiffness.

The conclusion changes when E and $\mathcal{B}$ are allowed to vary independently. In the anisotropic model, studied in Sections 4.10, 4.12, the inferred values of E remain of the same order as E_{string}, but the inferred values of $\mathcal{B}$ can be several orders of magnitude larger than $E_{\text{string}}I$. Therefore, if the axon is anisotropic, the elastic-string model may still give a reasonable estimate of the elastic modulus, but it does not provide a reliable estimate of the bending stiffness.

Although the full anisotropic model is underdetermined, the data still provide useful constraints. In particular, the zero-strain pinned case in Section 4.10 gives an upper bound for $\mathcal{B}$, equal to $L_x^3 a_1/48$, and the results suggest that E is bounded above by E_{string}. More importantly, the anisotropic model shows that the pulling data are compatible with bending stiffnesses of order $\mathcal{B} \sim 10^{-19}\,\text{Nm}^2$, consistent with estimates based on the microtubular structure of the axon shaft.

These results help resolve the apparent discrepancy in the literature between small isotropic estimates of bending stiffness and larger microstructure-based estimates. The discrepancy arises not from the data alone, but from the modelling assumption $\mathcal{B} = EI$. Further progress on determining $E, \mathcal{B}, \varepsilon_0$ will require additional measurements, for example measuring the load-deflection curve at larger H, so that E, $\mathcal{B}$ and ε_0 can be identified simultaneously within the extensible beam framework.

Chapter 5

ABC Applications

5.1 Overview

In this chapter, we use the model of axon guidance developed in Chapter 3 to study particular in-vivo and in-vitro scenarios where it is thought that durotaxis plays an important role.

A particularly common experimental setup is one where axons are cultured on a substrate that contains a sharp-interface between two regions of different environmental conditions. In Section 5.2, we investigate such scenarios by studying how axons interact with a sharp-interface between two regions of different local traction generation. Furthermore, in Section 5.3 we investigate an in-vitro experiment where neurites interact with such an interface between two regions of different stiffness.

In Section 5.4, we investigate the durotactic guidance of xenopus retinal ganglion cell axons. The durotactic guidance of these axons along the optic tract and to the optic tectum is one of the prime in-vivo examples of durotactic guidance for axons. Simpler models of axon durotaxis failed to account for it. For this reason, we apply the model of Chapter 3, and find that guidance to the optic tectum can be achieved purely by durotaxis.

Finally, in Section 5.5 we investigate the segmented outgrowth of axons during the patterning of the peripheral nervous system. Evidence suggests that this segmented outgrowth occurs by durotaxis. In this section, we use our model to investigate under what conditions the segmented outgrowth of motor axons can occur successfully by durotaxis alone.

The content found in Section 5.2 and Section 5.4 is based on the paper by Kassianides et al [35]. In that paper, we used a motor-clutch formulation that assumed a constant binding rate of stochastic linkers, an assumption that is valid in the case of a large pool of stochastic linkers. The traction stiffness curve under this formulation exhibits the same qualitative features as the traction stiffness curve under the formulation studied

in Chapter 2. We utilize the constant binding rate assumption in this chapter. Details about this formulation of the motor-clutch system can be found in Section A.8.

5.2 Reflection and refraction at a straight stiffness interface

We consider a heterogeneous field composed of two regions with different but uniform stiffnesses separated by a straight interface. In this case, the axon can either grow through the interface (refraction) or bounce against the interface (reflection), in analogy with optic ray theory. As the growth cone touches the interface, the force density along the growth cone margin becomes heterogeneous.

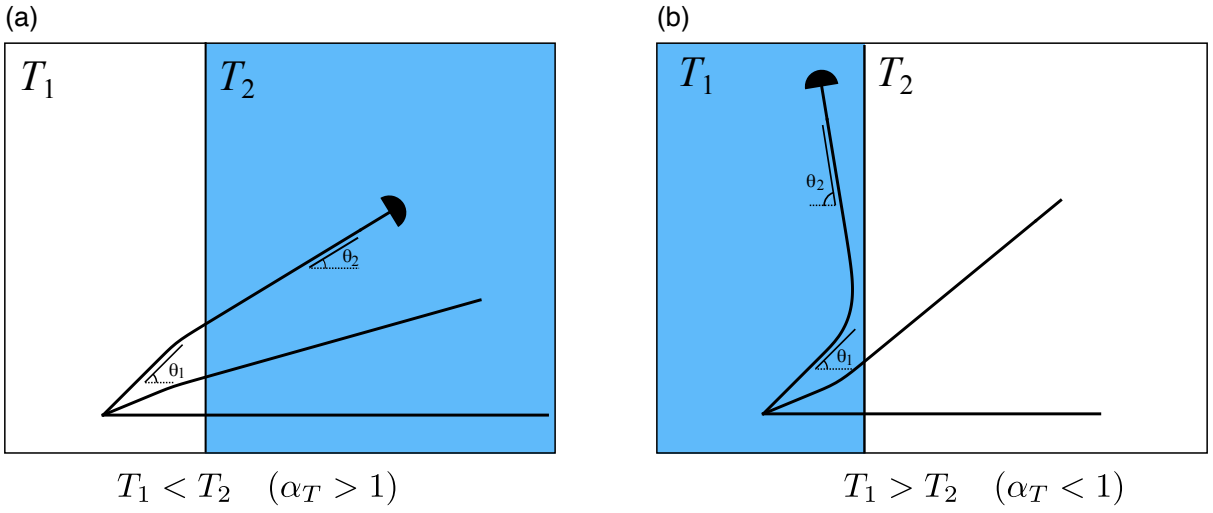


Figure 5.1: An illustration of the possible behaviours an axon exhibits when crossing a sharp interface between regions of different local growth cone force. Axons may cross, refract across, or reflect against the sharp interface. Parameters: (a) $\alpha_T = 5/4$ - (b) $\alpha_T = 4/5$ - Common $R = L/2$, $\lambda = R/4$, $\varphi_0 = \pi/2$, $\alpha_T = 4/5$, $\beta = 0.5, \varepsilon = 0.1$.

We assume that the axon grows from the region $x < 0$, as shown in Fig. 5.1(a), and approaches the boundary with an angle of incidence $\theta_1 \in [0, \pi/2)$ (the angle between the axon and the normal to the interface). We assume that the interface is sharp but numerically, we approximate this straight interface by

$$T(x, y) = \frac{T_1 + T_2}{2} + \frac{T_2 - T_1}{2} \tanh(x/\lambda), \tag{5.1}$$

where $T_1 = T(\chi_1)$ and $T_2 = T(\chi_2)$ are the force densities produced by the growth cone in the left-most and right-most regions, which depend on the stiffness of each region (χ_1, χ_2). The parameter λ determines the length scale of transition from T_1 to T_2 across the interface and is chosen small enough w.r.t. the growth cone size that the results are not

affected by further decreasing it (in practice, we found that $\lambda = R/4$ is suitable). The total force depends nonlinearly on the position and orientation of the growth cone via (3.1), since, here, the arbitrarily large steepness of the gradient $\sim (T_2 - T_1)/2\lambda$ precludes the use of the leading-order approximation (3.2).

Initially, we assume a clamp position $\boldsymbol{r}_0(0)$ far from the boundary in the incidence direction θ_1. As soon as the growth cone leaves the interface region, it follows a straight trajectory and as $t \to \infty$, we define the *refraction angle* θ_2 with the normal pointing into the right region. The axon may also reflect against the interface and stay in the left-most region as seen in Fig. 5.1(b). In this case, the *reflection angle* θ_2 is defined as the angle between the left normal and the direction of the axon. Let $\theta_\mathrm{m} = \lim_{t\to\infty} \theta_0(t) \mod 2\pi$, then restricting our attention to $\theta_\mathrm{m} \in [0, \pi)$ we have

$$\theta_2 = \begin{cases} \theta_\mathrm{m}, & \text{if } 0 \le \theta_\mathrm{m} < \pi/2, \\ \pi - \theta_\mathrm{m}, & \text{if } \pi/2 \le \theta_\mathrm{m} < \pi. \end{cases} \tag{5.2}$$

By choosing the characteristic force-scale of the system of equations (3.46a - 3.46c) to be $\rho R T_1$, characteristic length scale equal to L and characteristic timescale equal to $\tau = \eta/(\rho R T_1)$, it can be shown that the evolution of the state of the axon hence its final state is completely determined by the dimensionless parameters

$$\varepsilon := \frac{B}{L^2 \rho R T_1}, \alpha_T := \frac{T_2}{T_1}, \beta := \frac{R}{L}, \tag{5.3}$$

and on θ_1 and φ_0. We focus on $\varphi_0 = \pi/2$. In fact, assuming that the axon is straight in the limit $t \to +\infty$, we derive the relation

$$\frac{\hat{\theta}(+\infty) - \hat{\theta}(0)}{2} = \int_0^{+\infty} (\boldsymbol{f}\cdot\boldsymbol{t}) Y(1,T) + \boldsymbol{f}\cdot\hat{\boldsymbol{\nu}} + \varepsilon \frac{\partial^3 Y}{\partial S^3}(0,T)\mathrm{d}T, \tag{5.4}$$

where

$$\boldsymbol{f} = \int_{-\varphi_0}^{\varphi_0} \left[\frac{\alpha_T + 1}{2} + \frac{\alpha_T - 1}{2} H\left(X_\mathrm{tip} + \beta\, \boldsymbol{e}_\varphi \cdot \boldsymbol{e}_X\right)\right] \boldsymbol{e}_\varphi \,\mathrm{d}\varphi, \tag{5.5}$$

and

$$H(s) = \begin{cases} 1, & \text{if } s \ge 0, \\ -1, & \text{if } s < 0. \end{cases} \tag{5.6}$$

and $X_\mathrm{tip} = x_\mathrm{tip}/L$, x_tip being the position of the axon tip and $Y(X,T) = \mathsf{y}(LX, \tau T)/L$, where y solves the ABC system (Chapter 3) with $\mathsf{y}(x,0) = 0$ and $\hat{\theta}(0) = \theta_1$ and initial clamp $\hat{\boldsymbol{r}}(0)\cdot\boldsymbol{e}_x < -R$. This relation shows that the final direction of travel of the axon is completely determined by α_T, ε and the angle of incidence $\theta(0)$, assuming that $y(x,0) = 0$ always.

The dimensionless parameter ε describes how 'stiff' the axon is with respect to the force T_1, henceforth called the '*dimensionless bending stiffness*'. The smaller ε, the larger

the deflections exhibited by the axon. The dimensionless parameter α_T describes the ratio between the local growth cone tractions generated in each region, henceforth called the *traction ratio*. Note that the traction ratio for a given axon depends on which region it initially approaches the interface from. The importance of this will be explained later. The dimensionless parameter β describes the dimensionless radius of the growth cone and is a measure of the long-range sensing capacity of the growth cone.

We distinguish the two cases $\alpha_T < 1$ and $\alpha_T > 1$. When $\alpha_T > 1$–see Fig. 5.1(a)–the durotactic force in the right region is greater than in the left region, thus the durotactic force component tends to pull the axon towards the right region. This results in a refractive behaviour with θ_2 smaller than θ_1. Conversely, when $\alpha_T < 1$ the durotactic force component tends to pull the axon away from the right region. Consequently, both refraction and reflection can be observed, as shown in Fig. 5.1(b).

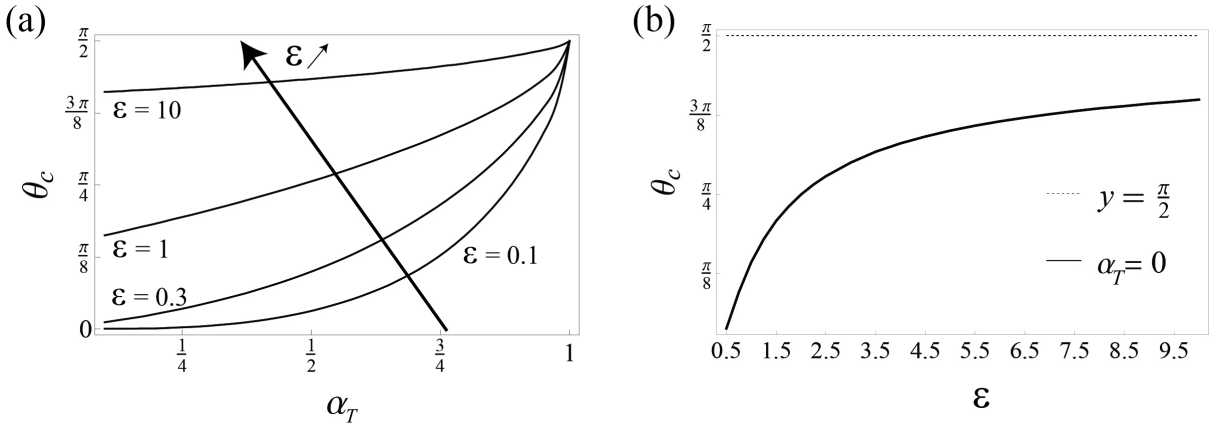


Figure 5.2: (a) Critical angle, θ_c, as a function of the traction ratio, α_T. Different curves indicate the critical angle function for different values of ε. (b) θ_c as a function of ε for $\alpha_T = 0$. Parameters: $\beta = 0.5$.

The behaviours described above confirm that under differential traction, individual axons exhibit refractive and reflective behaviours when interacting with sharp interfaces between regions of different local force densities.

5.2.1 Reflection and refraction curves, critical angle

In the case of geometric optics, the relation between angle of incidence and angle of refraction is neatly captured by Snell's law, which states that

$$n_1 \sin(\theta_1) = n_2 \sin(\theta_2),$$

where n_1, n_2 are the refractive indices of regions $1, 2$ respectively, region 1 being the region from which the ray originates, θ_1 is the angle of incidence and θ_2 is the angle of refraction.

Unlike geometric optics, there is no such simple relation relating θ_1, θ_2 in our axon model. Furthermore, the sines of the two angles, θ_1, θ_2, are not linearly related. Nonetheless, there are some interesting parallels between the two systems.

Firstly, we can draw a parallel between n_2/n_1 and $\alpha_T = T_2/T_1$. Reflection is possible in each system when these quantities are smaller than 1. Furthermore, in each case the critical angle, defined here as the angle beyond which there is reflection back into the originating domain, is an increasing function of each parameter. In the case of geometric optics, the critical angle can be given analytically by the expression $\theta_c = \arcsin(n_2/n_1)$. Notably, this is a convex function of n_2/n_1, which tends to 0 as the refractive index ratio tends to 0. In the ABC model, the critical angle is also a convex function of α_T. However, depending on the value of the dimensionless bending stiffness, the critical angle need not tend to 0 as α_T does.

There are a couple of things to note here, relating to θ_c. Firstly, it is clear that for $\alpha_T > 0$ we have $\theta_c \to \pi/2^-$ as $\varepsilon \to +\infty$. The reason is that for any fixed $0 < \alpha_T < 1$, increasing ε makes the axon stiffer with respect to the growth cone force. As the stiffness of the axon increases, the magnitude of the deflections that can be imposed on the axon by the growth cone force, generated through its interaction with the interface, diminishes. Therefore, the total turning angle that the axon undergoes is also diminished. This suggests that for a particular critical angle corresponding to a combination of α_T, ε, further increasing ε would set this angle of incidence under the threshold of reflection. Nonetheless, reflection can still be guaranteed by increasing the angle of incidence. Therefore, θ_c increases with ε.

In the limiting case of $\varepsilon = +\infty$, the axon is completely rigid and therefore does not deviate from its original trajectory. In this case there is no reflection, as the angle of refraction is equal to the angle of incidence. We equate this situation with a critical angle of $\pi/2$ as this is the only case in which the axon reflects back into region 1. Thus, for fixed $0 < \alpha_T < 1$, θ_c is an increasing function of ε with supremum equal to $\pi/2$. It follows that θ_c converges pointwise to $\pi/2$ as $\varepsilon \to +\infty$.

What exactly occurs when the angle of incidence is equal to the critical angle is unclear. This case is not one we can directly investigate numerically, as any floating point approximation of the critical angle is not equal to it. In geometric optics, light-rays travel parallel to the interface upon reflection when the angle of incidence is equal to the critical angle. Following the light-ray analogy would suggest that axons end up travelling parallel to the interface when the angle of incidence is equal to the critical angle. However, it is not clear that this is the case, as it can be directly shown that there does not exist any trajectory of the system where the axon travels precisely parallel to the interface. This is a consequence of the non-local force integration of the growth cone. Whenever

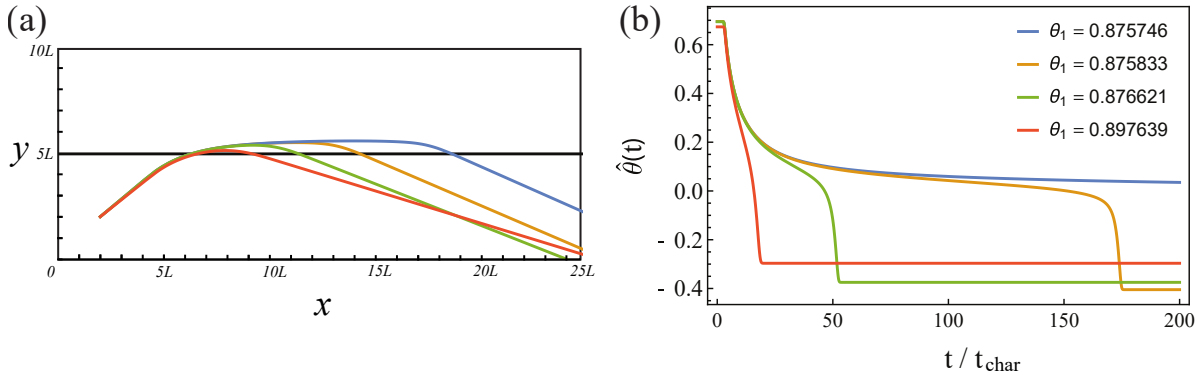


Figure 5.3: (a) Trace of axon trajectories for angles of incidence approaching the critical angle from above. Here, the critical angle θ_c belongs to the interval $(0.875744, 0.875746)$. (b) Plot of $\hat{\theta}(t)$ for each axon trajectory in (a) - same color corresponds to same trajectory. Parameters: $\alpha_T = 0$, $\beta = 1/2, \varepsilon = 2.5, t_{\text{char}} = 69.4$ hours.

the axon is parallel to the interface, the growth cone force points away from the interface and into the region with the higher local traction. Therefore, the axon deflects and grows away from the interface and into the higher traction region. We can investigate what occurs at the critical angle by looking at the limiting behavior of trajectories as the angle of incidence approaches the critical angle.

When the angle of incidence approaches the critical angle from below (refraction regime), the axon converges to a state travelling in a straight line with a clamp angle equivalent to the angle of refraction. This angle of refraction clearly tends to $\pi/2$.

As the angle of incidence tends towards the critical angle from above (reflection regime), axons end up travelling approximately parallel to the interface for a period of time before reflection. The closer the angle of incidence is to the critical angle, the longer the axon spends in this state before reflection (see Fig. 5.3(a)). One possibility is that the axon with angle of incidence equal to the critical angle attains a state parallel to the interface at $t = +\infty$. In this case, the limiting clamp angle is equal to 0 and so the angle of refraction is actually equal to $\pi/2$. Our numerics indicate that this could be the case (see Fig. 5.3(b)).

Although the critical angle function converges pointwise to $\pi/2$ as $\varepsilon \to +\infty$ for $0 < \alpha_T < 1$, a question remains as to what the behavior of this function is around $\alpha_T = 0$. For example, it could be the case that when $\alpha_T \to 0^+$ the interface force always becomes sufficiently repulsive to reflect any axon with an angle of incidence greater than 0. This would imply that $\theta_c(\alpha_T) \to 0^+$ as $\alpha_T \to 0^+$, for every fixed $\varepsilon > 0$. Such behavior of $\theta_c(\alpha_T)$ would require the formation of a boundary layer around $\alpha_T = 0$ such that for each fixed ε the critical angle tends to 0 as $\alpha_T \to 0^+$, but transitions smoothly but rapidly

to values close to $\pi/2$ for greater values of α_T. This possibility justifies an investigation of $\theta_c(\alpha_T = 0)$ for varying values of ε.

We investigate this case directly by simulating the case $\alpha_T = 0$, and finding the critical angle for various values of ε. We confirm that the critical angle can be non-zero even when $\alpha_T = 0$. For the range of values of ε we tested, the critical angle at $\alpha_T = 0$ is an increasing function of ε, seemingly tending to $\pi/2$ as $\varepsilon \to +\infty$ and tending to 0 as $\varepsilon \to 0^+$ (see Fig. 5.2(b)). It is important to note here that axons not reflected by their interaction with the interface, stop growing as soon as the growth cone fully crosses over into region 2, since the growth cone force becomes 0, and it is this force that drives growth in our model. Something to note is that there is a limit to how small a value of ε we can sample for $\alpha_T = 0$. The smaller ε is, the larger the deflections of the axon and the less valid the small deflection assumption becomes. This assumption was used to derive the ABC equations. Therefore, the ABC equations become an inaccurate description of the physical system when ε is sufficiently small.

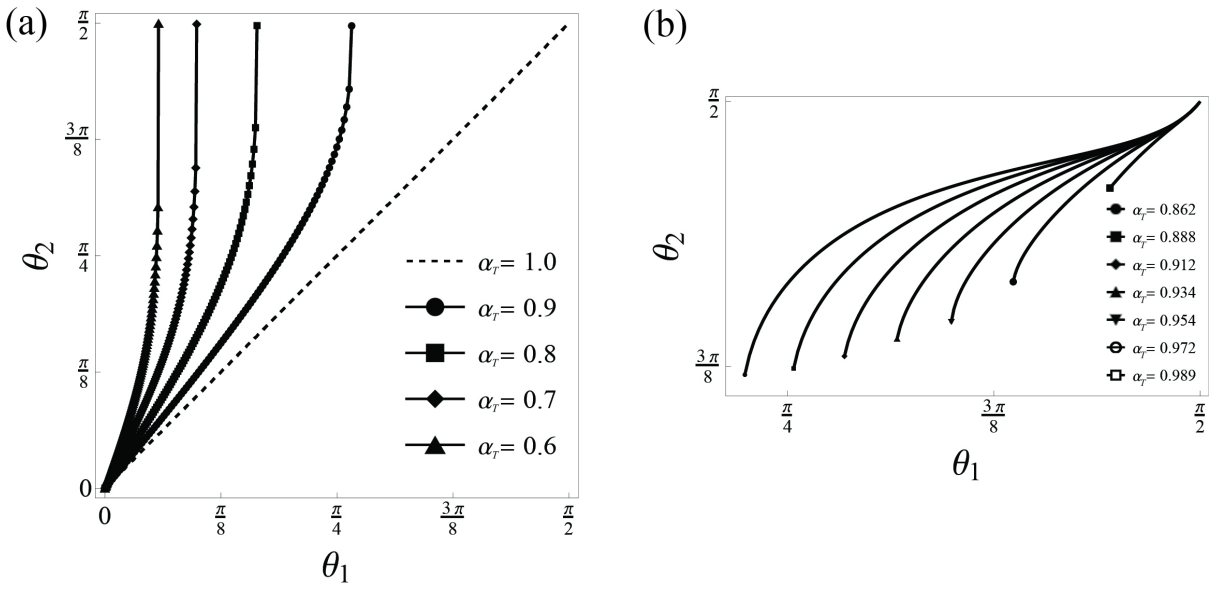


Figure 5.4: Refraction - Reflection curves. (a) Angle of refraction, θ_2, as a function of θ_1, for $\theta_1 < \theta_c$, for various values of $\alpha_T < 1$. (b) Angle of reflection, denoted by θ_2, as a function of θ_1, for $\theta_1 > \theta_c$, for various values of $\alpha_T < 1$. Parameters: $\beta = 0.5$, $\varepsilon = 0.1$.

Having characterized the behaviour of the critical angle, we move on to the specifics of the refraction and reflection curves. In the case $\alpha_T < 1$, for angles of incidence smaller than the critical angle, the angle of refraction is an increasing function of θ_1. As expected, the angle of refraction tends to $\pi/2$ as the angle of incidence tends to the same limit (see Fig. 5.4(a)). In the case of geometric optics, when the angle of incidence is greater than the critical angle the angle of reflection is equal to the angle of incidence. Surprisingly,

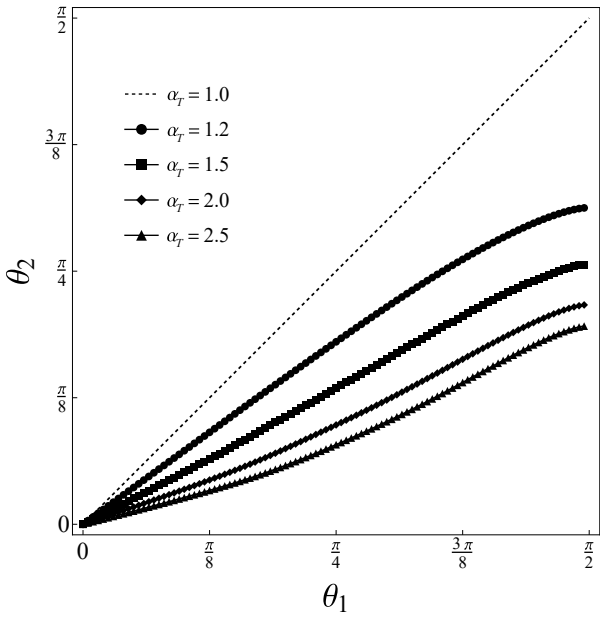


Figure 5.5: Refraction curves. Angle of refraction, θ_2, as a function of θ_1, for various values of $\alpha_T > 1$. Parameters: $\beta = 0.5$, $\varepsilon = 0.1$.

this is not the case for the ABC system. We explain the reason for this in Section 5.2.2. Rather, axons are reflected at angles close to $\pi/2$ (see Fig. 5.4(b)). Consequently, axons remain and travel close to parallel to the interface upon reflection.

In the case $\alpha_T > 1$, there is only refraction, as the region corresponding to T_2 pulls the axons in. Consequently, all angles of refraction are smaller than the angle of incidence. Furthermore, the pulling effect becomes greater for larger values of α_T (but fixed ε). It follows that the angle of refraction, as a function of the angle of incidence, tends pointwise to 0 as $\alpha_T \to +\infty$ (see Fig. 5.5).

5.2.2 Time Irreversibility

A fundamental difference between this model and both geometric optics and the bundle model of [53], is that this system lacks time-reversal symmetry when interacting with a sharp-interface. In the bundle model of [53], the time-reversal symmetry of the equations takes the form of $t \to -t, \theta \to \theta + \pi$ and implies that reflection occurs with $\theta_1 = \theta_2$ (see [53]). Numerically, it can be seen in Fig. 5.6 that this symmetry does not exist in our model, and in particular we observe that $\theta_1 \neq \theta_2$ after reflection (see Fig. 5.1(b)). In fact, when reflected, axons remain much more parallel to the interface than light rays do. By analytically investigating time reversal symmetry in our system we can understand the mechanism that leads to the breaking of this symmetry.

One feature that breaks time-reversal symmetry is the circular shape of the growth cone boundary, over which the integration of the local traction is performed. To show

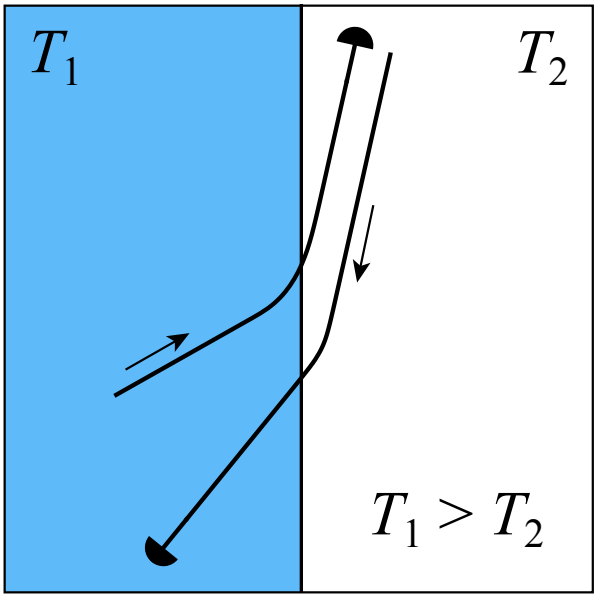


Figure 5.6: Demonstration of the absence of time-reversibility in the system. Approaching the interface from the left is not the same as approaching from the right. An axon travelling from blue to white with an angle w.r.t the vertical θ_1 ends with an angle θ_2. The same axon travelling from white to blue with an angle θ_2 will end in a direction given by $\tilde{\theta}_1 \neq \theta_1$. Parameters: $R = L/2$, $\lambda = R/4$, $\varphi_0 = \pi/2$, $\alpha_T = 4/5$, $\beta = 0.5, \varepsilon = 0.1$.

this, we derive necessary conditions for time reversibility, and show that these are violated for the local traction field of a sharp-interface. We focus on the case $\varphi_0 = \pi/2$.

Take a solution to the ABC equations $\left(\hat{x}(t), \hat{y}(t), \hat{\theta}(t), \mathsf{y}(S,t)\right)$ and transform the solution by $t \to -t, \hat{\theta} \to \hat{\theta} + \pi$. The transformed solution is given by the new variables $\left(\tilde{x}(t), \tilde{y}(t), \hat{\Theta}(t), \tilde{\mathsf{y}}(S,t)\right)$, where

$$\tilde{x}(t) = \hat{x}(-t), \tilde{y}(t) = \hat{y}(-t), \hat{\Theta}(t) = \hat{\theta}(-t) + \pi, \tilde{\mathsf{y}}(S,t) = \mathsf{y}(S,-t). \tag{5.7}$$

This transformation is a symmetry of the ABC system if and only if the transformed functions satisfy the ABC equations. Therefore, a necessary condition for this transformation being a symmetry is

$$\dot{\boldsymbol{R}} = \frac{\boldsymbol{F}\left(\tilde{\boldsymbol{x}}_{\text{tip}}, \tilde{\theta}_{\text{tip}}\right) \cdot \boldsymbol{t}\left(\tilde{\theta}_{\text{tip}}\right)}{\sqrt{\eta\,\zeta}} \hat{\boldsymbol{\tau}}\left(\hat{\Theta}\right), \tag{5.8}$$

where

$$\boldsymbol{R}(t) = (\tilde{x}(t), \tilde{y}(t)), \tag{5.9}$$

$$\tilde{\boldsymbol{x}}_{\text{tip}} = \boldsymbol{x}_{\text{tip}}\left(\tilde{x}(t), \tilde{y}(t), \tilde{\mathsf{y}}(L,t), \hat{\Theta}(t)\right), \tag{5.10}$$

$$\boldsymbol{x}_{\text{tip}}\left(\tilde{x}, \tilde{y}, \tilde{\mathsf{y}}, \hat{\Theta}\right) = (\tilde{x}, \tilde{y}) + L\,\hat{\boldsymbol{\tau}}\left(\hat{\Theta}\right) + \tilde{\mathsf{y}}\,\hat{\boldsymbol{\nu}}\left(\hat{\Theta}\right). \tag{5.11}$$

and $\tilde{\theta}_{\text{tip}}$ is the polar angle of the axon-tip of the transformed solution, and satisfies

$$\left(\cos\left(\tilde{\theta}_{\text{tip}}\right),\, \sin\left(\tilde{\theta}_{\text{tip}}\right)\right) = \frac{\hat{\boldsymbol{\tau}}\left(\hat{\Theta}\right) + \frac{\partial \tilde{\mathrm{y}}}{\partial \sigma}(L,t)\,\hat{\boldsymbol{\nu}}\left(\hat{\Theta}\right)}{\sqrt{1+\frac{\partial \tilde{\mathrm{y}}}{\partial \sigma}(L,t)^2}}.$$

It can be shown from the above definition that $\tilde{\theta}_{\text{tip}}(t) = \theta_{\text{tip}}(-t) + \pi$. From the definition of the transformed variables we obtain that

$$\frac{\hat{\boldsymbol{\tau}}\left(\hat{\Theta}\right) + \frac{\partial \tilde{\mathrm{y}}}{\partial \sigma}(L,t)\,\hat{\boldsymbol{\nu}}\left(\hat{\Theta}\right)}{\sqrt{1+\frac{\partial \tilde{\mathrm{y}}}{\partial \sigma}(L,t)^2}} = \frac{\hat{\boldsymbol{\tau}}\left(\hat{\theta}\,(-t)+\pi\right) + \frac{\partial \mathrm{y}}{\partial \sigma}(L,-t)\,\hat{\boldsymbol{\nu}}\left(\hat{\theta}\,(-t)+\pi\right)}{\sqrt{1+\frac{\partial \mathrm{y}}{\partial \sigma}(L,-t)^2}}.$$

Furthermore,

$$\frac{\hat{\boldsymbol{\tau}}\left(\hat{\theta}\,(-t)+\pi\right) + \frac{\partial \mathrm{y}}{\partial \sigma}(L,-t)\,\hat{\boldsymbol{\nu}}\left(\hat{\theta}\,(-t)+\pi\right)}{\sqrt{1+\frac{\partial \mathrm{y}}{\partial \sigma}(L,-t)^2}} = -\frac{\hat{\boldsymbol{\tau}}\left(\hat{\theta}\,(-t)\right) + \frac{\partial \mathrm{y}}{\partial \sigma}(L,-t)\,\hat{\boldsymbol{\nu}}\left(\hat{\theta}\,(-t)\right)}{\sqrt{1+\frac{\partial \mathrm{y}}{\partial \sigma}(L,-t)^2}}.$$

The RHS is equal to $\theta_{\text{tip}}(-t)+\pi$ because

$$\left(\cos\left(\theta_{\text{tip}}(T)\right),\, \sin\left(\theta_{\text{tip}}(T)\right)\right) = \frac{\hat{\boldsymbol{\tau}}\left(\hat{\theta}(T)\right) + \frac{\partial \mathrm{y}}{\partial \sigma}(L,T)\,\hat{\boldsymbol{\nu}}\left(\hat{\theta}(T)\right)}{\sqrt{1+\frac{\partial \mathrm{y}}{\partial \sigma}(L,T)^2}},$$

and

$$-\left(\cos\left(\theta_{\text{tip}}\right),\, \sin\left(\theta_{\text{tip}}\right)\right) = \left(\cos\left(\theta_{\text{tip}}+\pi\right),\, \sin\left(\theta_{\text{tip}}+\pi\right)\right).$$

From the definition of $\tilde{x}(t), \tilde{y}(t)$ it follows that

$$\dot{\boldsymbol{R}}(t) = -\dot{\hat{\boldsymbol{r}}}(-t). \tag{5.12}$$

Furthermore, it is true that

$$\dot{\hat{\boldsymbol{r}}}(-t) = \frac{\boldsymbol{F}\left(\boldsymbol{x}_{\text{tip}}(-t), \theta_{\text{tip}}(-t)\right) \cdot \boldsymbol{t}\left(\theta_{\text{tip}}(-t)\right)}{\sqrt{\eta\,\zeta}}\hat{\boldsymbol{\tau}}\left(\hat{\theta}(-t)\right). \tag{5.13}$$

This can be seen by looking at the governing equation for $\hat{\boldsymbol{r}}(t)$. Therefore, it follows from the definitions of the transformed variables and from the definition of the ABC system that

$$\dot{\boldsymbol{R}}(t) = -\frac{\boldsymbol{F}\left(\boldsymbol{x}_{\text{tip}}(-t), \theta_{\text{tip}}(-t)\right) \cdot \boldsymbol{t}\left(\theta_{\text{tip}}(-t)\right)}{\sqrt{\eta\,\zeta}}\hat{\boldsymbol{\tau}}\left(\hat{\theta}(-t)\right). \tag{5.14}$$

The RHS of the above equation can be partially expressed in terms of transformed variables as

$$\dot{\boldsymbol{R}}(t) = -\frac{\boldsymbol{F}\left(\boldsymbol{x}_{\text{tip}}(-t), \tilde{\theta}_{\text{tip}}-\pi\right) \cdot \boldsymbol{t}\left(\tilde{\theta}_{\text{tip}}-\pi\right)}{\sqrt{\eta\,\zeta}}\hat{\boldsymbol{\tau}}\left(\hat{\Theta}-\pi\right). \tag{5.15}$$

We note that

$$\boldsymbol{t}\left(\tilde{\theta}_{\text{tip}}-\pi\right)=-\boldsymbol{t}\left(\tilde{\theta}_{\text{tip}}\right), \tag{5.16}$$

$$\hat{\boldsymbol{\tau}}\left(\hat{\Theta}-\pi\right)=-\hat{\boldsymbol{\tau}}\left(\hat{\Theta}\right), \tag{5.17}$$

from which it follows that

$$\dot{\boldsymbol{R}}(t)=-\frac{\boldsymbol{F}\left(\boldsymbol{x}_{\text{tip}}(-t),\tilde{\theta}_{\text{tip}}-\pi\right)\cdot\boldsymbol{t}\left(\tilde{\theta}_{\text{tip}}\right)}{\sqrt{\eta\,\zeta}}\hat{\boldsymbol{\tau}}\left(\hat{\Theta}\right). \tag{5.18}$$

Therefore, for condition (5.8) to be satisfied it is required that

$$-\frac{\boldsymbol{F}\left(\boldsymbol{x}_{\text{tip}}(-t),\tilde{\theta}_{\text{tip}}-\pi\right)\cdot\boldsymbol{t}\left(\tilde{\theta}_{\text{tip}}\right)}{\sqrt{\eta\,\zeta}}\hat{\boldsymbol{\tau}}\left(\hat{\Theta}\right)=\frac{\boldsymbol{F}\left(\tilde{\boldsymbol{x}}_{\text{tip}},\tilde{\theta}_{\text{tip}}\right)\cdot\boldsymbol{t}\left(\tilde{\theta}_{\text{tip}}\right)}{\sqrt{\eta\,\zeta}}\hat{\boldsymbol{\tau}}\left(\hat{\Theta}\right). \tag{5.19}$$

The above necessary condition can equivalently be expressed as

$$-\boldsymbol{F}\left(\boldsymbol{x}_{\text{tip}}(-t),\tilde{\theta}_{\text{tip}}-\pi\right)\cdot\boldsymbol{t}\left(\tilde{\theta}_{\text{tip}}\right)=\boldsymbol{F}\left(\tilde{\boldsymbol{x}}_{\text{tip}},\tilde{\theta}_{\text{tip}}\right)\cdot\boldsymbol{t}\left(\tilde{\theta}_{\text{tip}}\right). \tag{5.20}$$

Since

$$\begin{aligned}\boldsymbol{x}_{\text{tip}}(-t)&=\boldsymbol{x}_{\text{tip}}\left(\hat{x}(-t),\hat{y}(-t),\mathsf{y}\left(L,-t\right),\hat{\theta}(-t)\right)\\&=\boldsymbol{x}_{\text{tip}}\left(\tilde{x}(t),\tilde{y}(t),\tilde{\mathsf{y}}\left(L,t\right),\hat{\Theta}(t)-\pi\right),\end{aligned}$$

we can re-write the above condition as

$$-\boldsymbol{F}\left(\boldsymbol{x}_{\text{tip}}\left(\tilde{x},\tilde{y},\tilde{\mathsf{y}},\hat{\Theta}-\pi\right),\tilde{\theta}_{\text{tip}}-\pi\right)\cdot\boldsymbol{t}\left(\tilde{\theta}_{\text{tip}}\right)=\boldsymbol{F}\left(\tilde{\boldsymbol{x}}_{\text{tip}},\tilde{\theta}_{\text{tip}}\right)\cdot\boldsymbol{t}\left(\tilde{\theta}_{\text{tip}}\right). \tag{5.21}$$

The necessary condition (5.21) for the transformation to be a symmetry can be expressed as follows: For the stated transformation to be a symmetry, it is required that when we rotate the axon by π radians, the component of the growth cone force vector tangential to the axon tip also rotates by π radians. For the particular case $\varphi=\pi/2$, the force vector is calculated by

$$\boldsymbol{F}\left(\boldsymbol{x},\Phi\right)=\rho R\int_{-\pi/2}^{\pi/2}T\left(\boldsymbol{x}+R\boldsymbol{e}_{\Phi}\left(\theta\right)\right)\boldsymbol{e}_{\Phi}\left(\theta\right)\mathrm{d}\theta, \tag{5.22}$$

where

$$\boldsymbol{e}_{\Phi}\left(\theta\right)=\cos\theta\,\boldsymbol{t}(\Phi)+\sin\theta\,\boldsymbol{t}^{\perp}(\Phi), \tag{5.23}$$

and the axon tip has spatial coordinate $\boldsymbol{x}$ and polar angle Φ. Therefore,

$$\boldsymbol{F}\left(\boldsymbol{x},\Phi\right)=\rho R\,\boldsymbol{t}(\Phi)\int_{-\pi/2}^{\pi/2}T\left(\boldsymbol{x}+R\boldsymbol{e}_{\Phi}\left(\theta\right)\right)\cos\theta\mathrm{d}\theta+\rho R\,\boldsymbol{t}^{\perp}(\Phi)\int_{-\pi/2}^{\pi/2}T\left(\boldsymbol{x}+R\boldsymbol{e}_{\Phi}\left(\theta\right)\right)\sin\theta\mathrm{d}\theta. \tag{5.24}$$

Noting that $\boldsymbol{t}\left(\tilde{\theta}_{\text{tip}}-\pi\right)=-\boldsymbol{t}\left(\tilde{\theta}_{\text{tip}}\right)$ and $\boldsymbol{t}^{\perp}\left(\tilde{\theta}_{\text{tip}}-\pi\right)=-\boldsymbol{t}^{\perp}\left(\tilde{\theta}_{\text{tip}}\right)$ we have that

$$\begin{aligned}&\boldsymbol{F}\left(\boldsymbol{x}_{\text{tip}}\left(\tilde{x},\tilde{y},\tilde{\mathrm{y}},\hat{\Theta}-\pi\right),\tilde{\theta}_{\text{tip}}-\pi\right)\cdot\boldsymbol{t}\left(\tilde{\theta}_{\text{tip}}\right)\\&=-\rho R\int_{-\pi/2}^{\pi/2}T\left(\boldsymbol{x}_{\text{tip}}\left(\tilde{x},\tilde{y},\tilde{\mathrm{y}},\hat{\Theta}-\pi\right)-R\,\boldsymbol{e}_{\tilde{\theta}_{\text{tip}}}(\theta)\right)\cos\theta\mathrm{d}\theta,\end{aligned}$$

and

$$\begin{aligned}&\boldsymbol{F}\left(\boldsymbol{x}_{\text{tip}}\left(\tilde{x},\tilde{y},\tilde{\mathrm{y}},\hat{\Theta}\right),\tilde{\theta}_{\text{tip}}\right)\cdot\boldsymbol{t}\left(\tilde{\theta}_{\text{tip}}\right)\\&=\rho R\int_{-\pi/2}^{\pi/2}T\left(\boldsymbol{x}_{\text{tip}}\left(\tilde{x},\tilde{y},\tilde{\mathrm{y}},\hat{\Theta}\right)+R\,\boldsymbol{e}_{\tilde{\theta}_{\text{tip}}}(\theta)\right)\cos\theta\mathrm{d}\theta.\end{aligned}$$

Condition (5.21) can then be expressed as

$$\begin{aligned}&0=\\&-\int_{-\pi/2}^{\pi/2}T\left(\boldsymbol{x}_{\text{tip}}\left(\tilde{x},\tilde{y},\tilde{\mathrm{y}},\hat{\Theta}-\pi\right)-R\,\boldsymbol{e}_{\tilde{\theta}_{\text{tip}}}(\theta)\right)\cos\theta\mathrm{d}\theta+\\&\int_{-\pi/2}^{\pi/2}T\left(\boldsymbol{x}_{\text{tip}}\left(\tilde{x},\tilde{y},\tilde{\mathrm{y}},\hat{\Theta}\right)+R\,\boldsymbol{e}_{\tilde{\theta}_{\text{tip}}}(\theta)\right)\cos\theta\mathrm{d}\theta.\end{aligned}$$

This condition must hold for every choice of $\tilde{x},\tilde{y},\tilde{\mathrm{y}},\hat{\Theta},\tilde{\theta}_{\text{tip}}$. Thus, it must be true when $\tilde{\mathrm{y}}=0,\tilde{\theta}_{\text{tip}}=\hat{\Theta}$. This specific case gives another necessary condition:

$$\begin{aligned}&0=\\&-\int_{-\pi/2}^{\pi/2}T\left(\boldsymbol{x}_{\text{tip}}\left(\tilde{x},\tilde{y},0,\hat{\Theta}-\pi\right)-R\,\boldsymbol{e}_{\hat{\Theta}}(\theta)\right)\cos\theta\mathrm{d}\theta+\\&\int_{-\pi/2}^{\pi/2}T\left(\boldsymbol{x}_{\text{tip}}\left(\tilde{x},\tilde{y},0,\hat{\Theta}\right)+R\,\boldsymbol{e}_{\hat{\Theta}}(\theta)\right)\cos\theta\mathrm{d}\theta,\end{aligned}$$

which in detail can be expressed as

$$\begin{aligned}&0=\\&-\int_{-\pi/2}^{\pi/2}T\left(\tilde{x}-L\cos\hat{\Theta}-R\cos\left(\theta+\hat{\Theta}\right),\tilde{y}-L\sin\hat{\Theta}-R\sin\left(\theta+\hat{\Theta}\right)\right)\cos\theta\mathrm{d}\theta+\\&\int_{-\pi/2}^{\pi/2}T\left(\tilde{x}+L\cos\hat{\Theta}+R\cos\left(\theta+\hat{\Theta}\right),\tilde{y}+L\sin\hat{\Theta}+R\sin\left(\theta+\hat{\Theta}\right)\right)\cos\theta\mathrm{d}\theta.\end{aligned}$$

In general, this condition is violated. To see this, let $\tilde{x} = -L, \tilde{y} = 0$. Then, the condition is not violated if

$$0 = -\int_{-\pi/2}^{\pi/2} T\left(-L - L\cos\hat{\Theta} - R\cos\left(\theta+\hat{\Theta}\right), -L\sin\hat{\Theta} - R\sin\left(\theta+\hat{\Theta}\right)\right)\cos\theta \mathrm{d}\theta + \int_{-\pi/2}^{\pi/2} T\left(-L + L\cos\hat{\Theta} + R\cos\left(\theta+\hat{\Theta}\right), L\sin\hat{\Theta} + R\sin\left(\theta+\hat{\Theta}\right)\right)\cos\theta \mathrm{d}\theta.$$

For the sake of clarity, we define

$$I_2 := \int_{-\pi/2}^{\pi/2} T\left(-L + L\cos\hat{\Theta} + R\cos\left(\theta+\hat{\Theta}\right), L\sin\hat{\Theta} + R\sin\left(\theta+\hat{\Theta}\right)\right)\cos\theta\,\mathrm{d}\theta, \tag{5.25}$$

$$I_1 := \int_{-\pi/2}^{\pi/2} T\left(-L - L\cos\hat{\Theta} - R\cos\left(\theta+\hat{\Theta}\right), -L\sin\hat{\Theta} - R\sin\left(\theta+\hat{\Theta}\right)\right)\cos\theta\,\mathrm{d}\theta. \tag{5.26}$$

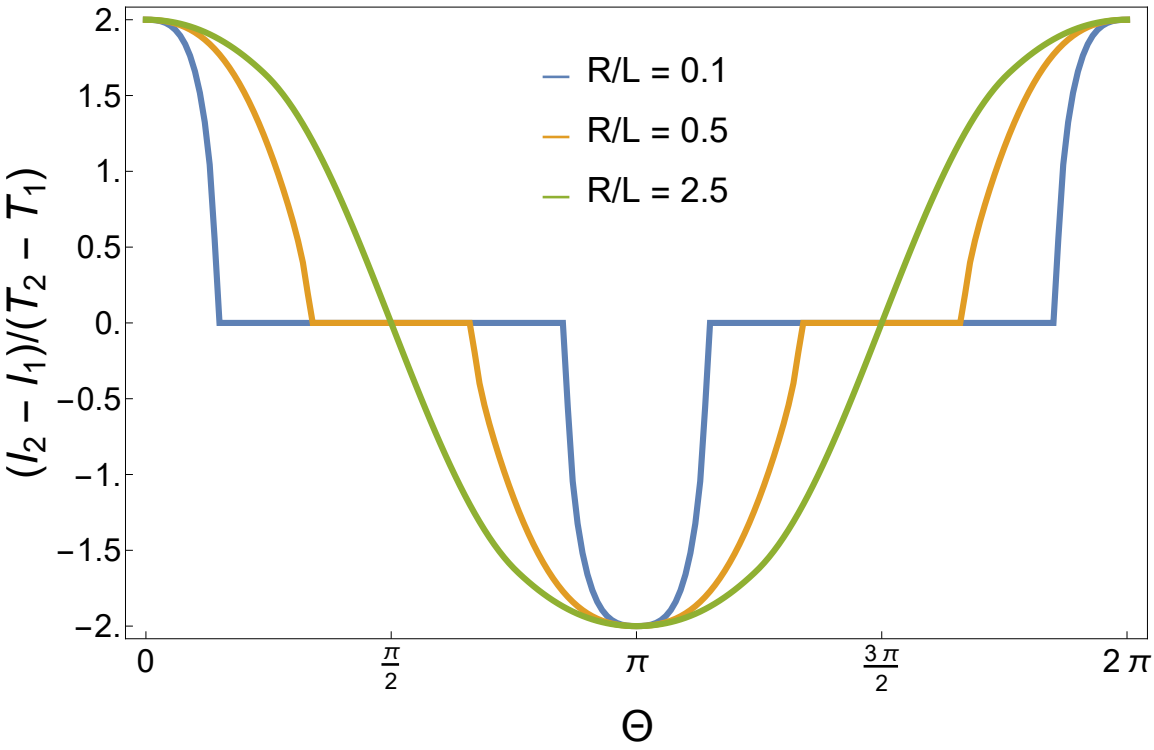


Figure 5.7: $(I_2 - I_1)\,/\,(T_2 - T_1)$ as a function of $\hat{\Theta}$ for various values of R/L.

Then, the necessary condition can be expressed as

$$I_2 - I_1 = 0. \tag{5.27}$$

The traction is given by

$$T(x,y) = T_1 + (T_2 - T_1)G\left[x\right],$$

where $G(x) = (H(x)+1)/2$, and $H(x)$ was already defined above (5.6). Therefore, integrals I_1, I_2 can be expressed as

$$I_2 = 2T_1 + (T_2 - T_1)\int_{-\pi/2}^{\pi/2} G\left[-1 + \cos\hat{\Theta} + \frac{R}{L}\cos\left(\theta + \hat{\Theta}\right)\right]\cos\theta \, \mathrm{d}\theta, \tag{5.28}$$

$$I_1 = 2T_1 + (T_2 - T_1)\int_{-\pi/2}^{\pi/2} G\left[-1 - \cos\hat{\Theta} - \frac{R}{L}\cos\left(\theta + \hat{\Theta}\right)\right]\cos\theta \, \mathrm{d}\theta. \tag{5.29}$$

In the particular case $\hat{\Theta} = 0$, we have

$$I_2 - I_1 = (T_2 - T_1)\int_{-\pi/2}^{\pi/2}\left(G\left[\cos\theta\right] - G\left[-2 - \frac{R}{L}\cos\theta\right]\right)\cos\theta \mathrm{d}\theta. \tag{5.30}$$

Since we have $\cos\theta > 0$ for all $\theta \in (-\pi/2, \pi/2)$, it follows that $-2 - (R/L)\cos\theta < 0$ for $\theta \in (-\pi/2, \pi/2)$. Therefore,

$$G\left[\cos\theta\right] = 1,\ G\left[-2 - \frac{R}{L}\cos\theta\right] = 0, \tag{5.31}$$

for $\theta \in (-\pi/2, \pi/2)$. Hence,

$$I_2 - I_1 = 2(T_2 - T_1), \tag{5.32}$$

which is not equal to zero for $\alpha_T \neq 1$. The values $(I_2 - I_1)/(T_2 - T_1)$ takes as a function of $\hat{\Theta}$ can be seen in Fig. 5.7 . Thus, for $T_1 \neq T_2$ condition (5.21) is violated, implying that the ABC system does not exhibit time-reversal symmetry when interacting with the traction field of a sharp-interface between two regions of unequal growth cone traction generation.

5.3 Sharp Boundary Experiment

The results of the above sections suggest that axons exhibit refractive and reflective behavior when interacting with a sharp boundary between two regions of different stiffness. Although reflective behaviour has been observed experimentally at such an interface for motile cells [45], there is a notable lack of such experiments that has been conducted for neurites. One notable exception is [73]. In this study, the authors developed a 'double rigidity' pattern, approximating a sharp interface between two regions of different rigidity. On this pattern, neurons were cultured and after their neurites had developed, the angles

that the neurites made with the interface on each side of it were recorded. The histogram of these angles on the soft side exhibited a peak around 0 degrees. The distribution of these angles is denoted by α.

Although it was not observed from which side the neurites originally migrated, this peak indicates that neurites might align themselves with the normal to the interface, as in the $\alpha_T > 1$ case described in the previous section. The results of this experiment provide a partial test for the predictions of our model. In this section we investigate under what conditions our model predictions are consistent with this observation.

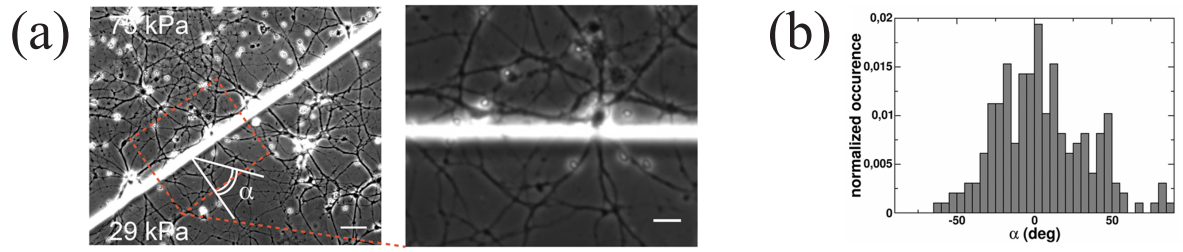


Figure 5.8: (a) (Left) Image of neurites cultured on a substrate approximating a sharp interface between a region with stiffness of 75 Pa (stiff) and another of stiffness 29 Pa (soft). Scale bar: 50μm. Angle between neurites and the normal to the interface, α, illustrated. (Right) Close up of outlined region from the experiment image. Scale bar: 20μm. (b) Observed distribution of α. Figure adapted from [73].

A decisive test of our model would be to reconstruct the observed trajectories of the neurites to a reasonable degree of accuracy. Equivalently, we could test whether the model can account for the angle of refraction of each neurite. Due to the lack of time-reversibility in the ABC system, the direction of migration factors in determining the angle of refraction. The fact that the direction of migration is unknown implies that the angle of incidence is a hidden variable and such an analysis would not be straight-forward.

Nonetheless, a consequence of the lack of time-reversal symmetry is that the direction of migration can, in principle, be determined from the complete spatial trajectory of a neurite across the interface, as time-irreversibility implies that only one of the two possible directions (soft $\rightarrow$ stiff or stiff $\rightarrow$ soft) would give a given spatial trace.

An additional difficulty arises from the fact that it can often be difficult to discern from the experiment image which neurite segments on either side of the interface are connected to form a single trajectory (see Fig. 5.8(a)). This means that rather than just having to distinguish the direction of migration for each neurite, we would need to determine both the direction of migration and which two segments on each side of the interface belong to the same neurite. Thus, under these constraints, and assuming that

each of the n neurites contributes exactly one segment to each side of the interface, the reconstruction of a collection of n neurites would require the comparison of $n! \cdot 2^n$ possible scenarios. For $n = 10$ neurites this number is already of order 10^9, which would require significant computational resources to evaluate in a timely manner. Given the computational difficulties that arise with the reconstruction of individual neurite trajectories, we constrain our investigation to coarser points of comparison - the distributions of angles that neurites make with the normal of the interface on each side.

To make such a comparison we would need to know the distribution of angles that neurites make with the interface normal on the stiff side. This distribution is not reported in the paper of [73] (the angle distribution on the soft side is known - see Fig. 5.8(b)). Depending on the distribution of these angles, which we call δ, one may reach different conclusions as to what the influence of the interface is on the axons. For example, an α distribution peaked at 0 could be explained by axons growing from stiff to soft, approaching the boundary with a distribution of angles peaked at 0 and the boundary having no effect on axon trajectories. In this case, ignoring any random effects on the trajectory of axons, the distributions α and δ would be equal and peaked at 0. The efficacy of the boundary can only be inferred from a statistically significant difference between the α and δ distributions. Although the distribution of δ is unknown, we can test which scenarios reproduce the empirically observed distribution of α, and report the corresponding distribution for δ. Whether the features of the corresponding δ distribution are reproduced in the data from the experiment would confirm or refute our model prediction.

To try and replicate the qualitative features of the empirically observed α distribution, we ran simulations of the sharp-interface scenario with $\varepsilon = 0.1$ and various values of the traction ratio T_2/T_1. It remains to decide the distribution of the angle of incidence. In our analysis we are ignoring any interactions between neurites and thus assume, as a first approximation, that these neurite trajectories are independent. Furthermore, we lack any prior information regarding this distribution. For this reason, we focused on the three simple scenarios: (i) all axons approach the interface from the stiff region with angles of incidence uniformly distributed on $(-\pi/2, \pi/2)$. (ii) all axons approach the interface from the soft region with angles of incidence uniformly distributed on $(-\pi/2, \pi/2)$. (iii) axons are equally likely to approach the interface from stiff or from soft region, in either case the angles of incidence being uniformly distributed on $(-\pi/2, \pi/2)$. In each case, the angles of incidence and refraction were added to a bin for α or δ depending on whether the segment of the axon forming the particular angle with the normal was in the soft or stiff region. We test cases with traction ratio $\alpha_T > 1$, assuming that axons exert higher tractions on the softer side and where T_2 corresponds to the growth cone traction on the soft side and T_1 the traction on the stiff side.

The results for each scenario and various values of the traction ratio are displayed in Fig. 5.9. In the stiff to soft scenario, neurites are pulled towards the soft side, resulting in refraction with angles of refraction smaller than the angle of incidence. Consequently, the α distribution is constrained on a strict subset of $(-\pi/2, \pi/2)$ centered on $\alpha = 0$. As the traction ratio increases, the length of this interval decreases, tending to 0 as $\alpha_T \to +\infty$. Simultaneously, as α_T increases from 1, the α distribution develops a peak around $\alpha = 0$. The height and curvature of this peak both increase as α_T increases. In this scenario, δ is distributed as the angle of incidence, i.e. as a uniform distribution on $(-\pi/2, \pi/2)$. Thus, we observe that in the case of neurites migrating from stiff to soft and for sufficiently large α_T, the α distribution is reminiscent of that observed experimentally, with a peak around $\alpha = 0$. Furthermore, in this case δ is uniformly distributed.

In the soft to stiff scenario, neurites are pushed away from the stiff side, resulting in neurite turning towards the soft side, with refracted neurites having angle of refraction greater than their angle of incidence. Furthermore, some neurites are reflected and so are not able to pass through to the stiff side. Specifically, only neurites with angles of incidence smaller than the critical angle are able to pass through to the stiff side.

In this scenario, the function relating the angle of refraction as a function of the angle of incidence is convex for incidence angles smaller than the critical angle (see Section 5.2.1) and a peak is created around the angle of refraction 0. This follows from the change of variables rule for probability density functions. That is, denoting $\theta_2 = f(\theta_1)$ for $\theta_1 \in [0, \theta_c)$, we have

$$p_{\theta_2}(\theta_2) = p_{\theta_1}\left(f^{-1}(\theta_2)\right) \left| \frac{\mathrm{d}}{\mathrm{d}\theta_2}\left[f^{-1}(\theta_2)\right] \right|, \tag{5.33}$$

where $p_{\theta_2}(\theta_2)$ is the probability density function of θ_2, $p_{\theta_1}(\theta_1)$ is the probability density function of θ_1 conditioned on θ_1 being in $[0, \theta_c)$ and $f^{-1}(\theta_2)$ is the inverse function of $f(\theta_1)$ whose existence is guaranteed by the fact that f is an increasing function on $[0, \theta_c)$.

By the Inverse Function Theorem we have the relation

$$\frac{\mathrm{d}f^{-1}}{\mathrm{d}\theta_2}(\theta_2) = \frac{1}{f'(f^{-1}(\theta_2))}.$$

It follows that $(f^{-1})'(\theta_2) > 0$, since $f(\theta_1)$ is increasing. Furthermore, since θ_1 is uniformly distributed on $[0, \pi/2)$ it follows that $p_{\theta_1}(\theta_1) = 1/\theta_c$. Combining all these elements together we obtain

$$p_{\theta_2}(\theta_2) = \frac{1}{\theta_c} \frac{1}{f'\left(f^{-1}(\theta_2)\right)}. \tag{5.34}$$

We can use this relation to show that $p_{\theta_2}(\theta_2)$ is decreasing for $\theta_2 > 0$. Differentiating (5.34), we obtain

$$\frac{\mathrm{d}p_{\theta_2}}{\mathrm{d}\theta_2} = -\frac{1}{\theta_c} \frac{f''\left(f^{-1}(\theta_2)\right)}{\left[f'\left(f^{-1}(\theta_2)\right)\right]^3}, \tag{5.35}$$

which is a negative quantity, as $f''(\theta_1) \geq 0$ on $[0, \theta_c)$ by convexity, thus showing that p_{θ_2} is decreasing. Considering then negative angles of incidence from $(-\theta_c, 0]$ would show that the distribution of θ_2 is increasing on $(-\theta_c, 0]$. From this it follows that there is a turning point and global maximum of the angle of refraction distribution at $\theta_2 = 0$, when axons travel from soft (high traction) to stiff (low traction) with angles of incidence which are uniformly distributed on $(-\theta_c, \theta_c)$.

Only these axons, which approach the interface with an angle of incidence within this interval show up in the δ distribution. Axons with a larger angle of incidence are reflected and thus appear twice in the α distribution, with the second appearance occuring at an angle greater than their angle of incidence (as axons are reflected close to parallel). Consequently, in the soft to stiff case, the δ distribution is peaked at 0 degrees, whilst the α distribution has an accumulation of angles at the edges of the distribution (close to $\pm\pi/2$ radians).

The final scenario, where axons approach the interface from all directions, constitutes a mixture of the previous two scenarios, exhibiting the characteristic features of the two scenarios in the α and δ distributions. Notably, α is peaked both at the ends of the distribution and around $\alpha = 0$. The accumulation of angles at the end of the distribution contradicts the experimentally sampled distribution, and thus we conclude that it is unlikely that this scenario describes the events that occured in the experimental setup.

We conclude that our model can reproduce the characteristic feature of the empirically observed distribution of α, the key feature being a peak about $\alpha = 0$. Further, under our model, there are two situations where a qualitatively similar distribution is observed. Although we assumed that traction is higher on the soft side than on the stiff side, we essentially used this terminology as a substitute for *high* and *low* traction regions. Angle distributions which are qualitatively similar to the observed α distribution are seen in the following scenarios: (i) On the high traction side, when axons travel from the low traction to the high traction region. In this case, the angle distribution is uniform on the low traction side. (ii) On the low traction side, when axons travel from the high traction to the low traction region. In this case, the angle distribution on the high traction side is peaked about the angles $-\pi/2, \pi/2$. Given that in [73] the distribution under consideration is observed on the soft side, our model predicts that one of the following holds: (i) the neurite growth cones exert a higher traction on the soft side than on the stiff side AND δ is uniformly distributed. (ii) the neurite growth cones exert a lower traction on the soft side AND the δ distribution exhibits an accumulation of angles around angles $-\pi/2$ and $\pi/2$.

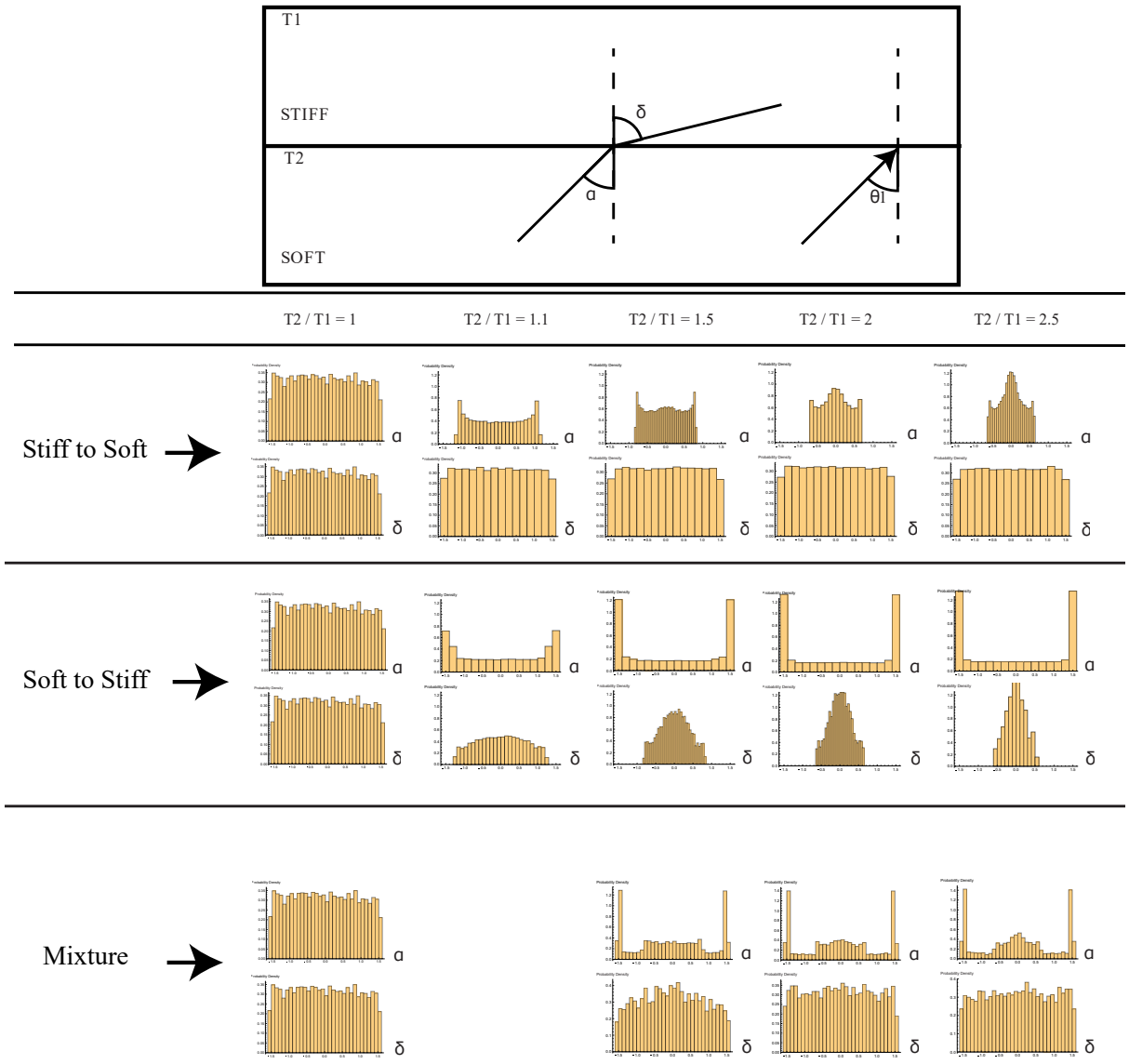


Figure 5.9: (Top Panel) Rays represent neurites. α denotes the angle between the unit normal of the interface and a given neurite, on the soft side of the interface. δ denotes the angle between the unit normal of the interface and a given neurite, on the stiff side of the interface. θ_1 denotes the angle of incidence - the angle with which the neurite initially approaches the interface, and may be equal to either α or δ depending on which side the neurite approaches the interface from. (Table) The α and δ distributions for different values of the traction ratio T_2/T_1, depending on which side the neurites initially approach the interface from. The *Mixture* case represents the scenario where neurites approach the interface from both sides.

5.4 Optic Tract

In this section, we address the problem of Xenopus RGC axons reaching the optic tectum by durotaxis alone. A previous attempt has been made to explain the guidance of these axons to the optic tectum by durotaxis in [53]. In their study, a model of axon bundle durotaxis was derived and simulated on the stiffness field of the Xenopus brain leading to the optic tectum. Although the model reproduced qualitative features of the trajectory of the optic tract, it failed to explain this guidance by durotaxis alone, as only 30% of axon bundles could reach the optic tectum. Here, we utilize our ABC model of axon durotaxis, in combination with the stiffness measurements of the region leading to the Xenopus optic tectum, to show that guidance of individual axons to the optic tectum can be achieved in principle by durotaxis alone.

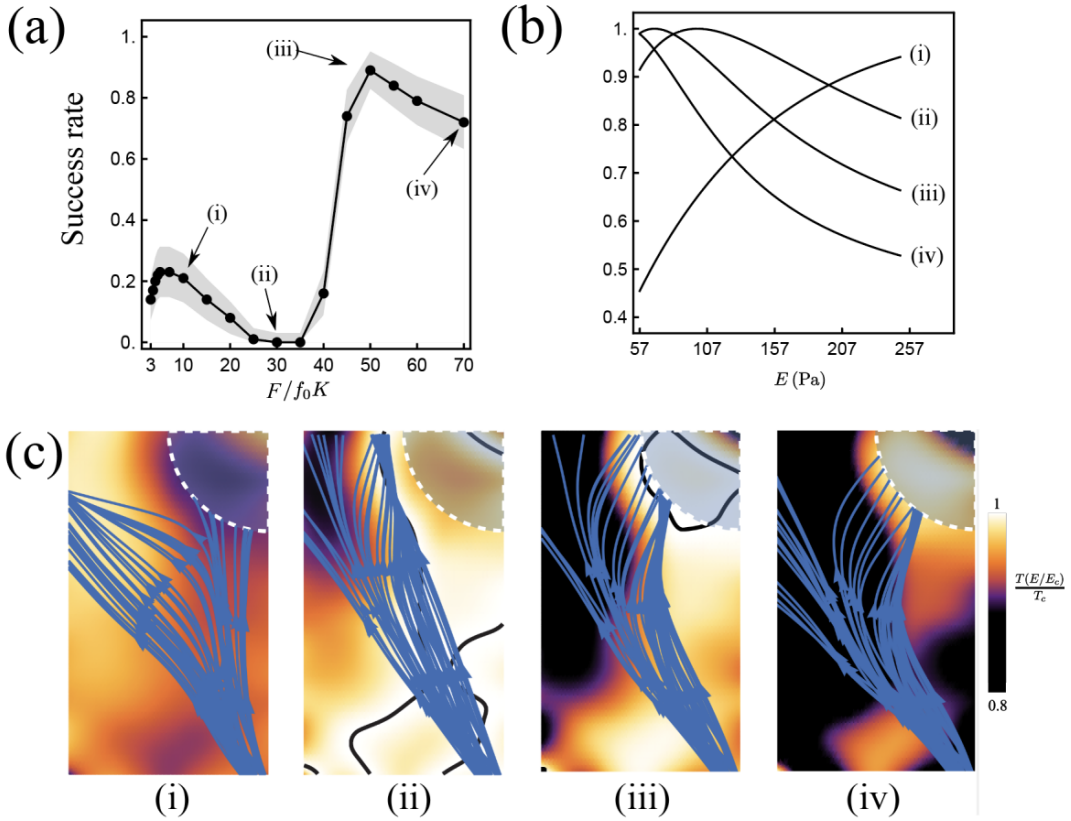


Figure 5.10: (a) Success rate as a function of F. (b) Traction as a function of E for the values of F indicated in (a). (c) Density map of traction for the values of F indicated in (a) overlaid with representative trajectories of axons for the given parameters. $L = 32$ μm, $\mathcal{B} = 10^{-19}$ Nm^2, $R = L/2$, $\varphi_0 = \pi/2$, $\xi = f_0K$, $K = 1/2$, $2\rho R f_0 K \mathcal{H}(r^*) = 10^{-9}$ N, $T_c = f_0 K \mathcal{H}(r^*)$, $\eta = 10^{-5}$Ns, $\zeta = 10^4$ Pa s and $E_c = 6$ kPa.

To study the trajectory of single axons in the optic tract we use a brain rigidity field, $E(x, y)$ with units of pressure, obtained by atomic force microscopy [72]. We investigate

the trajectories of axons growing on a substrate with stiffness field $\chi(x,y) = E(x,y)/E_c$, where E_c is a characteristic stiffness. We simulated $N = 100$ axons, varying their initial position and direction around the entry point of the domain. The target zone (optic tectum) was defined as the quadrant seen in Fig. 5.10(c) and for each set of parameters we record the success rate N_s/N, characterising the ratio of axons successfully reaching the target (with number N_s) to the total number N.

In Chapter 2, we showed that the key features of the traction-stiffness curve $T(\chi)$ relating to axon guidance are $\chi^*, T''(\chi^*)$. These features can be directly controlled through myosin contractility F (see Chapter 2) which can be targeted through pharmacological treatments in experiments such as application of the myosin inhibitor blebbistatin [39], or by modulating the number of myosin molecules; or via the clutch properties [4, 3].

We investigated the effect of myosin contractility on the success rate and found that success rate is a non-monotonic function of F. The analysis of the success rate as a function of contractility allows us to identify four regimes depending on F, where the success rate is in turn decreasing, constant, increasing and decreasing again; see Fig. 5.10(a).

We can understand this non-monotonic behaviour by looking at the resulting traction field $T(E(x,y)/E_c)$ in the four different regimes. We investigate a representative case from each regime; (i)-(iv) in Fig. 5.10(a). In the domain, the rigidity ranges from 57 Pa to 250 Pa. For $F/f_0K = 10$, the optimal stiffness is greater than 250 Pa. Therefore, traction is an increasing function of rigidity between 57 Pa and 250 Pa; see (i) in Fig. 5.10(b). Since the left side of the domain is stiffer than the right side, the traction $T(E(x,y)/E_c)$ smoothly increases from right to left. As a result, most axons are attracted to the left side of the domain leading to a poor success rate of 21%.

As F/f_0K increases further, the optimal stiffness decreases and enters the range of stiffness values present in the domain; see (ii) and (iii) in Fig. 5.10(b). As a result, contours of optimal stiffness form within the domain and axons tend to follow them. In the case of $F/f_0K = 35$, one of these contours leads most of the axons away from the target leading to a catastrophic success rate of 0%; see Fig. 5.10(c), (ii).

For greater values of F/f_0K, with the optimal stiffness decreasing further , the domain becomes roughly bisected by an interface with a region of high traction on the right side of the domain and a region of low traction on the left side of the domain. This situation is similar to the example studied in section Section 5.2 where axons can reflect against a sharp interface between regions of different rigidities. Indeed, we see that for $F/f_0K = 50$, most axons reflect against a well-formed interface between the two regions of low and high traction, and make it to the target; see Fig. 5.10(c), (iii). Because the interface is not perfectly straight, many axons that are not initially reflected by their interaction with the interface, approach again the interface later on. In this case, the axons are refracted

into the region of high traction and subsequently reach the target. This combination of reflection and refraction results in the high success rate of 89%. For $F/f_0K > 50$, a combination of reflection and refraction again results in high success rate. However, the placement of the interface is less favourable and fewer axons reach the target; see Fig. 5.10(c), (iv).

Notably, whilst the model described here can explain guidance of axons to the optic tectum by durotaxis, guiding up to 89% of axons to the target area, the axon bundle model described in [53] could at best achieve a 30% success rate to the target area. An important question is which novelty of the model allows for this increased performance.

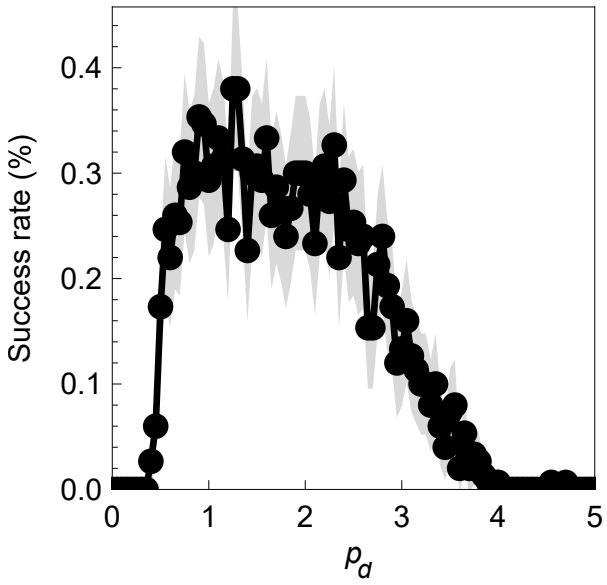


Figure 5.11: Success rate of the bundle model, without noise, as a function of the durotactic number p_d. This parameter, defined in [53] (and therein denoted simply as p), is a dimensionless quantity that governs how strongly an axon bundle steers along stiffness gradients. Modelling the axon bundle as a two-dimensional curve parameterized by arclength s with tangent angle θ, p_d relates the local curvature $\kappa(s) = \theta'(s)$ to the substrate stiffness gradient ∇E at the tip of the bundle via $\theta'(s) = -\frac{p_d}{E_{\max}-E_{\min}}(-\sin\theta, \cos\theta)\cdot\nabla E$.

Since [53] include the effect of noise on axon bundle trajectories, their results are not directly comparable to ours. In order to be able to compare the bundle model directly to the ABC model, we simulated the bundle model on $E(x, y)$, excluding noise. As can be seen in Fig. 5.11, the success rate of the bundle model does not exceed 45% even in the absence of noise.

This confirms that the high success rate exhibited by our model derives from some aspect of the model that is absent from the bundle model, and not due to the exclusion of noise. Thus, the high success rate is contingent on some aspect of the modelling of the axon mechanics and/or of traction generation.

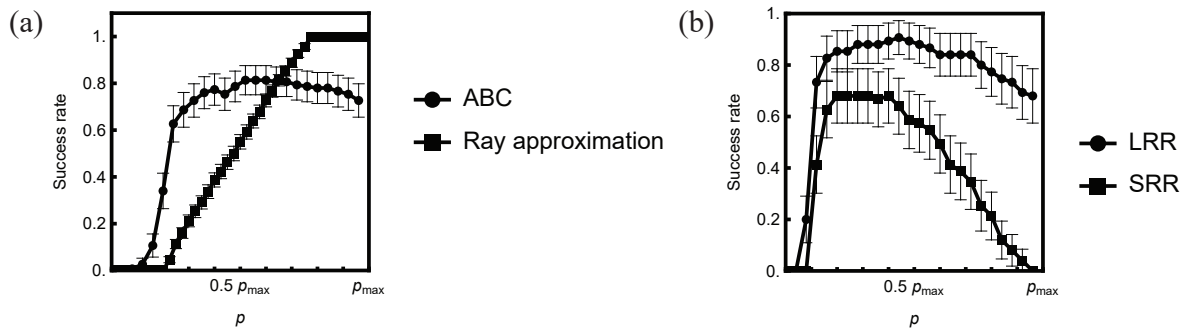


Figure 5.12: (a) Success rate of the: (i) ABC model with a linear traction - stiffness relation with slope $-p$. (ii). Ray approximation with $\varepsilon = 0.1$. (b) Success rate of the LRR and SRR models with a linear stiffness - traction relation with slope $-p$. ABC model was simulated with $L = 32$ μm, $\mathcal{B} = 10^{-19}$ Nm^2, $R = L/2$, $\varphi_0 = \pi/2$, $2\rho R\, T_c = 10^{-9}$N, $\eta = 10^{-5}$Ns, $\zeta = 10^4$ Pa s.

There are a couple of things to note about the better performance of the ABC model. Firstly, it is clear that this improved performance is not due to the non-linear traction-stiffness relation used. In fact, running the ABC model with a linear traction relation of the form

$$T\left(x,y\right)/T_c = 1 - p(E\left(x,y\right) - E_{\min}), \tag{5.36}$$

where $p > 0$ is the gradient of the non-dimensional traction-stiffness curve, provides for success rates as high as 90% (see Fig. 5.12(a)). Note that p can at most be equal to $p_{\max} = 1/\left(E_{\max} - E_{\min}\right)$ in order to exclude negative tractions.

Rather, an important feature seems to be the long range sensing capability that is captured by the model. For example, running the LRR model with the linear traction relation (5.36) results in similar performance and a qualitatively similar success rate curve, as a function of p, to the ABC model with linear traction. However, when this long range sensing capacity is eliminated by artificially setting $L = 0$ in the LRR model (dissociating L from η, ζ, see Section 3.5.3), then performance is reduced and the success rate curve is qualitatively more similar to that of the bundle model (see Fig. 5.12(b)). We call the LRR model with $L = 0$ the *Short Range Reduced* model, *SRR* for short.

Other properties of the ABC model which are decisive for the high success rate, are its refraction-reflection properties. These are in themselves related to the finite spatial extent of the ABC model. As pointed out in the analysis of representative cases appearing in Fig. 5.10, in cases where we observe a high success rate we observe axons reflecting off a virtual interface and ending up at the optic tectum. We observe the same behaviour in the linear traction case. The highest success rate occurs when trajectories are reflected at a virtual interface, around horizontal midpoint of the region (see Fig. 5.13). Most

axons reflect off this interface and reach the optic tectum. This reflection behavior is also exhibited by the LRR model.

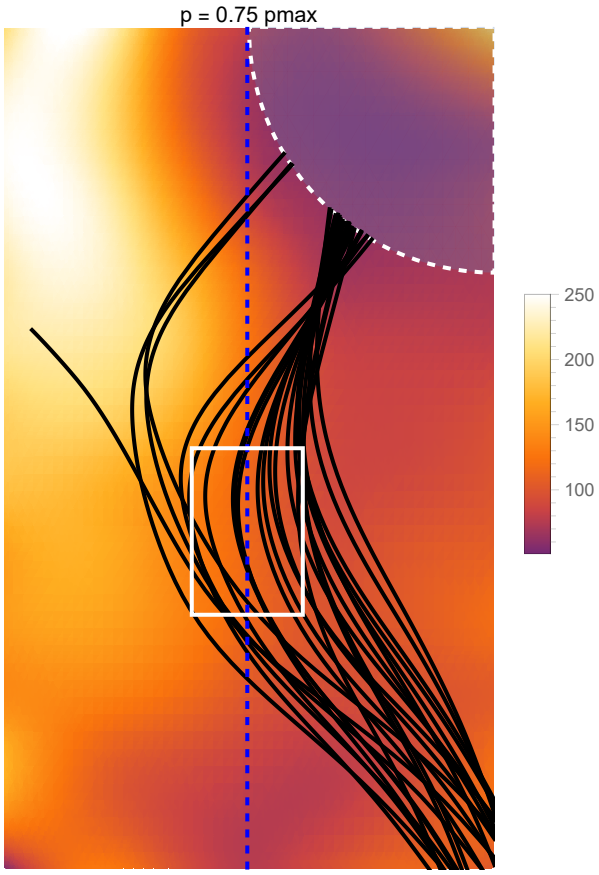


Figure 5.13: Simulated trajectories of ABC model under the linear traction relation for $p = 0.75\, p_{\max}$. Guidance success derives from behaviour reminiscent to reflection against an interface (blue dashed line). E_1, E_2 obtained by averaging stiffness field on each side of the interface within the white rectangle (see text).

To test whether reflection across a virtual interface is sufficient to explain the guidance of axons to the optic tectum by durotaxis alone, we approximate the stiffness field of the region of interest by that of a hard interface between two regions of different stiffness. That is, we assume

$$E(x, y) = \begin{cases} E_2, & \text{if } x < 2.2L \\ E_1, & \text{if } x \geq 2.2L, \end{cases} \tag{5.37}$$

where $x = 2.2L$ describes the horizontal coordinate of the virtual interface (blue-dashed line in Fig. 5.13).

We choose E_1, E_2 by averaging on either side of the interface over the respective half of the measured stiffness field within the indicated rectangle (white outline in Fig. 5.13). The

rectangle is chosen with a horizontal width of $2R$, in consideration of the spatial extent and range of the growth cone. Averaging, we obtain $E_2 = 126$ Pa and $E_1 = 106$Pa.

Furthermore, we approximate axons as rays, approaching the interface from the lower right corner of the region, at $(x, y) = (x_{\max}, y_{\max})$. We sample the angle of incidence, θ_1, of these rays from a uniform distribution on $(4\pi/15, 2\pi/5)$, which is equivalent to the sampling distribution for initial clutch directions in the ABC simulations. As a simplification, we assume that if a ray is not reflected, then it will not reach the optic tectum. If the axon is reflected, then we look at the angle of reflection and check whether this leads the ray to the optic tectum. Assuming the linear traction relation, the traction ratio is then given by

$$\alpha_T = \frac{1 - p\,(E_2 - E_{\min})}{1 - p\,(E_1 - E_{\min})}. \tag{5.38}$$

Assuming $\varepsilon = 0.1$, we obtain the success rate as a function of p. The resulting curve closely follows the qualitative behaviour of the ABC model under the linear traction relation. For $p = 0.0$, traction is equal on both sides of the interface, giving $\alpha_T = 1$. In this case, no axons are reflected, and none reach the optic tectum, resulting in a success rate of 0. As p increases, α_T decreases from 1. Consequently, the critical angle decreases, and a growing fraction of axons are reflected at the interface and reach the optic tectum, producing an approximately linear rise in success rate. As shown in Section 5.2, reflected axons travel at angles nearly parallel to the interface, ensuring that most—if not all—reach the optic tectum. With further increases in p, the critical angle approaches 0. Since the incidence angles of approaching axons have a lower bound, there exists a threshold value of p beyond which all incidence angles exceed the critical angle. Beyond this point, all axons are reflected and, with reflection angles close to $\pi/2$, reach the optic tectum. The success rate therefore saturates at 1.0 for p above this threshold, consistent with the saturation observed in the ABC model (see Fig. 5.12(a)).

The high proportion of axons which successfully reach the target area under the different variations of the ABC model suggests that differential traction generation due to variations in local stiffness can explain guidance of RGC axons to the optic tectum. Our results indicate that this guidance does not occur by following lines of optimal stiffness, and can be achieved with or without the optimal stiffness of RGC growth cones being attained by the stiffness field leading to the optic tectum. Rather, our analysis indicates that this guidance can be achieved as a consequence of reflection of axons off a virtual interface formed in the stiffness field leading to the optic tectum. Furthermore, this result is dependent on the finite spatial extent of the axon and its reflection-refraction properties.

5.5 Segmented outgrowth of motor axons in the PNS

In this section, we utilize the ABC model to investigate whether the segmented outgrowth of motor axons from the neural tube during patterning of the peripheral nervous system (PNS) can occur successfully by durotaxis alone. Firstly, we derive a model for the stiffness field of the environment motor axons encounter after their outgrowth from the neural tube. See Fig. 5.14 (A) for a schematic of the sclerotome and Fig. 5.14 (B) for a frontal section of the environment motor axons encounter after their outgrowth from the neural tube, taken from a developing chick embryo. Secondly, we describe a metric for efficient segmentation of motor axons, in order to quantify what it means for segmentation to have occurred successfully. Finally, we simulate the trajectories of axons through this stiffness field and show that, segmentation occurs most efficiently when axons follow lines of optimal stiffness around the posterior half somites.

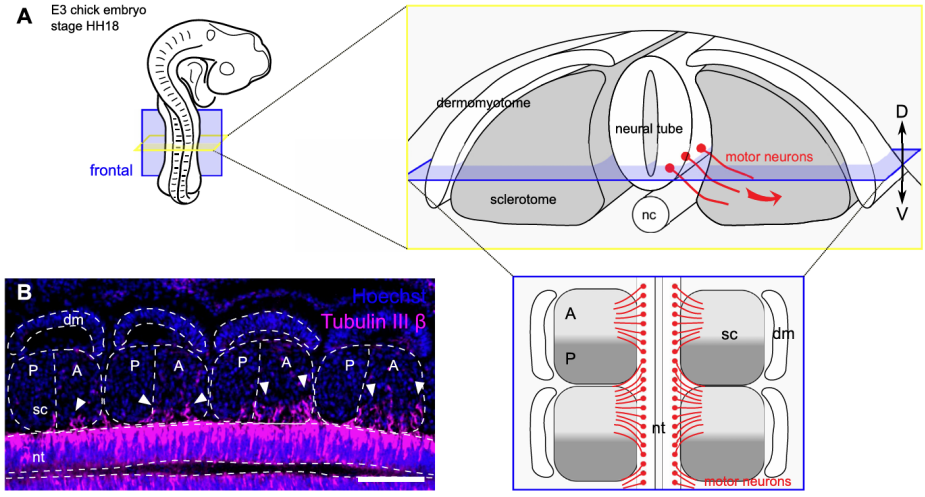


Figure 5.14: (A) Schematic of the developing chick embryo. Motor neuron axons (red) from the neural tube grow out of the neural tube into the sclerotome (sc). In Schaeffer et al [65], the frontal plane (in blue) is used to study the growth patterns of these axons. (B) Frontal section of a chick embryo showing motor axons (Tubulin III β) that have grown out of the neural tube (nt). Motor axons avoid the P regions and invade the A regions. Scale bar (white, lower right) represents 100µm. Figure adapted from Schaeffer et al [65].

5.5.1 2D Somite stiffness field

To investigate the segmentation of outgrowing motor axons using our model, a 2D stiffness field is required for the region of interest. From Schaeffer et al [65] we have a reasonable idea of what the stiffness field looks like along a certain horizontal strip of the domain, where the authors obtained stiffness measurements. The stiffness field along this strip

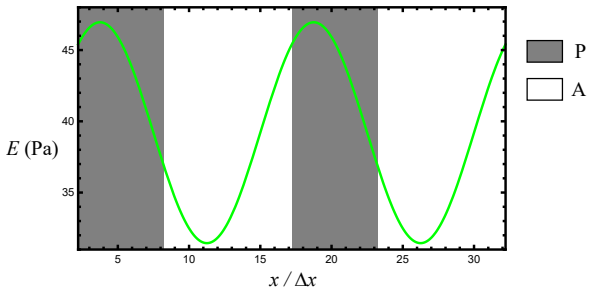


Figure 5.15: Horizontal stiffness field. Horizontal regions corresponding to posterior halves coloured in gray.

exhibits a periodic pattern of high and low stiffness which correlates with the placement of posterior-half (stiff) and anterior-half (soft) sclerotomes and is well approximated by a sinusoidal function of the form

$$E(x) = A\sin(\omega x) + B, \tag{5.39}$$

However, it is not clear how to continue the stiffness field along the vertical axis. The limited vertical data available from Schaeffer et al [65] indicates that as one approaches a posterior half vertically and from below, the stiffness rapidly transitions from a low to a high value, where this low value is comparable to the stiffness in the anterior-half sclerotomes. Based on this experimental fact we assume that the posterior somites constitute regions of higher stiffness surrounded by an environment of lower stiffness (including the anterior-half sclerotomes).

Thus, in our modelling, there are two desirable properties that the stiffness field ought to have. The further along the increasing vertical axis we go, the closer the horizontal stiffness field should be to (5.39). The further along the decreasing vertical axis we go, the more homogeneous the horizontal stiffness field should be. Mathematically, these properties can be expressed as $E(x,y) \to A\sin(\omega x) + B$ as $y \to +\infty$ and $E(x,y) \to E_\infty \in \mathbb{R}$ as $y \to -\infty$. Any field of the form

$$E(x,y) := (A\sin(\omega x) + B)\,G(y) + E_\infty\,(1 - G(y)), \tag{5.40}$$

where $G(y)$ satisfies $G(y) \to 1$ as $y \to +\infty$ and $G(y) \to 0$ as $y \to -\infty$, has the prerequisite properties. Here, $G(y)$ characterizes the transition of the stiffness field along the vertical axis from a homogeneous state (characterized by E_∞) to a periodic state (characterized by 5.39). A simple model for $G(y)$ is

$$G(y) = \frac{1}{2}\left[1 + \tanh\left(\frac{y - y_0}{\lambda}\right)\right], \tag{5.41}$$

where λ is the length scale of the transition.

Having given the general form of the field $E(x, y)$, we must determine the parameters $A, B, \omega, \lambda, y_0, E_\infty$. The choice of y_0 is of no consequence as long as axons are initialized far below the transition region, so we choose $y_0 = 0$. Schaeffer et al [65] estimate $\omega = 0.45/\Delta x \pm 0.064/\Delta x$, where $\Delta x = 15\mu\text{m}$ is the spatial fidelity of measurements. This spatial frequency is close to the theoretical prediction of $\omega = 2\pi/(15\Delta x) = 0.42/\Delta x$, which is arrived at by considering that a whole somite has an average length of $15\Delta x$. We choose the theoretical value $\omega = 2\pi/(15\Delta x)$ as, once we define the spatial extent of each posterior-half and anterior-half, this will ensure that the stiffness field along the horizontal is identical in all posterior halves and all anterior halves.

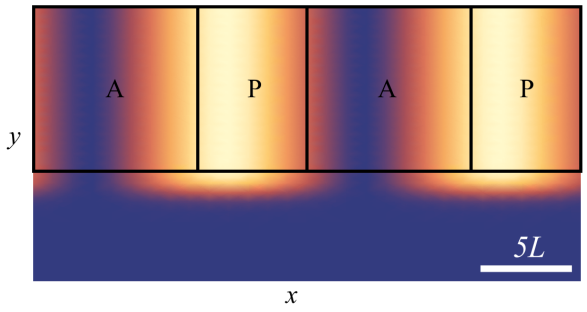


Figure 5.16: Density plot of the stiffness field of the sclerotome, $E(x, y)$. The black rectangles indicate the boundaries of the posterior halves, which on average are stiffer than the anterior halves. Scale bar (white line, lower right) represents a length of $5L$, where $L = 32\mu\text{m}$ and represents the length of the axon beam.

To determine the parameters A, B we consider the measured average horizontal apparent elastic modulus in the anterior-halves and posterior-halves of the sclerotomes. It is estimated that this quantity in the anterior-halves and posterior-halves is $\bar{E}_a = 36\,\text{Pa}$ and $\bar{E}_p = 44\,\text{Pa}$, respectively. A, B can be chosen so that the average of $E(x)$ (the theoretical value of the horizontal apparent elastic modulus at each horizontal point x) in an anterior-half somite and in a posterior-half somite equals $\bar{E}_a$ and $\bar{E}_p$, respectively. To do so, we first need to define the spatial extent and position of each half. From the measurements of Schaeffer et al [65] we know that each posterior half has an average length of $6\Delta x$ and each anterior-half has an average length of $9\Delta x$. The peak of each sinusoid is found within the posterior half and the trough in the anterior half. Each posterior half begins just before a peak of the sinusoid and ends just before the following trough, at which point the adjacent anterior half begins (See Fig. 5.15). We assume that the first posterior half on the positive x-axis begins at x_p where $(E(x_p) - B)/A = 0.8$. Equivalently, when $\sin(\omega x_p) = 0.8$ and x_p is before the first peak (which is at $x = \pi/(2\omega)$). Thus, the first posterior half spans the interval $[x_p, x_p + 6\Delta x)$ and the next anterior half the interval $[x_a, x_a + 9\Delta x)$, where $x_a = x_p + 6\Delta x$. The average, $\bar{E}$, of $E(x)$ on the interval

$[x_0, x_1]$ is given by

$$\bar{E} = \frac{1}{x_1 - x_0} \int_{x_0}^{x_1} E(x) \mathrm{d}x. \tag{5.42}$$

Therefore, using (5.39), the theoretical predictions for the average horizontal stiffness in the posterior and anterior half sclerotomes are given by

$$\bar{E}_p = B + \frac{A}{6\Delta x \times \omega} \left[\cos\left(\omega x_p\right) - \cos\left(\omega x_p + 6\Delta x \times \omega\right)\right], \tag{5.43}$$

$$\bar{E}_a = B + \frac{A}{9\Delta x \times \omega} \left[\cos\left(\omega x_a\right) - \cos\left(\omega x_a + 9\Delta x \times \omega\right)\right]. \tag{5.44}$$

The above two equations can be solved for the unknowns A, B. For the stated estimates for $\bar{E}_p, \bar{E}_a, \Delta x, \omega, x_p, x_a$, we determine

$$A = 7.75 \text{ Pa}, B = 39.2 \text{ Pa}. \tag{5.45}$$

The spatial resolution of measurements in the study was Δx. The transition from low to high stiffness over the vertical axis occurs between adjacent vertical measurement points, so the choice of $\lambda = \Delta x/2 = 7.5\mu\text{m}$ is appropriate. We choose $E_\infty = B - A$ such that the environment away from the somites has a stiffness equal to the minimum observed stiffness in the somites. This is the choice of $E(x, y)$ which we use in the following analysis (See Fig. 5.16). To obtain the non-dimensional stiffness, $\chi(x, y)$, we divide E by a characteristic stiffness E_c. That is, $\chi = E/E_c$.

5.5.2 Segmentation efficiency

To say that segmentation occurred successfully (or unsuccessfully) implies that we have a method by which we can compare different examples of segmentation. Having defined the environment on which we will simulate axons, we now provide a quantitative metric to characterize the degree of successful segmentation of outgrowing axons in the PNS, which will allow such comparisons.

During the segmentation process, axons must traverse the sclerotome, avoid the posterior-halves and grow through the anterior-halves, in order to avoid any obstructions from future cartilage of the vertebral column. Therefore, as we have characterized the segmentation process, there are two things that characterize successful segmentation: (1) Axons must traverse the sclerotome by reaching a minimal y value, which we denote by $y_{\min}$. (2) Axons must minimize growth in the regions labeled P (See Fig. 5.16).

The first condition can be quantified by a probability describing the likelihood that a randomly initialized axon reaches a chosen termination point $y = y_{\min}$. All else being equal, having an axon reach the termination point is better than not (see Fig. 5.17(i)).

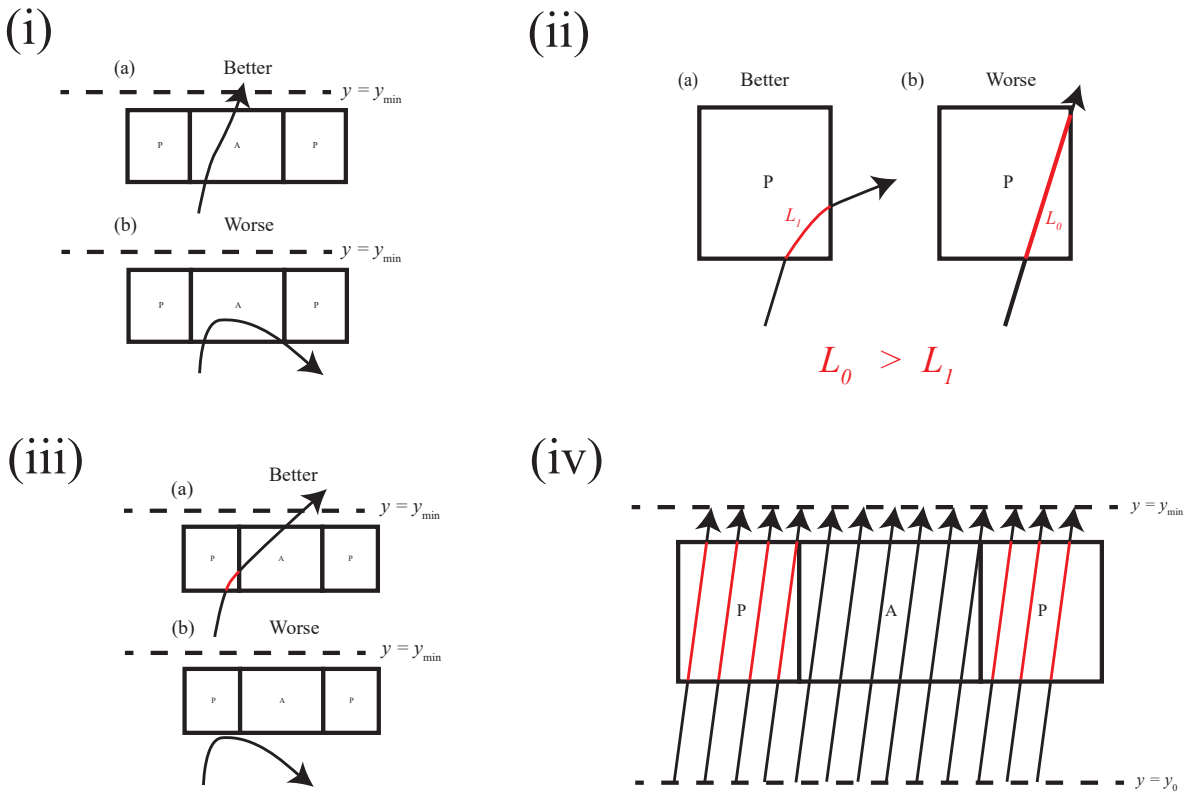


Figure 5.17: (i) When comparing two axon trajectories that do not cross into the P regions, segmentation is more efficient in the scenario where the axon crosses the sclerotome (a) than in the one where it does not (b). (ii) When comparing two axons trajectories that cross the sclerotome, segmentation is more efficient in the scenario in which the length of the crossing axon that is found within P is smaller (a) than the one with the large such length (b). (iii) Combining the ideas (i)-(ii) one obtains a metric of segmentation efficiency that may prefer a scenario where an axon penetrates slightly into a P region but crosses the sclerotome (a) than a scenario where the axon does not penetrate the P regions but does not cross (b). (iv) Example of axon trajectories under the baseline scenario where the environment is non-informative to axon trajectories. Such trajectories are used to compute the baseline efficiency η_0 as a function of the initial outgrowth angle of the axons.

We denote the probability of an axon doing so by p_{cross}. All else equal, the higher the value of p_{cross}, the more successfully segmentation has occurred.

For the second condition, better than simply counting how many axons cross into the posterior-halves is measuring the total length of axons which lie in the regions P. A situation where an axon enters a posterior half but then quickly exits it is better than a situation where an axon grows substantially into it before exiting (see Fig. 5.17(ii)). We denote the total length within all regions P of a randomly initialized axon by the random variable Λ. Initializing a large number of axons to explore the environment will result in a distribution of lengths contained within the regions P and this distribution is equal to the distribution of Λ. When comparing two examples of segmentation, with all else being equal, the scenario with the smaller total axon length in P is the more favorable one, with respect to segmentation. Equivalently, the one with a smaller mean axon length within regions P, equal to $\mathbb{E}[\Lambda]$, is more favorable. Therefore, all else being equal, the smaller $\mathbb{E}[\Lambda]$ is, the more successfully segmentation has occurred.

In certain cases, these two metrics for successful segmentation contradict each other. For example, one way to maximize p_{cross} is for axons to travel in straight trajectories across the sclerotome, to the termination line, whilst completely disregarding whether they cross into the P regions. In this way, all axons may cross, giving $p_{\text{cross}} = 1$. However, the mean axon length in P will be large and thus this instance of segmentation will perform poorly according to the second metric ($\mathbb{E}[\Lambda]$). Conversely, a way to minimize the mean length in P is to make axons reorient and travel in the negative y direction, thus never reaching the P or A regions. In this way, no axons cross into P, resulting in $\mathbb{E}[\Lambda] = 0$. However, this scenario leads to no axons crossing the sclerotome and thus $p_{\text{cross}} = 0$. Thus, for successful segmentation of the PNS to occur, a balance between a high p_{cross} and a low $\mathbb{E}[\Lambda]$ must be achieved.

A good metric for successful segmentation must take the tension between these two metrics into consideration. One that does so is

$$\eta_{\text{s}} = \frac{L\, p_{\text{cross}}}{\mathbb{E}[\Lambda] + L}, \tag{5.46}$$

which we call the *segmentation efficiency*. Ignoring the $+L$ term in the denominator, the segmentation efficiency is a dimensionless measure of the 'exchange' rate between the probability of an axon crossing and the mean axon length in the P regions. i.e. how many axons can get across per unit of 'wasted' axon length? The $+L$ term in the denominator is arbitrary and is introduced to ensure that the segmentation efficiency is a bounded function of p_{cross} and $\mathbb{E}[\Lambda]$. The higher the value of η_{s}, the more successful we consider axonal segmentation to have occured and the maximum value that can be obtained for efficiency is $\eta_{\text{s}} = 1$. We use this metric in the following analysis.

This definition of segmentation efficiency makes explicit the trade-off between crossing the sclerotome and avoiding the posterior halves. In particular, because η_s rewards successful crossing while penalizing axon length in the P regions, it may sometimes be more favorable for an axon to enter a P region over a short distance if doing so increases the likelihood of reaching the termination point, rather than failing to reach it altogether (see Fig. 5.17(iii)).

Later, it will be useful to compare η_s to η_0, which is the particular value of η_s for the case where axons ignore all environmental information and travel in straight lines (see Fig. 5.17(iv)).

5.5.3 Initial conditions

We initiate axons far below $y = 0$, with initial x- component of the beam clamp initialized with x-values $\hat{x}(0)_j = x_p + \frac{j}{N} \times 15\Delta x$, $j = 0, ..., N-1$, and with $\mathsf{y}(x, 0) = 0, \hat{\theta}(0) = \theta_0$. In the analysis we vary $\theta_0 \in (0, \pi)$ and use $N = 40$.

5.5.4 Results

We now evaluate the segmentation efficiency η_s under different conditions to determine whether durotaxis alone can generate segmented motor axon outgrowth in the stiffness field defined by (5.40). We compare three traction-stiffness relations: the motor clutch relation , a phenomenological Gaussian relation, and a phenomenological linear relation. The main results are as follows:

1. The motor clutch relation can improve segmentation efficiency relative to the baseline case (no durotaxis), but only weakly. In the parameter range explored, it does not produce sufficiently attractive lines of optimal stiffness.

2. Maximal segmentation efficiency is obtained when there exist lines of optimal stiffness surrounding the posterior-half regions P.

3. For the phenomenological Gaussian relation, maximal efficient segmentation can be achieved with an optimal stiffness near $E^* = 35$ Pa and a sufficiently large curvature near the optimal stiffness.

4. A purely linear decrease of traction with stiffness can improve segmentation, but this mechanism is less robust and is highly sensitive to the initial axon outgrowth angle.

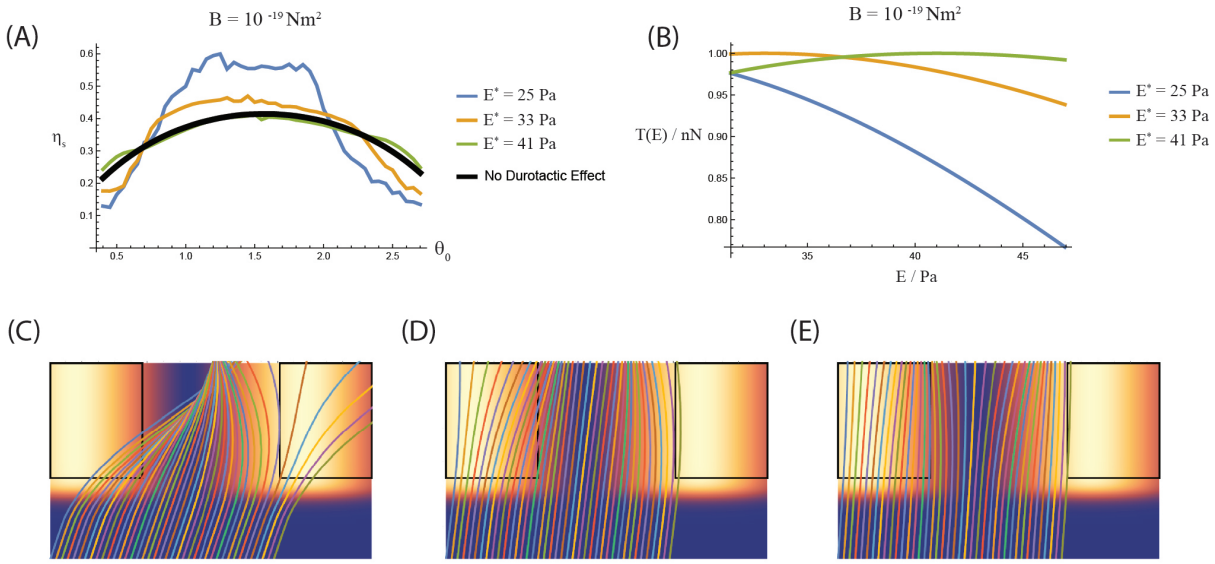


Figure 5.18: (A) Segmentation efficiency, η_s, as a function of initial axon outgrowth angle θ_0 for different traction-stiffness curves generated by the motor clutch model of Chapter 2. Baseline efficiency η_0 indicated in black. (B) Traction - stiffness curves for the particular cases $E^* = 25, 33, 41$ Pa. (C)-(E) Axon trajectories for each of the traction-stiffness curves corresponding to $E^* = 25, 33, 41$ Pa, with θ_0 chosen to maximize η_s in each case. Density plot represents the stiffness field $E(x, y)$ (5.40) . Parameters: $\mathcal{B} = 10^{-19}\text{Nm}^2$, $R = L/2$, $\varphi_0 = \pi/2$, $\eta = 10^{-5}$Ns, $\zeta = 10^4$ Pa s, $T_c = f_0 K\mathcal{H}(r^*)$, $2\rho R\sin(\varphi_0)\, T_c = 1$nN, $k_{\text{on}} = 1.0\,\text{s}^{-1}, k_{\text{off}} = 0.1\,\text{s}^{-1}$, $\Xi = 10^{-3}$Ns/m, $f_0 = 2$ pN, $k_c = 5 \cdot 10^{-3}$N/m, $N_T = 75$, $M = f_0 N_T k_{\text{on}}/k_{\text{off}} \approx 1.5$nN.

Motor clutch traction relation

To apply the motor clutch relation, we must relate the dimensionless stiffness χ to the dimensional stiffness E of the somite field. Since this requires the choice of a characteristic stiffness E_c, and since E_c is not directly determined by the present data, we vary E_c and express the results in terms of the dimensional optimal stiffness $E^* = E_c\chi^*$. Varying E_c shifts the location of the optimal stiffness and has a similar qualitative effect to varying the myosin contractility parameter F, although increasing E_c increases E^* whereas increasing F decreases it.

For each initial angle $\theta_0 \in (0, \pi)$, we simulate axon trajectories and compute η_s. Fig. 5.18(A) shows that the highest efficiencies occur when the initial outgrowth direction is approximately aligned with the y-axis. The motor clutch relation improves on the baseline efficiency η_0 when the optimal stiffness is around $E^* = 25$ Pa, but the improvement is modest. When $E^* = 41$ Pa, the efficiency is comparable to the baseline case.

The corresponding axon trajectories explain this behavior. For $E^* = 25$ Pa, trac-

tion decreases approximately linearly over the stiffness range present in the domain (Fig. 5.18(B)). Furthermore, the decrease in traction over this range is small, resulting in a weak guidance signal. This weak signal results in only a mild deflection of axons, leading to a reduction of their length inside the P regions while still reaching the termination line (Fig. 5.18(C)). By contrast, when $E^* = 41$ Pa, the traction-stiffness relation is nearly flat over the relevant stiffness range. The environment is then effectively non-informative, and the trajectories resemble the baseline case: axons cross the sclerotome, but do not avoid the P regions (Fig. 5.18(E)).

Thus, in the parameter range explored, the motor clutch model does not produce strong guidance by lines of optimal stiffness. Its best performance arises instead from an approximately monotone decrease of traction with stiffness.

Phenomenological Gaussian relation

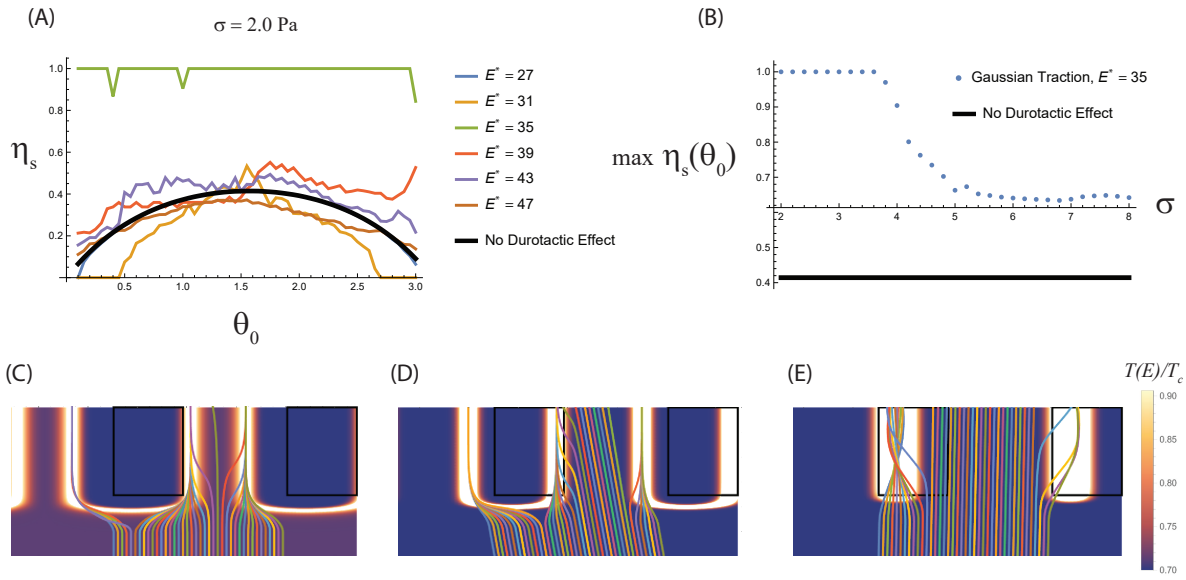


Figure 5.19: (A) Segmentation efficiency, η_s, as a function of initial axon outgrowth angle θ_0 for traction-stiffness curves generated by (5.47). Baseline efficiency η_0 indicated in black. (B) Maximum segmentation efficiency over $\theta_0 \in (0, \pi)$, as a function of σ. (C) - (E) Axon trajectories for each of the traction-stiffness curves generated by (5.47) corresponding to $E^* = 35, 39, 47$ Pa and $\sigma = 2.0$ Pa, with θ_0 chosen to maximize η_s in each case. Density plot indicates the local traction field at each point. Parameters: $2\rho R \sin(\varphi_0) T_c = 10^{-9}$N, $\mathcal{B} = 10^{-19}$Nm^2, $R = L/2$, $\varphi_0 = \pi/2$, $\eta = 10^{-5}$Ns, $\zeta = 10^4$ Pa s.

To isolate the effect of guidance by lines of optimal-stiffness, we next prescribe a phenomenological traction-stiffness relation in which the optimal stiffness and the curvature

at the optimum can be varied independently. We use

$$T(E) = T_0 + (T_c - T_0) \exp\left(-\frac{(E - E^*)^2}{\sigma^2}\right), \tag{5.47}$$

where T_c is the maximal traction, T_0 is the traction away from the optimum, and σ controls the width of the optimal-stiffness response. We choose $T_0 = 0.7\,T_c$. The curvature at the optimum is

$$T''(E^*) = -\frac{2(T_c - T_0)}{\sigma^2}. \tag{5.48}$$

Thus, smaller values of σ correspond to more attractive lines of optimal stiffness.

The highest segmentation efficiencies occur when $E^* = 35$ Pa and σ is sufficiently small (Fig. 5.19(A)). In this case, the lines of optimal stiffness form around the exterior of the P regions. Axons approaching a P region are captured by these lines and guided around it, producing axonal "highways" through the A regions (Fig. 5.19(C)). This yields efficient segmentation over a broad range of initial angles θ_0.

When the optimal stiffness is increased, the optimal-stiffness lines move into the P regions. Axons are then guided into the regions they should avoid, and segmentation efficiency decreases sharply (Fig. 5.19(D)–(E)). Thus, under this mode of guidance, efficient segmentation requires not merely the existence of an optimal stiffness, but its correct spatial placement relative to the P regions.

In addition to the correct placement of the lines of optimal stiffness, these lines must be sufficiently attractive to axons. In order to investigate how attractive these lines must be, we fixed $E^* = 35$ Pa and computed the dependence of the maximum efficiency achieved over $\theta_0 \in (0, \pi)$ on σ. The dependence on σ is shown in Fig. 5.19(B). For broad traction-stiffness curves, for example $\sigma \approx 8$ Pa, the maximum efficiency is approximately 0.6, comparable to the best motor clutch result. As σ decreases, the efficiency rises sharply and reaches the maximal value $\eta_s = 1$ for $\sigma \lesssim 3.5$ Pa. Therefore, near-maximal segmentation requires both $E^* \approx 35$ Pa and sufficiently large negative curvature $T''(E^*)$, corresponding to $\sigma \lesssim 3.5$ Pa.

Linear traction relation

The motor clutch simulations showed that the best motor clutch result occurred when the traction-stiffness relation was approximately linear over the stiffness range present in the domain. We therefore ask whether a purely linear traction-stiffness relation can also produce efficient segmentation. We consider

$$T(E) = T_c + m(E - E_{\min}), \tag{5.49}$$

where $m < 0$.

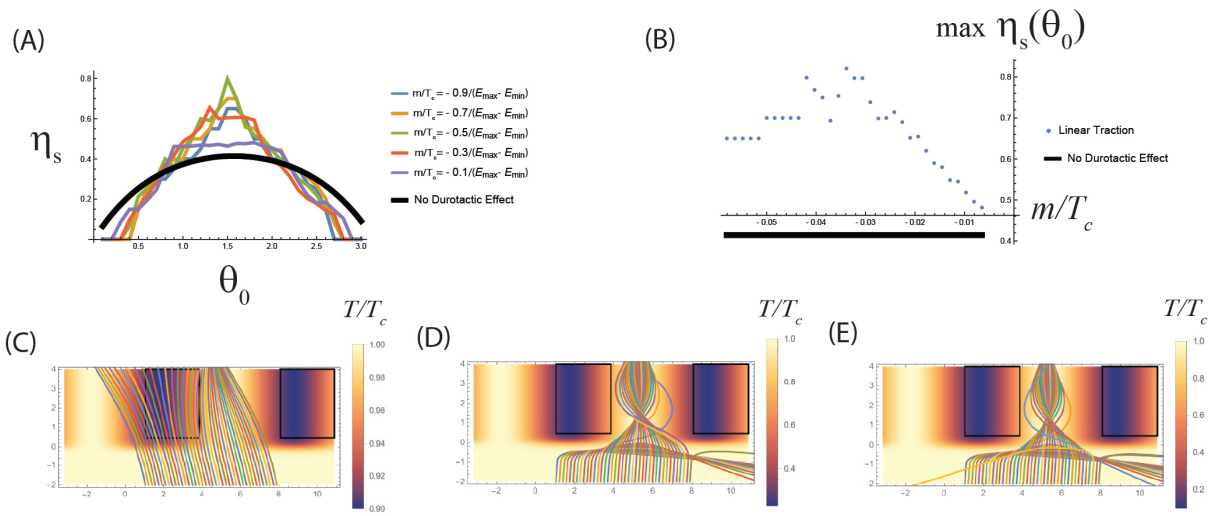


Figure 5.20: (A) Segmentation efficiency, η_s, as a function of initial axon outgrowth angle θ_0 for traction-stiffness curves generated by 5.49. Baseline efficiency η_0 indicated in black. (B) Maximum segmentation efficiency over $\theta_0 \in (0, \pi)$, as a function of m. (C) - (E) Axon trajectories for each of the traction-stiffness curves generated by 5.49 corresponding to $m/T_c = -0.1/(E_{\max} - E_{\min}), -0.775/(E_{\max} - E_{\min}), -0.9/(E_{\max} - E_{\min})\,\text{Pa}^{-1}$ and with θ_0 chosen to maximize η_s in each case. Density plot indicates the local traction field at each point. Parameters: $2\rho R \sin(\varphi_0) T_c = 10^{-9}\text{N}$, $\mathcal{B} = 10^{-19}\text{Nm}^2$, $R = L/2$, $\varphi_0 = \pi/2$, $\eta = 10^{-5}\text{Ns}$, $\zeta = 10^4$ Pa s.

Under the linear traction-stiffness relation, segmentation efficiency is maximized for intermediate negative slopes, around $m \approx -0.5 T_c/(E_{\max} - E_{\min})$, where the efficiency reaches approximately 0.8 (Fig. 5.20(B)). This is higher than the best motor clutch result, but lower than the maximal efficiency obtained with the phenomenological Gaussian relation. Moreover, the high-efficiency regime is narrow in θ_0: efficient segmentation occurs only when the initial axon direction is close to $\pi/2$ (Fig. 5.20(A)).

The reduction in efficiency for small and large $|m|$ has different causes. When $|m|$ is small, the traction field is weakly informative and the behavior approaches the baseline case. When $|m|$ is large, the transitions in traction near the boundaries of the P regions become steep. Axons then interact with these transitions in a manner analogous to refraction and reflection at a sharp interface. Since regions outside P correspond to higher traction, many axons are reflected away from P; however, axons interacting with the lower boundary of a P region can also be reflected back toward the bottom of the domain and fail to cross the sclerotome (Fig. 5.20(D)–(E)). Thus, for large $|m|$, the decrease in p_{cross} reduces the overall segmentation efficiency.

Limitations and discussion

These results indicate that segmented motor axon outgrowth can, in principle, occur efficiently by durotaxis alone. However, efficient segmentation is not produced by any traction-stiffness relation with an optimum. Rather, the optimal-stiffness lines must be positioned around the P regions and must be sufficiently attractive to redirect axons around them and through the A regions.

Within the parameter space explored, the motor clutch model does not satisfy this condition. Although it produces traction-stiffness curves with an optimal stiffness, the curvature near the optimum is too small to make the corresponding optimal-stiffness lines strongly attractive. As a result, the motor clutch relation produces only modest improvements over the baseline case. This suggests either that motor axon segmentation is not driven by the traction-based durotactic mechanism considered here, or that the motor clutch formulation used here is not sufficiently realistic for this biological setting.

The phenomenological models clarify what would be required for durotaxis to drive efficient segmentation. The optimal-stiffness relation shows that near-maximal efficiency is possible when E^* lies just outside the stiffness range of the P regions, so that the corresponding contours surround rather than enter them. The linear relation shows that monotone durotaxis can also improve segmentation, but in a less robust manner: it requires a favourable initial outgrowth direction and does not achieve maximal efficiency.

The model therefore makes a qualitative prediction. Perturbations that increase the dimensional optimal stiffness, for example by reducing myosin contractility in the growth cone, should move the optimal-stiffness lines into the P regions and reduce segmentation efficiency. Conversely, efficient durotactic segmentation would require a traction-stiffness response with sufficiently sharp attraction toward an optimal stiffness located along paths that guide axons around the P regions.

5.6 Conclusion

In Chapter 3 we developed a complete framework to study axon durotaxis. In this chapter, we utilized that framework to study a number of in-vivo and in-vitro scenarios where it is hypothesised that axon durotaxis plays a significant role. Specifically, we focused on applying our framework to investigate three scenarios of axon guidance: (1) axons interacting with a sharp interface; (2) axon durotaxis along the optic tract; (3) the role of axon durotaxis in the proper segmentation of the peripheral nervous system.

Application (1): Sharp Interfaces

A scenario that frequently appears in in-vitro experiments is that in which axons interact with a sharp interface between two regions of different environmental conditions [77, 75, 63, 73]. In Section 5.2 we studied how axons simulated from our ABC model interact with such an interface, modeling the difference in substrate conditions across the interface as a difference in local growth cone traction generation. The simulated axons exhibited refractive and reflective behaviors when interacting with the interface. Notably, reflected axons remained much more parallel to the interface than what light-rays or previous models of axon bundles would predict. This behavior is similar to the one that has been observed experimentally. It has been observed that axons travelling towards a boundary between a region of high adhesion and a region of low adhesion, reorient at the interface, preferring to travel parallel to the interface. Furthermore, this reorientation was shown to be contingent on the myosin contractility of the growth cone, a crucial component in traction generation. When myosin contractility was negated through the application of blebbistatin (and hence negating the traction generation of the growth cone) axons did not turn at the interface, instead crossing over into the low adhesion region, growing in straight lines. The contingency of the axon's ability to turn at the interface on myosin contractility and hence possibly on traction generation, creates a connection between these experimental results and our model predictions. Furthermore, we showed that our model lacks time-reversal symmetry, a crucial determinant of the reflective properties of both light-rays and the referenced axon bundle model.

A setup approximating that of a sharp interface between two regions of different stiffness was created by [73] and the behavior of axons on this environment was studied. The authors found that, after allowing axons to grow and traverse the boundary, the distribution of the angles that axons made with the normal to the interface on the soft side was peaked at 0 degrees (parallel to the interface normal), indicating some possible effect of the interface on axon trajectories. However, the authors could not determine from which side each axon had originated. In Section 5.3, we investigated whether our model could reproduce this data. A consequence of the lack of time reversal symmetry of axons interacting with a sharp interface, discussed in Section 5.2, is that one can in principle disambiguate the point of origin of each neurite just from the observation of its final shape. Running ensemble simulations of the sharp interface case, we find that a peaked distribution at 0 degrees on the soft side arises when either: (i) the neurite growth cones exert a higher traction on the soft side than on the stiff side AND δ is uniformly distributed. (ii) the neurite growth cones exert a lower traction on the soft side AND the δ distribution exhibits an accumulation of angles around angles $-\pi/2, \pi/2$. This analysis

illustrates how the specific features of our model, such as time-irreversibility, make a substantial difference in the behaviour predicted of neurites.

Application (2): Optic tract

In Section 5.4 we investigated the in-vivo scenario of Xenopus RGC axons navigating to the optic tectum. Understanding this guidance and the role of durotaxis in it has played a significant motivating role in the field of study of axon durotaxis [38, 72]. A previous study [53] that developed a specific model for axon bundles could not explain the reliable guidance of axons to the optic tectum by durotaxis alone. Conversely, here we find that by use of the ABC model, in combination with the motor clutch traction, it is possible for axons to be reliably guided to the optic tectum by durotaxis alone. Furthermore, we find that the ability of axons to be reliably guided to the tectum by durotaxis is independent of the particular form of the traction-stiffness relation, as similarly reliable guidance is achieved when the local traction is a linear traction-stiffness relation.

The fact that reliable guidance is independent of the particular form of the traction-stiffness relation indicates that the feature(s) that cause reliable guidance can arise from quite different traction relations. We found that in both cases, the probability that axons reach the optic tectum is high when the domain is roughly bisected into a region of high traction and a region of low traction. Axons originate from the region of high traction and initially grow towards the region of low traction. When the axons reach the interface between the two regions, they are reflected off the interface and towards the optic tectum, reproducing the stereotypical turn of axons observed in-vivo. In fact, approximating the domain by one which is bisected by a sharp interface into two regions of different stiffness, approximating axons as rays satisfying the refraction-reflection properties outlined in Section 5.2, and assuming that the local growth traction obeys a linear traction-stiffness relation, we find that the probability that axons reach the optic tectum as a function of the traction-stiffness slope parameter, qualitatively resembles that of the complete ABC model when simulated on the experimentally measured stiffness field. The results of Section 5.4 suggest that the key mechanism for reliable guidance of axons to the optic tectum by durotaxis is that of reflection. Thus, this scenario illustrates an example of in-vivo guidance by durotaxis where the refraction-reflection properties of axons may be utilised to achieve guidance targets.

Application (3): Segmentation of the PNS

Finally, in Section 5.5 we investigated the initial segmentation of motor axons outgrowing from the neural tube in the PNS. This scenario is another where axon durotaxis is thought to play a significant role, as the initial segmentation of motor axons occurs successfully

even in the absence of chemical signalling. In order to investigate the segmentation process, we used what information is available to construct a plausible stiffness field for the environment through which motor axons initially grow. To be able to quantify successful segmentation, we introduced a metric which we call segmentation efficiency, that balances the tension between successful crossing of the sclerotome and avoidance of the posterior half somites by axons. The results of our investigation indicate that segmentation can only occur efficiently under durotaxis if there exist lines of optimal stiffness which surround the posterior-half somites which axons need to avoid. Furthermore, these lines of optimal stiffness need to be sufficiently attractive to capture and redirect axons to grow around the posterior-halves and into the anterior-halves of somites. Thus, our results indicate that the initial segmentation of motor axons could be a particular instance of the use of guidance by lines of optimal stiffness to achieve reliable and precise guidance targets during the development of the nervous system.

The work in this chapter is the culmination of the research conducted in this thesis. In Section 5.2, we introduced a further mode of axon guidance - reflection and refraction and its particulars as predicted by the ABC model. In investigating the in-vivo examples of Section 5.4 and Section 5.5, we illustrated how the key concepts generated by this thesis may appear and play a significant role in how durotaxis produces stereotypical axon guidance during the development of the nervous system. These ideas and concepts along with the traction based framework introduced provide a foundation for a richer and deeper understanding of axon guidance.

Chapter 6

Conclusion

In this thesis, we set out to develop a mechanical, multiscale theory for axon guidance, with particular emphasis on axon durotaxis. The central premise of our theory is that guidance cues influence axonal trajectories by modulating the traction forces generated by the growth cone, and that these forces then reorient the axon shaft through its mechanical response. This perspective provides a route from molecular-scale adhesion dynamics to cellular-scale axon trajectories, and therefore addresses a gap in existing theories of axon guidance: the absence of a framework that directly links environmental mechanical properties, focal-adhesion mediated traction generation, and the deformation and turning of the axon.

The analysis in this thesis was organised from the microscale to the macroscale. We began by studying focal adhesion dynamics and the generation of traction forces at the growth cone. We then formulated a remodelling beam model for the axon shaft, which describes how these forces can deform and reorient the axon. Finally, we combined these two components to investigate specific guidance scenarios, thereby connecting molecular-scale adhesion dynamics to cellular-scale axon turning.

6.1 Summary of results

In Chapter 2, we studied the interaction between myosin motors, focal adhesions and a deformable substrate. The main contributions of this chapter are:

- We formulated the motor-clutch-deformable substrate system using a Chapman-Kolmogorov (CK) framework, which describes the exact statistics of the stochastic system.
- We analysed the CK steady state exactly for the single-linker system. This yielded an explicit statistical characterisation of the qualitative dynamical regimes pre-

viously described in the literature, providing a quantitative definition that had previously been absent.

- We developed a mean-field analysis of the many-linker system, with particular emphasis on steady-state traction. This allowed us to derive an explicit expression for the optimal substrate stiffness, determine the conditions under which this optimum exists, and study the curvature of the traction-stiffness curve at the optimal stiffness.

More broadly, this chapter provides the first CK-based analysis of the motor-clutch-deformable substrate system and provides a foundation for future analytical investigations of this system.

In Chapter 3, we developed a mechanical framework for understanding the trajectories of growing axons. The main contributions of this chapter are:

- We developed a remodelling beam model for the axon that links growth cone traction to axonal growth trajectories.
- We analysed simple motions of this model. In particular, by studying the motion of an axon subject to a constant growth cone force, we derived an expression for the timescale of turning of the axon.
- We studied axon motion in a stiffness field with constant gradient. This analysis showed that, within our model, axons can exhibit both positive and negative durotaxis. It also predicted a new mode of axon guidance: convergence towards trajectories parallel to lines of optimal stiffness. Furthermore, this convergence depends on the finite spatial extent of the axon, an aspect of the problem that is neglected in most previous models of axon guidance.

Together with the insights obtained from the simple guidance scenarios studied, this chapter lays the foundation for studying axon guidance during development using the traction-based framework.

In Chapter 4, we addressed the problem of inferring the mechanical parameters of an axon from pulling experiments. Previous approaches typically model the axon as an elastic string, which provides a useful baseline but neglects bending stiffness. To include the effect of bending rigidity, we developed and applied an extensible beam model for the pulling experiment.

As discussed in Chapter 4, there is a discrepancy in the reported values of axonal bending stiffness in the literature. Some methods estimate $\mathcal{B} \sim 10^{-19}\text{Nm}^2$, whereas methods based on pulling experiment data estimate $\mathcal{B} \sim 10^{-21}\text{Nm}^2$. We showed that the same pulling experiment data can lead to either estimate, depending on the constraints imposed on the extensible beam model. For example, if the axon is assumed to be isotropic, so that the bending stiffness is constrained by $\mathcal{B} = EI$, the inferred value is $\mathcal{B} \sim 10^{-21}\text{Nm}^2$. By contrast, if the axon is treated as anisotropic and the extensional and bending stiffnesses are assumed to be independent, values of order $\mathcal{B} \sim 10^{-19}\text{Nm}^2$ can be obtained. The analysis also showed that estimates of the elastic modulus are relatively stable across the different assumptions.

In Chapter 5, the final part of this thesis, we applied the framework developed in Chapter 3 to biologically motivated guidance scenarios:

- We studied the interaction of axons with sharp interfaces between regions that generate different levels of growth cone traction. The simulated axons exhibited reflection- and refraction-like behaviours, but with important differences from optical analogies and previous axon-bundle models. In particular, reflected axons tended to reorient and travel approximately parallel to the interface, consistent with experimental observations of axons encountering boundaries between regions of different adhesive or mechanical properties.

- We studied the guidance of axons to the optic tectum in *Xenopus*. By running simulations of individual axons on the measured stiffness field along the optic tract, we showed that axons can, in principle, reach the optic tectum through durotaxis alone. Furthermore, we showed that the stereotypical caudal turn exhibited by both simulated and physical axons approaching the optic tectum can be explained by reflection off a sharp boundary near the location where a sharp stiffness transition is observed in vivo.

- We investigated whether durotaxis could contribute to the segmented outgrowth of motor axons in the peripheral nervous system. Our analysis showed that efficient segmentation can occur in principle if the traction-stiffness relation generates sufficiently attractive lines of optimal stiffness positioned near the posterior-half regions.

Taken together, the results of this thesis support the view that axon durotaxis can be understood, at least in part, as arising from the differential generation of traction on substrates of different stiffness. The framework developed here provides an integrated

multiscale theory of this hypothesis, linking molecular-scale adhesion dynamics, growth cone traction generation, axon shaft mechanics and emergent guidance trajectories.

6.2 Limitations

The analysis conducted in this thesis is not without limitations. These limitations largely reflect the scope of the modelling framework: the thesis isolates a particular mechanical hypothesis of axon guidance in order to understand its consequences as clearly as possible. As a result, several biological mechanisms remain outside the scope of the present analysis.

In Chapter 2, the motor-clutch model was deliberately kept minimal. Although the Chapman-Kolmogorov formulation provides an exact statistical description of the system studied here, the model does not include many biochemical and structural features of real focal adhesions, such as catch-bond behaviour, talin unfolding, vinculin recruitment, etc. Moreover, the analysis focused primarily on steady-state traction. This allowed us to characterise the traction-stiffness relation and derive conditions for the existence of an optimal stiffness, but it did not provide a detailed dynamical analysis of transient behaviours such as collective load-and-fail cycles. Finally, the focal adhesion results were not directly fitted to, or systematically compared with, experimental traction data. The predictions of the model should therefore be interpreted as mechanistic and theoretical rather than as quantitatively calibrated descriptions of a particular biological system. A further limitation is that focal adhesions at the periphery of the growth cone were treated as independent traction-generating units. In reality, their dynamics are likely to be coupled through the actin cytoskeleton, membrane mechanics, substrate deformation and the diffusion of the unbound adhesive proteins, so that traction generation may be spatially correlated across the growth cone.

In Chapter 3, the axon was modelled as a planar remodelling beam. This two-dimensional description is a natural first approximation, but real axons grow in three-dimensional, heterogeneous environments. The model also focuses on continuous growth and turning, and therefore does not attempt to reproduce behaviours such as stalling, retraction, pausing or branching. A further limitation is the lack of experimental datasets that simultaneously measure growth cone traction, local mechanical properties and the subsequent evolution of axon trajectories. Such data would be required to test the central assumption of the model: that spatial variation in traction generation is sufficient to drive axon reorientation.

In Chapter 4, the main limitation is the scarcity of experimental data. The analysis demonstrates how pulling experiments can be interpreted using an extensible beam model rather than an elastic string model. However, the limited dataset considered in the

chapter is insufficient to obtain reliable estimates of the mechanical parameters of axons or neurites.

In Chapter 5, we isolated durotaxis from other guidance mechanisms in investigating the axon guidance scenarios. In vivo, guidance in these scenarios almost certainly results from the integration of mechanical, chemical and other cues. Moreover, our model does not include possible interactions between neighbouring axons or collective effects that may influence axon trajectories in vivo. The simulations therefore should not be interpreted as claiming that durotaxis alone is responsible for the full guidance behaviour in each case. Rather, they identify what traction-based guidance can explain in isolation. In the motor axon segmentation example, a further limitation is the absence of detailed stiffness field data at the relevant spatial scale. Consequently, the segmentation simulations relied on idealised stiffness fields. Within the parameter ranges explored, the motor-clutch traction law produced only modest improvements over baseline straight growth. This suggests either that the specific traction-based mechanism considered here is not the dominant driver of motor axon segmentation, or that the motor-clutch description used in Chapter 5 is too simple to capture the relevant biology in that setting. The phenomenological traction laws were therefore useful because they clarified what would be required for traction-based durotaxis to be effective: sufficiently strong attraction towards appropriately positioned lines of optimal stiffness.

6.3 Future work

The results and limitations of this thesis suggest several directions for future work. Broadly, the next step is to relax some of the assumptions made in the present framework and to move towards a quantitatively calibrated theory that can be tested directly against experimental data.

One important direction is to extend the focal-adhesion model studied in Chapter 2. An immediate extension would be to incorporate additional molecular mechanisms known to influence focal-adhesion dynamics. These include catch-bond behaviour, in which the kinetic off-rate depends non-monotonically on linker extension, and adhesion reinforcement, in which the kinetic on-rate increases in response to sufficiently large linker forces. Although such mechanisms have been investigated computationally [1, 17], comparatively little work has been done to describe them within an analytical Chapman-Kolmogorov framework. A natural starting point would be to analyse these mechanisms in the single-linker system, where the problem may remain analytically tractable.

A related direction is to extend the analytical treatment of the Chapman-Kolmogorov equation to systems with small but finite numbers of linkers, particularly $N_T = 2$. This

case may be simple enough to admit analytical progress, while still introducing interactions between linkers through their shared mechanical environment. Such a model could provide useful insight into how collective effects emerge in the motor-clutch-deformable substrate system.

Another important extension concerns the role of space in focal-adhesion dynamics and growth cone traction generation. In our analysis, the net growth cone traction was obtained by assuming that the focal adhesions at the periphery of the growth cone are independent traction-generating units. Consequently, under homogeneous substrate stiffness conditions, traction generation is uniform across the growth cone periphery. Experimentally, however, growth cones on substrates of homogeneous stiffness, and in the absence of chemical cues, can develop transient local traction-stress peaks [60]. This suggests that spatial organisation may play an important role even when the external environment is mechanically uniform. Therefore, a useful future direction would be to embed focal adhesions on a line or in a two-dimensional spatial domain, and to determine under what conditions such models can reproduce the experimentally observed localisation of traction stresses.

A second set of future directions concerns the remodelling beam model developed in Chapter 3. A natural next step would be to obtain experimental datasets that measure both growth cone traction forces and the subsequent trajectories of axons. Ideally, such datasets would include axons growing on both homogeneous substrates and prescribed stiffness fields. The remodelling beam model could then be fitted to these data in order to test the central assumption of the present framework: that traction forces generated at the growth cone can reorient the axon shaft through its mechanical response. Such a dataset would also allow the axon model parameters to be calibrated, thereby making the framework more suitable for quantitative prediction.

Although the remodelling beam model provides a useful first approximation, it should ultimately be extended to three dimensions. This is particularly important for applying the theory to in vivo guidance problems, where axons do not grow on planar substrates and where mechanical properties may vary in all spatial directions. A three-dimensional formulation would also make it possible to test whether the guidance behaviours identified in this thesis, such as convergence towards lines of optimal stiffness, persist in 3D.

Future work should also incorporate additional behaviours exhibited by real axons that were not included in the present model. For example, axons may pause, retract, branch, or change their growth state in response to environmental conditions. Including such behaviours would move the framework closer to a realistic theory of axon guidance.

More generally, future applications of the framework should combine durotaxis with other guidance mechanisms. A natural direction is to couple the remodelling beam model

to models of chemotaxis. Within the present framework, this could be done by allowing chemical cues to modulate the kinetic parameters of the focal-adhesion model. In this way, chemotactic signals would influence axon trajectories through their effect on traction generation. Such an extension would make it possible to study when mechanical cues dominate, when they reinforce chemical cues, and when they oppose them.

The results of Chapter 4 also suggest several directions for future work. A natural next step is to obtain a larger dataset from axon or neurite pulling experiments and apply the inference framework developed in this thesis to estimate the extensional stiffness E and bending stiffness $\mathcal{B}$. Since these parameters are non-identifiable in the anisotropic model from the available measurements alone, it would be useful to reformulate the inference problem in a Bayesian setting. This would allow one to study the posterior distributions of E and $\mathcal{B}$ under different prior assumptions, and to quantify the degree of uncertainty associated with each inferred parameter.

Appendix A

Focal Adhesions

A.1 Numerical simulation of the focal adhesion dynamics

In this section, we outline the numerical method used to simulate trajectories of the focal adhesion system Chapter 2.

Between binding and unbinding events, the system evolves deterministically. For a deformable substrate, the extension rate of bound proteins is given by

$$v_e(\boldsymbol{x}, \boldsymbol{q}) = \frac{1}{\xi} \frac{F - \kappa \sum_{i=1}^{N_T} q_i x_i}{1 + \chi^{-1} \sum_{i=1}^{N_T} q_i}. \tag{A.1}$$

Thus, for fixed $\boldsymbol{q}$, the extensions satisfy the system

$$\dot{x}_i = \frac{1}{\xi} \frac{F - \kappa \sum_{j=1}^{N_T} q_j x_j}{1 + \chi^{-1} \sum_{j=1}^{N_T} q_j}, \qquad i = 1, \dots, N_T. \tag{A.2}$$

To solve this system, define

$$N := \sum_{j=1}^{N_T} q_j, \qquad S(t) := \sum_{j=1}^{N_T} q_j x_j(t).$$

Then the system reduces to

$$\dot{x}_i = \frac{1}{\xi} \frac{F - \kappa S(t)}{1 + \chi^{-1} N}, \qquad i = 1, \dots, N_T.$$

Summing with weights q_i yields a closed equation for $S(t)$:

$$\dot{S}(t) = \frac{N}{\xi} \frac{F - \kappa S(t)}{1 + \chi^{-1} N}.$$

This linear ODE admits the explicit solution

$$S(t) = \frac{F}{\kappa} + \left(S(0) - \frac{F}{\kappa} \right) \exp\left(-\frac{\kappa N}{\xi(1 + \chi^{-1} N)} \, t \right).$$

Since all components share the same time derivative, their pairwise differences remain constant. For $N \neq 0$, this implies

$$x_i(t) = x_i(0) + \frac{S(t) - S(0)}{N},$$

so that the deterministic evolution over a time interval Δt is given by

$$\Delta x = \frac{1}{N}\left(\frac{F}{\kappa} - S(0)\right)\left(1 - \exp\left[-\frac{\kappa N}{\xi(1+\chi^{-1}N)}\,\Delta t\right]\right). \tag{A.3}$$

To generate sample trajectories, the deterministic evolution is coupled to stochastic binding and unbinding events using a time-discretised scheme. Given a time step $\Delta t > 0$, the simulation proceeds as follows:

- The extensions of all currently bound proteins are updated using the deterministic solution over the interval Δt.
- Each bound protein detaches with probability

  $$p_{\text{off}} = k_{\text{off}}\Delta t \exp\left(\frac{\kappa x_i}{f_b}\right), \tag{A.4}$$

  reflecting force-dependent Bell kinetics.
- Each unbound protein attaches with probability

  $$p_{\text{on}} = k_{\text{on}}\Delta t. \tag{A.5}$$

Following each update, the extensions of unbound proteins are reset to zero. We initiate the system with all proteins unbound.

This procedure yields a discrete-time approximation of the underlying piecewise-deterministic stochastic process governing focal adhesion dynamics.

A.2 Properties of N, constant extension case

As a function of $\mathcal{K}$, N is non-negative and strictly increasing, with $N = 0$, when $\mathcal{K} = 0$. Furthermore, $N \to N_T$ as $\mathcal{K} \to +\infty$.

Noting that $-\frac{1}{\nu}\exp\left(\frac{1}{\nu}\right)\text{Ei}\left(-\frac{1}{\nu}\right)$ is a positive and strictly decreasing function of ν, satisfying

$$-\frac{1}{\nu}\exp\left(\frac{1}{\nu}\right)\text{Ei}\left(-\frac{1}{\nu}\right) \to 1, \quad \text{as} \quad \nu \to 0^+,$$
$$-\frac{1}{\nu}\exp\left(\frac{1}{\nu}\right)\text{Ei}\left(-\frac{1}{\nu}\right) \to 0, \quad \text{as} \quad \nu \to +\infty,$$

it follows that $N \to N_T\,\mathcal{K}/(1+\mathcal{K})$ as $\nu \to 0^+$ and $N \to 0$ as $\nu \to +\infty$.

A.3 Properties of $\tau(d_1, k)$

In the limit $k \to 0^+$

Expanding τ for small k we obtain,

$$\tau\,(d_1, k) = k\,\mathcal{H}(d_1) + \mathcal{O}(k^2). \tag{A.6}$$

In terms of d_1, the first order term has identical properties with $\mathcal{H}(x)$.

In the limit $k \to +\infty$

Expanding τ for small $1/k$, we obtain

$$\tau\,(d_1, k) = \frac{\mathcal{H}(d_1)}{\mathcal{G}(d_1)} + \mathcal{O}(1/k). \tag{A.7}$$

The function $\mathcal{H}(d_1)/\mathcal{G}(d_1)$ is a positive, strictly decreasing function of d_1, satisfying

$$\frac{\mathcal{H}(d_1)}{\mathcal{G}(d_1)} \to +\infty, \quad \text{as } d_1 \to 0^+,$$
$$\frac{\mathcal{H}(d_1)}{\mathcal{G}(d_1)} \to 0, \quad \text{as } d_1 \to +\infty.$$

Existence of turning points for all $k > 0$

The function $\tilde{\tau}(d_1) = \tau(d_1, k)$, has a turning point for all $k > 0$. This can be shown by proving that for every $k > 0$, there exists some $D_1 \in \mathbb{R}_+$ that satisfies

$$\frac{\partial \tau}{\partial d_1}(D_1, k) = 0. \tag{A.8}$$

We have that

$$\frac{\partial \tau}{\partial d_1} = \frac{k\mathcal{H}'(d_1)\,(1 + k\,\mathcal{G}(d_1)) - k^2\,\mathcal{H}(d_1)\mathcal{G}'(d_1)}{(1 + k\,\mathcal{G}(d_1))^2}. \tag{A.9}$$

For fixed $k > 0$, $\partial\tau/\partial d_1$ is continuous for $d_1 > 0$. Therefore, to prove the existence of D_1, it is sufficient to show that $\partial\tau/\partial d_1$ is somewhere positive and somewhere negative on $\mathbb{R}_+/\{0\}$. Having done so, the existence of D_1 follows from the Intermediate Value Theorem.

Since the denominator on the right-hand side of (A.9) is always positive, it suffices to show that the numerator

$$Q_1(d_1, k) := k\mathcal{H}'(d_1)\,(1 + k\,\mathcal{G}(d_1)) - k^2\mathcal{H}(d_1)\,\mathcal{G}'(d_1), \tag{A.10}$$

attains positive and negative values in the interior of $\mathbb{R}_+$.

First we show that $\partial\tau/\partial d_1\,(u^*,k) < 0$, for all $k > 0$. From the facts that, $\mathcal{H}'(u^*) = 0$ (because $\mathcal{H}(x)$ has a turning point at $x = u^*$), that $\mathcal{H}(u^*) > 0$ and that $\mathcal{G}'(u^*) > 0$ (because $\mathcal{G}(x)$ is a strictly increasing function), it follows that

$$Q_1(u^*,k) = -k^2\mathcal{H}(u^*)\,\mathcal{G}'(u^*) < 0. \tag{A.11}$$

Now, we show the existence of some $\delta_1 < u^*$ where $\partial\tau/\partial d_1$ is positive. We note that

$$Q_1(d_1,k) \sim \frac{1}{2}k\log(d_1)^2, \quad \text{as} \quad d_1 \to 0^+. \tag{A.12}$$

Thus, $Q_1(d_1,k) \to +\infty$ as $d_1 \to 0^+$. It follows that $Q_1(d_1,k) > 0$ for sufficiently small $d_1 > 0$. So there exists some $\delta_1 > 0$ such that $Q_1(\delta_1,k) > 0$. This δ_1 can be chosen such that $\delta_1 < u^*$.

In the above argument, we have shown that there exist two positive real numbers, δ_1, u^*, with $\delta_1 < u^*$, such that $\partial\tau/\partial d_1(\delta_1) > 0$ and $\partial\tau/\partial d_1(u^*) < 0$, as required. It follows from the Intermediate Value Theorem that there exists a root D_1 of $\partial\tau/\partial d_1$ that satisfies $0 < D_1 < u^*$. The above proof holds for any value of $k > 0$. We note that in general, the value of the root D_1 will depend on k.

With the above argument, we have only shown the existence of a critical point of τ in d_1, for each k, and have said nothing about uniqueness of this critical point. Numerically, we observe that only one such turning point exists for each k. If this is the case, then we can construct a well-defined function $d_1^*(k)$ on $\mathbb{R}_+/\{0\}$ which gives the location of the turning point for each k. i.e. there exists a function $d_1^*(k)$ which satisfies

$$\frac{\partial\tau}{\partial d_1}(d_1^*(k),k) = 0. \tag{A.13}$$

Properties of $d_1^*(k)$

Here, we describe and derive some properties of $d_1^*(k)$.

The derivative $\partial\tau/\partial d_1$ is continuously differentiable for both variables $d_1, k > 0$. Thus, given that for each $k > 0$ there exists a root of $\partial\tau/\partial d_1$, the Implicit Function Theorem guarantees the local existence of a continuously differentiable function $d_1(k)$ which, at least locally, solves the functional equation

$$\frac{\partial\tau}{\partial d_1}(d_1(k),k) = 0. \tag{A.14}$$

If it is true that for each k there exists only one turning point, then it must be the case that the function provided by the Implicit Function Theorem, $d_1(k)$, must coincide with $d_1^*(k)$. By the repetition of this argument for every $k > 0$, it follows that $d_1^*(k)$

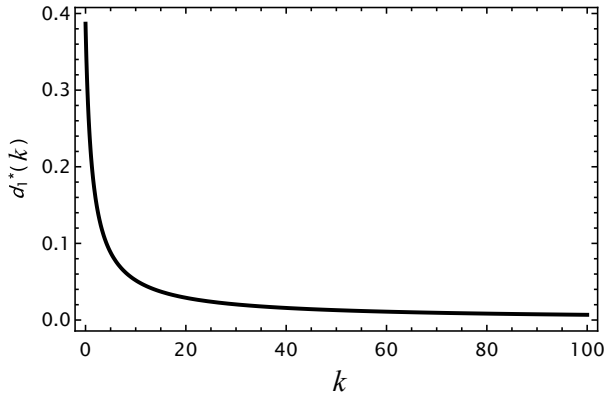


Figure A.1: Plot of $d_1^*(k)$. The function $d_1^*(k)$ denotes the location of the turning point for each k. As can be seen from the plot, this function is decreasing, tending to 0 as $k \to +\infty$.

is everywhere continuously differentiable on $\mathbb{R}_+/\{0\}$. Its derivative can be obtained by differentiating (A.13) and rearranging:

$$d_1^{*\prime}(k) = -\frac{\frac{\partial^2 \tau}{\partial k \partial d_1}(d_1^*(k), k)}{\frac{\partial^2 \tau}{\partial {d_1}^2}(d_1^*(k), k)}. \tag{A.15}$$

The above ODE can be integrated to obtain the whole of $d_1^*(k)$, as long as one knows or can approximate the value of $d_1^*(k_0)$ for some value of $k_0 \geq 0$. One can see the result of such an integration in Fig. A.1 . We find that $d_1^*(k)$ is a positive and strictly decreasing function, with $d_1^*(k) \to 0$ as $k \to +\infty$. Furthermore, $d_1^*(0^+) = u^*$. This can be established through the following argument: For $k > 0$, any root of $\partial\tau/\partial d_1$ must also satisfy

$$\mathcal{H}'(d_1)\,(1 + k\,\mathcal{G}(d_1)) - k\,\mathcal{H}(d_1)\mathcal{G}'(d_1) = 0, \tag{A.16}$$

(see (A.9)). Therefore,

$$\mathcal{H}'(d_1^*(k))\,(1 + k\,\mathcal{G}(d_1^*(k))) - k\,\mathcal{H}(d_1^*(k))\mathcal{G}'(d_1^*(k)) = 0. \tag{A.17}$$

By taking the limit $k \to 0^+$, and assuming that $d_1^*(0^+) \in \mathbb{R}_+$, we obtain

$$\mathcal{H}'(d_1^*(0^+)) = 0, \tag{A.18}$$

which holds if and only if $d_1^*(0^+) = u^*$.

A.4 Properties of T

In the limit $k \to 0^+$

From (A.6), it follows that

$$T = F_b\,N_T\,\tau\,(d_1, k) = F_b\,N_T\,k\,\mathcal{H}(d_1) + \mathcal{O}(k^2), \tag{A.19}$$

for small k. As a function of d_1, in this limit, the traction has a single turning point which is a global maximum at $d_1 = u^*$. It follows that as a function of v_e, it has a single turning point which is a global maximum.

In the limit $k \to +\infty$

From (A.7), it follows that

$$T = F_b\, N_T\, \tau\,(d_1, k) = F_b\, N_T\, \frac{\mathcal{H}(d_1)}{\mathcal{G}(d_1)} + \mathcal{O}(1/k), \tag{A.20}$$

as $k \to +\infty$. Since $d_1 = 1/\nu$, it follows that in this limit, T is a positive and strictly increasing function of ν, satisfying

$$\begin{aligned} &T \to 0, \quad \text{as } \nu \to 0^+, \\ &T \to +\infty, \quad \text{as } \nu \to +\infty. \end{aligned}$$

Existence of turning points for all $k > 0$

T, as a function of the extension rate v_e, has a turning point for all (admissible) system parameter values. This can be seen through the following argument: Differentiating T by v_e, we obtain

$$\frac{\partial T}{\partial v_e} = -\frac{k_{\text{off}}\, N_T\, F_b^2}{\kappa\, v_e^2}\, \frac{\partial \tau}{\partial d_1}\left(\frac{k_{\text{off}} F_b}{v_e \kappa}, \frac{k_{\text{on}}}{k_{\text{off}}}\right). \tag{A.21}$$

Therefore,

$$\frac{\partial T}{\partial v_e} = 0 \iff \frac{\partial \tau}{\partial d_1} = 0. \tag{A.22}$$

Therefore, T has a turning point at

$$v_e = v^* = \frac{k_{\text{off}} F_b}{\kappa\, d_1^*(k)}. \tag{A.23}$$

We identify v^* with the location of the global maximum, which we observe numerically. The function v^* is an increasing function of k_{on} when holding k_{off} and the other parameters fixed. Similarly, it is an increasing function of k_{off} when holding k_{on} and the other parameters fixed.

A.5 Behaviour of F_{crit}

Here, we study the behaviour of F_{crit} under variation of the kinetic parameters k_{on}, k_{off}. To do so, we define the non-dimensional critical myosin force by

$$f_{\text{crit}} = \frac{F_{\text{crit}}}{N_T F_b}. \tag{A.24}$$

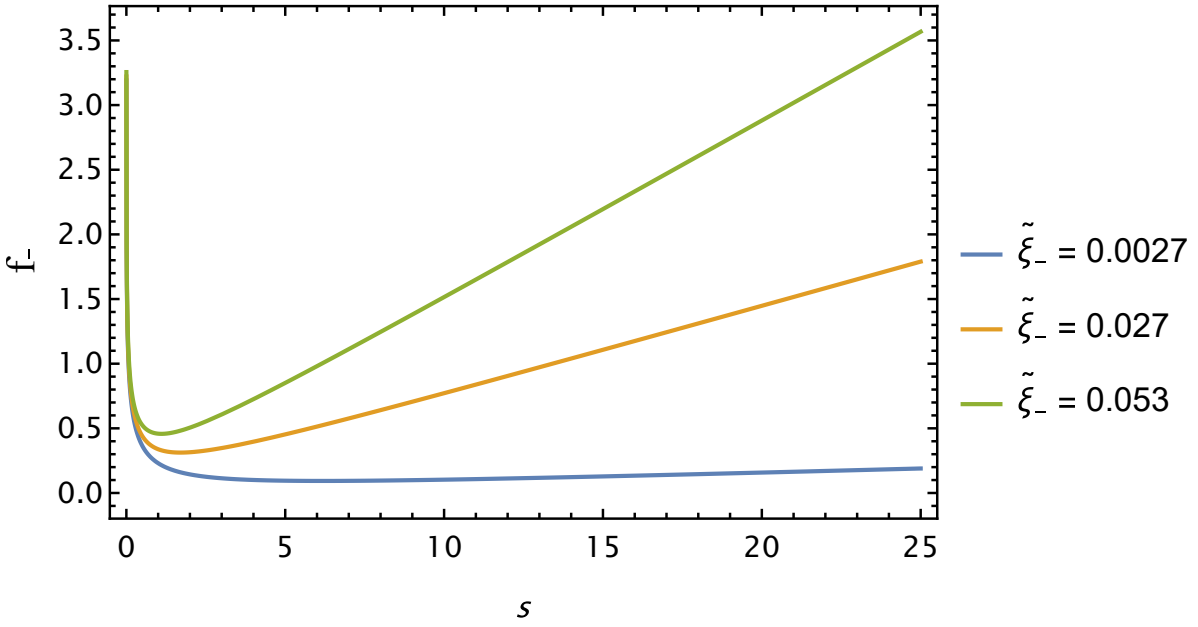


Figure A.2: Plot of $f_-(s;\tilde{\xi}_-)$ for different values of $\tilde{\xi}_-$. As can be seen in the plot, as a function of s and for each value of $\tilde{\xi}_-$, $f_-(s;\tilde{\xi}_-)$ is initially decreasing, reaching a global minimum, and then increasing.

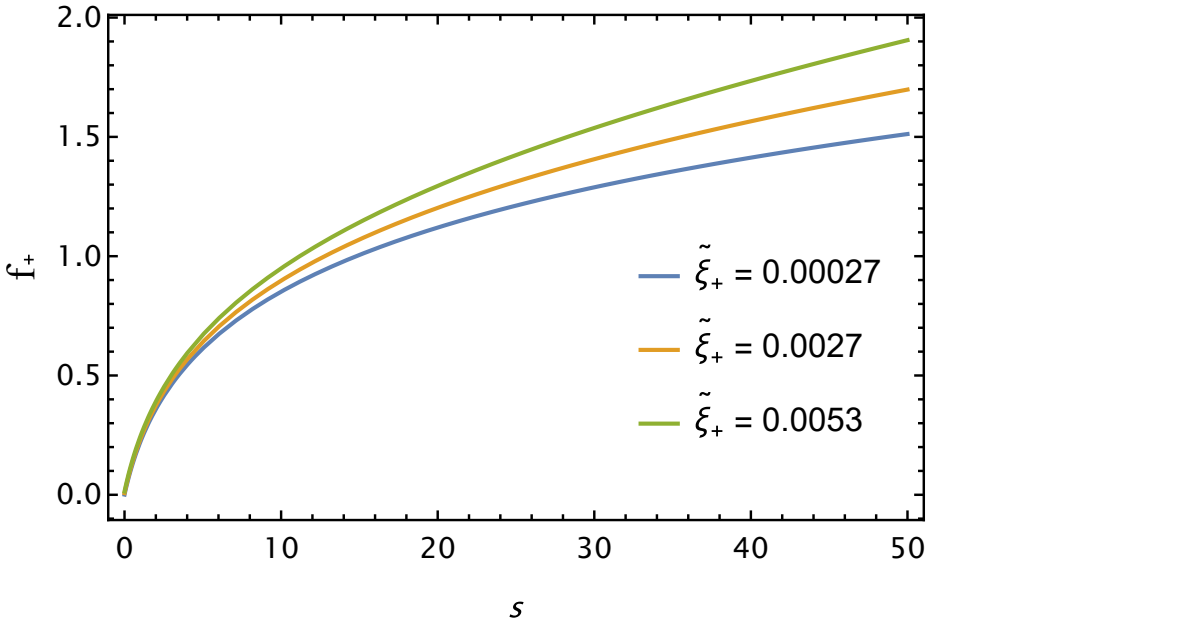


Figure A.3: Plot of $f_+(s;\tilde{\xi}_+)$ for different values of $\tilde{\xi}_+$. As can be seen in the plot, as a function of s and for each value of $\tilde{\xi}_+$, $f_+(s;\tilde{\xi}_+)$ is strictly increasing.

We first consider the dependence of f_{crit} on k_{on}, with all other parameters held fixed. We find that increasing k_{on} leads to a monotonic increase in the critical force, with $f_{\text{crit}} \to +\infty$ as $k_{\text{on}} \to +\infty$. This reflects the strengthening of the adhesion through increased binding. To show this, let $s = k_{\text{on}}/k_{\text{off}}$. The critical force may be written as

$$f_{\text{crit}} = \tau\big(d_1^*(s), s\big) + \frac{k_{\text{off}}\,\xi}{\kappa N_T}\frac{1}{d_1^*(s)}. \tag{A.25}$$

Defining

$$\tilde{\xi}_+ = \frac{k_{\text{off}}\,\xi}{\kappa N_T}, \quad f_+(s;\tilde{\xi}_+) = \tau\big(d_1^*(s), s\big) + \tilde{\xi}_+\frac{1}{d_1^*(s)}, \tag{A.26}$$

we have

$$f_{\text{crit}} = f_+(s;\tilde{\xi}_+). \tag{A.27}$$

Thus, the behaviour of f_{crit} as a function of k_{on} is completely determined by $f_+(s;\tilde{\xi}_+)$. As can be seen in Fig. A.3, $f_+(s;\tilde{\xi}_+)$ is positive and strictly increasing in s, with

$$f_+(s;\tilde{\xi}_+) \to +\infty \quad \text{as } s \to +\infty, \tag{A.28}$$

and

$$f_+(0;\tilde{\xi}_+) = \tau\big(d_1^*(0), 0\big) + \tilde{\xi}_+\frac{1}{d_1^*(0)} = \frac{\tilde{\xi}_+}{u^*}. \tag{A.29}$$

We next consider the dependence of f_{crit} on k_{off}. We find that f_{crit} diverges in both limits $k_{\text{off}} \to 0^+$ and $k_{\text{off}} \to +\infty$. Furthermore, as a function of k_{off}, f_{crit} has a single global minimum. To show that f_{crit} diverges in the specified limits, we fix k_{on} and introduce

$$x = \frac{k_{\text{off}}}{k_{\text{on}}}, \quad \tilde{\xi}_- = \frac{k_{\text{on}}\xi}{\kappa N_T}, \quad f_-(x;\tilde{\xi}_-) = \tau\big(d_1^*(1/x), 1/x\big) + \frac{\tilde{\xi}_-\,x}{d_1^*(1/x)}. \tag{A.30}$$

With these definitions, we have

$$f_{\text{crit}} = f_-(x;\tilde{\xi}_-). \tag{A.31}$$

We now examine the asymptotic behaviour of f_-. Since $\tau > 0$, we have

$$f_-(x;\tilde{\xi}_-) > \frac{\tilde{\xi}_- x}{d_1^*(1/x)}. \tag{A.32}$$

Furthermore, since $d_1^*(1/x) \to u^*$ as $x \to +\infty$, it follows that

$$\frac{\tilde{\xi}_- x}{d_1^*(1/x)} \sim \frac{\tilde{\xi}_-}{u^*}x, \quad \text{as } x \to +\infty. \tag{A.33}$$

Because of the above asymptotic relation, the fact that $\tilde{\xi}_-\,x/u^* \to +\infty$ as $x \to +\infty$ implies that $\frac{\tilde{\xi}_- x}{d_1^*(1/x)} \to +\infty$ as $x \to +\infty$. Furthermore, because $\tilde{\xi}_-\,x/d_1^*(1/x)$ is a lower bound for f_- (A.32) and since $\tilde{\xi}_-\,x/d_1^*(1/x) \to +\infty$ as $x \to +\infty$, it follows that

$$f_-(x;\tilde{\xi}_-) \to +\infty \quad \text{as } x \to +\infty. \tag{A.34}$$

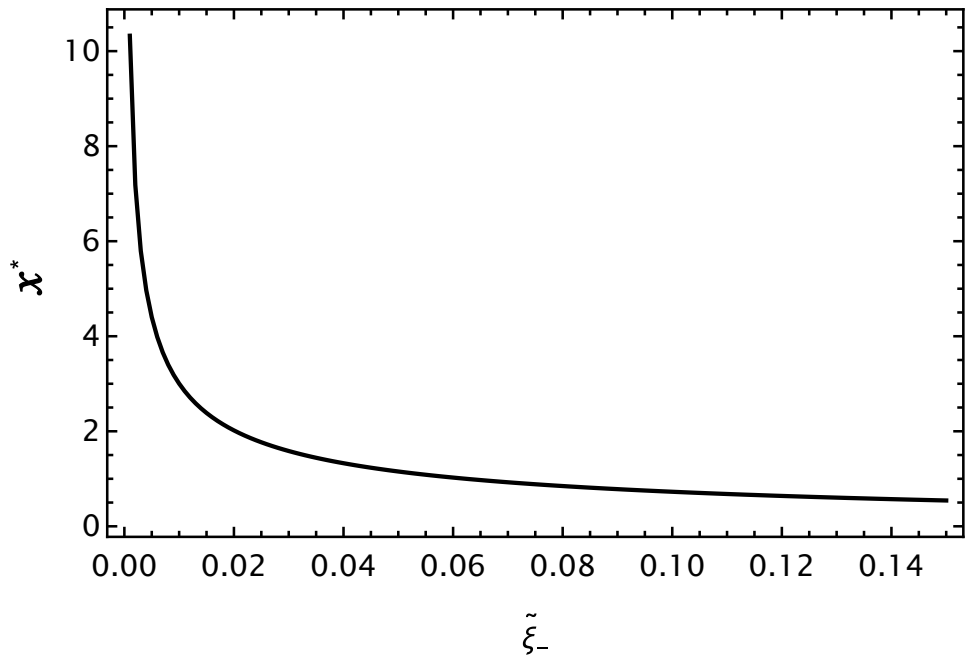


Figure A.4: Plot of $x^*\left(\tilde{\xi}_-\right)$. The value of $x^*\left(\tilde{\xi}_-\right)$ denotes the location of the minimum of $f_-(x,\tilde{\xi}_-)$ in the variable x for each value of $\tilde{\xi}_-$.

We now examine the limit $x \to 0^+$. We have $f_-(x;\tilde{\xi}_-) \to +\infty$ as $x \to 0^+$. This follows from a combination of facts. Firstly,

$$f_-\left(x,\tilde{\xi}_-\right) > \tau\left(d_1^*\left(1/x\right),1/x\right),$$

where

$$\tau\left(d_1^*\left(1/x\right),1/x\right) = \frac{1}{1+\frac{x}{\mathcal{G}(d_1^*(1/x))}}\frac{\mathcal{H}(d_1^*(1/x))}{\mathcal{G}(d_1^*(1/x))}.$$

We proceed by establishing the behaviour of $\tau\left(d_1^*\left(1/x\right),1/x\right)$ in the limit $x \to 0^+$. In order to do so, we first establish the behaviour of $\mathcal{H}(d_1^*(1/x))/\mathcal{G}(d_1^*(1/x))$ in the specified limit. Since $d_1^*\left(1/x\right) \to 0$ as $x \to 0^+$, the behaviour of $\mathcal{H}(d_1^*(1/x))/\mathcal{G}(d_1^*(1/x))$ is determined by the behaviour of $\mathcal{H}(u)/\mathcal{G}(u)$ in the limit $u \to 0^+$. We have

$$\mathcal{H}(u) \sim \frac{1}{2}u\,\ln(u)^2 \quad \text{as} \quad u \to 0^+,$$

$$\mathcal{G}(u) \sim -u\,\ln(u) \quad \text{as} \quad u \to 0^+.$$

Therefore,

$$\frac{\mathcal{H}(u)}{\mathcal{G}(u)} \sim -\frac{1}{2}\,\ln(u) \quad \text{as} \quad u \to 0^+.$$

Therefore,

$$\frac{\mathcal{H}(d_1^*(1/x))}{\mathcal{G}(d_1^*(1/x))} \to +\infty \quad \text{as} \quad x \to 0^+. \tag{A.35}$$

Our numerics indicate that

$$\frac{x}{\mathcal{G}(d_1^*(1/x))} = \mathcal{O}(1), \quad \text{as} \quad x \to 0^+.$$

Supposing that $x/\mathcal{G}(d_1^*(1/x))$ is indeed bounded for $x \ll 1$, it follows that

$$\frac{1}{1+\frac{x}{\mathcal{G}(d_1^*(1/x))}} = \mathcal{O}(1), \quad \text{as} \quad x \to 0^+. \tag{A.36}$$

Then combining all the above means that

$$\tau\left(d_1^*\left(1/x\right), 1/x\right) \to +\infty \quad \text{as} \quad x \to 0^+. \tag{A.37}$$

Thus, $f_-(x;\tilde{\xi}_-) \to +\infty$ as $x \to 0^+$.

Thus, $f_-(x;\tilde{\xi}_-)$ diverges in both limits $x \to 0^+$ and $x \to +\infty$. Numerical results (see Fig. A.2) show that f_- possesses a single turning point, corresponding to a global minimum. Denoting its location by $x^*(\tilde{\xi}_-)$, we find that it is a decreasing function of $\tilde{\xi}_-$ (see Fig. A.4).

Overall, the above analysis shows that k_{on} and k_{off} influence the critical myosin force in different ways. Increasing k_{on} leads to a monotonic increase in f_{crit}, consistent with progressive adhesion strengthening. In contrast, the dependence on k_{off} is non-monotonic: f_{crit} initially decreases, reaches a single global minimum, and then increases without bound.

A.6 Behaviour of χ^* as a function of $k_{\text{on}}, k_{\text{off}}$

Here we examine the effect of the kinetic parameters $k_{\text{on}}, k_{\text{off}}$. When only varying k_{on}, χ^* can be re-expressed as

$$\chi^* = \frac{N_T\ \tilde{\xi}_+}{\frac{F}{F_b N_T} - f_+(s;\tilde{\xi}_+)} \times \mathcal{J}\left(s\right), \tag{A.38}$$

where $s = k_{\text{on}}/k_{\text{off}}$ and

$$\mathcal{J}(s) := \frac{1}{d_1^*\left(s\right)} \times \frac{\mathcal{Z}\left[1/d_1^*(s),\ s\right]}{1+\mathcal{Z}\left(1/d_1^*(s), s\right)}, \tag{A.39}$$

is a positive, strictly increasing function of $s > 0$. Since both $f_+(s;\tilde{\xi}_+)$ and $\mathcal{J}(s)$ increase with $s > 0$, it follows that so does χ^*, tending to $+\infty$ as $f_+ \to F/\left(F_b N_T\right)$, which occurs at a finite value of $s > 0$, which we denote by s_+. The optimal stiffness does not exist for values of s greater than s_+.

When only varying k_{off}, it is useful to express χ^* as

$$\chi^* = \frac{N_T\,\tilde{\xi}_-}{\frac{F}{F_b N_T} - f_-(x;\tilde{\xi}_-)} \times x \times \mathcal{J}\left(1/x\right), \tag{A.40}$$

where $x = 1/s$. It follows from our results on f_- that the above expression is only positive on a finite interval $x \in (x_L, x_R)$, where $f_-(x_L; \tilde{\xi}_-) = f_-(x_R; \tilde{\xi}_-) = F/(F_b\, N_T)$. Furthermore, we have that $\chi^* \to +\infty$ in both limits $x \to x_L^+$, $x \to x_R^-$. Between the two end-points x_L, x_R, χ^* initially decreases and then increases, exhibiting a global minimum for some $x^* \in (x_L, x_R)$.

A.7 Properties of $\frac{\partial^2 T}{\partial {v_e}^2}(v^*)$

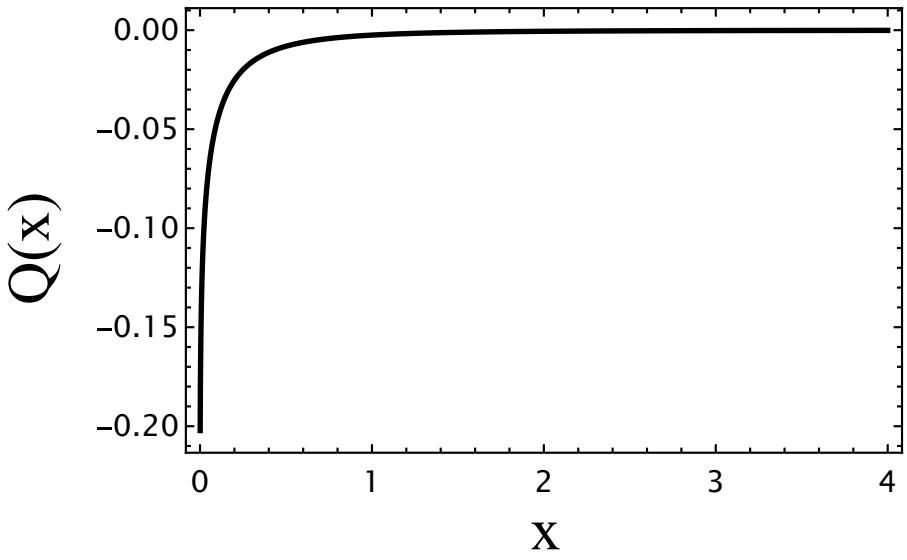


Figure A.5: Plot of $Q(x)$. As can be seen in the plot, $Q(x)$ is a negative, strictly increasing function with $Q(x) \to 0$ as $x \to +\infty$.

Here we investigate the properties of the second derivative of T at $v_e = v^*$. Its exact value is

$$\frac{\partial^2 T}{\partial {v_e}^2}(v^*) = \frac{\kappa^2\, N_T}{F_b} \times \frac{1}{k_{\text{off}}^2} \frac{\partial^2}{\partial \nu^2} \left[\tau \left(1/\nu, \frac{k_{\text{on}}}{k_{\text{off}}} \right) \right]_{\nu = 1/d_1^*(k_{\text{on}}/k_{\text{off}})} . \tag{A.41}$$

The effect due to each of κ, N_T, F_b is clear. Of greater interest is the behaviour of $\partial^2 T/\partial v_e^2(v^*)$ as a function of each of the kinetic parameters.

To determine the behaviour of $\partial^2 T/\partial v_e^2(v^*)$ as function of k_{off}, we note that

$$\frac{\partial^2 T}{\partial {v_e}^2}(v^*) = \frac{\kappa^2\, N_T}{k_{\text{on}}^2\, F_b} \times Q\left(\frac{k_{\text{off}}}{k_{\text{on}}} \right), \tag{A.42}$$

where

$$Q(x) := \frac{1}{x^2} \frac{\partial^2}{\partial \nu^2} \left[\tau \left(1/\nu, \frac{1}{x} \right) \right]_{\nu = 1/d_1^*(1/x)}, \tag{A.43}$$

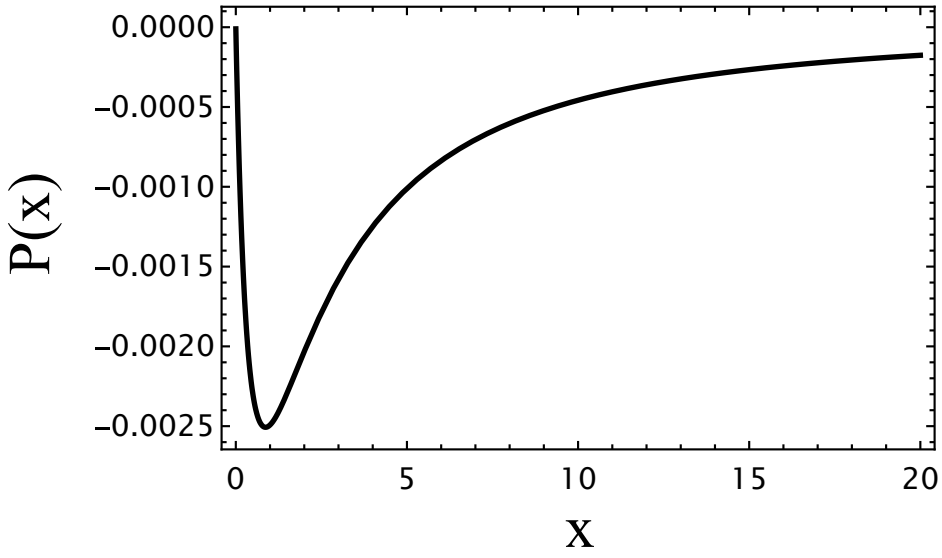


Figure A.6: Plot of $P(x)$. As can be seen in the plot, $P(x)$ is a negative function that initially decreases, then increases, tending to 0 as $x \to +\infty$.

and so, when holding k_{on} and the other parameters fixed, the behaviour of $\partial^2 T/\partial v_e^2(v^*)$ when varying k_{off} is determined by $Q(x)$. As can be seen in Fig. A.5, $Q(x)$ is negative and strictly increasing, tending to 0 as $x \to +\infty$. From this fact, it follows that the magnitude of $\partial^2 T/\partial v_e^2(v^*)$ is strictly decreasing with increasing k_{off} and all other parameters held constant.

To determine the behaviour of $\partial^2 T/\partial v_e^2(v^*)$ as function of k_{on}, we note that

$$\frac{\partial^2 T}{\partial {v_e}^2}(v^*) = \frac{\kappa^2 N_T}{k_{\text{off}}^2 F_b} \times P\left(\frac{k_{\text{on}}}{k_{\text{off}}}\right), \tag{A.44}$$

where

$$P(x) := \frac{\partial^2}{\partial \nu^2} \left[\tau\left(1/\nu, x\right)\right]_{\nu = 1/d_1^*(x)}, \tag{A.45}$$

and so, when holding k_{off} and the other parameters fixed, the behaviour of $\partial^2 T/\partial v_e^2(v^*)$ when varying k_{on} is determined by $P(x)$. As can be seen in Fig. A.6, $P(x)$ is a negative function that is initially decreasing, and then increasing, tending to 0 as $x \to +\infty$. Interestingly, it follows that, when all other parameters are fixed, there exists a value of k_{on} which maximizes the magnitude of $\partial^2 T/\partial v_e^2(v^*)$.

A.8 Formulation with constant binding rate

In Kassianides et al. [35], we assumed a constant binding rate for unbound proteins. This changes the mean-field equation (2.64) to

$$\frac{\partial n(x,t)}{\partial t} + \frac{F - \kappa \int_0^{+\infty} x\, n(x,t)\, \mathrm{d}x}{\xi\left(1 + \chi^{-1} N\right)} \frac{\partial n(x,t)}{\partial x} = -k_{\text{off}} \mathrm{e}^{\frac{\kappa x}{F_b}} n(x,t) + S_0\, \delta(x), \tag{A.46}$$

for constant binding rate $S_0 > 0$.

The qualitative features of the traction-stiffness curve obtained from this formulation are largely similar to those obtained in Chapter 2. Indeed, the constant binding-rate formulation can be recovered as a limiting case of the more general model studied in Chapter 2. In the limit $k_{\text{on}}/k_{\text{off}} \ll 1$, the number of bound proteins remains small relative to the total number of available proteins, so that $N_T - N \approx N_T$. The binding term may therefore be approximated by a constant source term, with $S_0 = k_{\text{on}} N_T$.

Under the constant-binding-rate assumption, the traction can be expressed as a function of the extension rate v_e as

$$T = F_b \frac{S_0}{k_{\text{off}}} \mathcal{H}\left(\frac{k_{\text{off}} F_b}{v_e \kappa}\right). \tag{A.47}$$

As in the formulation studied in Chapter 2, the resulting traction-stiffness curve exhibits an optimal stiffness when the applied motor force is sufficiently large. The expression for this optimal stiffness is

$$\chi^* = \frac{\left(\frac{\xi k_{\text{off}} F_b}{\kappa\, u^*}\right) \frac{S_0}{k_{\text{off}}}\, u^* \mathrm{e}^{u^*}\, \Gamma(0, u^*)}{F - F_b \frac{S_0}{k_{\text{off}}} \mathcal{H}(u^*) - \frac{\xi k_{\text{off}} F_b}{\kappa\, u^*}}. \tag{A.48}$$

This optimum exists provided that $F > F_{\text{crit}}$, where

$$F_{\text{crit}} = F_b \frac{S_0}{k_{\text{off}}} \mathcal{H}(u^*) + \frac{\xi k_{\text{off}} F_b}{\kappa\, u^*}. \tag{A.49}$$

Appendix B

Bending stiffness

B.1 Elastic String Model: Extracting load-deflection curves from Bernal et al. [9]

Fig. B.1 (taken from Bernal et al. [9]) gives the $F = F(\theta)$ curves for three neurites. Each curve can be transformed to the equivalent $F = F(H)$ curve for the same neurite by using the transformation

$$H = \frac{L_x}{2} \tan \theta. \tag{B.1}$$

This transformation requires that L_x is known for each neurite. This information is not given in the figure. In Section B.2, we address how a best estimate can be obtained for L_x and A for each curve by the use of some of the other figures appearing in the paper.

We first extract $F(\theta)$ from the figure by manually annotating the printed datapoints on image-editing software and scaling to appropriate units. We then use the above transformation to obtain $F(H)$. We fit polynomials of the form $F = a_1 H + a_2 H^3$ to the transformed datasets to obtain the series coefficients (a_1, a_2) for each neurite.

An issue arises when fitting the curve of Neurite 2. Specifically, we obtain $a_1 < 0$. If this were the case, it would suggest that the axon in question was in compression. This would contradict the elastic string modeling assumption, as elastic strings cannot sustain compression. Furthermore, given the underlying biophysics and the experimental setup this seems unlikely to be the case – axons are expected to be in tension [42]. Thus, there is a strong prior expectation that $T_0 \geq 0$. Leaving $T_0 < 0$ would lead to some counterintuitive and unobserved behaviors.

Due to this consideration, we enforce $a_1 = 0$ when fitting the load-deflection curve for Neurite 2, but also ignore it in the analysis of Chapter 4. The fits for the load-deflection

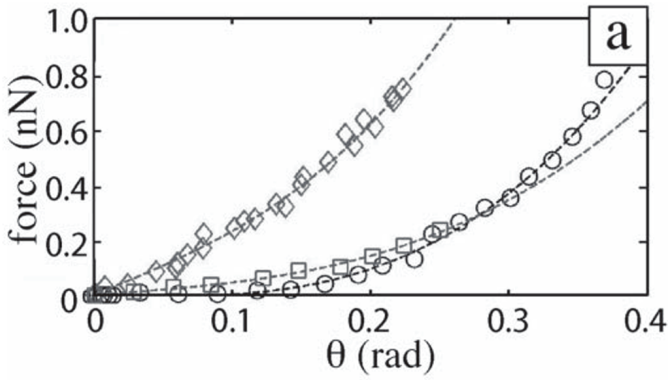


Figure B.1: Figure taken from [9]. (a) Force - angle deflection curves of three axons, where the angle is calculated according to $\theta = \arctan(2H/L_x)$, H being the mid-point deflection.

curves of the neurites are

$$F_1(H) = 5.05 \cdot 10^{-5} \frac{\mathrm{N}}{\mathrm{m}} H + 337559 \frac{\mathrm{N}}{\mathrm{m}^3} H^3, \tag{B.2a}$$

$$F_2(H) = 43214 \frac{\mathrm{N}}{\mathrm{m}^3} H^3, \tag{B.2b}$$

$$F_3(H) = 5.57 \cdot 10^{-6} \frac{\mathrm{N}}{\mathrm{m}} H + 34517 \frac{\mathrm{N}}{\mathrm{m}^3} H^3. \tag{B.2c}$$

Using (4.49), we calculate that

$$(E_1, (\varepsilon_0)_1) = (5312.35\,\mathrm{Pa}, 4.40\%)\,, \tag{B.3}$$

$$(E_2, (\varepsilon_0)_2) = (9023.27\,\mathrm{Pa}, 0.\%)\,, \tag{B.4}$$

$$(E_3, (\varepsilon_0)_3) = (3937.85\,\mathrm{Pa}, 2.07\%)\,, \tag{B.5}$$

and

$$(T_0)_1 = 1.04\,\mathrm{nN},\ (T_0)_2 = 0\,\mathrm{nN}, (T_0)_3 = 0.174\,\mathrm{nN}, \tag{B.6}$$

where E_i denotes the elastic modulus of neurite i, $(\varepsilon_0)_i$ its initial strain and $(T_0)_i$ its initial tension. The mean elastic modulus of the three axons is 6091.16 Pa, almost exactly half the stated value from the paper.

B.2 Extracting A and L_x

In the paper, the particular values of the cross-sectional area A and the axon length L_x for the neurites of Fig. B.1 are not given. However, we can use the information found in Fig. B.2 and Fig. B.3 to estimate these values for the three neurites.

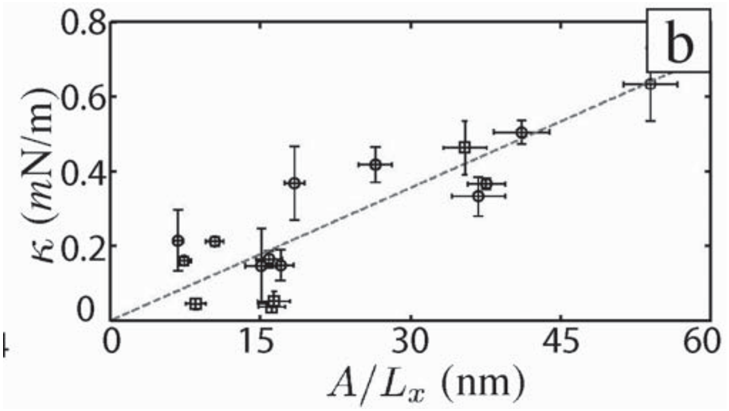


Figure B.2: Figure taken from Bernal et al. [9]. (a) Estimated values spring constants of neurites against measured A/L_x.

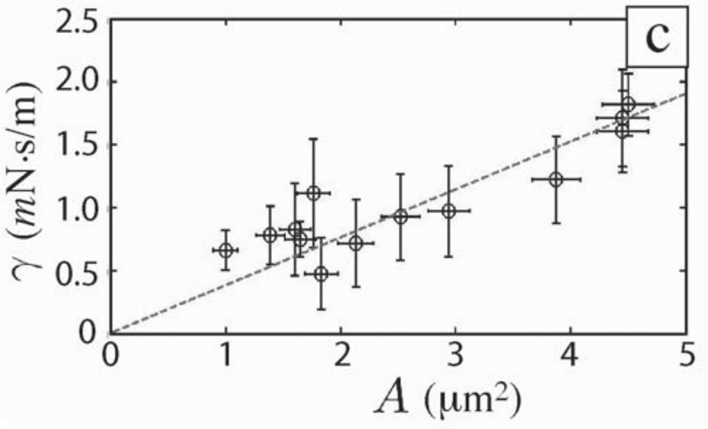


Figure B.3: Figure taken from Bernal et al. [9]. (a) Estimated values of parameter γ against A.

Fig. B.3 provides values of the pair (A, γ), which can be extracted to provide candidate values for the cross-sectional areas A of the neurites. Fig. B.2 provides values of the spring constant κ as a function of A/L_x, where A is the neurite cross-sectional area and L_x is the span of the neurite before midpoint displacement. Thus, each point from the κ-A/L_x plot gives a pair (r, κ), where $r := \frac{A}{L_x}$. This information alone is not sufficient to determine A and L_x, since it only fixes their ratio. We can combine the information from the two plots to estimate L_x and A for each neurite. To separate them, we combine the values of $(A/L_x, \kappa)$ with the force-angle relation obtained from the load-deflection curves.

For each neurite, the extracted force-angle data are fitted by a cubic relation of the form

$$F = b_1\theta + b_2\theta^3.$$

The authors estimated that $b_2 \approx \kappa L_x/2$. Since the plot gives $r = A/L_x$, we have

$$L_x = \frac{A}{r}.$$

Therefore, the cubic coefficient predicted by a given point (r, κ) and a candidate cross-sectional area A is

$$b_2^{\text{pred}} = \frac{1}{2}\kappa L_x = \kappa\frac{A}{2r}.$$

The inference procedure is therefore as follows. For each neurite, we consider the available candidate values of the cross-sectional area A together with the plot values of $(A/L_x, \kappa)$ from the published plot. For each possible combination, we compute the predicted cubic coefficient

$$b_2^{\text{pred}} = A\frac{\kappa}{2r}.$$

We then select the combination that minimises the error

$$\left|A\frac{\kappa}{2r} - b_2\right|.$$

The selected value of A is then taken as the inferred cross-sectional area of the neurite. The corresponding span is obtained from

$$L_x = \frac{A}{r}.$$

Using the above procedure, we estimate that

$$(L_x^1, A_1) = \left(82.5\mu\text{m}, 4.46\,(\mu\text{m})^2\right), \tag{B.7}$$

$$(L_x^2, A_2) = \left(132.1\mu\text{m}, 1.38\,(\mu\text{m})^2\right), \tag{B.8}$$

$$(L_x^3, A_3) = \left(125\mu\text{m}, 2.14\,(\mu\text{m})^2\right). \tag{B.9}$$

B.3 Resolution of the identified inconsistency

In Bernal et al. [9], the authors aimed to infer E of a population of axons by using an axon-pulling setup (see Fig. 4.1). The axon is a viscoelastic structure that behaves elastically on short time scales. Therefore, its mechanical parameters (such as E) can be inferred by studying its initial response to the pulling experiment.

An axon fixed between two points was pulled perpendicularly in its midsection with a fixed force F, as shown in the schematic Fig. 4.1(A). The maximum deflection of the axon is observed in the midsection and is denoted by H. The length of the axon before displacement (span) is denoted by L_x. Taking the profile of the deformed axon to be an isosceles triangle, one can compute the deflection angle θ using

$$\sin\theta = \frac{2H}{L}, \tag{B.10}$$

where L denotes the total length of the deformed axon.

It is possible to infer the elastic modulus of the axon, E, by studying the curve $F = F(\theta)$. It is assumed that the axon behaves as an elastic string and that it is pinned at its two ends. For an elastic string with spring constant κ and rest length L_0 and current length L, the tension in the string is given by

$$T = \kappa(L - L_0). \tag{B.11}$$

For an axon pinned between two points a distance L_x apart, the tension can be expressed as

$$T = \kappa(L - L_x) + T_0, \tag{B.12}$$

where $T_0 = \kappa(L_x - L_0)$ is the initial tension of the axon before displacement of the midpoint. When the axon is pulled, the axon deforms in such a way that the vertical component of the internal tension balances the pulling force (see Fig. 4.1(A)). That is,

$$F = 2T\sin\theta = 2T_0\sin\theta + 2\kappa L_x\left(\frac{1}{\cos\theta} - 1\right)\sin\theta. \tag{B.13}$$

When the deflection is small, $\theta \ll 1$, the right-hand side of the above relation can be expanded. Expanding to third order in θ, we obtain

$$F = 2T_0\theta + \left(\kappa L_x - \frac{T_0}{3}\right)\theta^3. \tag{B.14}$$

Fitting a cubic $F = b_1\theta + b_2\theta^3$ to data of the form $\{(\theta_i, F_i)\}_i$ which are obtained from the axon allows for the recovery of the series coefficients (b_1, b_2). Subsequently, we can recover (κ, T_0) by solving the system

$$\begin{aligned} b_1 &= 2T_0, \\ b_2 &= \kappa L_x - \frac{T_0}{3}. \end{aligned}$$

The authors further suggest that $T_0 \ll \kappa L_x$, which would justify the use of the simplification

$$F = 2T_0\theta + \kappa L_x \theta^3. \tag{B.15}$$

At this point we can introduce the erroneous formula that appears in [9]:

$$F = 2T_0\theta + \kappa \frac{L_x}{2} \theta^3, \tag{B.16}$$

which we were unable to justify. This may be a typesetting error, in which case formula (B.14) or formula (B.15) would have been used to analyze the data. If, however, formula (B.16) was used instead, then the true value of κ for each axon would be half of that estimated by the authors. Consequently, the true population mean of E would also be half of the value stated in the paper. That is, $E \sim 6 \pm 1$ kPa instead of $E \sim 12 \pm 2$ kPa, which is the value reported in the paper.

At the time of writing, the raw experimental data from Bernal et al. [9] were not available to us, and we did not receive a response to our request for access to them. Therefore, we cannot determine directly which of the two formulae was used in the original analysis. Nevertheless, the load-deflection curves presented in the paper allow for a partial quantitative check.

The central question is whether Bernal et al. [9] used (B.16) or instead used the correct approximation (B.15). As discussed above, if (B.16) was used, then the reported values of E would be larger than the corresponding corrected values by a factor of two. In that case, the distribution reported as

$$E \sim 12 \pm 2 \text{ kPa}$$

would instead correspond to

$$E \sim 6 \pm 1 \text{ kPa}.$$

We can formulate this comparison as a Bayesian model selection problem. Let M_1 denote the model in which the corrected elastic moduli are distributed according to

$$M_1 : \qquad E \sim \mathcal{N}\left(6000 \text{ Pa}, (1000 \text{ Pa})^2\right),$$

and let M_2 denote the model corresponding to the values reported in Bernal et al. [9],

$$M_2 : \qquad E \sim \mathcal{N}\left(12000 \text{ Pa}, (2000 \text{ Pa})^2\right).$$

The question is then which of these two distributions better explains the elastic moduli extracted from the published load-deflection curves.

Let the extracted values be denoted by E_1, E_2, E_3. The posterior probability of each model is then given by

$$\pi(M_i \mid E_1, E_2, E_3) = \frac{p(E_1, E_2, E_3 \mid M_i)\pi(M_i)}{p(E_1, E_2, E_3 \mid M_1)\pi(M_1) + p(E_1, E_2, E_3 \mid M_2)\pi(M_2)},$$

where $p(E_1, E_2, E_3 \mid M_i)$ is the likelihood of the data given model M_i and $\pi(M_i)$ is the prior probability of model M_i. In the absence of a prior reason to favour either possibility, we assign equal prior probabilities,

$$\pi(M_1) = \pi(M_2) = \frac{1}{2}.$$

Using the values extracted in Section B.1,

$$E_1 = 5312.35 \text{ Pa}, \qquad E_2 = 9023.27 \text{ Pa}, \qquad E_3 = 3937.85 \text{ Pa},$$

we obtain

$$\pi(M_1 \mid \text{data}) \approx 0.999953,$$

and

$$\pi(M_2 \mid \text{data}) \approx 0.0000468.$$

Thus, under the assumptions of this calculation, the posterior probability is overwhelmingly concentrated on M_1.

This result provides quantitative support for the interpretation that the elastic moduli inferred from the published load-deflection curves are more consistent with the corrected distribution

$$E \sim 6 \pm 1 \text{ kPa}$$

than with the distribution

$$E \sim 12 \pm 2 \text{ kPa}$$

reported in Bernal et al. [9]. Equivalently, this supports the hypothesis that the factor of $1/2$ appearing in (B.16) was used in the original parameter inference, rather than being merely a typographical error. This conclusion should be interpreted with some caution, since it relies on values extracted from the published figures rather than on the original raw data.

B.4 Extensible beam perturbation series for $f \ll 1$

Equations for $\tilde{\theta}_i$:

$$
\begin{aligned}
& \tilde{\theta}_0 = 0, \\
\mathcal{O}(f): \quad & \tilde{\theta}_1'' + (1+n_0)\left(\frac{1}{2} - n_0\,\tilde{\theta}_1\right) = 0, \quad \tilde{\theta}_1'(0) - \tilde{\kappa}\tilde{\theta}_1(0) = 0,\ \tilde{\theta}_1\left(\frac{L_0}{2\lambda}\right) = 0, \\
\mathcal{O}\left(f^2\right): \quad & \tilde{\theta}_2'' - (1+n_0)\left(n_0\,\tilde{\theta}_2 + n_1\,\tilde{\theta}_1\right) + n_1\left(\frac{1}{2} - n_0\,\tilde{\theta}_1\right) = 0, \quad \tilde{\theta}_2'(0) - \tilde{\kappa}\tilde{\theta}_2(0) = 0,\ \tilde{\theta}_2\left(\frac{L_0}{2\lambda}\right) = 0, \\
\mathcal{O}\left(f^3\right): \quad & \tilde{\theta}_3'' + \frac{1}{2}\left(\frac{1}{2} - n_0\,\tilde{\theta}_1\right)\left(2n_2 - n_0\,\tilde{\theta_1}^2 + \tilde{\theta}_1\right) \quad - \\
& n_1\left(n_1\tilde{\theta}_1 + n_0\tilde{\theta}_2\right) \quad + \\
& \frac{1}{12}\,(n_0+1)\left(-12n_2\tilde{\theta}_1 - 12n_1\tilde{\theta}_2 + 2n_0\tilde{\theta_1}^3 - 12n_0\tilde{\theta}_3 - 3\tilde{\theta_1}^2\right) = 0, \\
& \tilde{\theta}_3'(0) - \tilde{\kappa}\tilde{\theta}_3(0) = 0,\ \tilde{\theta}_3\left(\frac{L_0}{2\lambda}\right) = 0.
\end{aligned}
$$

Equations for n_i:

$$
\begin{aligned}
\mathcal{O}(f): \quad & L_0\,(1+n_0) = L_x, \\
\mathcal{O}\left(f^2\right): \quad & \int_0^{L_0/(2\lambda)} \cos\tilde{\theta}_0\,\sin\tilde{\theta}_0 - 2\,\tilde{\theta}_1\,\sin\tilde{\theta}_0 - 4\,n_0\,\tilde{\theta}_1\,\cos\tilde{\theta}_0\,\sin\tilde{\theta}_0 + 2\,n_1\,\cos\tilde{\theta}_0^2\,\mathrm{d}\sigma = 0, \\
\mathcal{O}\left(f^3\right): \quad & \int_0^{L_0/(2\lambda)} \Big[n_2 - \tilde{\theta}_1^2\cos\tilde{\theta}_0 + \cos 2\tilde{\theta}_0\left(n_2 + \tilde{\theta}_1 - 2n_0\tilde{\theta}_1^2\right) \\
& -2\,\tilde{\theta}_2\,\sin\tilde{\theta}_0 - 2\sin\left(2\tilde{\theta}_0\right)\left(n_1\tilde{\theta}_1 + n_0\tilde{\theta}_2\right)\Big]\,\mathrm{d}\sigma = 0
\end{aligned}
$$

B.5 Anisotropic model: Neurite 3

Solution curves for $E, \mathcal{B}$ and T_0 under the anisotropic beam model for Neurite 3 (see Fig. B.4).

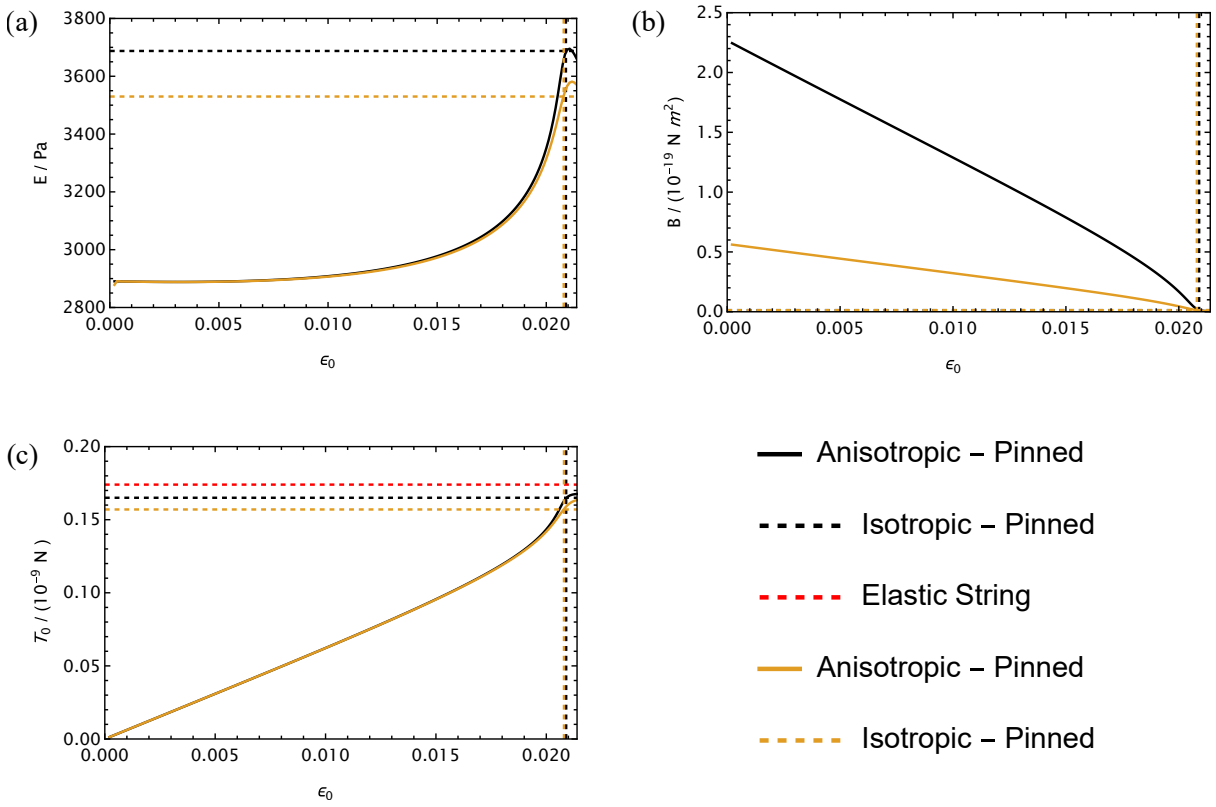


Figure B.4: Estimated values of E, $\mathcal{B}$, and T_0 for Neurite 3, shown in panels (a), (b), and (c), respectively, as functions of ε_0 under the anisotropic beam model. Results are shown for pinned boundary conditions (black solid line) and clamped boundary conditions (orange solid line).

Bibliography

[1] Roberto Alonso-Matilla, Paolo P. Provenzano, and David J. Odde. Optimal cell traction forces in a generalized motor-clutch model. *Biophysical Journal*, 122(18): 3573–3587, 2023. doi: 10.1016/j.bpj.2023.07.012.

[2] B. L. Bangasser and D. J. Odde. Master equation-based analysis of a motor-clutch model for cell traction force. *Cellular and Molecular Bioengineering*, 6(4):449–459, 2013.

[3] Benjamin L Bangasser, Steven S Rosenfeld, and David J Odde. Determinants of maximal force transmission in a motor-clutch model of cell traction in a compliant microenvironment. *Biophysical journal*, 105(3):581–592, 2013. doi: 10.1016/j.bpj.2013.06.027. URL https://www.cell.com/biophysj/fulltext/S0006-3495(11)00376-6.

[4] Benjamin L. Bangasser, Ghaidan A. Shamsan, Clarence E. Chan, Kwaku N. Opoku, Erkan Tüzel, Benjamin W. Schlichtmann, Jesse A. Kasim, Benjamin J. Fuller, Brannon R. McCullough, Steven S. Rosenfeld, and David J. Odde. Shifting the optimal stiffness for cell migration. *Nature Communications*, 8:15313, 2017. doi: 10.1038/ncomms15313.

[5] Milan Batista. Large deflections of a beam subject to three-point bending. *International Journal of Non-Linear Mechanics*, 69:84–92, 2015.

[6] Milan Batista. Analytical solution for large deflection of reissner s beam on two supports subjected to central concentrated force. *International Journal of Mechanical Sciences*, 107:13–20, 2016.

[7] Milan Batista. A closed-form solution for reissner planar finite-strain beam using jacobi elliptic functions. *International Journal of Solids and Structures*, 87:153–166, 2016.

[8] George I. Bell. Models for the specific adhesion of cells to cells. *Science*, 200(4342): 618–627, 1978. doi: 10.1126/SCIENCE.347575.

[9] Roberto Bernal, Pramod A Pullarkat, and Francisco Melo. Mechanical properties of axons. *Physical review letters*, 99(1):018301, 2007.

[10] Roberto Bernal, Francisco Melo, and Pramod A Pullarkat. Drag force as a tool to test the active mechanical response of pc12 neurites. *Biophysical journal*, 98(4): 515–523, 2010.

[11] Roman Borisyuk, Tom Cooke, and Alan Roberts. Stochasticity and functionality of neural systems: mathematical modelling of axon growth in the spinal cord of tadpole. *Biosystems*, 93(1-2):101–114, 2008.

[12] Paul C Bressloff. Stochastic resetting and the mean-field dynamics of focal adhesions. *Physical Review E*, 102(2):022134, 2020. doi: 10.1103/PhysRevE.102.022134.

[13] Clarence E. Chan and David J. Odde. Traction dynamics of filopodia on compliant substrates. *Science*, 322(5908):1687–1691, dec 2008. ISSN 00368075. doi: 10.1126/science.1163595.

[14] Jen-San Chen and Shao-Yu Hung. Exact snapping loads of a buckled beam under a midpoint force. *Applied Mathematical Modelling*, 36(4):1776–1782, 2012.

[15] Jen-San Chen and Huai-Wen Tsao. Static snapping load of a hinged extensible elastica. *Applied Mathematical Modelling*, 37(18-19):8401–8408, 2013.

[16] T. J. Dennerll, P. Lamoureux, R. E. Buxbaum, and S. R. Heidemann. The cytomechanics of axonal elongation and retraction. *Journal of Cell Biology*, 109(6 I): 3073–3083, 1989. ISSN 00219525. doi: 10.1083/jcb.109.6.3073.

[17] Alberto Elosegui-Artola, Elsa Bazellières, Michael D Allen, Ion Andreu, Roger Oria, Raimon Sunyer, Jennifer J Gomm, John F Marshall, J Louise Jones, Xavier Trepat, et al. Rigidity sensing and adaptation through regulation of integrin types. *Nature materials*, 13(6):631–637, 2014.

[18] Alberto Elosegui-Artola, Roger Oria, Yunfeng Chen, Anita Kosmalska, Carlos Pérez-González, Natalia Castro, Cheng Zhu, Xavier Trepat, and Pere Roca-Cusachs. Mechanical regulation of a molecular clutch defines force transmission and transduction in response to matrix rigidity. *Nature cell biology*, 18(5):540–548, 2016.

[19] Alberto Elosegui-Artola, Xavier Trepat, and Pere Roca-Cusachs. Control of mechanotransduction by molecular clutch dynamics. *Trends in Cell Biology*, 28(5):356–367, 2018. doi: 10.1016/j.tcb.2018.01.008.

[20] T Erdmann and Ulrich S Schwarz. Stability of adhesion clusters under constant force. *Physical review letters*, 92(10):108102, 2004.

[21] Jaime A Espina, Cristian L Marchant, and Elias H Barriga. Durotaxis: the mechanical control of directed cell migration. *The FEBS journal*, 289(10):2736–2754, 2022. doi: 10.1111/febs.15862.

[22] Kristian Franze. Integrating chemistry and mechanics: the forces driving axon growth. *Annual review of cell and developmental biology*, 36(1):61–83, 2020.

[23] Kristian Franze and Jochen Guck. The biophysics of neuronal growth. *Reports on Progress in Physics*, 73(9), sep 2010. ISSN 00344885. doi: 10.1088/0034-4885/73/9/094601.

[24] Fernanda Gárate, María Pertusa, Yahaira Arana, and Roberto Bernal. Non-invasive neurite mechanics in differentiated pc12 cells. *Frontiers in cellular neuroscience*, 12: 194, 2018.

[25] JA Garcia, JM Pena, S McHugh, and A Jérusalem. A model of the spatially dependent mechanical properties of the axon during its growth. *Computer Modeling in Engineering & Sciences(CMES)*, 87(5):411–432, 2012.

[26] A Goriely, J Garcia-Grajales, and A Jérusalem. Continuum mechanical modeling of axonal growth. *Computer Methods in Applied Mechanics and Engineering*, 314, 2016.

[27] Alain Goriely. *The mathematics and mechanics of biological growth*, volume 45 of *Interdisciplinary applied mathematics*. Springer-Verlag, New York, 1 edition, 2017. doi: 10.1007/978-0-387-87710-5.

[28] Alain Goriely, Silvia Budday, and Ellen Kuhl. Neuromechanics: From neurons to brain. In *Advances in Applied Mechanics*, volume 48, pages 79–139. Academic Press Inc., 2015. doi: 10.1016/bs.aams.2015.10.002.

[29] H. G.E. Hentschel and A. Van Ooyen. Models of axon guidance and bundling during development. *Proceedings of the Royal Society B: Biological Sciences*, 266(1434): 2231–2238, nov 1999. ISSN 14712970. doi: 10.1098/rspb.1999.0913.

[30] HGE Hentschel and A Van Ooyen. Dynamic mechanisms for bundling and guidance during neural network formation. *Physica A: Statistical Mechanics and its Applications*, 288(1-4):369–379, 2000.

[31] Ouyang Hui, Eric Nauman, and Riyi Shi. Contribution of cytoskeletal elements to the mechanical property of axons. In *2010 18th Biennial University/Government/Industry Micro/Nano Symposium*, pages 1–5. IEEE, 2010.

[32] Chyanbin Hwu. *Infinite Space, Half-Space, and Bimaterials*, pages 87–113. Springer US, Boston, MA, 2010. ISBN 978-1-4419-5915-7. doi: 10.1007/978-1-4419-5915-7_4. URL https://doi.org/10.1007/978-1-4419-5915-7_4.

[33] Callen Hyland, Aaron F Mertz, Paul Forscher, and Eric Dufresne. Dynamic peripheral traction forces balance stable neurite tension in regenerating aplysia bag cell neurons. *Scientific reports*, 4(1):4961, 2014.

[34] Aleksi Isomursu, Keun-Young Park, Jay Hou, Bo Cheng, Mathilde Mathieu, Ghaidan A Shamsan, Benjamin Fuller, Jesse Kasim, M Mohsen Mahmoodi, Tian Jian Lu, et al. Directed cell migration towards softer environments. *Nature Materials*, pages 1–10, 2022. doi: 10.1038/s41563-022-01294-2.

[35] Christoforos Kassianides, Alain Goriely, and Hadrien Oliveri. The multiscale mechanics of axon durotaxis. *Journal of the Mechanics and Physics of Solids*, 200: 106134, 2025.

[36] MICHAEL J Katz. How straight do axons grow? *Journal of Neuroscience*, 5(3): 589–595, 1985. doi: 10.1523/jneurosci.05-03-00589.1985.

[37] Daniel Koch, William J Rosoff, Jiji Jiang, Herbert M Geller, and Jeffrey S Urbach. Strength in the periphery: growth cone biomechanics and substrate rigidity response in peripheral and central nervous system neurons. *Biophysical journal*, 102(3):452–460, 2012. doi: 10.1016/j.bpj.2011.12.025.

[38] David E. Koser, Amelia J. Thompson, Sarah K. Foster, Asha Dwivedy, Eva K. Pillai, Graham K. Sheridan, Hanno Svoboda, Matheus Viana, Luciano da Fontoura Costa, Jochen Guck, Christine E. Holt, and Kristian Franze. Mechanosensing is critical for axon growth in the developing brain. *Nature neuroscience*, 19(12):1592, 2016. doi: https://doi.org/10.1038/nn.4394.

[39] Mihály Kovács, Judit Tóth, Csaba Hetényi, András Málnási-Csizmadia, and James R Sellers. Mechanism of blebbistatin inhibition of myosin ii. *Journal of Biological Chemistry*, 279(34):35557–35563, 2004.

[40] Michael Krieg, Jan Stühmer, Juan G Cueva, Richard Fetter, Kerri Spilker, Daniel Cremers, Kang Shen, Alexander R Dunn, and Miriam B Goodman. Genetic defects

in β-spectrin and tau sensitize c. elegans axons to movement-induced damage via torque-tension coupling. *Elife*, 6:e20172, 2017.

[41] Johannes K Krottje and Arjen van Ooyen. A mathematical framework for modeling axon guidance. *Bulletin of mathematical biology*, 69(1):3–31, 2007.

[42] Philip Lamoureux, Robert E Buxbaum, and Steven R Heidemann. Direct evidence that growth cones pull. *Nature*, 340(6229):159–162, 1989.

[43] Georgina E Lang, Sarah L Waters, Dominic Vella, and Alain Goriely. Axonal buckling following stretch injury. *Journal of Elasticity*, 129(1):239–256, 2017.

[44] Chihung H Lin, Enilza M Espreafico, Mark S Mooseker, and Paul Forscher. Myosin drives retrograde f-actin flow in neuronal growth cones. *Neuron*, 16(4):769–782, 1996. doi: 10.1016/s0896-6273(00)80097-5.

[45] Chun-Min Lo, Hong-Bei Wang, Micah Dembo, and Yu-li Wang. Cell movement is guided by the rigidity of the substrate. *Biophysical journal*, 79(1):144–152, 2000.

[46] Simon W Moore, Nicolas Biais, and Michael P Sheetz. Traction on immobilized netrin-1 is sufficient to reorient axons. *Science*, 325(5937):166–166, 2009.

[47] Dean Mortimer, James Feldner, Tim Vaughan, Irina Vetter, Zdenka Pujic, William J. Rosoff, Kevin Burrage, Peter Dayan, Linda J. Richards, and Geoffrey J. Goodhill. A bayesian model predicts the response of axons to molecular gradients. *Proceedings of the National Academy of Sciences of the United States of America*, 106(25):10296–10301, 2009. doi: 10.1073/pnas.0900715106.

[48] Duncan Mortimer, Thomas Fothergill, Zac Pujic, Linda J. Richards, and Geoffrey J. Goodhill. Growth cone chemotaxis. *Trends in Neurosciences*, 31(2):90–98, 2008. ISSN 0166-2236. doi: 10.1016/j.tins.2007.11.008.

[49] Duncan Mortimer, Peter Dayan, Kevin Burrage, and Geoffrey J. Goodhill. Bayes-optimal chemotaxis. *Neural Computation*, 23(2):336–373, 2011. doi: 10.1162/NECO_a_00075.

[50] Faustino Mujika, Ainhoa Arrese, Itziar Adarraga, and Usue Oses. New correction terms concerning three-point and four-point bending tests. *Polymer Testing*, 55:25–37, 2016.

[51] Alice Nicolas, Achim Besser, and Samuel A Safran. Dynamics of cellular focal adhesions on deformable substrates: consequences for cell force microscopy. *Biophysical journal*, 95(2):527–539, 2008. doi: 10.1529/biophysj.107.127399.

[52] Hadrien Oliveri and Alain Goriely. Mathematical models of neuronal growth. *Biomechanics and Modeling in Mechanobiology*, 21:89–118, jan 2022. ISSN 1617-7940. doi: 10.1007/S10237-021-01539-0.

[53] Hadrien Oliveri, Kristian Franze, and Alain Goriely. Theory for durotactic axon guidance. *Physical Review Letters*, 126(11):118101, 2021.

[54] Hadrien Oliveri, Rijk de Rooij, Ellen Kuhl, and Alain Goriely. Rheology of growing axons. *Physical Review Research*, 4(3):033125, 2022.

[55] Matthew O'Toole and Kyle E. Miller. The role of stretching in slow axonal transport. *Biophysical Journal*, 100(2):351–360, jan 2011. ISSN 15420086. doi: 10.1016/j.bpj.2010.12.3695.

[56] Matthew O'Toole, Phillip Lamoureux, and Kyle E. Miller. A physical model of axonal elongation: Force, viscosity, and adhesions govern the mode of outgrowth. *Biophysical Journal*, 94(7):2610–2620, 2008. ISSN 15420086. doi: 10.1529/biophysj.107.117424.

[57] Yanthe E Pearson, Emilio Castronovo, Tara A Lindsley, and Donald A Drew. Mathematical modeling of axonal formation part i: geometry. *Bulletin of mathematical biology*, 73(12):2837–2864, 2011.

[58] Stephen J Peter and Mohammad RK Mofrad. Computational modeling of axonal microtubule bundles under tension. *Biophysical journal*, 102(4):749–757, 2012.

[59] Samuel Poincloux, Tian Chen, Basile Audoly, and Pedro M Reis. Bending response of a book with internal friction. *Physical Review Letters*, 126(21):218004, 2021.

[60] Robert J Polackwich, Daniel Koch, Ryan McAllister, Herbert M Geller, and Jeffrey S Urbach. Traction force and tension fluctuations in growing axons. *Frontiers in cellular neuroscience*, 9:417, 2015.

[61] William H Press, Saul A Teukolsky, William T Vetterling, and Brian P Flannery. *Numerical Recipes The Art of Scientific Computing*. Cambridge University Press, 3rd edition, 2007. ISBN 0521880688. URL http://apps.nrbook.com/empanel/index.html{#}.

[62] Alan Roberts, Deborah Conte, Mike Hull, Robert Merrison-Hort, Abul Kalam Al Azad, Edgar Buhl, Roman Borisyuk, and Stephen R Soffe. Can simple rules control development of a pioneer vertebrate neuronal network generating behavior? *Journal of Neuroscience*, 34(2):608–621, 2014.

[63] Estuardo Robles and Timothy M Gomez. Focal adhesion kinase signaling at sites of integrin-mediated adhesion controls axon pathfinding. *Nature neuroscience*, 9(10): 1274–1283, 2006.

[64] B. Sabass and U. S. Schwarz. Modeling cytoskeletal flow over adhesion sites: competition between stochastic bond dynamics and intracellular relaxation. *Journal of Physics: Condensed Matter*, 22(19):194112, 2010.

[65] Julia Schaeffer, Isabell P. Weber, Amelia J. Thompson, Roger J. Keynes, and Kristian Franze. Axons in the chick embryo follow soft pathways through developing somite segments. *Frontiers in Cell and Developmental Biology*, 10, 2022. ISSN 2296-634X. doi: 10.3389/fcell.2022.917589. URL https://www.frontiersin.org/articles/10.3389/fcell.2022.917589.

[66] Pierre Sens. Rigidity sensing by stochastic sliding friction. *Europhysics Letters*, 104 (3):38003, 2013. doi: 10.1209/0295-5075/104/38003.

[67] Adam Shellard and Roberto Mayor. Durotaxis: The hard path from in vitro to in vivo. *Developmental Cell*, 56(2):227–239, 2021. ISSN 1534-5807. doi: 10.1016/j.devcel.2020.11.019. URL https://www.sciencedirect.com/science/article/pii/S153458072030928X.

[68] Wendy Kuhn Silk and Ralph O. Erickson. Kinematics of plant growth. *Journal of Theoretical Biology*, 76(4):481–501, 1979. ISSN 0022-5193. doi: https://doi.org/10.1016/0022-5193(79)90014-6. URL https://www.sciencedirect.com/science/article/pii/0022519379900146.

[69] Akbar Solhtalab, Ali H Foroughi, Lana Pierotich, and Mir Jalil Razavi. Stress landscape of folding brain serves as a map for axonal pathfinding. *Nature Communications*, 16(1):1187, 2025.

[70] M. Srinivasan and S. Walcott. Binding site models for friction due to the formation and rupture of bonds: state-function formalism, force–velocity relations, response to slip velocity transients, and slip stability. *Physical Review E*, 80(4):046124, 2009.

[71] Daniel M. Suter and Kyle E. Miller. The emerging role of forces in axonal elongation. *Progress in Neurobiology*, 94(2):91–101, jul 2011. ISSN 03010082. doi: 10.1016/j.pneurobio.2011.04.002.

[72] Amelia J Thompson, Eva K Pillai, Ivan B Dimov, Sarah K Foster, Christine E Holt, and Kristian Franze. Rapid changes in tissue mechanics regulate cell behaviour in

the developing embryonic brain. *eLife*, 8:e39356, jan 2019. ISSN 2050-084X. doi: 10.7554/eLife.39356. URL https://doi.org/10.7554/eLife.39356.

[73] Caterina Tomba, Camille Migdal, David Fuard, Catherine Villard, and Alice Nicolas. Poly-l-lysine/laminin surface coating reverses glial cell mechanosensitivity on stiffness-patterned hydrogels. *ACS Applied Bio Materials*, 5(4):1552–1563, 2022.

[74] Lloyd N Trefethen. *Spectral methods in MATLAB*. SIAM, 2000.

[75] Stephen G Turney and Paul C Bridgman. Laminin stimulates and guides axonal outgrowth via growth cone myosin ii activity. *Nature neuroscience*, 8(6):717–719, 2005.

[76] Goto Yoshiaki, Yoshimitsu Tomoo, and Obata Makoto. Elliptic integral solutions of plane elastica with axial and shear deformations. *International Journal of Solids and Structures*, 26(4):375–390, 1990.

[77] Xiaojun Yu and Ravi V Bellamkonda. Dorsal root ganglia neurite extension is inhibited by mechanical and chondroitin sulfate-rich interfaces. *Journal of neuroscience research*, 66(2):303–310, 2001.